Plasmonics and Magnetism from Doped Colloidal Indium Oxide Nanocrystals

A thesis

submitted in partial fulfilment

of the requirements for the

Doctorate of Philosophy

By

Bharat Tandon

(20132010)

Department of Chemistry,

Indian Institute of Science Education and Research (IISER),

Pune, India – 411008

January 2019

DECLARATION

I declare that this written submission represents my ideas in my own words and wherever other's ideas have been included, I have adequately cited and referenced the original sources. I also declare that I have adhered to all principles of academic honesty and integrity and have not misrepresented or fabricated or falsified any idea / data / fact / source in my submission. I understand that violation of the above will cause for disciplinary action by the Institute and can also evoke penal action from the sources which have thus not been properly cited or from whom proper permission has not been taken when needed.

Date:

Mr. Bharat Tandon
(ID: 20132010)

CERTIFICATE

This is to certify that this dissertation entitled "**Plasmonics and Magnetism from Doped Colloidal Indium Oxide Nanocrystals**" towards the partial fulfilment of the Integrated PhD dual degree programme at the Indian Institute of Science Education and Research, Pune represents original research carried out by Bharat Tandon at IISER Pune under my supervision. Part of the work was completed at Prof. Delia Milliron's laboratory at the University of Texas at Austin (USA). The work presented here or any part of it has not been included in any other thesis submitted previously for the award of any degree or diploma from any other university or institution.

Date:

Dr. Angshuman Nag
(Research Supervisor)

Acknowledgement

On successful completion of this thesis, it is my pleasure to acknowledge all those who have contributed towards it, be it through encouragement, guidance and/or support.

I would first like to express my sincere gratitude towards my research supervisor Dr. Angshuman Nag for his excellent guidance throughout the course of my doctoral studies. His understanding behavior, emphasis on rigorousness of concepts and constant encouragement at every step of the research has allowed me to mold into an independent researcher. I also thank him for permitting me to work on this research problem and encouraging me to cultivate my own understanding of the literature.

I am also grateful to Prof. Delia J. Milliron for guiding me during my nine-month stay at the University of Texas at Austin. The freedom and, access to facilities that she provided helped me immensely in designing research problems at my own and examine my mettle as an independent researcher. It was nothing less than an honor to work under her guidance and develop an understanding that would have otherwise taken me a lot of time to develop on my own.

I want to thank my RAC Members, Dr. Pramod Pillai and Dr. B. L. V. Prasad for their valuable comments during our annual RAC meetings. Their criticality and attention to detail encouraged me to investigate my claims and understanding of concepts more thoroughly before presenting, whether in written or oral form.

I want to thank all my lab mates in both Dr. Nag's and Prof. Milliron's group for reviewing my work critically, suggesting me with experiments and comforting me during several roadblocks during this long tenure of 6 years.

I can't imagine my Ph.D. with the constant love and support of my family and friends specially the awesome iPhD batch of 2013. They have played a very significant role in ensuring that I am always in the best mental health to conduct my research and cope with the failures therein.

I would like to also thank SAIF (IIT-Bombay), University of Mumbai, NCL-Pune, University of Pune and Texas Material Research Institute where a lot of the experiments were carried out and all the agencies who have funded me during the tenure of my doctoral studies particularly, CSIR, Fulbright-Nehru Doctoral Research fellowship, USIEF, and UT-Austin.

List of Abbreviations

AZO: Al-doped ZnO

BMP: Bound Magnetic Polaron

BE: Binding Energy

CBM: Conduction Band Minimum

DMSO: Dilute Magnetic Semiconductor Oxide

DMS: Dilute Magnetic Semiconductor

DMF: N, N-Dimethylformaminde

EDX: Energy Dispersive X-ray Absorption

EP: Ellipsometric Porosimetry

EXAFS: Extended X-ray Absorption Fine Structure

EPR: Electron Paramagnetic Resonance

FC: Field Cooling

FMR: Ferromagnetic Resonance

FTIR: Fourier Transform Infrared

FWHM: Full Width at Half Maximum

HWHM: Half Width at Half Maximum

HRTEM: High Resolution Transmission Electron Microscopy

ITO: Sn-doped In_2O_3

ICP-AES: Inductively Coupled Plasma Atomic Emission Spectroscopy

LSPR: Localized Surface Plasmon Resonance

MIR: Mid-Infrared

MG-EMA: Maxwell-Garnet Effective Medium Approximation

NC: Nanocrystal

NIR: Near-Infrared

Q-factor: Quality Factor

RT: Room Temperature

SC: Semiconductor

SEC: Spectroelectrochemistry

SEIRA: Surface Enhanced Infrared Absorption

STEM: Scanning Transmission Electron Microscopy

TBATFSI: Tetrabutylammonium bis (trifloromethanesulfonyl) imide

TCO: Transparent Conducting Oxide

TCE: Tetrachloroethylene

TGA: Thermogravimetric Analysis

TEM: Transmission Electron Microscopy

T.M.: Transition Metal

VBM: Valence Band Maximum

XANES: X-ray Absorption Near-Edge Structure

XPS: X-ray Photoelectron Spectroscopy

XRD: X-ray Diffraction

ZFC: Zero Field Cooling

PCGA: Potentiondynamic Cycling with Galvanostatic Acceleration

Synopsis

This thesis focuses on utilizing codoping in nanocrystals (NCs) as an approach to introduce multifunctionality in a system. Dopants capable of introducing different functionalities are incorporated in the host lattice simultaneously and interactions between the dopants and the functionalities introduced by them are investigated. More specifically, simultaneous inclusion of Sn^{4+} and a transition metal dopant in In_2O_3 NCs allows the codoped NCs to exhibit tunable high electrical conductivity, localized surface plasmon resonance (LSPR) and magnetism. The transition metal dopant is persistently changed between thesis Chapters 2-4A to maximize the efficiency of either LSPR or magnetism. In Chapter 4B, we rationalize the properties of a dopant to exhibit LSPR with a high figure of merit and discover a new LSPR system using the strategy. In Chapter-5, we use one of the codoped NC system synthesized by us to fundamentally understand the different parameters that govern electrochemical LSPR modulation under an applied external potential. We summarize the impacts of our results on the current literature and the future potential of our NC systems in the outlook and future directions section.

Chapter-1: Introduction

In this chapter, we first introduce transparent conducting oxides (TCOs) as metal oxide systems that can simultaneously exhibit mutually exclusive properties of high electrical conductivity and transparency to the visible light. We then define how the approach of lattice doping could enhance these properties and even introduce new ones. Even decreasing the size of highly doped TCOs to nano-regime enhances the optical properties by introducing LSPR. We define the thesis motivation as the approach of combining the power of doping and size to yield codoped TCO NCs that could allow either a new control over the existing properties or yield never-observed properties by interactions between the dopants. The choice of host system and dopants to yield these codoped TCO NCs is rationalized along with the research objectives we intend to accomplish through the work. For a reader to better understand the research carried out in the thesis, we have also discussed fundamentals of doping, LSPR, magnetism and colloidal synthesis of NCs.

Chapter-2: Tunable Plasmonics and Magnetism from Fe-Sn Codoped In_2O_3 Nanocrystals

With In_2O_3 as the host lattice, we chose Fe^{3+} and Sn^{4+} as the two dopants to yield Fe-Sn codoped In_2O_3 NCs. While Sn^{4+} doping introduces high electrical conductivity and LSPR in the near-infrared (NIR) region, the localized spins introduced through Fe^{3+} doping in In_2O_3 was expected

to induce magnetism. The Fe-Sn codoped In_2O_3 NCs synthesized by us is the first report of colloidally prepared In_2O_3 codoped NCs in the literature. More importantly, we observe interactions between the two dopants. While keeping the Sn doping constant, an increase in the Fe codoping concentration tunes LSPR band from 2200-3500 nm and decreases electrical conductivity systematically. Elucidating the local structure through EXAFS and XANES studies revealed partial conversion of Fe^{3+} to Fe^{2+} ions by consuming the electrons released by Sn^{4+}. On the other hand, an increase in Sn codoping (while keeping the Fe doping percentage constant) increased the extent of magnetization imparted in the system by coupling distantly located Fe^{3+} ions through electron-mediated magnetic coupling. Attributed to the interactions between dopants, Fe-Sn codoped In_2O_3 NCs can thus exhibit tunable LSPR, electrical conductivity and magnetism from the same system which has not been observed in literature so far.

Chapter-3: Delocalized Electron-Mediated Magnetic Coupling in Mn-Sn Codoped In_2O_3 Nanocrystals

Due to the conversion of a fraction of Fe^{3+} to Fe^{2+} in Fe-Sn codoped In_2O_3 NCs, the strength of the electron-mediated magnetic coupling couldn't be quantified as the increase in magnetization due to coupling of distant Fe^{3+} ions through delocalized electrons was countered by a simultaneous decrease in magnetization due to smaller magnetic moment of Fe^{2+} ion. For this purpose, we replaced Fe^{3+} with Mn^{2+}, another d^5 electronic configuration system but with a stable oxidation state. Based on this motivation, Mn-Sn codoped In_2O_3 NCs were synthesized. We used the LSPR band (an optical signature) to identify the presence of delocalized electrons (instead of the usually employed electrical conductivity, an electrical signature) that would help mediated coupling between distant Mn^{2+} ions. Our results show that there is a net increase of 30% in the magnetization as Sn^{4+} is codoped along with Mn^{2+} in In_2O_3 NCs compared to only Mn-doped In_2O_3 NCs with the same Mn doping percentage. This electron-mediated magnetic coupling helped achieve nearly ideal 4.8 μ_B/Mn^{2+} ion in 1.3% Mn-10% Sn codoped In_2O_3 NCs against 3.5 μ_B/Mn^{2+} ion for 1.3% Mn-doped In_2O_3 NCs.

Chapter-4A: Size-Induced Enhancement of LSPR Quality Factor from Cr-Sn Codoped In_2O_3 Nanocrystals

Even though we were able to demonstrate electron-mediated magnetic coupling in Fe-Sn and Mn-Sn codoped In_2O_3 NCs, the LSPR in both these system was abysmally weak, mostly because Fe and Mn decrease the effective electron density along with scattering electrons through electrostatic

interactions. We, therefore, decided to replace Mn^{2+} with Cr^{3+}, which is isovalent with In^{3+} of the host lattice In_2O_3. Increase in Cr doping in In_2O_3 increases the NC diameter systematically which allowed us to probe the dependence of the figure of merit (Q-factor, defined as the ratio of LSPR peak energy to LSPR linewidth) on the NC diameter. Surprisingly, Cr-Sn codoped In_2O_3 NCs display the highest Q-factors (5.0-7.2) from any doped In_2O_3 NC system. We used the defect chemistry of Sn-doped In_2O_3 (ITO) to fundamentally understand this unexpected observation. We concluded that a change in the ratio of concentration of Sn in the core and surface of NCs increases the LSPR energy whereas a decrease in ionized impurity scattering and surface scattering leads to low LSPR linewidth and hence exceptionally high Q-factors.

Chapter 4B: Dopant Selection Strategy for High LSPR Quality Factor from Doped In_2O_3 Nanocrystals

While exceptionally high LSPR Q-factors could be obtained from Cr-Sn codoped In_2O_3 NCs, we understand that it was an accidental observation and we neither expected nor intended to achieve such high LSPR Q-factors. However, high LSPR Q-factors are more than desirable for different applications and difficult to achieve. We, therefore, developed a selection strategy that employs the properties of an element (such as charge-to-radius ratio, electronegativity, reduction potential) to determine whether it would yield high Q-factors in a particular host. We then used the same selection strategy to discover Zr^{4+}-doped In_2O_3 NCs as a high LSPR Q-factor material. Not only that, dopant activation and LSPR linewidth in Zr^{4+}-doped In_2O_3 NCs is comparable to one of the best among all degenerately doped LSPR materials.

Chapter 5: Understanding Electrochemical Modulation of LSPR from Cr-Sn Codoped In_2O_3 Nanocrystals

LSPR modulation using an external applied potential is particularly interesting due to their application in electrochromic windows which can change the solar transmittance according to the comfort and energy requirement. However, the LSPR modulation achieved per unit electric potential was difficult to predict due to lack of knowledge of primary factors that enable LSPR modulation in the first place. Recently proposed model attributed the LSPR modulation to the presence of depletion layer on the NC surface and showed that the extent of LSPR modulation is directly proportional to volume fraction of the depletion layer. Depletion effects which determine LSPR modulation on an individual NC scale are countered by NC-NC coupling in films. Using Cr-Sn codoped In_2O_3 NCs, we, in this chapter show that along with depletion effects, LSPR

coupling between NCs is also a primary factor in governing the LSPR modulation, however both the primary factors operate in different size regimes. While depletion effects govern LSPR modulation for small size NCs, the LSPR modulation for large size NCs is governed by LSPR coupling between NCs.

Table of Contents

Chapter-1

Introduction

1.1 Transparent conducting oxides

The human race ever since its inception, is in a constant pursuit to invent a single solution for their multiple problems. Individuals tend to prefer a Walmart or an IKEA over visiting different stores even if it is more expensive, purely for convenience purposes. Similarly, any compound machine that does the job of several simple ones would be preferred. Interestingly, this corollary could be extended to the research of materials as well. A material capable of being employed in different applications would be more suited than discrete materials fused together. Designing and discovering such materials is a key aspect to the future of human race.

Transparent conducting oxides (TCOs) are an example of such multifunctional materials that combine the visible light transparency of glass (not conducting) with the high electrical conductivity of metals (not transparent).[1] Generally, transparency to the visible light and high electrical conductivity are mutually exclusive properties in most materials. Their inclusion in a single material allows TCOs to be employed in a large number of commercial applications like solar cells, television displays, and almost all optoelectronic systems. TCOs mainly comprises of doped metal oxides such as Sn-doped In_2O_3, Al-doped ZnO, F-doped SnO_2, to name a few.[2]

The visible light transparency of TCOs is due to their large band-gap (>3 eV) which is greater than the highest energy of visible light. The presence of charged atomic-scale point defects such as oxygen vacancies and aliovalent dopants which donate a high electron density ($10^{19\text{-}21}$ cm^{-3}) contribute towards a high electrical conductivity.[2]

1.2 Doping as a tool to enhance a material's performance

The population of intrinsic defects such as oxygen vacancies in a given TCO is typically very low and therefore, to optimize the performance of a TCO to suit different commercial applications, new charged/neutral point defects are intentionally introduced in the TCO during the synthesis. This process is known as doping, where host ions are partially replaced by a foreign atoms/ions called as a dopant (Figure 1.1). Depending upon the extent and type of dopant, a dopant could either enhance an existing property of the system or even introduce a new one.

For example, Sn^{4+} doping in In_2O_3 generates extra free electrons in the lattice of In_2O_3 which increases the electron density from 10^{19} cm^{-3} for undoped In_2O_3 to $10^{20\text{-}21}$ cm^{-3} for Sn-doped In_2O_3.[2-3] This increase in electron density is also reflected as a drastic enhancement in electrical

conductivity while maintaining visible light transparency, enabling Sn-doped In_2O_3 to be one of the most commercially employed TCO in optoelectronic applications.[1]

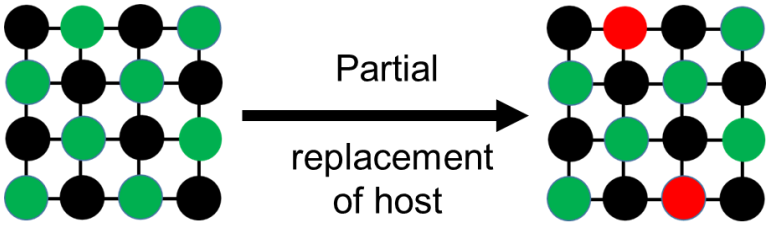

Figure 1.1: A schematic representing the concept of doping where some of the green spheres on the left (host ions) have been replaced by the dopant in red spheres. Black spheres are counter-ions in the lattice.

On the other hand, doping a magnetic ion such as Fe^{3+} (five unpaired electrons) can introduce magnetism in the system. Doping a magnetic ion in minute amounts can transform the system into a dilute magnetic semiconductor (DMS).[4] The major advantage of a DMS is that it could enable interactions between the localized spins of the magnetic ions and the delocalized charge carriers.[5] These interactions can lead to the introduction of ferromagnetism at room temperature (RT) which can help create spin-polarized electric currents, i.e. the flow of electrons is not only determined by its charge, rather it would also be dependent upon the magnetic moment of an electron. This is highly desirable for spintronics, a field of electronics that utilizes the spin of an electron along with its charge to manipulate the speed and performance of next-generation electronic devices.[6]

It is to be noted that dopants are often specific to a particular host system. This implies that while Sn^{4+} doping leads to an increase in the electrical conductivity of In_2O_3, it may not do so for another system, say ZnO. Therefore, choosing a particular dopant while considering the host-guest interactions becomes the ultimate criterion to decide whether an intended property could be achieved or not, at least theoretically.

1.3 Characterizing dopant incorporation

The different properties introduced by doping as described in the aforementioned section and thereafter can only be obtained through lattice doping, i.e. when dopants substitute the host atoms/ions in the lattice rather than just sitting on the surface of the material. This is the most non-trivial type of doping and is rather difficult to achieve synthetically. Therefore, understanding whether lattice doping is achieved or not and probing its efficiency through different characterization techniques is of paramount importance to understand the effect of doping on the properties of a material. Independent inferences obtained from multiple

characterization techniques are required to conclude lattice doping in a particular host material. Here, we briefly discuss about some of the relevant characterization techniques.

1.3.1 Composition and extended structure

Elemental analysis through energy dispersive X-ray spectroscopy (EDX) and inductively coupled plasma atomic emission spectroscopy (ICP-AES) is almost always the most basic characterization step for all doped materials. It gives an estimation of the relative atomic percentage of dopant with respect to the host atoms, or in other words, doping percentage.

X-ray photoelectron spectroscopy (XPS) can also be used to estimate the composition of a doped material. While ICP-AES or EDX gives an estimate of the overall composition, XPS being a surface sensitive technique gives an idea about the surface composition.[7] More importantly, XPS gives information about oxidation state of dopant ions in the product. Using a combination of XPS and ICP-AES, one can also comment on the radial distribution of the dopant in the material. If the doping percentage estimated by XPS is greater than that determined by ICP-AES, the dopant is present preferentially on the surface. Conversely, if doping percentage estimated by XPS is less than that determined by ICP-AES, the dopant is present preferentially in the core. A comparison of doping percentage obtained from EDX, ICP-AES or XPS can help one to determine the efficiency of doping, however, they can't differentiate between lattice doping and surface doping and should only be taken as the relative number of dopants per unit of host atoms/ions.

X-ray diffraction (XRD), on the other hand, can reveal a lot of information about the lattice doping, for relatively high level of doping, particularly when the atomic/ionic radii of the dopant and the host atom/ion are significantly different. Due to this mismatch, the lattice either expands or contracts to accommodate the incoming dopant which is larger or smaller than the host atom/ion respectively. The extent of modification of lattice parameters is directly dependent on the doping concentration, as a direct consequence of Vegard's law[8] and is often a strong signature of lattice doping (see Figure 1.2). It should be noted here that even when the size of the dopant and host ion are quite similar to each other, lattice parameters can change systematically due to modification in the concentration of point defects in the system. Similarly, this change in concentration of point defects also leads to a compensatory behavior, i.e. a decrease in the lattice parameters due to lattice doping is compensated by an increase in the lattice parameters due to change in the concentration of point defects[9] and, vice-versa.[10] XRD data, therefore, can't always convey if the structural disorder is brought up by the dopant

or by a change in the concentration of point defects and whether no lattice doping has been achieved if there is no change in the position of the diffraction peaks and vice-versa. XRD also can't probe presence of amorphous impurities and, crystalline impurities in trace amounts, but these limitations can be overcome by elucidating the local structure of the material.

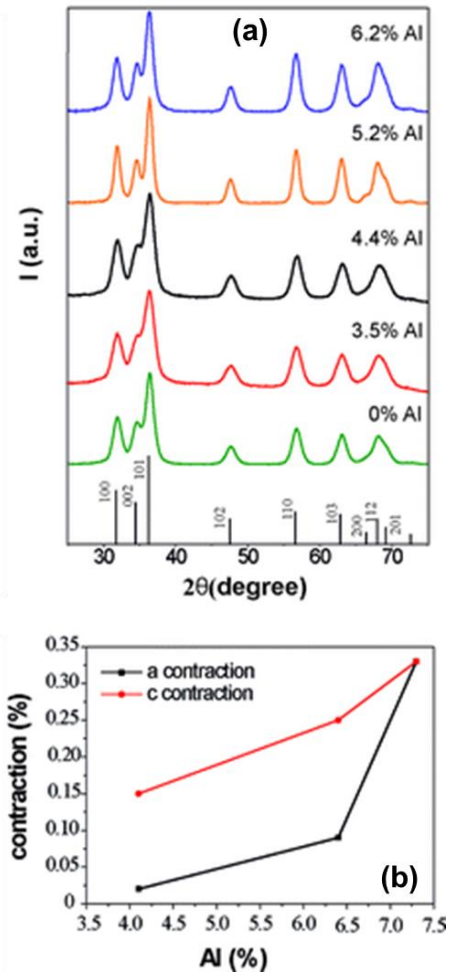

Figure 1.2: A systematic decrease in the lattice parameters of ZnO nanocrystals (NCs) with an increase in Al^{3+} doping indicating lattice doping of Al^{3+} ions. Reprinted with permission from reference 11. Copyright 2011 American Chemical Society.

1.3.2 Local structure elucidation

To effectively probe the source of the structural disorder and negate the presence of any amorphous or crystalline impurity, the local structure around each atom needs to be elucidated. The chemical environment around each atom/ion can help to determine whether the dopant is present on the surface or is doped within the lattice. X-ray absorption spectroscopy such as X-ray absorption near-edge structure (XANES) and extended X-ray absorption fine structure (EXAFS) are powerful techniques to gain information about the coordination number, valence state and nearest-neighbor information of the absorbing element.[3]

In X-ray absorption spectroscopy, an X-ray travelling through the thickness of the sample gets absorbed depending upon the incident energy of the X-ray and the composition of the sample. If the energy of the X-ray is greater than the binding energy of core electron of an atom, a photoelectron is ejected increasing the absorption sharply and resulting in an absorption edge. The photoelectron that is ejected interacts with the atoms in its vicinity and gives constructive and destructive interferences visible in the high energy regions of the absorption edge (usually 100-2000 eV greater than the absorption edge). This high energy region of the absorption edge is called EXAFS region. It can therefore reveal a lot of information about the coordination environment such as coordination number, neighboring atoms and bond distance of the element probed. Since, a mere presence of an element is enough to result in an absorption edge, it can probe both amorphous and crystalline samples and reveal the radial position of an element and whether any impurity is present or not. XANES, on the other hand, includes a small portion (~50 eV) just before and after the absorption edge and gives information about the oxidation state and coordination number of the element under consideration.

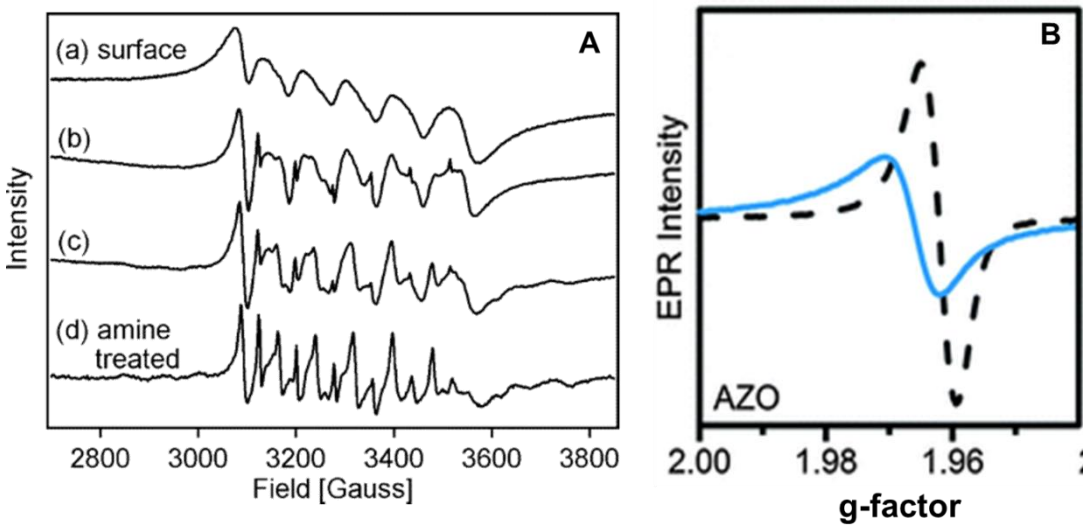

Figure 1.3: (A) X-band EPR spectra able to differentiate between surface and core-bound Mn^{2+} ions during the course of synthesis (a)-(d) of Mn^{2+} doped ZnO nanocrystals. Reprinted with permission from reference 12. Copyright 2004 American Chemical Society. (B) EPR being used to detect the presence of extra electrons introduced through Al^{3+} doping in ZnO and their partially localized behavior due to a smaller g-factor as compared to that of a free electron (g = 2.003). Reprinted with permission from reference 13. Copyright 2012 Royal Society of Chemistry.

Electron paramagnetic resonance (EPR) spectroscopy is another powerful tool to characterize the presence of paramagnetic species and the local environment around them. These paramagnetic species can arise due to the incorporation of transition metal/lanthanide dopants and/or due to the introduction of charge carriers by a particular dopant. Since EPR is very sensitive to the local coordination environment associated with the paramagnetic ion, it can

also be used to determine whether the dopant is surface-bound or core-doped. For dopants with a finite nuclear magnetic spin, while also revealing information about the oxidation state of the dopant. EPR has been instrumental in assessing the incorporation of Mn^{2+} and its radial position by determining its local structure (Figure 1.3a). On the other hand, EPR can also tell if carriers have been introduced through doping and the g-value obtained EPR can also reveal information about the extent of localization of these charge carriers inside the lattice. (Figure 1.3b)

1.4 Characterization of dopant by properties

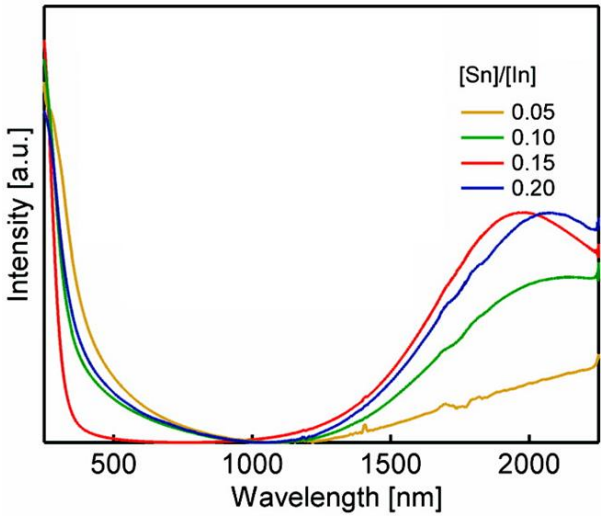

Figure 1.4: Burstein-Moss shift in Sn-doped In_2O_3 depicting that with an increase in the Sn doping percentage, the optical band-gap in the UV region increases. Reprinted with permission from reference 14. Copyright 2011 American Chemical Society.

Dopants often give rise to new properties in the system in terms of electrical, optical and magnetic properties. These properties are very sensitive to the surrounding of dopant ions and therefore, become very useful in the characterizing the presence of dopants. For example, if the dopant introduces an optical response, then optical spectroscopy becomes a tool through which lattice doping can be characterized. The states introduced by the dopant can influence the optical properties of the host in many different ways such as if the localized state of the dopant is very close to the conduction band minimum (CBM)/valence band maximum (VBM) and the dopant has a donor/acceptor behavior, it will modify the electron density associated with the system. If the dopant has a donor behavior, it is called n-type doping and if it has an acceptor nature, it is called p-type doping. In case of high doping, also known as degenerate doping (such that the fermi level is situated inside the band edges), one can observe an increase in the optical band-gap also known as Burstein-Moss shift.[14] Sn^{4+} doping in In_2O_3 can be characterized through the increase in optical band-gap as the concentration of Sn doping is increased (Figure 1.4). In a different case, there can be optical transitions within the localized

state of the incorporated dopant such as a d-d transition or a charge transfer transition. Co^{2+} doping is almost always characterized by the d-d optical transition of Co^{2+} ions. For example, for the case of Co^{2+} doping in ZnO, one can observe a transition from pink to blue when the coordinating environment surrounding the Co^{2+} ions is changed (Figure 1.5).[15]

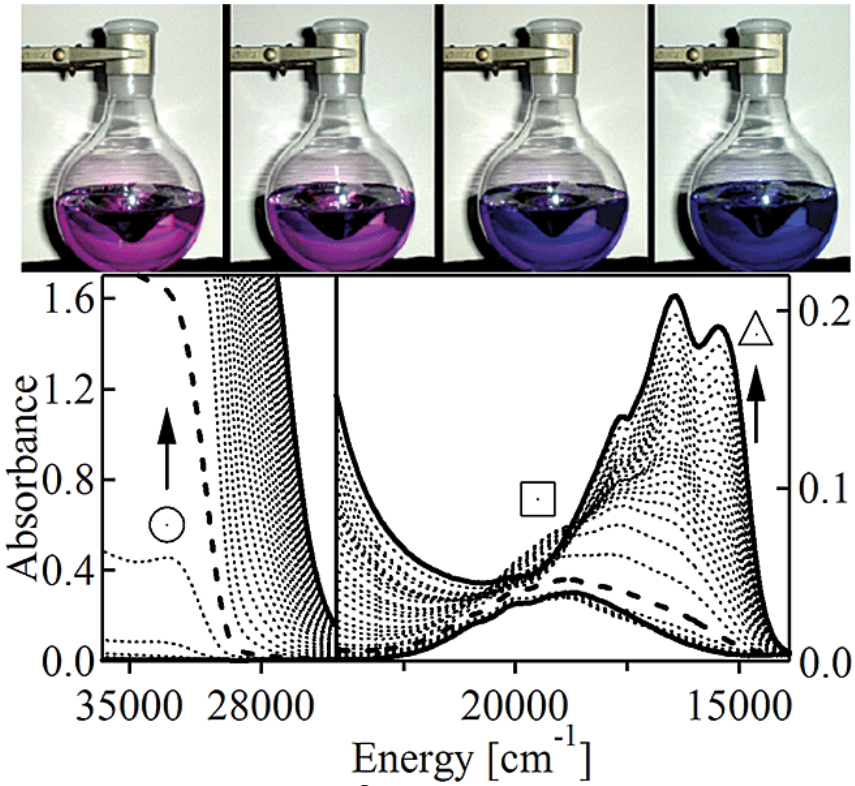

Figure 1.5: Top: During preparation of Co^{2+}-doped ZnO, the color of the dimethylsulfoxide solution changes from pink to blue with the addition of a base, indicating conversion of octahedral Co^{2+} to tetrahedral Co^{2+}. **Bottom:** Electronic absorption spectra in the ZnO band gap (left) and Co^{2+} ligand-field (right) energy regions collected with titration of 0.2 equivalent aliquots of $N(Me)_4OH$ to a DMSO solution of 98% $Zn(OAc)_2$/2% $Co^{2+}(OAc)_2$. The band gap (○), intermediate Co^{2+} ligand field (□), and substitutionally doped Co^{2+}: ZnO ligand-field (Δ) intensities are indicated. Reprinted with permission from reference 15. Copyright 2013 American Chemical Society.

1.5 Localized surface plasmon resonance (LSPR) from nanocrystals of doped TCOs

Other than doping, most properties associated with a material also vary as the size of the crystal is modified. As we increase the surface-to-volume ratio (or decrease the size of the crystal), properties associated with the bulk of crystal (such as electrical conductivity) are depressed, whereas properties associated with the surface of crystal (such as catalysis) are enhanced. Therefore, just by a variation of crystal size, one could enhance or depress a particular property of the system.

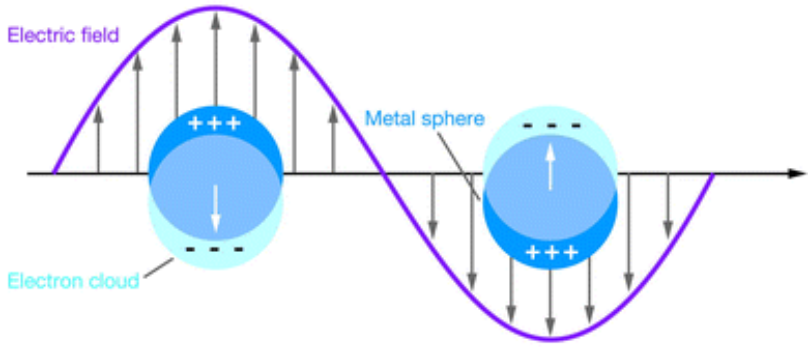

Figure 1.6: A schematic showing the phenomenon of LSPR. Reprinted with permission from Reference 16. Copyright 2007 Annual Reviews.

More specifically in this regard, when the size of the crystal is reduced to the nanometer regime, the optical properties of materials with very high carrier densities transform drastically. For example, nanocrystals (NCs) of a noble metal like Au having a carrier density in the range 10^{22-23} cm^{-3} lose their golden luster and exhibit colors ranging from wine red to purple depending upon the size of the NC.[17] This drastic change in the optical absorption for NCs is attributed to localized surface plasmon resonance (LSPR).[18] LSPR is an optical phenomenon that is observed when carrier density (>10^{18} cm^{-3}) present in a nanomaterial oscillates at a frequency resonating with the frequency of the irradiated electromagnetic radiation (see schematic in Figure 1.6).[19] Achievement of LSPR is associated with intense electric fields at the NC surface and high absorption and scattering coefficients. The frequency at which LSPR is achieved is dependent on the carrier density present and the relationship can be represented as equation (1)

$$\omega_P^2 = \frac{n_e e^2}{\varepsilon_o m^*} \qquad (1)$$

where ω_P is the bulk plasma frequency, n_e is the carrier density in cm^{-3}, e is the electronic charge, ε_o is the dielectric permittivity of vacuum/air and m^* is the effective carrier mass. Consequently, Au NCs having an electron density 5.9 x 10^{22} cm^{-3} show LSPR in the red region of the visible spectrum whereas Ag NCs exhibit LSPR in the blue region due to a higher carrier density (7.6 x 10^{22} cm^{-3}).[16, 20]

Degenerate doping in TCOs leads to the generation of large free carrier density (10^{19-21} cm^{-3}) such that the fermi level gets shifted inside the conduction band (n-type doping) or valence band (p-type doping) and subsequently, the band structure resembles closely to that of a metal. Therefore, NCs of doped TCOs also show LSPR. Over the last decade, LSPR has been observed from a variety of doped TCOs such as Sn-doped In_2O_3,[21] In-doped CdO,[5] Al-doped

ZnO[11] and vacancy- doped WO_{3-x}[22] and $Cu_{2-x}Se/S$.[19, 23] Figure 1.7 shows LSPR of different doped TCOs and other semiconductor (SC) NCs systems.[20]

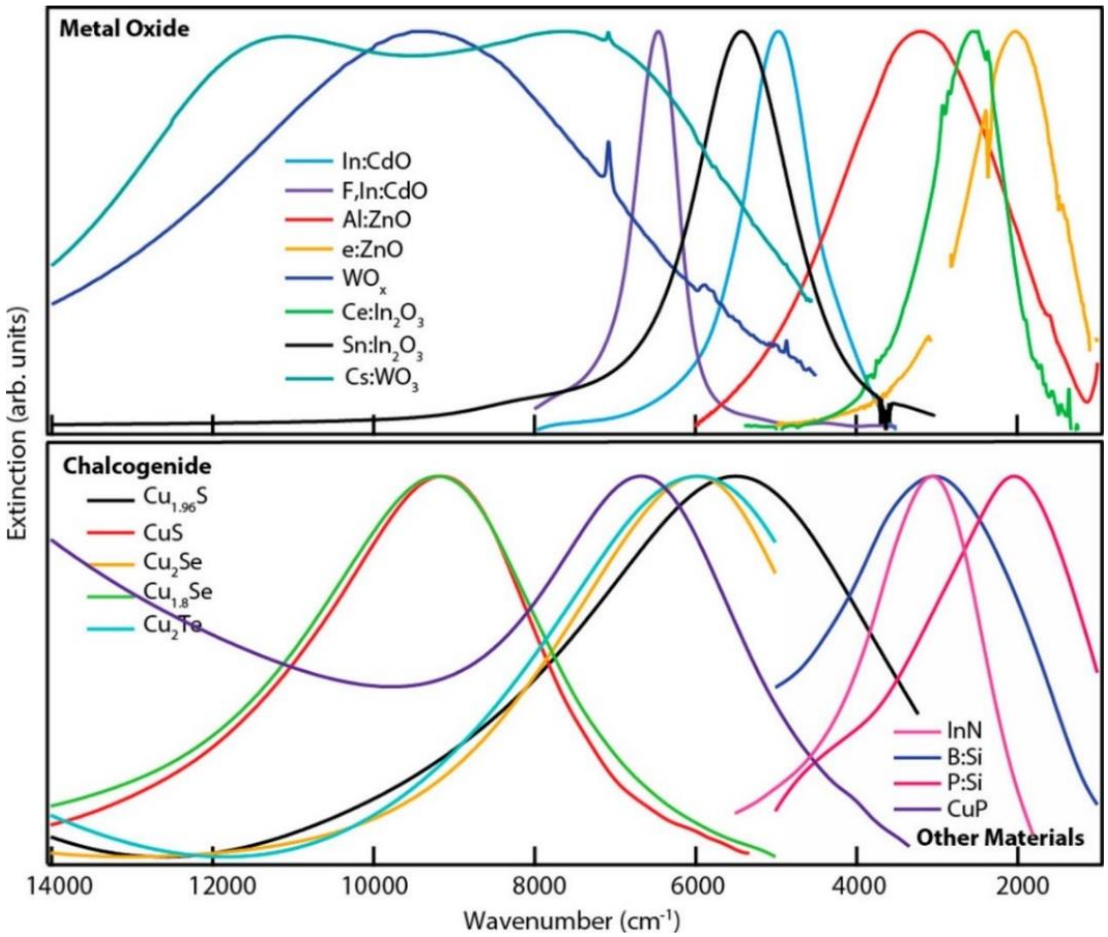

Figure 1.7: LSPR exhibited by different non-noble metal NC systems. Reprinted with permission from reference 20. Copyright 2018 American Chemical Society.

1.6 Difference between LSPR of noble metal NCs and doped TCO NCs

Even though the electronic band structure of noble metals and degenerately doped TCO are qualitatively similar to each other which enables their NCs to exhibit LSPR, there are some fundamental differences between the LSPR exhibited by the noble metal NCs and doped TCO NCs.

As described in section 1.5, the position of the LSPR band or the LSPR band peak energy is directly proportional to the square root of the carrier density in the material. Therefore, metal NCs having carrier density in the range $10^{22\text{-}23}$ cm^{-3} show LSPR band in the visible region of the electromagnetic spectrum. On the other hand, the carrier density in doped TCOs is much smaller ($10^{19\text{-}21}$ cm^{-3}) which is responsible for their LSPR band in the near-infrared (NIR) to the mid-infrared (MIR) region (Figure 1.7).

The full width at half maximum (FWHM) of the LSPR band represents the damping of the LSPR and is contributed by the scattering of charge carriers that are responsible for the LSPR. While in the case of metal NCs, electron-electron, electron-phonon, and phonon-phonon scattering are majorly responsible for the LSPR FWHM, carriers responsible for the LSPR in the doped TCO NCs are scattered extensively due to interaction of the charge carriers with the impurity ions (dopants).[24]

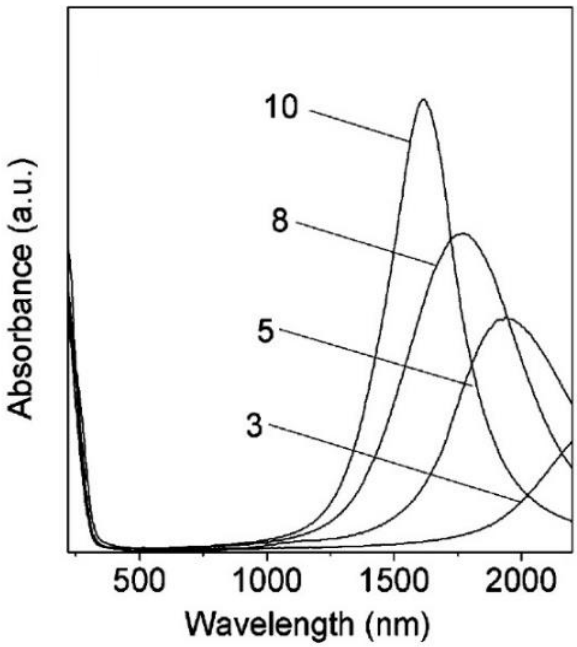

Figure 1.8: Tuning of the NIR LSPR band of Sn-doped In_2O_3 NCs by just changing the Sn doping concentration. Reprinted with permission from reference 21. Copyright 2009 American Chemical Society.

In the case of noble metal NCs, the total carrier density in the material is not tunable. Therefore, unless there is a significant change in the size and shape of the metal NC, the LSPR peak position remains almost stagnant. On the other hand, in the case of doped TCOs, the LSPR peak position can be easily controlled by changing the composition of the doped TCO or in other words, the concentration of the impurity ions that generate the carrier density (Figure 1.8). Another interesting aspect is that in the case of doped TCOs, the interband transition (valence band maximum to conduction band minimum) typically lies in the UV region of the electromagnetic spectrum and therefore, well-separated from the LSPR in the NIR region. However, in the case of noble metals, the interband transition has significant overlap with the LSPR band.

1.7 Response of the LSPR band to external stimuli

Since the LSPR peak energy is chiefly governed by the carrier density, one should ideally be able to control its position by changing the carrier density through external stimuli. This

external stimulus can be a redox agent, a photodopant or an applied potential. Here again, due to the very high carrier density of metal NCs as compared to doped TCO (or SC) NCs, change in carrier density is much more appreciable for TCO NCs than metal NCs by employing external stimuli and hence tunability of LSPR band is easily achievable in TCO NCs (Figure 1.9).

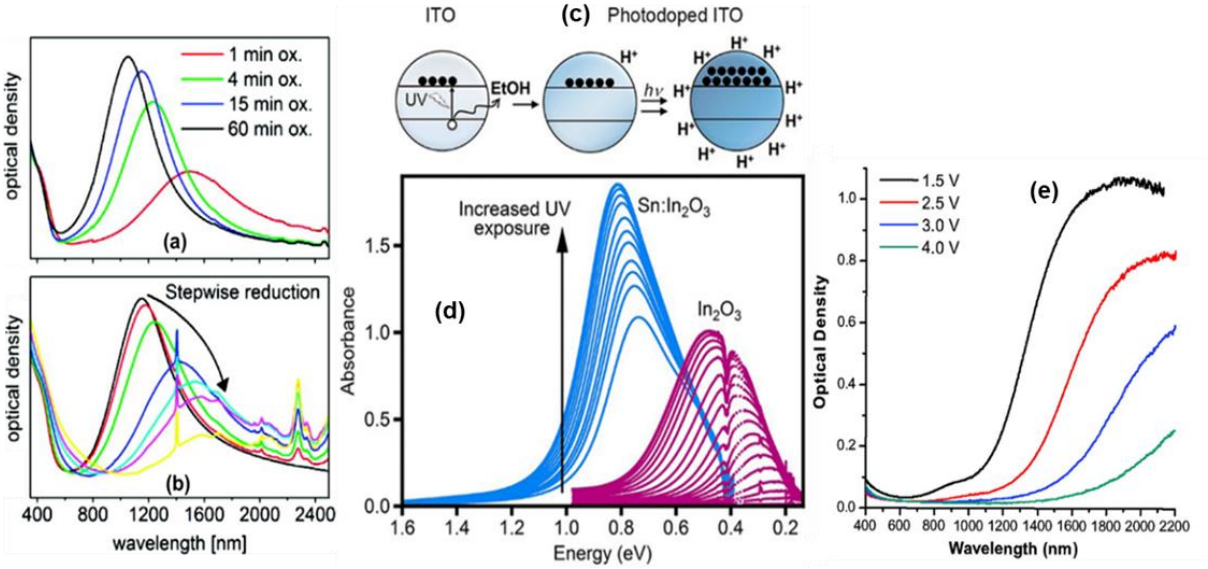

Figure 1.9: Tuning of the $Cu_{2-x}Se$ LSPR band through (a) an oxidizing agent and (b) a reducing agent. Reprinted with permission from reference 23. Copyright 2011 American Chemical Society (c) A schematic depicting the generation of charge carriers in the conduction band of Sn-doped In_2O_3 through photodoping. (d)Tuning the NIR LSPR band of Sn-doped In_2O_3 NCs and undoped In_2O_3 NCs by photodoping through UV radiation. Figure 1.9c and 1.9d have been reprinted from reference 25 which is an open-access article under the ACS Editor's Choice category, American Chemical Society. (e) Tuning the NIR LSPR band of Sn-doped In_2O_3 NCs by applying an external potential. Reprinted with permission from reference 26. Copyright 2011 American Chemical Society.

Particularly in the case of Figure 1.9e, it is practically possible to absorb a range of infrared radiations with high absorption coefficients just by changing the electric potential applied to the NC film. This possibility has emerged as a great advantage in designing smart windows. Smart windows are defined as coated-glass panes that can independently control the transmittance of light in the visible and the infrared region (Figure 1.10).[27] Since, IR radiations are associated with heat, controlling the extent of IR radiations can modulate the temperature of the room according to personal comfort and can help reduce the electricity bills by reducing the energy consumed in air-conditioning. Electrochromic windows based on plasmonics are expected to much more superior to the conventional smart windows due to faster switching times, higher absorption coefficients and higher sensitivity of transmittance to the change in the electric potential.[28]

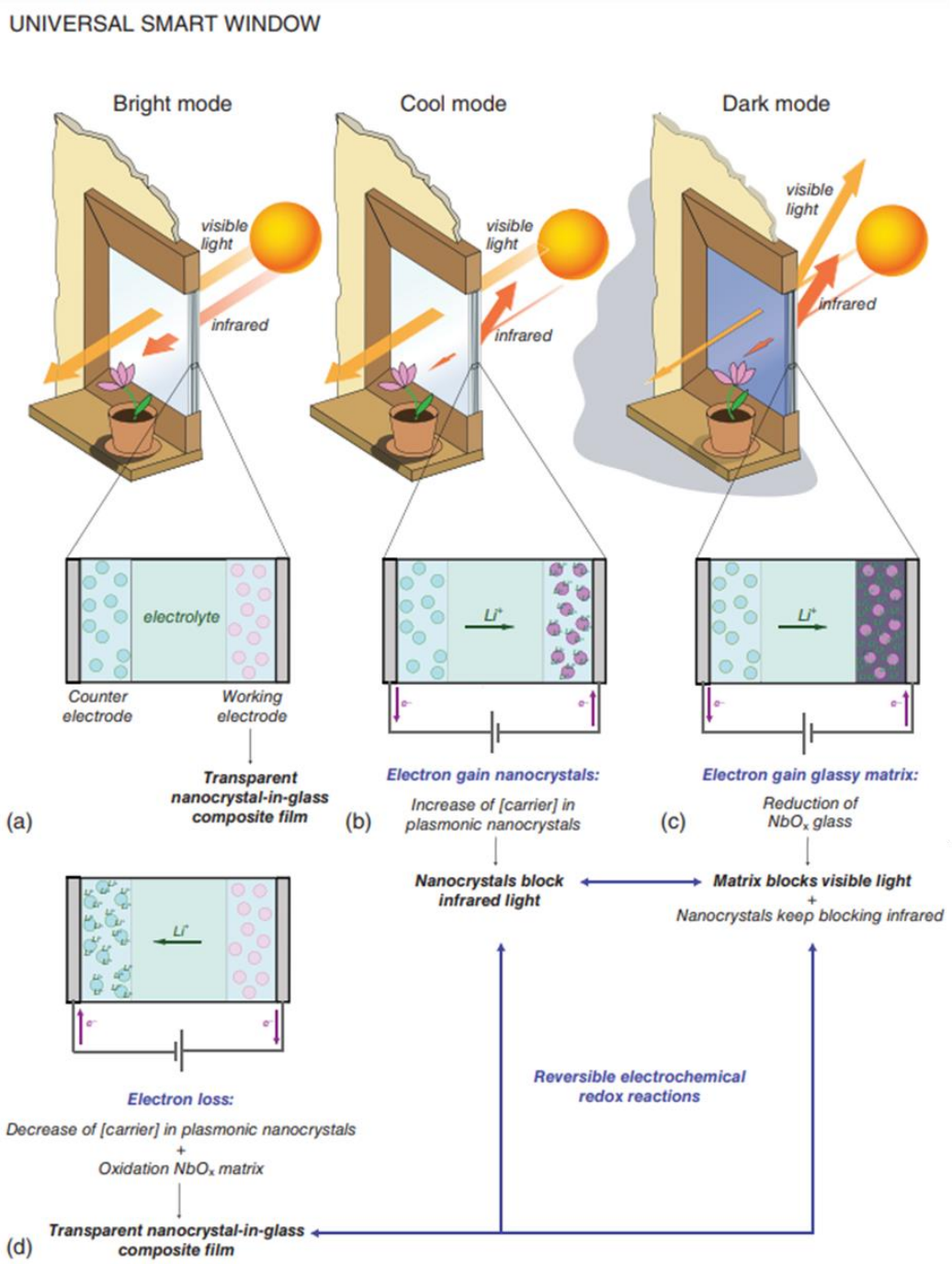

Figure 1.10: A Universal smart window made from nanocrystal-glass composite allowing independent control of the visible and infrared transmittance dynamically through dual-band electrochromism. At no external potential, the window exhibits a "bright" mode by allowing both visible and infrared radiations to enter the room. At large reducing potentials, the window accepts a "cool" mode by blocking infrared radiation while allowing visible light to pass through. At lower reducing potentials, the window switches to "dark" mode, restricting both visible and infrared radiations to enter the room. These three switching modes allows an individual to optimize the temperature and visibility in the room according to personal comfort while saving energy. Reprinted with permission from reference 27. Copyright 2013 Nature Publishing Group.

1.8 Colloidal synthesis of doped TCO NCs

Dopant incorporation with high efficiency in the NC core is a rather difficult territory to conquer and lattice doping has been non-trivial to the point that NCs were once considered as "undopable". Even though the exact reasons for this still remain unclear and vary from system to system, the difficulty associated with lattice doping was often been attributed with "self-purification" behavior of NCs which tends to expel out impurities (dopants) due to the higher formation energy of the defects.[29]

The synthesis of doped NCs takes place at much lower temperatures (<400˚C) than a macroscopic crystal and hence dopant incorporation is expected to be governed by the kinetics of the reaction and not thermal equilibrium or in general, thermodynamics. This essentially means that only after establishing a delicate balance between the growth rates of the dopant and the host, dopant incorporation could be achieved. More precisely, the efficiency of dopants incorporated in the NC is directly proportional to the amount of time they are bound to the NC surface during the growth stage of NC. Tuning the reactivity of the dopant and the host molecular precursors, their concentration, choice of surfactants and synthesis temperature to achieve this balance are the most important factors and the biggest challenge in yielding NCs with high doping levels.[29-30]

A general mechanism for yielding colloidal NCs (whether doped or undoped) uses a laboratory setup similar to shown in Figure 1.11a and relies on the understanding developed through the Lamer-Dinegar model shown in Figure 1.11b.[31] NC synthesis through a colloidal route can be divided into 3 stages. Stage (I) involves the reaction of metal precursors with the surfactants (usually organic molecules with large alkyl chains) at moderately high temperatures (typically 200-350˚C) to yield chemically reactive species known as monomers. With an increase in the duration of the reaction, the monomer concentration in the reaction mixture increases. The rate of this monomer generation is dependent on the reaction temperature with higher temperature yielding monomers faster than at lower temperature. When the monomer reaches the saturation concentration (C_s), the nucleation event can take place, however, doesn't happen due to an activation barrier for the nucleation. When the monomer concentration reaches C_{nu}^{min}, a "burst nucleation" event marks the beginning of the stage (II). As the monomer concentration reaches the supersaturation limit C_{nu}^{max}, there is an accelerated consumption of the monomers resulting in growth of the nuclei (see the exponential drop towards the end of the tage (II) in Figure 1.11b) and marking the onset of the stage (III), the growth process. The growth process relieves

the monomer concentration from the supersaturation limit, as the nuclei consumes monomers for the growth of NCs. As the growth stage proceeds, the nuclei start getting bigger and bigger.

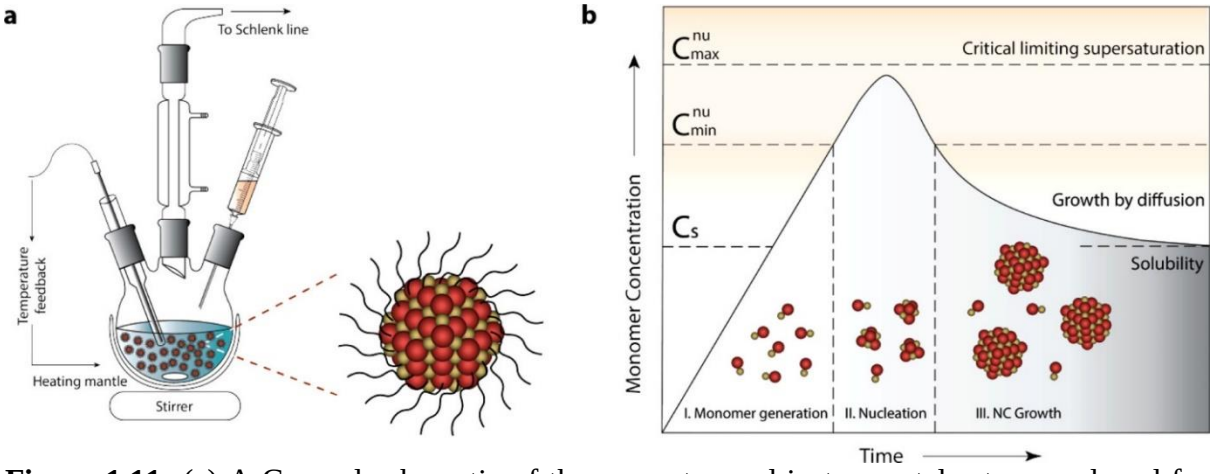

Figure 1.11: (a) A General schematic of the apparatus and instrumental setup employed for colloidal synthesis. (b) LaMer-Dinegar model of colloidal NC formation. Reprinted with permission from reference 20. Copyright 2018 American Chemical Society.

To have a control over the size and shape homogeneity of the NCs, the nucleation and the growth have to be separated from each other so as to avoid a secondary nucleation step. Based on this fundamental understanding, colloidal synthesis of TCO NCs can be categorized into three strategies: (i) heat-up method, (ii) hot-injection method, and (iii) continuous injection/slow-injection method.[20]

The heat-up method involves mixing all the reaction components such as precursors, surfactants, and solvent in a single flask and heating them under inert conditions to commence nucleation followed by subsequent growth of NCs. The precursors react with the surfactants to produce monomers which accumulate eventually to reach the critical concentration for nucleation event. Since there is an activation barrier for nucleation, nucleation and growth are decoupled temporarily as the monomer concentration drops following the growth of NCs. The extent of this decoupling can be controlled by optimizing the precursor concentration and reactivity while tuning the temperature profile during the course of the reaction. However, since there is a constant supply of heat, the monomer generation doesn't stop post the nucleation step and there can be a significant overlap between the nucleation and growth step. This can lead to a secondary nucleation event which could lead to a compromise with the size and shape homogeneity of the NCs. However, due to little complexity in the reaction procedure, the heat-up approach leads to easy scalability and a high degree of reproducibility for NCs.[32]

The hot-injection synthesis, on the other hand, requires heating up two precursors in separate reaction vessels and at a particular temperature, one of the precursors is injected rapidly into the other one. The objective is to produce a single nucleation event just after the injection followed by a growth stage such that both nucleation and growth steps are completely isolated from each other and no secondary nucleation occurs. Consequently, NCs prepared through a hot-injection have narrow size distribution and well-defined shape.[33] We note that due to the complexity involved in mixing two precursors at high temperatures, the hot-injection method is difficult to scale up, however, is incredibly useful for studies where the physical properties of the NCs are size-and shape dependent, such as LSPR.

Just like the hot-injection method, continuous injection procedure involves the injection of one precursor into another or injection of two precursors in a particular solvent. However, the injection rate in the continuous injection procedure is controlled through a syringe pump and doesn't happen instantaneously like the hot-injection technique. Injection at slow-rate results in layer by layer deposition of monomers on the NC surface resulting in highly uniform, size-controlled NCs. Such a strategy helps to avoid the Ostwald ripening that results in thermodynamically favorable size and shape during the extended growth period (after fast nucleation) in the hot-injection.[34] The continuous injection procedure also allows for deposition of the shell of a different material around the NC core just by changing the reactant solution and consequently, a precise control of dopant radial distribution in LSPR-active NCs can be achieved. Such a control over the dopant radial distribution is not allowed through the hot-injection or heat-up synthesis method and makes continuous injection procedure one of the most lucrative techniques to synthesize TCO NCs of different sizes with precise dopant distribution and NC composition.[35]

1.9 Thesis motivation: The idea of codoping in TCO NCs

As noticed in section 1.2 and 1.5, by changing the type and extent of doping or change in size, one can enhance the electrical, magnetic or optical properties in a material. Therefore, if one combines codoping (replacing host ions with two different type of dopants, Figure 1.12) with size in TCO NCs, it should be possible to design new multifunctional materials with a wide variety of applications. This is particularly important for a lot of different reasons such as:

a. It can introduce mutually exclusive properties in the material. These two functionalities may stem from two different dopants, however, will contribute towards making the system multifunctional as a whole.

b. There is a significant probability that the two dopants interact with each other being part of the same system and confined in a small NC. It could provide a new control over the existing properties implying the properties of one dopant could be controlled through the second dopant or even better could lead to new properties altogether in the system, ones which could only be observed from heterostructures till now.

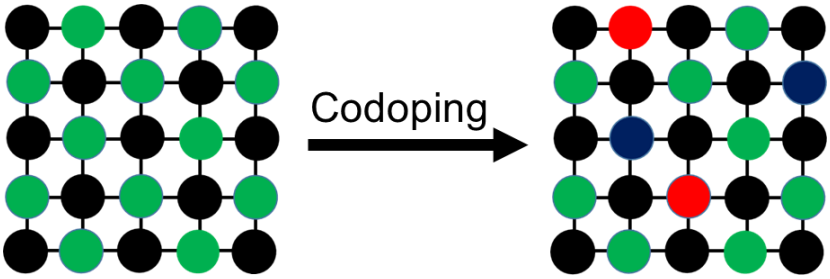

Figure 1.12: Schematic representing the concept of codoping in a lattice. In codoping, a fraction of host ions (green spheres) is replaced by dopant 1 (red) and dopant 2 (blue) simultaneously. The resulting codoped NCs will allow the two dopants to contribute to the multifunctionality of the system by introducing functionalities both individually and through interactions between one another.

1.10 Choice of the host and dopants for this thesis

For the purpose of codoping in TCO NCs, In_2O_3 was chosen as the host lattice as it is one of the most commercially important TCO and the defect chemistry of In_2O_3 is well-established. This is particularly important because the inclusion of foreign atoms in the lattice is likely to change the concentration of point defects both in the bulk and the surface of NC.[30] Fundamental understanding of these point defects is necessary to administer and pick dopants that can be doped with efficiency in the In_2O_3 lattice thereby increasing the probability that both the dopants are part of the same system.

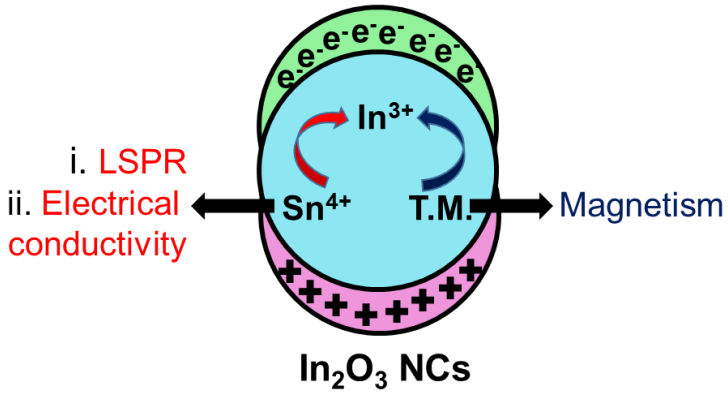

Figure 1.13: Schematic representing the system with the dopants and the functionalities introduced by the two dopants. T.M. implies transition metal.

Sn^{4+} was the choice of the first dopant because it imparts high electrical conductivity (an electrical property) and LSPR (an optical property) when doped in the In_2O_3 NC lattice. Sn-

doped In_2O_3 popularly known as indium tin oxide is one of the most commercially employed TCOs in optoelectronic applications and can be doped with high percentages in In_2O_3 lattice.[2] LSPR from Sn-doped In_2O_3 NCs has only been recently discovered and much needs to be investigated to study how the defect chemistry and presence of other codopants in the vicinity affects its LSPR.

We plan to study this perspective by codoping Sn-doped In_2O_3 with another dopant, a transition metal (T.M.) dopant. Many T.M. dopants are known to impart magnetic properties to the system and theoretical studies by Dietl. et. al[36] predicted that, in small doping concentrations, the T.M. dopants distant from each other can interact with each other through charge carriers in metal oxides which can help create spin-polarized currents. These spin-polarized currents would enable create next-generation electronic devices where the current in the circuit could be controlled through applying a magnetic field.[6] Therefore, Sn^{4+} and T.M. codoped In_2O_3 NCs was the hypothetical system designed where Sn^{4+} would provide high electrical conductivity and LSPR, whereas the T.M. dopant would yield magnetism to the system (Figure 1.13).

Another direction of choosing dopants is to optimize the LSPR properties. In this regards, we chose the dopant ions that have electron donor state either shallow or within the conduction band of In_2O_3. In addition, other relevant properties that reduce the electron scattering by ionized dopant centers are taken into account while choosing the dopants.

1.11 Objectives of the thesis

The objective of the thesis was divided into four parts.

a. Whether it is possible to colloidally synthesize a codoped In_2O_3 NC system or not? Also synthesis design for dopants to achieve the best quality of LSPR in the NIR and MIR region.

b. Considering that one might be able to synthesize such a material, are there any interactions present between the two dopants? There can be different types of interactions between the two dopants such as those listed below.

(i) Interactions between the dopants Sn^{4+} and T.M. ion. Such an interaction would mean that the properties of one dopant could be controlled by the other dopant and vice-versa due to the chemical interactions between the dopants.

(ii) Interactions between the functionalities. While Sn^{4+} donate free electrons to the In_2O_3 lattice, a T.M. ion would provide localized magnetic spins. An interaction between the functionalities would mean if the interactions between the localized magnetic spins could be

altered by the presence of free electrons donated by Sn^{4+} or the LSPR and electrical conductivity due to the free electrons could be modified by the localized magnetic spins of the T.M. ion.

(c) Whether the dopant selection can be optimized for increasing the strength of the LSPR band? The strength of the LSPR band is measured by its figure of merit known as the Quality factor or the Q-factor. Quantitatively, Q-factor is a ratio of LSPR peak energy to the LSPR FWHM and, often regarded as an important parameter for employment of LSPR in different applications such as sensing, photovoltaics and photothermal therapy. Appropriate dopant incorporation can increase the electron density in the system increasing the LSPR energy while decreasing the electron scattering that governs the LSPR FWHM, ultimately increasing the LSPR Q-factor.

(d) What are the parameters governing electrochemical modulation of LSPR? As described in section 1.7, electrochemical modulation of NIR LSPR allows it to be employed in smart window applications, however, the factors governing LSPR modulation which is responsible for absorbing a spectrum of IR radiations haven't been elucidated yet completely.

1.12 References

1. Chopra, K. L.; Major, S.; Pandya, D. K. Transparent conductors—A Status Review. *Thin Solid Films* **1983,** *102*, 1-46.
2. Ginley, D. S.; Bright, C. Transparent Conducting Oxides. *MRS Bull.* **2011,** *25*, 15-18.
3. González, G. B. Investigating the Defect Structures in Transparent Conducting Oxides Using X-ray and Neutron Scattering Techniques. *Materials* **2012,** *5*, 818.
4. Dietl, T. A Ten-Year Perspective on Dilute Magnetic Semiconductors and Oxides. *Nat. Mater.* **2010,** *9*, 965.
5. Calderón, M. J.; Das Sarma, S. Theory of Carrier Mediated Ferromagnetism in Dilute Magnetic Oxides. *Ann. Phys.* **2007,** *322*, 2618-2634.
6. Ohno, H. A Window on the Future of Spintronics. *Nat. Mater.* **2010,** *9*, 952.
7. Sarma, D. D.; Santra, P. K.; Mukherjee, S.; Nag, A. X-ray Photoelectron Spectroscopy: A Unique Tool To Determine the Internal Heterostructure of Nanoparticles. *Chem. Mater.* **2013,** *25*, 1222-1232.
8. Vegard, L. Die Konstitution der Mischkristalle und die Raumfüllung der Atome. *Z. Phys.* **1921,** *5*, 17-26.
9. An, Y.; Wang, S.; Duan, L.; Liu, J.; Wu, Z. Local Mn Structure and Room Temperature Ferromagnetism in Mn-doped In_2O_3 films. *Appl. Phys. Lett.* **2013,** *102*, 212411.
10. Nadaud, N.; Lequeux, N.; Nanot, M.; Jové, J.; Roisnel, T. Structural Studies of Tin-Doped Indium Oxide (ITO) and $In_4Sn_3O_{12}$. *J. Solid State Chem.* **1998,** *135*, 140-148.
11. Buonsanti, R.; Llordes, A.; Aloni, S.; Helms, B. A.; Milliron, D. J. Tunable Infrared Absorption and Visible Transparency of Colloidal Aluminum-Doped Zinc Oxide Nanocrystals. *Nano Lett.* **2011,** *11*, 4706-4710.

12. Norberg, N. S.; Kittilstved, K. R.; Amonette, J. E.; Kukkadapu, R. K.; Schwartz, D. A.; Gamelin, D. R. Synthesis of Colloidal Mn^{2+}:ZnO Quantum Dots and High-T_C Ferromagnetic Nanocrystalline Thin Films. *J. Am. Chem. Soc.* **2004,** *126*, 9387-9398.
13. Schimpf, A. M.; Ochsenbein, S. T.; Buonsanti, R.; Milliron, D. J.; Gamelin, D. R. Comparison of Extra Electrons in Colloidal n-Type Al^{3+}-Doped and Photochemically Reduced ZnO Nanocrystals. *Chem. Commun.* **2012,** *48*, 9352-9354.
14. Wang, T.; Radovanovic, P. V. Free Electron Concentration in Colloidal Indium Tin Oxide Nanocrystals Determined by Their Size and Structure. *J. Phys. Chem. C* **2011,** *115*, 406-413.
15. Schwartz, D. A.; Norberg, N. S.; Nguyen, Q. P.; Parker, J. M.; Gamelin, D. R. Magnetic Quantum Dots: Synthesis, Spectroscopy, and Magnetism of Co^{2+}- and Ni^{2+}-Doped ZnO Nanocrystals. *J. Am. Chem. Soc.* **2003,** *125*, 13205-13218.
16. Willets, K. A.; Duyne, R. P. V. Localized Surface Plasmon Resonance Spectroscopy and Sensing. *Annu. Rev. Phys. Chem.* **2007,** *58*, 267-297.
17. Liz-Marzán, L. M. Tailoring Surface Plasmons through the Morphology and Assembly of Metal Nanoparticles. *Langmuir* **2006,** *22*, 32-41.
18. Noguez, C. Surface Plasmons on Metal Nanoparticles: The Influence of Shape and Physical Environment. *J. Phys. Chem. C* **2007,** *111*, 3806-3819.
19. Luther, J. M.; Jain, P. K.; Ewers, T.; Alivisatos, A. P. Localized Surface Plasmon Resonances Arising from Free Carriers in Doped Quantum Dots. *Nat. Mater.* **2011,** *10*, 361.
20. Agrawal, A.; Cho, S. H.; Zandi, O.; Ghosh, S.; Johns, R. W.; Milliron, D. J. Localized Surface Plasmon Resonance in Semiconductor Nanocrystals. *Chem. Rev.* **2018,** *118*, 3121-3207.
21. Kanehara, M.; Koike, H.; Yoshinaga, T.; Teranishi, T. Indium Tin Oxide Nanoparticles with Compositionally Tunable Surface Plasmon Resonance Frequencies in the Near-IR Region. *J. Am. Chem. Soc.* **2009,** *131*, 17736-17737.
22. Manthiram, K.; Alivisatos, A. P. Tunable Localized Surface Plasmon Resonances in Tungsten Oxide Nanocrystals. *J. Am. Chem. Soc.* **2012,** *134*, 3995-3998.
23. Dorfs, D.; Härtling, T.; Miszta, K.; Bigall, N. C.; Kim, M. R.; Genovese, A.; Falqui, A.; Povia, M.; Manna, L. Reversible Tunability of the Near-Infrared Valence Band Plasmon Resonance in $Cu_{2-x}Se$ Nanocrystals. *J. Am. Chem. Soc.* **2011,** *133*, 11175-11180.
24. Lounis, S. D.; Runnerstrom, E. L.; Llordés, A.; Milliron, D. J. Defect Chemistry and Plasmon Physics of Colloidal Metal Oxide Nanocrystals. *J. Phys. Chem. Lett.* **2014,** *5*, 1564-1574.
25. Schimpf, A. M.; Lounis, S. D.; Runnerstrom, E. L.; Milliron, D. J.; Gamelin, D. R. Redox Chemistries and Plasmon Energies of Photodoped In_2O_3 and Sn-Doped In_2O_3 (ITO) Nanocrystals. *J. Am. Chem. Soc.* **2015,** *137*, 518-524.
26. Garcia, G.; Buonsanti, R.; Runnerstrom, E. L.; Mendelsberg, R. J.; Llordes, A.; Anders, A.; Richardson, T. J.; Milliron, D. J. Dynamically Modulating the Surface Plasmon Resonance of Doped Semiconductor Nanocrystals. *Nano Lett.* **2011,** *11*, 4415-4420.
27. Llordés, A.; Garcia, G.; Gazquez, J.; Milliron, D. J. Tunable Near-Infrared and Visible-Light Transmittance in Nanocrystal-In-Glass Composites. *Nature* **2013,** *500*, 323.
28. De Trizio, L.; Buonsanti, R.; Schimpf, A. M.; Llordes, A.; Gamelin, D. R.; Simonutti, R.; Milliron, D. J. Nb-Doped Colloidal TiO_2 Nanocrystals with Tunable Infrared Absorption. *Chem. Mater.* **2013,** *25*, 3383-3390.
29. Erwin, S. C.; Zu, L.; Haftel, M. I.; Efros, A. L.; Kennedy, T. A.; Norris, D. J. Doping Semiconductor Nanocrystals. *Nature* **2005,** *436*, 91.
30. Buonsanti, R.; Milliron, D. J. Chemistry of Doped Colloidal Nanocrystals. *Chem. Mater.* **2013,** *25*, 1305-1317.
31. LaMer, V. K.; Dinegar, R. H. Theory, Production and Mechanism of Formation of Monodispersed Hydrosols. *J. Am. Chem. Soc.* **1950,** *72*, 4847-4854.

32. Van Embden, J.; Chesman, A. S. R.; Jasieniak, J. J. The Heat-Up Synthesis of Colloidal Nanocrystals. *Chem. Mater.* **2015,** *27*, 2246-2285.
33. Kwon, S. G.; Hyeon, T. Formation Mechanisms of Uniform Nanocrystals via Hot-Injection and Heat-Up Methods. *Small* **2011,** *7*, 2685-2702.
34. Peng, X.; Wickham, J.; Alivisatos, A. P. Kinetics of II-VI and III-V Colloidal Semiconductor Nanocrystal Growth: "Focusing" of Size Distributions. *J. Am. Chem. Soc.* **1998,** *120*, 5343-5344.
35. Jansons, A. W.; Plummer, L. K.; Hutchison, J. E. Living Nanocrystals. *Chem. Mater.* **2017,** *29*, 5415-5425.
36.Dietl, T.; Ohno, H.; Matsukura, F.; Cibert, J.; Ferrand, D. Zener Model Description of Ferromagnetism in Zinc-Blende Magnetic Semiconductors. *Science* **2000,** *287*, 1019-1022.

Chapter-2

Tunable Plasmonics and Magnetism from Fe-Sn Codoped In_2O_3 Nanocrystals

---

Following articles have been published from the work presented in this chapter.

1. Tandon, B.; Shanker, G. S.; Nag, A.; "Multifunctional Sn- and Fe-Codoped In_2O_3 Colloidal Nanocrystals: Plasmonics and Magnetism" *J. Phys. Chem. Lett.* **2014,** *5*, 2306-2311.
2. Shanker, G. S.; Tandon, B.; Shibata, T.; Chattopadhyay, S.; Nag, A.; "Doping Controls Plasmonics, Electrical Conductivity, and Carrier-Mediated Magnetic Coupling in Fe and Sn Codoped In_2O_3 Nanocrystals: Local Structure Is the Key" *Chem. Mater.* **2015**, *27*, 892-900

EXAFS and XANES study in this chapter was done through collaboration with Dr. Tomohiro Shibata and Dr. Soma Chattopadhyay at the Argonne National Laboratory, USA.

Summary

Multifunctional Fe-Sn codoped colloidal In_2O_3 nanocrystals (NCs) have been prepared through a codoping approach. While Sn^{4+} doping provides with free electrons in the conduction band yielding high electrical conductivity and, localized surface plasmon resonance (LSPR) in the near-infrared (NIR) region, the localized magnetic spins introduced by Fe^{3+} doping result in weak room-temperature ferromagnetism. Results show that codoping leads to an interaction between both the lattice dopants influencing the properties exhibited by them. Consequently, LSPR and electrical conductivity introduced by Sn^{4+} ions can be regulated by modifying the Fe codoping concentration. Local structure elucidation using x-ray absorption fine structure (EXAFS) and x-ray absorption near-edge spectroscopy (XANES) reveals that the electron density donated by Sn^{4+} is used by some Fe^{3+} ions to get reduced to Fe^{2+} thereby manipulating the LSPR band and electrical conductivity. On the other hand, free electrons donated by Sn^{4+} mediate magnetic coupling between distant Fe^{3+} ions thus changing the extent of magnetism.

Graphical Abstract

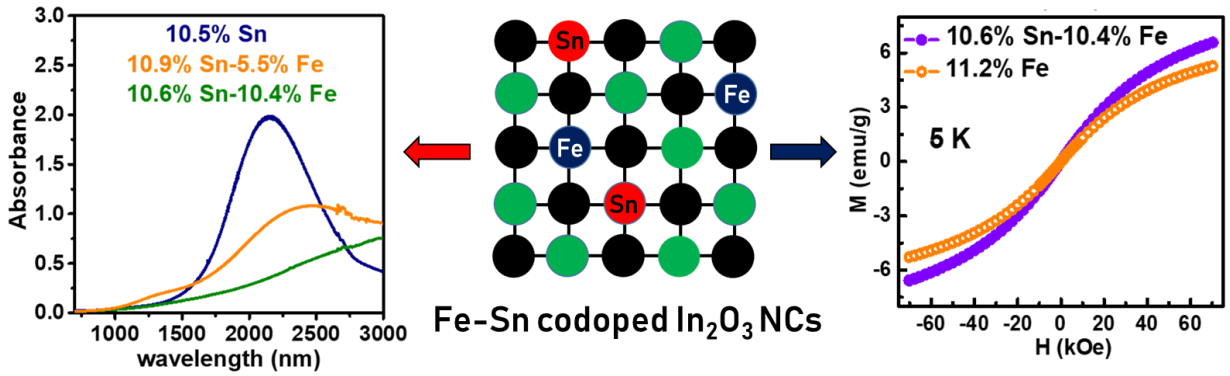

2.1 Introduction

Multifunctional nanocrystals (NCs) are nanocrystalline systems that exhibit multiple functionalities and more importantly, the functionalities interact with each other. Such multifunctionality is usually achieved either by fabricating hetero-structures or doping the surface or lattice with impurities.[1-2] In this chapter, we chose to achieve that with codoping Fe^{3+} and Sn^{4+} in In_2O_3 NC lattice. Here, Sn^{4+} donates electron density to the conduction band of In_2O_3 through its shallow donor states yielding localized surface plasmon resonance (LSPR) and high electrical conductivity whereas Fe^{3+} having five unpaired electrons was expected to introduce magnetism. Then properties arising from the interaction of both dopants are studied.

Search for a near-infrared (NIR) plasmonic and magnetic property within the same system has gained momentum in the past decade for selective photothermal therapy and imaging of tumor cells simultaneously.[3] While the magnetic component can be used as an MRI contrast agent to detect tumor, the NIR plasmonic component can destroy the tumor region selectively through generation of localized heat by absorbing NIR radiations.[3-5] Till now, hetero-structured NC composites such as Fe_3O_4/Au[4] and $Fe_3O_4/Cu_{2-x}S$[6] core/shell NCs were demonstrated where the core exhibited magnetic property and the shell exhibited plasmonic property, however with no or insignificant interactions between them which limited their use in certain applications. In contrast to these hetero-structured NCs, our Fe-Sn codoped In_2O_3 NCs are expected to exhibit strong interactions between the multiple functionalities since both Fe and Sn are homogeneously doped in a single lattice. Therefore, introduction of Fe can tailor LSPR properties arising mainly because of Sn and on the other hand, codoping of Sn can tailor magnetic properties arising from Fe. Particularly, properties such as carrier-mediated magnetic coupling is an interesting one.

Our results indeed show that the LSPR displayed by the free electron density (donated by Sn^{4+}) can be tuned between 2200-3500 nm by changing the Fe codoping concentration. Since the position of the LSPR peak is majorly governed by the free electron density, we suspected that Fe codoping might be modifying the extent of electron density present within the NC. This ability of Fe to regulate the electron density was further confirmed by four-probe electrical conductivity measurements where an increase in Fe codoping concentration (while keeping other parameters same) led to a systematic decrease in the electrical conductivity of the NC pellet. Elucidating the microscopic local structure through x-ray absorption near-edge spectroscopy (XANES) and

extended x-ray absorption fine structure (EXAFS) revealed that a fraction of Fe^{3+} ions spontaneously gets converted to Fe^{2+} by consuming the electrons released by Sn^{4+} thereby influencing both LSPR and electrical conductivity.

On the other hand, Fe^{3+}-doped In_2O_3 is a dilute magnetic semiconductor[7-8] where the d^5 electronic configuration in the high-spin environment of In_2O_3 lattice produces magnetism. The free electrons added through Sn^{4+} codoping can facilitate exchange interactions between distant Fe^{3+} ions thereby affecting the extent of magnetism exhibited by the NC. Electron paramagnetic resonance (EPR) studies of Fe-Sn codoped In_2O_3 NCs showed that the EPR signal of isolated Fe^{3+} ions was distorted by the addition of free electrons through Sn^{4+} codoping indicating that electron-mediated magnetic coupling could be present in our NCs. A comparison of magnetization vs magnetic field curves for different Fe and Fe-Sn codoped In_2O_3 NCs showed that Sn codoping (while keeping the Fe doping concentration same) was associated with an increased extent of magnetism thereby confirming the presence of electron-mediated magnetic coupling in our NCs. Fe-Sn codoped In_2O_3 NCs, therefore, display tunable LSPR, electrical conductivity, and magnetism along with visible transparency from the same system which hasn't been observed in literature so far.

2.2 Experimental Section

2.2.1 Synthesis of Fe-Sn codoped In_2O_3 NCs

All Fe-Sn codoped In_2O_3 NCs were synthesized employing a colloidal route using standard Schlenk line techniques and inert N_2 atmosphere. Stoichiometric amounts of In, Fe and Sn precursor were weighed to achieve a target composition. For example: to synthesize 10% Fe-10% Sn codoped In_2O_3 NCs, 0.03 mmol of iron(III) acetylacetonate, 0.03 mmol of tin(IV) bis(acetylacetonate) dichloride and 0.24 mmol of indium(III) acetylacetonate were weighed in a three-neck round bottom flask and 10.0 mL of oleylamine solvent was added to it. The mixture was subjected to alternating atmospheres of N_2 and vacuum at room temperature for 30 minutes to remove dissolved gases followed by 30 minutes of vacuum at 100 ˚C to get rid of adsorbed water molecules. The temperature of the solution was then gradually increased to 220 ˚C at the rate of ~10 ˚C/min under N_2 conditions and allowed uninterrupted heating 220 ˚C at for 5 hours with vigorous stirring. The mixture was subsequently cooled down to room temperature and NCs were obtained by precipitating them with excess methanol (~30 mL) followed by centrifugation at 6000 rpm for 6 min. The washing procedure was repeated twice to get rid of the excess oleylamine

solvent and the NCs obtained were then dispersed in different non-polar solvents such as hexane and tetrachloroethylene for different characterization purposes.

2.2.2 Characterization of Fe-Sn codoped In_2O_3 NCs

Inductively coupled plasma atomic emission spectroscopy (ICP-AES): The elemental compositions of NCs were determined through the ICP-AES technique performed on a Perkin−Elmer Optima 7000 DV machine. ~1-2 mg of NC powder was dissolved in 70% HNO_3 and the solution volume was diluted with milli-Q water to result in a 2% v/v HNO_3 acid solution. Standard solutions with variable concentrations of a particular element were prepared by diluting the commercial ICP standard with 2% v/v HNO_3 solution.

Energy dispersive X-ray analysis (EDX): The elemental compositions of all Fe-Sn codoped In_2O_3 NCs obtained from ICP-AES were complemented with those determined through EDX spectroscopy on a Zeiss Ultra Plus SEM instrument operating at an energy of 20 kV.

Powder x-ray diffraction (p-XRD): To determine the crystal structure and phase purity of different NCs, p-XRD patterns were recorded on a Bruker D8 Advance X-ray diffractometer employing monochromated Cu Kα (λ=1.5406 Å) as an x-ray source. Contribution from Cu Kα2 (λ=1.5444 Å) and the background was subtracted from the XRD pattern obtained from the instrument.

Transmission electron microscopy (TEM): Morphology of the Fe-Sn codoped In_2O_3 NCs was imaged through TEM. A dilute solution of NCs in hexane was drop-casted on a carbon coated TEM grid and analyzed in JEOL JEM 2100F microscope operated at 200 kV. The TEM micrographs obtained were processed in ImageJ software to calculate the average diameter and standard deviation of NCs.

UV-Vis-NIR absorption spectroscopy: To avoid the vibrational peaks of different bonds in the infrared region which would interfere in the NIR LSPR spectra, dilute solution of NCs were prepared in tetrachloroethylene solvent and UV-Vis-NIR spectra were recorded on Perkin Elmer, Lambda-950 UV/Vis spectrometer.

Four probe electrical conductivity: NC powder was pressed into hard pellets using a KBr die and four-probe conductivity measurements were executed on a Keithley Four-Probe Conductivity Instrument (Model 6220/6221 Current Source and Model 2182A nanovoltmeter). Point contacts

were made between the tips of probe and surface of circular pellets. The probes were collinear, equally spaced (2.0 mm), and each having a diameter of 0.54 mm. Prior to measurements, pellets were annealed inside the glove box at 200 ^oC for an hour which was high enough to remove residual solvents but not to affect the crystallite size. The conductivity σ is expressed as, $\sigma = 1/\rho$, where ρ is resistivity given by the equation $\rho = 2\pi s(V/I)/f(w/s)$, where, V, I and s are voltage, current, and spacing between the electrodes respectively, and f(w/s) is a function depending upon width of the pellet (w) and s.[9]

EXAFS and XANES: To unravel the local microstructure of Fe-Sn codoped In_2O_3 NCs, XANES and EXAFS spectroscopy was carried out using a beam size of 500 μm x 500 μm at the 10ID undulator beamline at Advanced Photon Source in Argonne National Laboratory.[10] Fe K edge data were measured in fluorescence mode utilizing an ion chamber in Stern-Heald geometry.[11] The energy calibration was performed with Fe foil at the first inflection point of 7111 eV, and samples were aligned with reference Fe foil positioned between the transmission and reference ion chamber for data collection. Higher energy x-rays were eliminated through the rhodium coated harmonic rejection mirror. Well-known self-absorption error was insignificant when compared with the transmission data due to the presence of heavy elements (In, and Sn) in the samples. Fe^{3+} and Fe^{2+} standards Fe_2O_3 and FeO respectively were measured in transmission geometry. Similarly, for In K edge (27940 eV) and Sn K edge (29200 eV), data were recorded in the transmission geometry, however with a Pt-coated harmonic rejection mirror. For Fe, In, and Sn K edge measurements, 5% absorption and 20% transmission in the ion chamber at the respective energies was optimized by filling the incident monitor ion chamber was filled with gas, thus ensuring the linearity of the detector sets. The EXAFS signals $\chi(k)$, with k being a photoelectron wavenumber, were extracted in a conventional manner utilizing ATHENA program.[12] k^2 weight $\chi(k)$ were Fourier transformed to real space ($|\chi(R)|$) and coordination numbers, bond lengths, bond lengths distribution (Debye-Waller factor) parameters were acquired by fitting to a model constructed using ab initio calculation code FEFF6 employing ARTEMIS program.[12] The EXAFS spectra were fit in real space $|\chi(R)|$ including two coordination shells.

EPR: To study the local structure and presence of magnetic interactions between dopant ions, EPR spectra of NC powders was recorded at X-band frequency on a Bruker-ER073 spectrometer equipped with an EMX microX source.

Magnetic measurements: Magnetic properties were quantified using a SQUID magnetometer instrument (Quantum Design MPMS XL-7 Magnetometer). Magnetization vs magnetic field curves was measured through the magnetic field range ±7T at different sample temperatures. Zero-field-cooled (ZFC) and field-cooled (FC) data were recorded in the temperature range of 5−300 K at a low magnetic field of 100 Oe after cooling the ampules in zero field or in a 100 Oe field, respectively.

2.3 Results and Discussion

2.3.1 Structure and morphology

The elemental compositions obtained through ICP-AES and EDX are in good correlation with the precursor ratios (Table 2.1) employed for the synthesis. Since ICP-AES is a more accurate description of the doping percentages, we will use them throughout the chapter to represent different Sn and Fe doping percentages. Figure 2.1 shows the powder XRD patterns of different Fe-Sn codoped In_2O_3 NCs where the doping percentages of either dopant range from 0% to 10%. It can be clearly perceived that all Fe-Sn codoped In_2O_3 NC exhibit the same cubic bixbyite structure (space group 206, *Ia3*) as that of the bulk In_2O_3 reference without the presence of any impurity phase. The diffraction peaks, however, are significantly broadened as compared to the bulk reference which is a characteristic of the formation of NCs.[13]

Table 2.1: Elemental analysis of Fe and Sn codoped In_2O_3 NCs using both ICP-AES and EDX.

In : Fe : Sn		
Precursor	**ICP-AES**	**EDX**
95 : 5 : 0	94.3 : 5.7 : 0	95.3 : 4.7 : 0
90 : 10 : 0	88.8 : 11.2 : 0	90.5 : 9.5 : 0
95 : 0 : 5	94.5 : 0 : 5.5	94.8 : 0 : 5.2
90 : 0 : 10	89.5 : 0 : 10.5	90.9 : 0 : 9.1
90 : 5 : 5	90.2 : 4.8 : 5.0	89.3 : 5.1 : 5.6
85 : 10 : 5	83.9 : 10.8 : 5.3	86.3 : 8.9 : 4.8
85 : 5 : 10	83.6 : 5.5 : 10.9	85.6 : 4.8 : 9.6
80 : 10 : 10	79.0 : 10.4 : 10.6	81.4 : 9.0 : 9.6

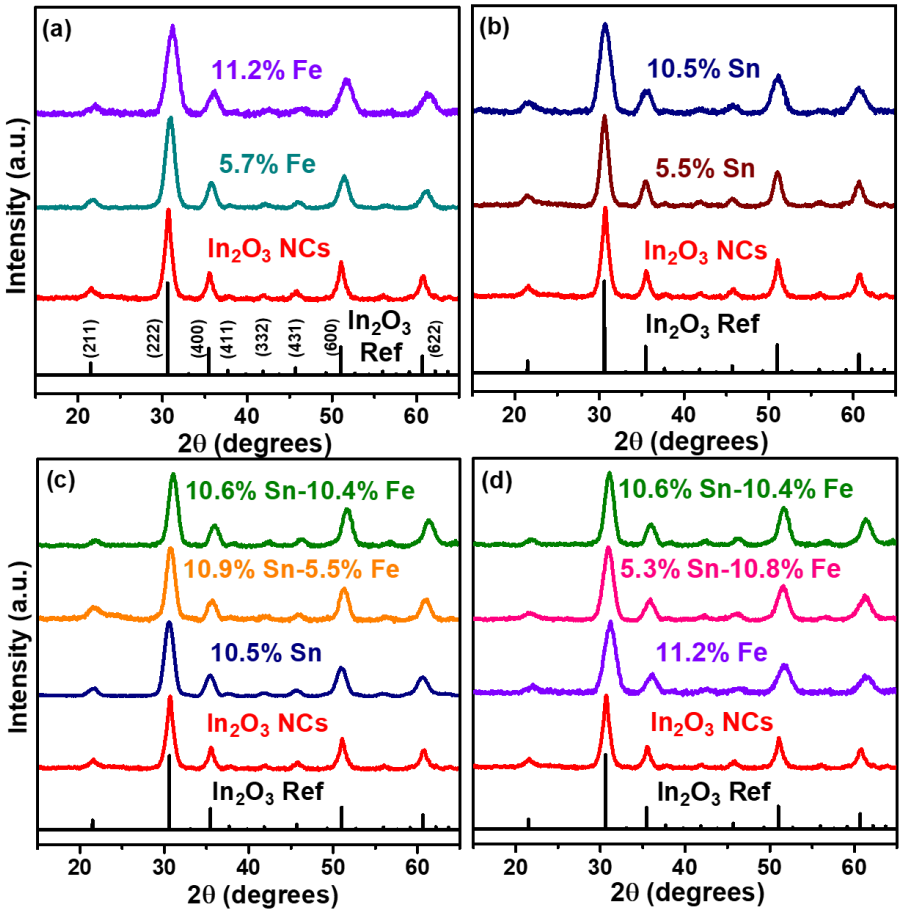

Figure 2.1: Powder XRD patterns of different Fe-Sn codoped In_2O_3 NCs signifying the retention of the bulk In_2O_3 cubic bixbyite phase in NCs despite a huge variation in the Fe and Sn doping percentages.

Additionally, the diffraction peak positions for different Fe-Sn codoped In_2O_3 NCs show a systematic trend. While an increase in the Fe doping concentration shifts the diffraction peaks to higher 2θ values, their position is almost unaffected with an increase in Sn doping concentration. The change in diffraction peak position with the extent and type of doping can be interpreted in terms of change of interplanar distances as In^{3+} ions in the lattice are substituted by dopants Fe^{3+} and Sn^{4+}, which is a direct consequence of Vegard's law.[14] Since Fe^{3+} has a smaller effective ionic radii as compared to In^{3+},[15] lattice substitution of Fe^{3+} leads to a decrease in the interplanar distances which is reflected as diffraction peaks shifting to higher 2θ values. Interestingly, Sn^{4+} doping doesn't cause a change in lattice parameters despite having a smaller ionic radii than In^{3+}.[15] While initially it may lead someone to interpret that Sn^{4+} ions are not lattice doped, careful investigation of the literature[16-17] reveals that a decrease in lattice parameters due to Sn^{4+} substitution is counter-balanced by repulsions between Sn^{4+} ions in the proximity of each other

(due to under compensation by the electron density). Therefore, the XRD data suggests that Sn and Fe are incorporated in the In_2O_3 substitutionally, both in the doped and the codoped form.

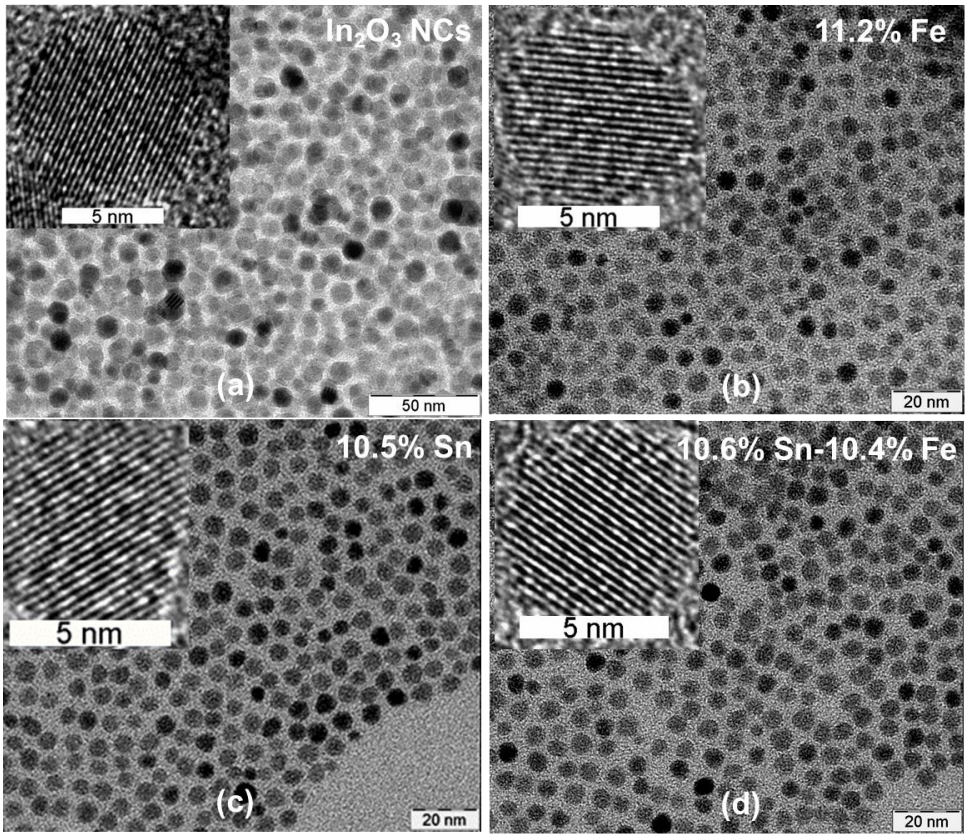

Figure 2.2: TEM images of different Fe-Sn codoped In_2O_3 NCs with their representative high-resolution TEM (HRTEM) images in the inset.

Figure 2.2 shows the TEM images of different Fe-Sn codoped In_2O_3 NCs. The morphology of all NCs is nearly spherical, however, the average diameter of undoped In_2O_3 NCs is markedly different from the Fe-Sn codoped In_2O_3 NCs. While the average diameter of undoped In_2O_3 NCs is approximately 9.1 nm, Fe-Sn codoped In_2O_3 NCs are sized between 6-7 nm across different doping percentages. This observation is supported by the narrower peaks for undoped In_2O_3 NCs as compared to the doped In_2O_3 NCs in their respective XRD patterns. Their respective HRTEM images (insets) show highly crystalline nature of all NCs and the lattice fringes correspond to the interplanar distance of the {222} plane of the cubic bixbyite structure. The interplanar distance of 2.94 Å calculated for undoped In_2O_3 NCs and 10.5% Sn-doped In_2O_3 NCs decreases to 2.86 Å for 11.2% Fe-doped and 10.6% Sn-10.4% Fe codoped In_2O_3 NCs which is in perfect correlation with the observed decrease in the interplanar distance in XRD patterns and reiterates our claim of lattice doping of Fe and Sn ions in In_2O_3 without segregation of an impurity phase.

2.3.2 Effect of Fe codoping on the properties arising from Sn doping

The primary objective of Sn^{4+} doping in In_2O_3 NCs was to induce high electrical conductivity and optical properties such as LSPR by generation of the free electron density. Fe^{3+} doping, on the other hand, is isovalent with In^{3+} and any influence of Fe^{3+} codoping on the properties exhibited by Sn^{4+} is therefore not obvious. We will now investigate how LSPR and electrical conductivity vary when Fe^{3+} is codoped with Sn^{4+} in In_2O_3 NCs.

Figure 2.3a shows the optical absorption of Fe-Sn codoped In_2O_3 NCs in the UV-vis range. Undoped In_2O_3 NCs show a sharp absorption edge near 3.6 eV which corresponds to the band-gap transition of In_2O_3.[18] The size of our In_2O_3 NCs (~9 nm) is much greater than the Bohr-exciton radii for In_2O_3 (2.13 nm)[19] and hence the presence of any quantum confinement effect can be ruled out in these NCs. Sn^{4+} doping in In_2O_3 NCs leads to an apparent widening of the optical band-gap energy which can be attributed to the Burstein-Moss effect (Figure 2.3b).[19-20] In undoped In_2O_3 (left), the fermi level is situated in the mid band-gap region and a transition takes place from the valence band maximum (VBM) to the conduction band minimum (CBM) of the In_2O_3 when electrons are excited through optical irradiation. An increase in the n-type doping (through Sn^{4+}) shifts the fermi level towards the CBM while bringing VBM and CBM closer to each other through free-electron interactions.[8] However, at a particular doping concentration, the fermi level shifts inside the conduction band filling the edge density (also known as degenerate doping) and electronic excitation of electron takes place from the VBM to the fermi level situated inside the conduction band. The effect of free-electron interactions in decreasing the band-gap is usually much smaller than the Burstein-Moss shift observed and hence there is a net increase in the optical band-gap with degenerate doping in semiconductors. Another interesting observation in Figure 2.3a is the bleaching of the weak shoulder-like excitonic feature with Sn doping. This can't be explained by consideration of larger size as ITO NCs are actually smaller than undoped In_2O_3 NCs and have a similar size distribution. Instead, we suspect that the free electrons contributed by Sn doping screen the electron-hole Coulomb attraction required to form an excitonic state. Charged ZnO NCs with free electrons in the CB have also been found to show similar excitonic bleaching.[21-22]

Codoping of Fe^{3+} along with Sn^{4+} leads to a decrease in the energy of the absorption edge compared to ITO NCs. This decrease indicates that either the free-electron interactions are increasing

(decreasing the electronic band-gap between VBM and CBM) or the net electron density in the system is decreasing (decreasing the Burstein-Moss shift) with Fe codoping. Since Fe^{3+} doping is isovalent with In^{3+}, one would assume no change in carrier density, however, that would also mean that Fe^{3+} codoping shouldn't significantly affect the LSPR and the electrical conductivity.

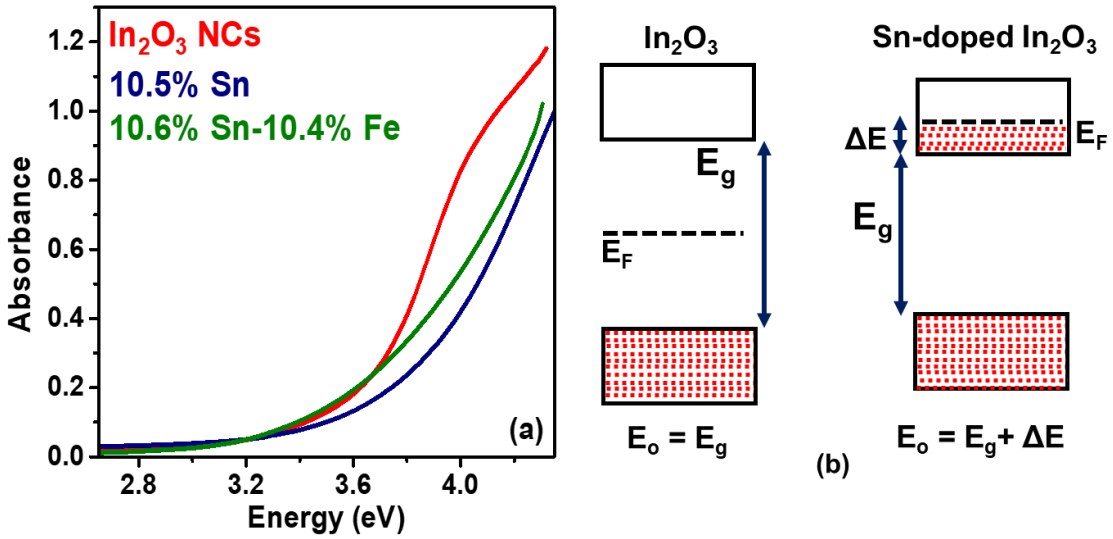

Figure 2.3: (a) Change in the optical band-gap with Fe codoping in Sn-doped In_2O_3 NCs (b) Schematic depiction of the Burstein-Moss effect. Here E_F represents the position of the fermi level whereas E_g and E_o denote the electrical and optical band-gap of the material respectively. ΔE is the shift in the optical band-gap due to Burstein-Moss effect. Refer to reference 19 for more information.

Figure 2.4a shows the NIR LSPR spectra of Sn-doped In_2O_3 NCs with varying Sn doping percentages. It can be easily observed that in case of only Sn-doped In_2O_3 NCs (0% Fe codoping), both the LSPR peak energy and the peak absorbance increase with an increase in the Sn doping percentage due to an increased number density of electrons.[23-24] However, at very high doping percentages, the effective electron density responsible for LSPR decreases due to the formation of the irreducible clusters that trap electron density around them.[25-26] Since both LSPR energy and peak absorbance are directly correlated with the free electron density available in the material, a small variation in the electron density systematically influences both the LSPR peak energy and the peak absorbance. Figure 2.4b shows the optical NIR absorption spectra of Fe-Sn codoped In_2O_3 NCs with an almost constant Sn doping percentage and different Fe codoping percentages. Interestingly, with an increase in the Fe codoping percentage, both the LSPR peak energy (wavelength) and peak absorbance decreases systematically along with an increase in the LSPR linewidth. This trend can be observed for a variety of compositions as shown in Figure 2.4c,d.

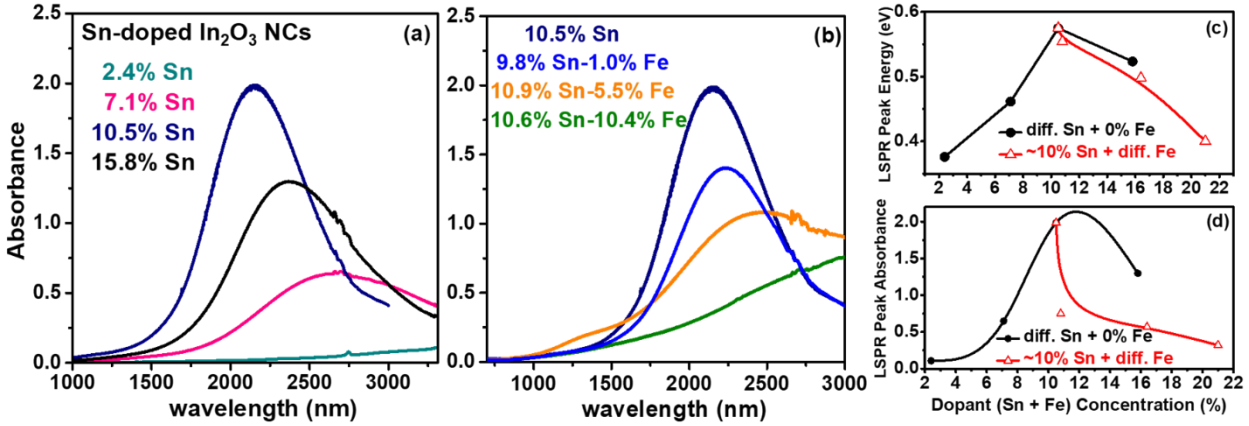

Figure 2.4: (a) NIR LSPR spectra of Sn-doped In_2O_3 NCs with different Sn doping percentages (b) NIR LSPR spectra of different Fe-Sn codoped In_2O_3 NCs with varying Fe codoping concentration. (c) Variation in the LSPR peak energy and (d) the peak absorbance while changing the Sn and Fe codoping concentration independently.

Other than electron density, LSPR peak position and absorbance also depends upon the size, shape and the effective dielectric medium surrounding the electron density.[27] These factors, however, do not vary drastically between different compositions of Fe-Sn codoped In_2O_3 NCs and hence unlikely to affect the LSPR position. We therefore believe that, Fe^{3+} codoping, even though isovalent in nature is somehow affecting the electron density, possibly through electron trapping around the Fe^{3+} centers, just like in the case of high Sn doping percentages. But since the influence of Fe is much stronger than Sn in high doping percentage, the mechanism operating for electron-trapping is likely to be different in both cases. However, if this is true, then the electrical conductivity of the Fe-Sn codoped In_2O_3 NCs should also be affected in the same manner.

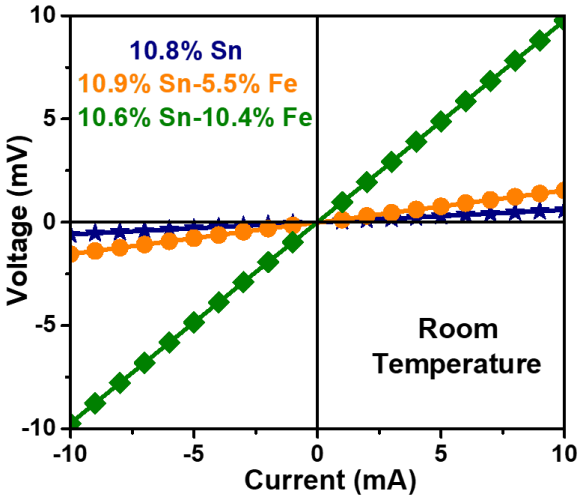

Figure 2.5: Variation in the four-probe electrical conductivity of Fe-Sn codoped In_2O_3 NCs with an increase in the Fe codoping percentage.

Figure 2.5 shows the variation in the four-probe electrical conductivity of the Fe-Sn codoped In_2O_3 NC pellets with an increase in the Fe codoping percentage. According to Ohm's law, the slope of the voltage vs current represents the resistance in the material. As the Fe doping percentage is increased, the resistance of the Fe-Sn codoped In_2O_3 NCs increases signifying that the electron density in the NCs is diminishing as Fe codoping percentage is increased. Quantitatively, the electrical conductivity decreases from 35 S/cm to 14 S/cm to 2 S/cm as the Fe codoping concentration is increased from 0% to 5.5% to 10.4% respectively. Therefore, both optical and electronic measurements seem to suggest that Fe is strongly influencing the properties of the Sn by decreasing the electron density associated with the NC composition.

2.3.3 Origin of the tunability in LSPR and electrical conductivity: The role of local structure

There are different ways through which Fe can decrease the electron density associated with Fe-Sn codoped In_2O_3 NCs. For example, Fe can resist incorporation of Sn in the codoped NCs which would lead to smaller doping percentages and hence lesser electron density generated. The ICP-AES results are contradictory to this hypothesis as the amount of Sn incorporated seem to be independent on the Fe doping concentration. Another possibility could be that same amount of free electron density is produced in both Sn-doped and Fe-Sn codoped In_2O_3 NCs initially but Fe being a transition element takes up some of the electron density and converts its oxidation state from Fe^{3+} to Fe^{2+}. Prior literature suggests that Fe-doped In_2O_3 films treated in reducing conditions have been found to contain a significant amount of Fe^{2+} ions.[28] While the source of the consumed electrons, in this case, was oxygen vacancies, more electrons are produced in our NCs due to Sn^{4+} doping along with the presence of oxygen vacancies.

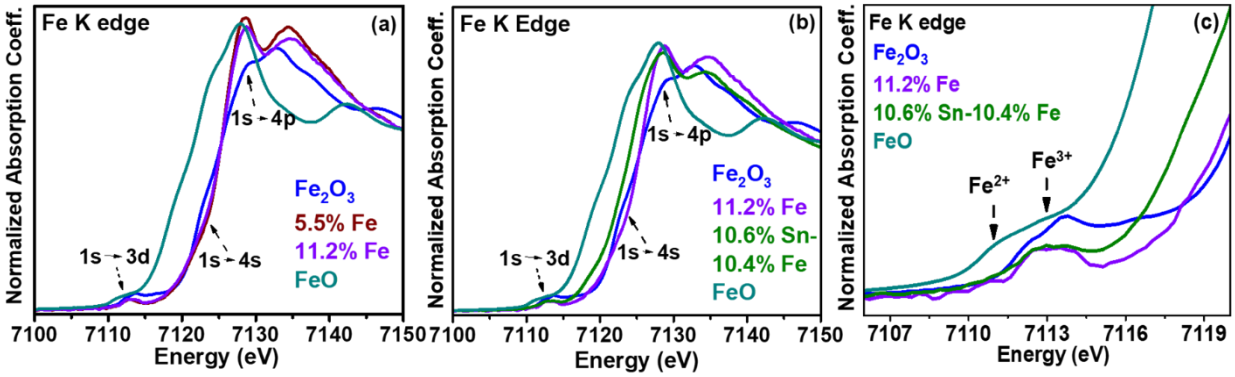

Figure 2.6: Comparison of the Fe K edge XANES spectrum for Fe-doped In_2O_3 NCs and Fe-Sn codoped In_2O_3 NCs with bulk reference for +2 (FeO) and +3 (Fe_2O_3) oxidation state.

To investigate this prospect, we employed synchrotron-based EXAFS and XANES technique and elucidated the local structure by combining the information from In K edge, Sn K edge and Fe K edge. Figure 2.6a compares the normalized absorption coefficient of Fe K edge at the near edge XANES region for 5.5% and 11.2% Fe-doped In_2O_3 NCs with bulk references for +2 (FeO) and +3 (α-Fe_2O_3) oxidation state. In XANES, several features have their origin in the electronic transitions from the core level (1s) to empty electronic levels near the fermi level. Thus, the position of peaks in the Fe K edge XANES spectrum is expected to be governed significantly by the local coordination geometry and oxidation state(s) of Fe. For Fe K edge, pre-edge peak at 7113 eV (1s→3d), shoulder (1s→ 4s) and crest of the edge (1s → 4p) are distinctly visible in Figure 2.6a,b for Fe-doped and Fe-Sn codoped In_2O_3 NCs.[29,30,31,32] The crest edge positions for both 5.5% and 11.2% Fe-doped In_2O_3 NC samples lie close to α-Fe_2O_3, indicating that Fe is present in the +3 oxidation state. The spectral features of Fe in In_2O_3 NCs however, are quite different from Fe in α-Fe_2O_3 suggesting a difference in the coordination environment owing to lattice doping of Fe in In_2O_3.

Interestingly, as Sn is codoped with Fe, the crest of the edge shifts towards lower energy (~0.3 eV for 1s→4p transition) (Figure 2.6b) for 10.6% Sn-10.4% Fe codoped In_2O_3 NCs. Moreover, the edge of the codoped sample broadens with more contribution from the lower energy side (Figure 2.6c). Such lower energy contribution suggests a reduction of some of the Fe^{3+} ions to Fe^{2+} (or $Fe^{3-\delta}$) in the presence of Sn in the codoped sample.[32] A similar partial reduction of Fe^{3+} to Fe^{2+} was also observed in Fe-Cu codoped bulk In_2O_3 NCs when prepared under a low O_2 partial pressure. We note here that the increase in lattice disorder can also broaden the XANES spectrum,[33], however, signatures of such lattice disorder (broadening) is not observed in Sn and In edge obtained from the same Fe-Sn codoped NCs (Figure 2.7a). Compared to FeO, XANES of 10.6% Sn – 10.4% Fe codoped In_2O_3 NCs is at a significantly higher energy suggesting the majority of Fe in the codoped sample are still in the Fe^{3+} state, while a smaller fraction has got reduced to Fe^{2+} (or $Fe^{3-\delta}$). The pre-edge position (Figure 2.6c) of the codoped sample also remains at 7113 eV suggesting the dominance of Fe^{3+} ions in the codoped NCs. The partial reduction of Fe^{3+} even in the presence of excess Sn suggests that a fraction of Fe^{3+} is somehow easily reducible. The exact origin of this preferential reduction of a fraction of Fe^{3+} is not understood presently, but probably surface Fe ions are behaving differently compared to Fe ions in the core.

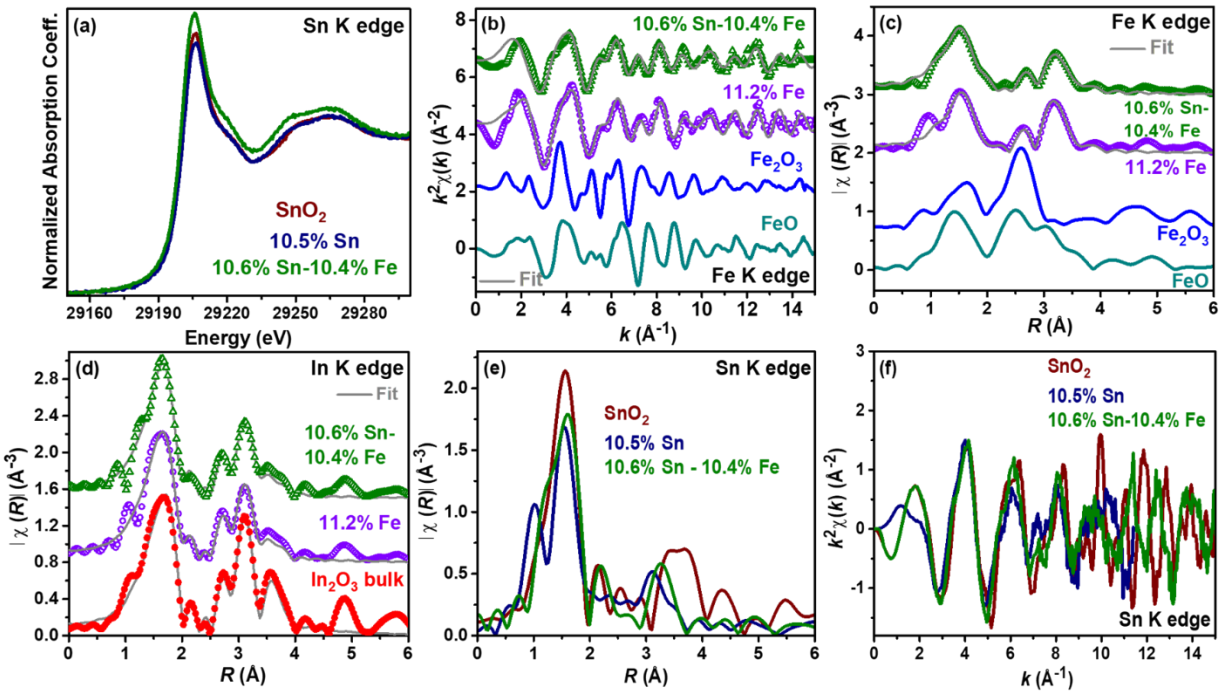

Figure 2.7: XANES and EXAFS data for different elements K edges in Fe-Sn codoped In_2O_3 NCs compared with the bulk references (a) Sn K edge XANES data implying +4 oxidation state (b) Fe K edge EXAFS data. Comparison of k^2 weighted χ(k) data and (c) magnitude of Fourier transformed data in R-space. Data were shifted vertically for a better representation. Fit parameters are listed in Table 2.2 (d) In K edge EXAFS data along with the best fit. The magnitude of the real space data, where $k^2\chi$ is Fourier transformed in k space for k = 2–11 $Å^{-1}$. Fit parameters are shown in Table 2.4. Data were shifted vertically for a better presentation (e) Sn K edge EXAFS data Comparison of k^2 weighted χ(k) data and (f) magnitude of Fourier transformed data for *k* range of *k* = 2-10 $Å^{-1}$. The fit parameters are shown in Table 2.3.

Visual inspection of the representative Fe-edge EXAFS data in Figure 2.7b-c shows that the spectrum for Fe-doped and Fe-Sn codoped NCs are similar and very different from both α-Fe_2O_3 and FeO reference samples. Here $k^2\chi(k)$ and their Fourier transform between *k* = 2-13 $Å^{-1}$ to real space data |χ(R)| are shown in Figure 2.7b, and Figure 2.7c respectively along with the best fit results. The fit was done for χ (R) between R = 1 - 4 Å, including Fe-O, and Fe-In/Sn correlations. For all the NC samples and reference samples, 1st nearest neighbor is Fe-O, however, the difference mainly lies in 2nd and farther nearest neighbor seen at R > 2 Å shown in Figure 2.7c. Note that the peak of the Fourier amplitude appears at a shorter distance than the actual bond lengths due to a backscattering phase shift of photoelectrons. For, all iron oxide compounds, 2nd nearest neighbor is Fe-Fe, but for doped NCs, the second nearest neighbor can be Fe-Fe, Fe-In, and Fe-Sn (for Fe-Sn codoped In_2O_3 NCs). However, Fe-Sn correlation cannot be distinguished from Fe-In

correlations, since Sn is located immediately after In in the periodic table, and therefore, exhibit very similar backscattering functions.

Table 2.2: Fe K edge EXAFS fit results. The fit was performed in R space, χ (R) where $k^2\chi(k)$ was Fourier transformed for k = [2,13 $Å^{-1}$]. The fit range R = [1, 4 Å] includes the first neighbor Fe-O and Fe-In/Sn. Including Fe-Fe bond does not improve the fit quality indicating the Fe-Fe correlation is small. N = Coordination Number, R = bond length, σ^2 = mean square displacement of the distance between the atoms. The photoelectron threshold (ΔE) is used as a variable for the fit. The error bar is written in the bracket in the last digit of the fit results.

Bond	Parameter	11.2% Fe	10.6% Sn-10.4% Fe
Fe-O	N	6.1(9)	5.0(8)
	R(Å)	2.04(1)	2.05(1)
	σ^2($Å^2$)	0.010(3)	0.008(3)
Fe-In(Sn)	N	3(1)	4(1)
	R(Å)	3.30(1)	3.31(1)
	σ^2($Å^2$)	0.005(2)	0.002(3)
Fe-In(Sn)	N	3(2)	2(1)
	R(Å)	3.76(2)	3.77(2)
	σ^2($Å^2$)	0.007(4)	0.003(6)

The best-fit parameters (Table 2.2) show the first neighbor around Fe is oxygen for the doped NCs, and fit with 5 to 6 coordination numbers with the Fe-O bond lengths of 2.04 to 2.05 Å for 11.2% Fe and 10.6% Sn-10.4% Fe codoped NCs respectively. The first Fe-O bond of doped NCs shows higher intensity than Fe_2O_3 standards, indicating the bond length distribution (Debye-Waller factor) is smaller for our doped NCs suggesting more symmetric FeO_6 octahedron, consistent with the weaker pre-edge for doped NCs in the XANES results (Figure 2.6c). The second neighbor of doped NCs can be fitted with two different Fe-In distances at 3.32 Å and 3.79 Å. Coordination numbers are somewhat smaller than expected for NC and is often observed in NCs because of large surface to volume ratio.[34]

Figure 2.7d shows EXAFS data for In K edge for representative samples. The In K edge EXAFS remains essentially unaltered for all NC samples. Near-edge data establish that In is in 3+ oxidation state for all NC samples, as expected (not shown). The obtained In-O bond length is 2.17 Å, and two different In-In (or In-Fe, or In-Sn) distances are 3.37 and 3.85 Å (Table 2.3). The similarity in second nearest neighbor data for both Fe-edge and In-edge confirms that that Fe is doped in the In_2O_3 NC lattice. For Fe-doped and Fe-Sn-doped In_2O_3 NCs, the obtained nearest neighbor Fe-O bond length (2.05 Å) is similar to that in Fe_2O_3 (R= 1.98 and 2.08 Å), but significantly shorter than

In-O bond lengths (2.17 Å). This is expected from the larger ionic radius of In^{3+} compared to Fe^{3+}, and such differences fade out as we move to second and farther neighbors.[35]

Table 2.3: Sn K edge EXAFS fits for the samples studied. $k^2\chi$ is Fourier transformed for 2-10 $Å^{-1}$, and fit includes Sn-O, Sn-In/Sn bond for R = 1-4 Å range. The number in parenthesis is error bar of the last digit. N = Coordination Number, R = bond length, σ^2 = mean square displacement of the distance between the atoms.

Bond	Parameter	SnO_2 bulk	10.5% Sn	10.6% Sn-10.4% Fe
Sn-O	N	6	6.1(3)	7.3(10)
	R(Å)	2.05(1)	2.096(9)	2.07(1)
	$\sigma^2(Å^2)$	0.002(1)	0.005	0.006(2)
Sn-In(Sn)	N	2	4.6(8)	4.9(9)
	R(Å)	3.20(2)	3.36(2)	3.33(2)
	$\sigma^2(Å^2)$	0.002(1)	0.005	0.005
Sn-In(Sn)	N	8	2.2(15)	3.6(19)
	R(Å)	3.72(9)	3.72(9)	3.84(4)
	$\sigma^2(Å^2)$	0.03(2)	0.005	0.005(4)

Table 2.4: In K edge fit results of the samples studied. $k^2\chi$ is Fourier transformed for 2-11 $Å^{-1}$, and fit includes In-O, In-In/Sn bond for R = 1–4 Å range. The In-Fe contribution was evaluated, but due to much weaker scattering amplitude, the contribution is very small. The number in parenthesis is error bar of the last digit. N = Coordination Number, R = bond length, σ^2 = mean square displacement of the distance between the atoms.

Bond	Parameter	In_2O_3 bulk	In_2O_3 NCs	10.5% Sn	11.2% Fe	10.6% Sn-10.4% Fe
In-O	N	6	5.6(6)	6.1(4)	5.8(5)	5.7(6)
	R(Å)	2.172(6)	2.167(9)	2.168(6)	2.170(8)	2.169(9)
	$\sigma^2(Å^2)$	0.0056(8)	0.005(1)	0.006(1)	0.006(1)	0.006(1)
In-In(Sn)	N	6	7(1)	6(1)	4(1)	5(1)
	R(Å)	3.364(4)	3.370(9)	3.376(8)	3.37(1)	3.36(5)
	$\sigma^2(Å^2)$	0.0040(4)	0.006(1)	0.005(1)	0.004(2)	0.006(2)
In-In(Sn)	N	6	3(1)	3.6(7)	2.6(7)	3(1)
	R(Å)	3.840(9)	3.85(1)	3.86(1)	3.86(2)	3.854(5)
	$\sigma^2(Å^2)$	0.0050(9)	0.003(3)	0.005(1)	0.005(2)	0.006(2)
In-Fe	N				0.3(5)	0.3(6)
	R(Å)				3.37	3.37
	$\sigma^2(Å^2)$				0.005	0.006

Sn K-edge XANES and EXAFS data of representative samples are shown in Figure 2.7a and Figure 2.7e. Sn near edge data of all NC samples is similar to that of SnO_2 signifying the oxidation state of Sn is 4+ in all NC samples. The Sn-O bond lengths are 2.05, 2.09 and 2.07 Å for SnO_2, 10.5% Sn-doped In_2O_3 NCs and 10.6% Sn-10.4% Fe codoped In_2O_3 NCs, along with similar

coordination number of 6 (Table 2.4) which is consistent with prior studies on Sn-doped In_2O_3.[36] $k^2\chi(k)$ spectra (Figure 2.7f) for SnO_2 and doped NCs are different above k = 10 $Å^{-1}$. This indicates that the correlations from a 2nd nearest neighbor (in the present case Sn or In) of doped NCs are different from that of SnO_2 excluding the possibility of segregation of separate SnO_2. These EXAFS results suggest a lattice substitution of In^{3+} ions with both Fe^{3+} and Sn^{4+} ions, without forming any detectable impurity phase segregation, however in Sn-Fe codoped NCs, a smaller fraction of the Fe^{3+} ion get reduced to Fe^{2+} ($Fe^{3-\delta}$), whereas, neither In^{3+} nor Sn^{4+} changes its oxidation state. This partial change in the oxidation state of Fe^{3+} ions is responsible for the tunability in the optical and electrical properties of electrons donated by Sn^{4+} and makes a strong case for interactions between the two dopants in the In_2O_3 lattice. It would be interesting to see if these interactions are limited to Fe influencing the properties of Sn only or Sn can also influence the properties exhibited by Fe^{3+} ions.

2.3.4 Effect of Sn codoping on the magnetic properties arising from Fe doping

High-Curie temperature (T_C) ferromagnetism in transition metal doped dilute magnetic semiconductor oxides (DMSO) is a crucial area of research, particularly for spin-based electronic and magneto-optical applications.[7, 37-38] Magnetic properties of DMSO NCs depend strongly on the interactions between the magnetic dopant and delocalized carriers arising from different point defects.[39-41] In multiple literature reports, room-temperature ferromagnetism was observed in the Fe-doped In_2O_3 system with some attributing it to the presence of nearly-free electrons of oxygen vacancies or other lattice defects.[42-46] On the contrary, paramagnetism too has been reported from Fe-doped In_2O_3 films prepared from a different synthetic procedures.[47] A final conclusion on whether free electron-mediated magnetic interactions exist in these systems or not can't be drawn. We, therefore, decided to study the existence of these interactions by codoping Fe^{3+} with Sn^{4+} which releases free electrons thus facilitating the investigation of any such interactions.

Figure 2.8 shows magnetization (M) vs magnetic field strength (H) plots for 11.2% Fe-doped In_2O_3 NCs capped with oleylamine. Clearly, the M vs H plot is nonlinear S-shaped at 5 K but without saturation. Nonlinearity in M vs H is also present at 300 K as shown in magnified data in the inset of Figure 2.8b. In fact, the inset shows hysteresis at 300 K with small coercivity ~ 25 Oe. The non-linear M vs H plots along with weak hysteresis suggests the possibility of weak ferromagnetism at room temperature. The obtained coercivity is about an order of magnitude smaller when compared

to bulk samples, although, similar to previous reports of Fe-doped In_2O_3 NCs.[45-46] Temperature dependent magnetization (M vs T) for 11.2% Fe-doped In_2O_3 NCs with zero-field-cooled (ZFC) and field-cooled (FC, 100 Oe) conditions are shown in Figure 2.8b. There is a clear divergence between the FC and ZFC even closer to 300 K, which agrees with the weak ferromagnetic hysteresis (inset) observed at room temperature. Also, there is a paramagnetic-like contribution exhibited by an increasing magnetization at lower temperatures. We note that the observed M vs T and M vs H plots for our 11.2% Fe-doped In_2O_3 NCs are similar to prior reports without any major differences.[43, 45] M vs H plots in Figure 2.8c shows that 10.6% Sn-10.4% Fe codoped In_2O_3 NCs also exhibit qualitatively similar behavior when compared to Figure 2.8a without the Sn codoping.

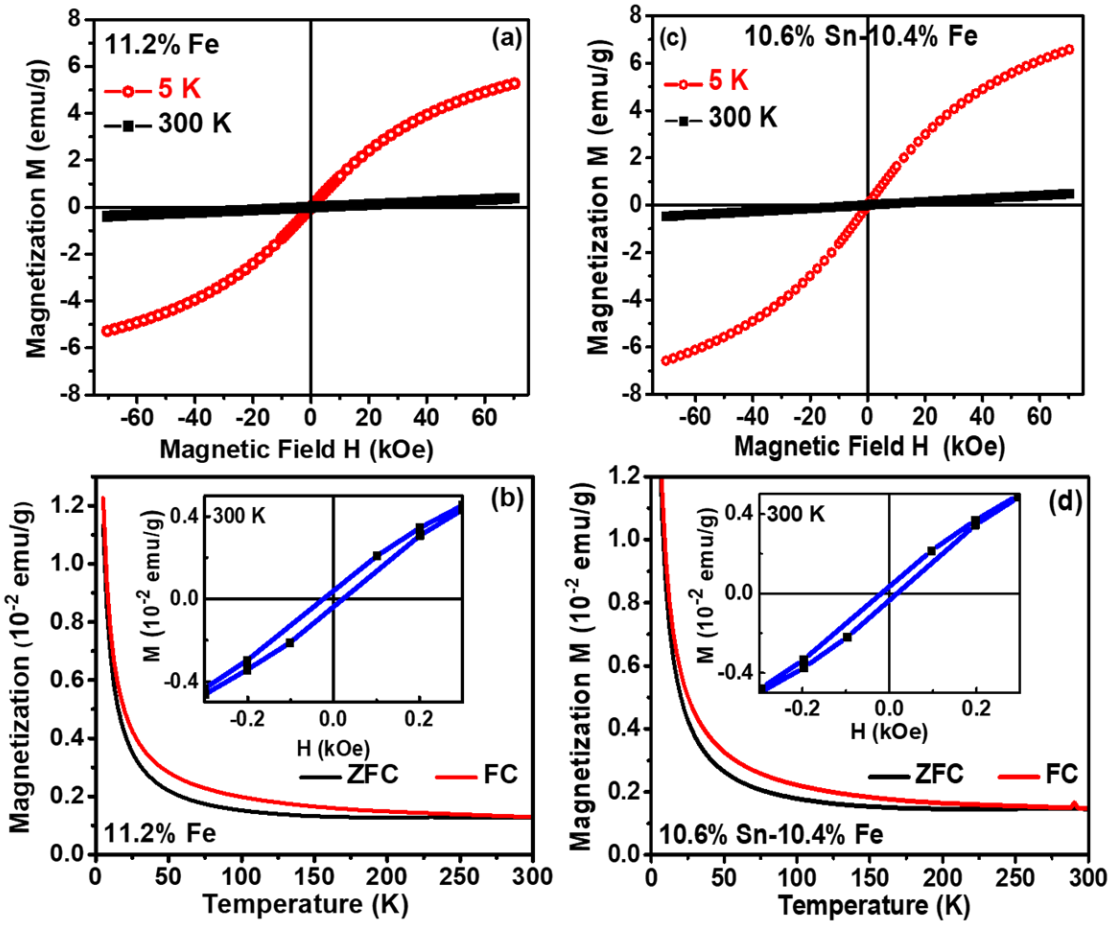

Figure 2.8: (a) M vs H plots for 11.2% Fe-doped In_2O_3 NCs at different temperatures (b) M vs T curves for 11.2% Fe-doped In_2O_3 NCs under ZFC and FC (100 Oe) conditions. The inset shows the presence of hysteresis and coercivity in magnified M vs H plot at 300 K (c) M vs H plots for 10.6% Sn–10.4% Fe codoped In_2O_3 NCs (d) M vs T curves for 10.6% Sn–10.4% Fe codoped In_2O_3 NCs. The inset shows the presence of hysteresis and coercivity in magnified M vs H plot at 300 K.

Figure 2.8d also shows a similar hysteresis and coercivity at room temperature along with divergence in M vs T curves at ZFC and FC (100 Oe) conditions signifying the presence of weak room-temperature ferromagnetism in 10.6% Sn-10.4% Fe codoped In_2O_3 NCs as well.

Quantitatively, there is a small increase in magnetization after the codoping with Sn for both 5K and at 300 K, as shown in Figure 2.9a and 2.9b. Similarly, a small increase in the magnetic moment for 1% Fe – 9.8% Sn codoped In_2O_3 NCs was observed when compared to only 1% Fe-doped In_2O_3 NCs (Figure 2.9c). Sn doping provides mobile free electrons in the conduction band. The increase in magnetization after codoping with electron donating Sn for the same amount of Fe content might be because of the increase in delocalized electron-mediated ferromagnetic interaction in the co-doped sample.[28] However, more evidence needs to be gathered to visualize if this is actually the status-quo.

Figure 2.9d shows the EPR spectra of different Fe-Sn codoped In_2O_3 NCs. The EPR spectra for 11.2% Fe-doped In_2O_3 NCs is similar to spectra observed in previous literature.[45] The derivative spectrum is governed by a broad signal C (as indicated in Figure 2.9d) with g ~2.2 and has been attributed to ferromagnetic resonance (FMR) because of the coupling between electron spins of Fe^{3+} ions. Also, there are two other weak derivative EPR signals indicated by arrows A, and B, on top of the large background of signal C. All three EPR signals are because of Fe^{3+} ions. Signal A and signal B have been assigned to isolated Fe^{3+} with different crystal fields. Signal B with g ~2.0 is to Fe^{3+} in the octahedral cationic site of the In_2O_3 lattice, whereas signal A with g ~4.3 correspond to a lower symmetry rhombic site (possibly distorted octahedral).[45, 48]

To see the presence of electron-mediated magnetic coupling, our major interest lies in studying how Sn doping (addition of free electrons) can influence the EPR spectra. Heavily codoped samples such as 10.6% Sn-10.4% Fe-doped NCs show EPR spectra (not shown) similar to that of 11.2% Fe-doped NCs, because Fe^{3+} ions are located close enough to interact with each other in both samples, even in the absence of free electrons. Therefore, in order to observe any noticeable change due to Sn doping, we chose 0.5% and 1% Fe doping, where the Fe^{3+} ions are expected to be at a far distance in such NCs. As expected, Figure 2.9d shows that the EPR contribution from coupled Fe^{3+} ions (broad signal C) decreases significantly with decreasing Fe content from 11.2% to 1% to 0.5% Fe-doped In_2O_3 NCs, thereby, making signal A and B (corresponding to isolate Fe^{3+} ions) more prominent.

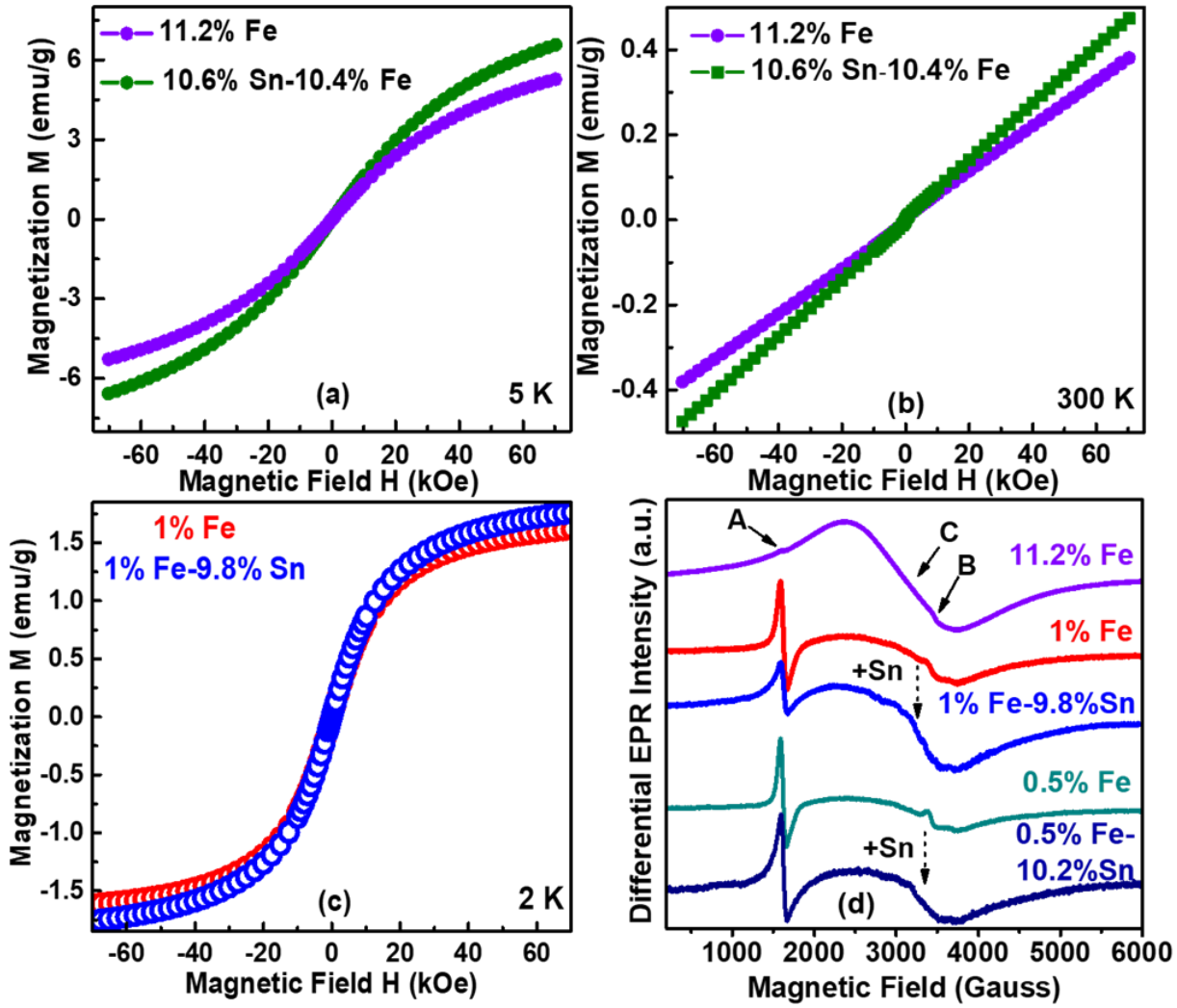

Figure 2.9: Investigating presence of electron-mediated magnetic coupling in Fe-Sn codoped In_2O_3 NCs. Comparison of M vs H for 11.2% Fe and 10.6% Sn-10.4% Fe codoped In_2O_3 NCs at (a) 5 K (b) 300 K. (c) Comparison of M vs H for 1% Fe and 1% Fe-9.8% Sn codoped In_2O_3 NCs at 2 K (d) EPR spectra measured at 300 K for Fe-Sn codoped In_2O_3 NCs with different dopant concentrations.

Now, if we compare the EPR spectra after addition of Sn, as shown by black arrows in Figure 2.9d, 1% Fe-9.8% Sn codoped NCs exhibit more contribution from coupled Fe^{3+} ions compared to 1% Fe-doped NCs. Particularly, peak B becomes invisible under the background of the broad signal, after Sn doping. Similarly, 0.5% Fe-10.2% Sn codoped NCs exhibit more contribution from coupled Fe^{3+} ions compared to 0.5% Fe-doped NCs. This enhancement of coupling between distant Fe^{3+} ions just by Sn^{4+} doping suggests the free electron-mediated magnetic interactions in our Sn and Fe codoped NCs. However, we did not observe a significant increase in EPR intensity for the codoped samples.

While the broadening of the EPR signal establishes the electron-mediated magnetic coupling in codoped NCs, the decrease in magnetic spin via reduction of a fraction of Fe^{3+} to Fe^{2+} probably opposes the enhancement of EPR intensity that is expected from the free electron-mediated magnetic coupling. On the other hand, Fe^{2+} possesses integral spin exhibiting larger zero-field splitting compared to energy at X-band and also short spin-lattice relaxation times; making it EPR inactive within our experimental conditions.[49-50] We have also not observed any typical contribution from Fe^{2+} ion in the magnetic data of codoped samples. Similar results were also observed in prior reports of semiconductor nanocrystals doped with both Fe^{3+} and Fe^{2+}, [49, 51] probably because of both smaller amount of Fe^{2+} and smaller magnetic spin per Fe^{2+} compared to Fe^{3+} ions.

2.4 Conclusions

In conclusion, we report here synthesis and properties of Fe-Sn codoped colloidal In_2O_3 NCs, for the first time. Sn^{4+} doping provides free electrons in the In_2O_3 lattice giving rise to high electrical conductivity and LSPR in the NIR region. Fe^{3+} doping, on the other hand, leads to the realization of weak room-temperature ferromagnetism. Codoping enables interactions between the two dopants, Fe and Sn, which leads to tunability in the properties exhibited by them. The peak position of the NIR LSPR band that arises due to the free electrons generated by Sn^{4+} can be tuned from the 2200-3000 nm by changing the Fe codoping concentration. Similarly, the electrical conductivity varies from 34 S/cm to 2 S/cm as the Fe codoping concentration is increased. Elucidating the local structure through EXAFS and XANES reveals that a fraction of Fe^{3+} reduced to Fe^{2+} by consuming the free electrons generated by Sn^{4+} leading to tunability in the properties exhibited by Sn. Sn codoping, on the other hand, controls the extent of magnetism observed in Fe-Sn codoped In_2O_3 NCs through electron-mediated magnetic coupling. The free electrons generated by Sn^{4+} mediate ferromagnetic interactions between distant Fe^{3+} ions thereby increasing the extent of magnetism and broadening the EPR signal of Fe^{3+} ions. The strength of this coupling is difficult to quantify as the increase of magnetism due to electron-mediated magnetic interactions is countered by the decrease in magnetism due to the conversion of Fe^{3+} to Fe^{2+}. All in all, Fe-Sn codoped In_2O_3 NCs is the first system in literature where tunable electrical conductivity, LSPR, and magnetism along with visible transparency can be observed from the same system. This tunability is attributed to the interactions between the two dopants introduced by codoping in NCs.

2.5 References

1. Son, J. S.; Lee, J. S.; Shevchenko, E. V.; Talapin, D. V. Magnet-in-the-Semiconductor Nanomaterials: High Electron Mobility in All-Inorganic Arrays of FePt/CdSe and FePt/CdS Core-Shell Heterostructures. *J. Phys. Chem. Lett.* **2013,** *4*, 1918-1923.
2. Santra, P. K.; Kamat, P. V. Tandem-Layered Quantum Dot Solar Cells: Tuning the Photovoltaic Response with Luminescent Ternary Cadmium Chalcogenides. *J. Am. Chem. Soc.* **2013,** *135*, 877-885.
3. Bardhan, R.; Chen, W. X.; Perez-Torres, C.; Bartels, M.; Huschka, R. M.; Zhao, L. L.; Morosan, E.; Pautler, R. G.; Joshi, A.; Halas, N. J. Nanoshells with Targeted Simultaneous Enhancement of Magnetic and Optical Imaging and Photothermal Therapeutic Response. *Adv. Funct. Mater.* **2009,** *19*, 3901-3909.
4. Kim, J.; Park, S.; Lee, J. E.; Jin, S. M.; Lee, J. H.; Lee, I. S.; Yang, I.; Kim, J. S.; Kim, S. K.; Cho, M. H.; Hyeon, T. Designed Fabrication of Multifunctional Magnetic Gold Nanoshells and Their Application To Magnetic Resonance Imaging And Photothermal Therapy. *Angew. Chem.-Int. Ed.* **2006,** *45*, 7754-7758.
5. Dong, W. J.; Li, Y. S.; Niu, D. C.; Ma, Z.; Gu, J. L.; Chen, Y.; Zhao, W. R.; Liu, X. H.; Liu, C. S.; Shi, J. L. Facile Synthesis of Monodisperse Superparamagnetic Fe_3O_4 Core@hybrid@Au Shell Nanocomposite for Bimodal Imaging and Photothermal Therapy. *Adv. Mater.* **2011,** *23* (45), 5392-5397.
6. Tian, Q. W.; Hu, J. Q.; Zhu, Y. H.; Zou, R. J.; Chen, Z. G.; Yang, S. P.; Li, R. W.; Su, Q. Q.; Han, Y.; Liu, X. G. Sub-10 nm Fe_3O_4@$Cu_{2-x}S$ Core-Shell Nanoparticles for Dual-Modal Imaging and Photothermal Therapy. *J. Am. Chem. Soc.* **2013,** *135*, 8571-8577.
7. Dietl, T.; Ohno, H.; Matsukura, F.; Cibert, J.; Ferrand, D. Zener Model Description Of Ferromagnetism in Zinc-Blende Magnetic Semiconductors. *Science* **2000,** *287*, 1019-1022.
8. Zhou, T.; Wei, L.; Xie, Y. R.; Li, Q. H.; Hu, G. X.; Chen, Y. X.; Yan, S. S.; Liu, G. L.; Mei, L. M.; Jiao, J. Effects of Sn Doping on the Morphology and Properties of Fe-doped In_2O_3 Epitaxial Films. *Nanoscale Res. Lett.* **2012,** *7*, (661).
9. Dhara, B.; Ballav, N. In Situ Generation of Conducting Polymer in a Redox-Active Metal-Organic Gel. *RSC Adv.* **2013,** *3*, 4909-4913.
10. www.mrcat.iit.edu
11. Stern, E. A.; Heald, S. M. X-Ray Filter Assembly for Fluorescence Measurements of X-Ray Absorption Fine-Structure. *Rev. Sci. Instrum.* **1979,** *50*, 1579-1582.
12. Ravel, B.; Newville, M. Athena, Artemis, Hephaestus: Data Analysis for X-Ray Absorption Spectroscopy using Ifeffit. *J. Synchrot. Radiat.* **2005,** *12*, 537-541.
13. Langford, J. I.; Wilson, A. J. C. Scherrer after Sixty Years: A Survey and Some New Results in the Determination of Crystallite Size. *J. Appl. Crystallogr.* **1978,** *11*, 102-113.
14. Vegard, L. Die Konstitution der Mischkristalle und die Raumfüllung der Atome. *Z. Phys.* **1921,** *5*, 17-26.
15. Shannon, R. D.; Prewitt, C. T. Effective Ionic Radii in Oxides and Fluorides. *Acta Crystallogr. Sect. B* **1969,** *25*, 925-946.
16. Nadaud, N.; Lequeux, N.; Nanot, M.; Jové, J.; Roisnel, T. Structural Studies of Tin-Doped Indium Oxide (ITO) and $In_4Sn_3O_{12}$. *J. Solid State Chem.* **1998,** *135*, 140-148.
17. González, G. B.; Mason, T. O.; Quintana, J. P.; Warschkow, O.; Ellis, D. E.; Hwang, J.-H.; Hodges, J. P.; Jorgensen, J. D. Defect Structure Studies of Bulk and Nano-Indium-Tin Oxide. *J. Appl. Phys.* **2004,** *96*, 3912-3920.

18. King, P. D. C.; Veal, T. D.; Fuchs, F.; Wang, C. Y.; Payne, D. J.; Bourlange, A.; Zhang, H.; Bell, G. R.; Cimalla, V.; Ambacher, O.; Egdell, R. G.; Bechstedt, F.; McConville, C. F. Band Gap, Electronic Structure, and Surface Electron Accumulation of Cubic and Rhombohedral In_2O_3. *Phys. Rev. B* **2009,** *79*, 205211.
19. Gilstrap, R. A.; Capozzi, C. J.; Carson, C. G.; Gerhardt, R. A.; Summers, C. J. Synthesis of a Nonagglomerated Indium Tin Oxide Nanoparticle Dispersion. *Adv. Mater.* **2008,** *20*, 4163-4166.
20. Wang, T.; Radovanovic, P. V. Free Electron Concentration in Colloidal Indium Tin Oxide Nanocrystals Determined by Their Size and Structure. *J. Phys. Chem. C* **2011,** *115*, 406-413.
21. Shim, M.; Guyot-Sionnest, P. Organic-Capped ZnO Nanocrystals: Synthesis and n-type Character. *J. Am. Chem. Soc.* **2001,** *123*, 11651-11654.
22. Faucheaux, J. A.; Jain, K. Plasmons in Photocharged ZnO Nanocrystals Revealing the Nature of Charge Dynamics. *J. Phys. Chem. Lett.* **2013,** *4*, 3024-3030.
23. Kanehara, M.; Koike, H.; Yoshinaga, T.; Teranishi, T. Indium Tin Oxide Nanoparticles with Compositionally Tunable Surface Plasmon Resonance Frequencies in the Near-IR Region. *J. Am. Chem. Soc.* **2009,** *131*, 17736-17737.
24. Lounis, S. D.; Runnerstrom, E. L.; Llordés, A.; Milliron, D. J. Defect Chemistry and Plasmon Physics of Colloidal Metal Oxide Nanocrystals. *J. Phys. Chem. Lett.* **2014,** *5*, 1564-1574.
25. Warschkow, O.; Ellis, D. E.; González, G. B.; Mason, T. O. Defect Cluster Aggregation and Nonreducibility in Tin-Doped Indium Oxide. *J. Am. Ceram. Soc.* **2003,** *86*, 1707-1711.
26. González, G. B.; Mason, T. O.; Okasinski, J. S.; Buslaps, T.; Honkimäki, V. Determination of the Solubility of Tin in Indium Oxide Using In Situ and Ex Situ X-Ray Diffraction. *J. Am. Ceram. Soc.* **2012,** *95*, 809-815.
27. Faucheaux, J. A.; Stanton, A. L. D.; Jain, P. K. Plasmon Resonances of Semiconductor Nanocrystals: Physical Principles and New Opportunities. *J. Phys. Chem. Lett.* **2014,** *5*, 976-985.
28. Yu, Z. G.; He, J.; Xu, S. F.; Xue, Q. Z.; van't Erve, O. M. J.; Jonker, B. T.; Marcus, M. A.; Yoo, Y. K.; Cheng, S. F.; Xiang, X. D. Origin of Ferromagnetism in Semiconducting $(In_{1-x-y}Fe_xCu_y)_2O_3$-σ. *Phys. Rev. B* **2006,** *74*, 165321.
29. Andrew J. Berry, A. J.; Hugh St. C.O'Neill, Kasthuri D.Jayasuriya, Stewart J. Cambell, and Garry J. Foran, *Am. Mineral*., **2003**, *88*, 967-977.
30. Elizabeth Cottrell, Katherin A. Kelly, Antonio Lanzirotti, Rebecca A. Fischer, *Chem. Geol.* **2009,** *268*, 167-179.
31. Max Wilke, Francois Farges, Pierre-Emmanueal PeTit, Gordon E. Brown Jr. and Francois Martin, *Am. Mineral.*, **2001,** *86*, 714-730.
32. Westre, T. E.; Kennepohl, P.; DeWitt, J. G.; Hedman, B.; Hodgson, K. O.; Solomon, E. I. A Multiplet Analysis of Fe K-edge 1s->3d Pre-edge Features of Iron Complexes. *J. Am. Chem. Soc.* **1997,** *119*, 6297-6314.
33. Chen, L. X.; Liu, T.; Thurnauer, M. C.; Csencsits, R.; Rajh, T. Fe_2O_3 Nanoparticle Structures Investigated by X-Ray Absorption Near-edge Structure, Surface Modifications, and Model Calculations. *J. Phys. Chem. B* **2002,** *106*, 8539-8546.
34. Rao, M. J.; Shibata, T.; Chattopadhyay, S.; Nag, A. Origin of Photoluminescence and XAFS Study of $(ZnS)_{1-x}(AgInS_2)_x$ Nanocrystals. *J. Phys. Chem. Lett.* **2014,** *5*, 167-173.
35. Mukherjee, S.; Nag, A.; Kocevski, V.; Santra, P. K.; Balasubramanian, M.; Chattopadhyay, S.; Shibata, T.; Schaefers, F.; Rusz, J.; Gerard, C.; Eriksson, O.; Segre, C. U.; Sarma, D. D. Microscopic Description of the Evolution of the Local Structure and an Evaluation of the Chemical Pressure Concept in a Solid Solution. *Phys. Rev. B* **2014,** *89*, 224105.

36. Mason, T. O.; Kammler, D. R.; Ingram, B. J.; Gonzalez, G. B.; Young, D. L.; Coutts, T. J. Key Structural and Defect Chemical Aspects of Cd-In-Sn-O Transparent Conducting Oxides. *Thin Solid Films* **2003,** *445*, 186-192.
37. Yu, J. H.; Liu, X. Y.; Kweon, K. E.; Joo, J.; Park, J.; Ko, K. T.; Lee, D.; Shen, S. P.; Tivakornsasithorn, K.; Son, J. S.; Park, J. H.; Kim, Y. W.; Hwang, G. S.; Dobrowolska, M.; Furdyna, J. K.; Hyeon, T. Giant Zeeman Splitting in Nucleation-Controlled Doped CdSe:Mn^{2+} Quantum Nanoribbons. *Nat. Mater.* **2010,** *9*, 47-53.
38. Viswanatha, R.; Naveh, D.; Chelikowsky, J. R.; Kronik, L.; Sarma, D. D. Magnetic Properties of Fe/Cu Codoped ZnO Nanocrystals. *J. Phys. Chem. Lett.* **2012,** *3*, 2009-2014.
39. Sapra, S.; Sarma, D. D.; Sanvito, S.; Hill, N. A. Influence of Quantum Confinement on the Electronic and Magnetic Properties of (Ga,Mn)As Diluted Magnetic Semiconductor. *Nano Lett.* **2002,** *2*, 605-608.
40. Kittilstved, K. R.; Gamelin, D. R. Activation Of High-T_C Ferromagnetism in Mn^{2+}-Doped ZnO using Amines. *J. Am. Chem. Soc.* **2005,** *127*, 5292-5293.
41. Zheng, W. W.; Strouse, G. F. Involvement of Carriers in the Size-Dependent Magnetic Exchange for Mn:CdSe Quantum Dots. *J. Am. Chem. Soc.* **2011,** *133*, 7482-7489.
42. Yoo, Y. K.; Xue, Q.; Lee, H. C.; Cheng, S. F.; Xiang, X. D.; Dionne, G. F.; Xu, S. F.; He, J.; Chu, Y. S.; Preite, S. D.; Lofland, S. E.; Takeuchi, I. Bulk Synthesis and High-Temperature Ferromagnetism of $(In_{1-x}Fe_x)_2O_3$-σ with Cu Co-doping. *Appl. Phys. Lett.* **2005,** *86*, 042506.
43. Chu, D.; Zeng, Y. P.; Jiang, D.; Ren, Z. Tuning the Crystal Structure and Magnetic Properties of Fe-doped In_2O_3 Nanocrystals. *Appl. Phys. Lett.* **2007,** *91*, 262503.
44. Jayakumar, O. D.; Gopalakrishnan, I. K.; Kulshreshtha, S. K.; Gupta, A.; Rao, K. V.; Louzguine-Luzgin, D. V.; Inoue, A.; Glans, P. A.; Guo, J. H.; Samanta, K.; Singh, M. K.; Katiyar, R. S. Structural and Magnetic Properties of $(In_{1-x}Fe_x)_2O_3$ ($0.0 <= x <= 0.25$) System: Prepared by Gel Combustion Method. *Appl. Phys. Lett.* **2007,** *91*, 052504.
45. Singhal, A.; Achary, S. N.; Manjanna, J.; Jayakumar, O. D.; Kadam, R. M.; Tyagi, A. K. Colloidal Fe-Doped Indium Oxide Nanoparticles: Facile Synthesis, Structural, and Magnetic Properties. *J. Phys. Chem. C* **2009,** *113*, 3600-3606.
46. Jiang, F. X.; Xu, X. H.; Zhang, J.; Fan, X. C.; Wu, H. S.; Alshammari, M.; Feng, Q.; Blythe, H. J.; Score, D. S.; Addison, K.; Al-Qahtani, M.; Gehring, G. A. Room Temperature Ferromagnetism in Metallic and Insulating $(In_{1-x}Fe_x)_2O_3$ Thin Films. *J. Appl. Phys.* **2011,** *109*, 053907.
47. Berardan, D.; Guilmeau, E. Magnetic Properties of Bulk Fe-doped Indium Oxide. *J. Phys.-Condes. Matter* **2007,** *19*, 236224.
48. Chakradhar, R. P. S.; Yasoda, B.; Rao, J. L.; Gopal, N. O. Mixed Alkali Effect in Li_2O-Na_2O-B_2O_3 glasses containing Fe_2O_3 - An EPR and Optical Absorption Study. *Mater. Res. Bull.* **2006,** *41*, 1646-1656.
49. Karmakar, D.; Mandal, S. K.; Kadam, R. M.; Paulose, P. L.; Rajarajan, A. K.; Nath, T. K.; Das, A. K.; Dasgupta, I.; Das, G. P. Ferromagnetism in Fe-doped ZnO Nanocrystals: Experiment and Theory. *Phys. Rev. B* **2007,** *75*, 144404.
50. Misra, S. K.; Diehl, S.; Tipikin, D.; Freed, J. H. A Multifrequency EPR study of Fe^{2+} and Mn^{2+} Ions in a $ZnSiF_6.6H_2O$ Single Crystal at Liquid-Helium Temp. *J. Magn. Reson.* **2010,** *205*, 14-22.
51. Chu, D. W.; Zeng, Y. P.; Jiang, D. L.; Ren, Z. M.; Ren, W. L.; Wang, J. H.; Zhang, T. Structural, Optical, and Magnetic Properties of Fe-doped In_2O_3 Nanocubes. *J. Mater. Res.* **2008,** *23*, 2597-2601.

Chapter-3

Delocalized Electron-Mediated Magnetic Coupling in Mn-Sn Codoped In_2O_3 Nanocrystals

---

Following article has been published from the work presented in this chapter.

1. Tandon, B.; Yadav, A.; Nag, A.; "Delocalized Electrons Mediated Magnetic Coupling in Mn-Sn codoped In_2O_3 NCs" *Chem. Mater.* **2016**, *28*, 3620-3624.

Summary

Interactions between the localized spins of magnetic ions and delocalized charge carriers are highly desirable for spin-based applications of different dilute magnetic semiconductors. More often than not, these interactions are restricted due to the localized nature of the charge carriers. We report here such interactions between the conduction band (CB) electrons and Mn^{2+} in Mn-Sn codoped In_2O_3 nanocrystals (NCs). Sn^{4+} doping provides delocalized CB electrons whereas Mn^{2+} provides localized magnetic spins. The localized surface plasmon resonance (LSPR) exhibited by these NCs asserts the delocalized nature of the electrons and, therefore allows us to study the magnetic interactions between the localized magnetic spins of Mn^{2+} and delocalized electrons. 1.3% Mn-doped In_2O_3 NCs exhibit antiferromagnetic superexchange interactions between neighboring Mn^{2+} ions yielding a near-saturation magnetic moment (M_S) of 3.5 μ_B/Mn^{2+} at 2 K. After codoping with Sn^{4+} in 1.3% Mn-10% Sn codoped In_2O_3 NCs, the CB electron - Mn^{2+} interactions facilitate ferromagnetic exchange coupling between distant Mn^{2+} ions consequently dominating the antiferromagnetic superexchange interaction of neighboring Mn^{2+} ions and increasing the M_S to a nearly ideal value of 4.8 μ_B/Mn^{2+} at 2 K.

Graphical Abstract

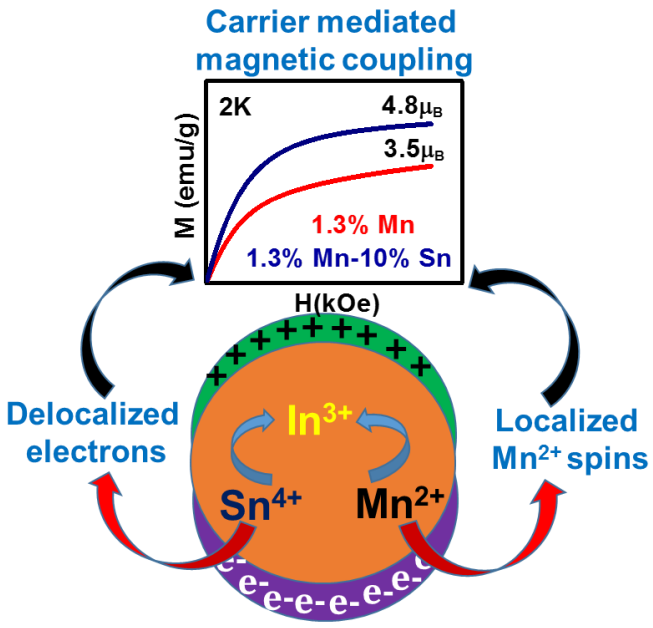

3.1 Introduction

Dilute magnetic semiconductor oxides (DMSO) are metal oxides doped with magnetic ions, where interaction between delocalized charge carrier such as a conduction band (CB) electron and localized magnetic spin (for example, dopant Mn^{2+} ion) decides it's potential as a future spintronic material.[1-2] Localization of charge carriers restricts most DMSO from realizing the full potential of the exchange interactions between the charge carriers and localized magnetic spins. By generating delocalized charge carriers through photoexcitation in an anaerobic environment, ferromagnetic exchange interactions between CB electrons and Mn^{2+} in Mn-doped ZnO NCs have been demonstrated by Ochsenbein et al.[3] The strength of these carrier-Mn^{2+} exchange interactions can also be manipulated through quantum confinement of charge carriers in a semiconductor (SC) NC.[4-5] We here introduce these CB electrons by Sn^{4+} codoping in Mn-Sn codoped In_2O_3 NCs (CB electrons completely air-stable unlike those resulting from photoexcitation), that exhibit CB electron – Mn^{2+} ferromagnetic exchange interactions, yielding nearly ideal (~4.8 μ_B/Mn^{2+} ion) magnetic moment at 2 K and 70 kOe.

One of the major problem hindering these ferromagnetic exchange interactions in a doped SC NC is the intrinsic antiferromagnetic superexchange coupling between next-to-nearest neighbor magnetic cations such as Mn^{2+}-O^{2-}-Mn^{2+}.[3, 6-9] The CB electron–Mn^{2+} interaction, however, is ferromagnetic in nature and has the potential to overcome this antiferromagnetic superexchange interaction. For example, (i) Strouse and coworker suggested carrier-mediated ferromagnetic interaction in Mn-doped CdSe NCs, but the carriers were not CB electrons, instead came from surface defect states of ultra-small (<3 nm) NCs,[7] (ii) Ochsenbein et al. showed CB electron – Mn^{2+} ferromagnetic exchange interaction in the photo-excited Mn-doped ZnO NCs,[3] and (iii) we reported the possibility of CB electron – Fe^{3+} exchange interaction in Fe-Sn codoped In_2O_3 NCs in Chapter-2. However, a fraction of Fe^{3+} reduces to Fe^{2+} ions after Sn^{4+} codoping, which in turn has the opposing effect of decreasing magnetic moment.[10-11] To get rid of the problem of change in the oxidation state of Fe^{3+}, we replace it with another d^5 system, namely Mn^{2+} and synthesized Mn-Sn codoped In_2O_3 NCs.

The motivation for codoping Sn^{4+} along with magnetic ions in In_2O_3 stems from the fact that Sn-doped In_2O_3 (popularly known as ITO) is already a benchmark transparent conducting oxides (TCO), possessing CB electrons in the ground state and doping magnetic ions in TCOs along with

it helps could enable one to study the CB electron – magnetic ion interactions.[1, 12-13] Careful studies show that good quality single crystals of magnetically doped TCOs do not exhibit ferromagnetism, instead, polycrystalline films exhibit ferromagnetism.[1,14] Electrical conductivity of such polycrystalline magnetically doped TCO films typically exhibits non-metallic behavior, which may arise from the extensive contribution from insulating grain boundaries in spite of carriers are metal-like delocalized within a grain.[15] Importantly, plasmonic band of Sn-doped In_2O_3 (ITO) NCs provides a way to distinguish delocalized CB electrons from defect-bound localized electrons, unlike electrical characterization that suffers from grain boundary related problems and allows us to study CB electrons-Mn^{2+} magnetic interactions with more confidence.

3.2 Experimental Section

3.2.1 Synthesis of Mn-Sn codoped In_2O_3 NCs

All Mn-Sn codoped In_2O_3 NCs were synthesized in a similar fashion as previously reported Fe-Sn codoped In_2O_3 NCs.[10-11] Stoichiometric amounts of In, Mn and Sn precursor were weighed to achieve a target composition. For example: to synthesize 12.2% Mn-10% Sn codoped In_2O_3 NCs, 0.083 mmol of manganese(II) acetylacetonate, 0.065 mmol of tin(IV) bis(acetylacetonate) dichloride and 0.486 mmol of indium(III) acetylacetonate were weighed in a three-neck round bottom flask and 10.0 mL of oleylamine solvent was added to it. The mixture was subjected to alternating atmospheres of N_2 and vacuum at room temperature for 30 minutes to remove dissolved gases followed by 30 minutes of vacuum at 100 ˚C to get rid of adsorbed water molecules. The temperature of the solution was then gradually increased to 220 ˚C at the rate of ~10˚C/min under N_2 conditions and allowed uninterrupted heating 220 ˚C at for 5 hours with vigorous stirring. The mixture was subsequently cooled down to room temperature and NCs were obtained by precipitating them with excess methanol (~30 mL) followed by centrifugation at 6000 rpm for 6 min. The washing procedure was repeated twice to get rid of the excess oleylamine solvent and the NCs obtained were then dispersed in different non-polar solvents such as hexane and tetrachloroethylene for different characterization purposes.

3.2.2 Characterization of Mn-Sn codoped In_2O_3 NCs

Energy dispersive X-ray analysis (EDX): The elemental composition of all Mn-Sn codoped In_2O_3 NCs was determined through EDX spectroscopy on a Zeiss Ultra Plus SEM instrument operating at an energy of 20 kV.

Inductively coupled plasma atomic emission spectroscopy (ICP-AES): The elemental compositions obtained from EDX spectroscopy were complemented with ICP-AES technique performed on a Perkin−Elmer Optima 7000 DV machine. ~1-2 mg of NC powder was dissolved in 70% HNO_3 and the solution volume was diluted with milli-Q water to result in a 2% v/v HNO_3 acid solution. Standard solutions with variable concentrations of a particular element were prepared by diluting the commercial ICP standard with 2% v/v HNO_3 solution.

X-ray diffraction (XRD): To determine the crystal structure and phase purity of different NCs, XRD patterns were recorded on a Bruker D8 Advance X-ray diffractometer employing monochromated Cu Kα (λ=1.5406 Å) as an X-ray source. Contribution from Cu Kα2 (λ=1.5444 Å) and the background was subtracted from the XRD pattern obtained from the instrument.

Raman spectroscopy: To examine the presence of an amorphous impurity, Raman measurements were carried out on all Mn-Sn codoped In_2O_3 NCs. Nanocrystal powder was first transferred on a glass slide and then Raman spectra were recorded on a Horiba LabRam HR instrument consisting of a He-Ne laser with 632.8 nm excitation source.

Transmission electron microscopy (TEM): Morphology of the Mn-Sn codoped In_2O_3 NCs was imaged through TEM. A dilute solution of NCs in hexane was drop-casted on a carbon coated TEM grid and analyzed in JEOL JEM 2100F microscope operated at 200 kV. The TEM micrographs obtained were processed in ImageJ software to calculate the average diameter and standard deviation of NCs.

Electrical measurements: Keithley Four-Probe Conductivity Instrument (Model 6220/6221 Current Source and Model 2182A nanovoltmeter) was used to measure four probe DC electrical conductivity on ~1.0 mm thick NC pellets having a diameter of 13 mm. The collinear probes having a diameter of 1 mm and separated by a distance of 2.24 mm were used to establish contact with the surface of the pellet. All the pellets were annealed in N_2 filled glove box for 2 hrs at 200℃. AC impedance was measured using a computer enabled PARSTAT 2273 galvanostat/potentiostat in a two probe geometry on a glass substrate. Thin films used for measurements were made using doctor blading technique. Two spring loaded gold electrodes separated by 1.5 mm were used to make contact with films (colloidal silver paste was applied on films to reduce contact resistance) in athe ir. A constant 500 mV AC perturbing voltage was applied in the frequency range 2 MHz -

100 mHz. Data obtained were fitted with ZSimpWin 3.2 electrochemical impedance modelling software.

UV-Vis-NIR absorption spectroscopy: To avoid the vibrational peaks of different bonds in the infrared region which would interfere in the NIR LSPR spectra, dilute solution of NCs were prepared in tetrachloroethylene solvent and UV-Vis-NIR spectra were recorded on Perkin Elmer, Lambda-950 UV/Vis spectrometer and Shimadzu UV-3600 Plus UV-Vis-NIR spectrophotometer.

Electron paramagnetic resonance (EPR): EPR measurements were performed on NC powder filled in a capillary on JEOL JES-FA200 ESR spectrometer filled with Q-band attachment.

Thermogravimetric analysis (TGA): To determine the amount of inorganic and organic core, TGA analysis was performed on nanocrystal powder between room temperature to 800˚C using a PerkinElmer STA 6000 simultaneous thermal analyzer.

Magnetic measurements: Magnetic measurements were done on a SQUID magnetometer (Quantum Design MPMS XL-7 Magnetometer). Zero-field cooled (ZFC) and field-cooled (FC) data were acquired within the temperature range of 2−300 K at magnetic field, H = 100 Oe after samples were cooled in zero field or in a 100 Oe field, respectively. It was found from TGA data that NCs are composed of ~84% inorganic core and 16% organic ligands (oleylamine). This weight of inorganic core was used to calculate the magnetization in emu/g, and thereafter, in calculating the magnetization in terms of μ_B/Mn^{2+} ion.

3.3 Results and Discussion

3.3.1 Structure and morphology

The elemental compositions of the Mn-Sn codoped In_2O_3 NCs were investigated by the EDX technique (Table 3.1). For all NCs, the doping percentages estimated from EDX are in excellent correlation with the precursor molar ratios. Such high level of doping efficiency has been achieved earlier in similar systems, where precursors with pre-bonded metal-oxygen moieties were used for synthesis.[10, 16-17] To avoid any error in the quantification of properties, we will use the obtained EDX compositions throughout the manuscript. We note here that the obtained EDX compositions have been complemented with the results from ICP-AES analysis (not shown), as results from EDX can have higher error margins, at low doping percentages.

Table 3.1: Comparison of some of the nanocrystal compositions estimated by the EDX technique with the precursor molar ratios used in the synthesis.

In : Mn : Sn	
Precursor Ratio	EDX Composition
92.5 : 7.5 : 0	93.5 : 6.5 : 0
82 : 13 : 5	83.4 : 12.4 : 4.5
83.5 : 6.5 : 10	83.7 : 5.9 : 10.4
88.5 : 1.5 : 10	88.7 : 1.3 : 10
98.5 : 1.5 : 0	98.6 : 1.4 : 0
87 : 13 : 0	87.7 : 12.5 : 0
77 : 13 : 10	78.3 : 12.2 : 9.5

Figure 3.1 shows the powder XRD patterns of different Mn-Sn codoped In_2O_3 NCs where the doping percentage of Sn varies from 0-10.4% and that of Mn varies from 0-12.5%, in the final NC product. All Mn-Sn codoped In_2O_3 NCs exhibit the same cubic bixbyite structure (space group 206, *Ia3*) as that of the In_2O_3 NCs and bulk In_2O_3 reference (JCPDS 88-2160) without showing the presence of any crystalline impurity phase. The position of the diffraction peaks, however, seems to be dependent on the type and extent of doping, reflecting a change in lattice constants.

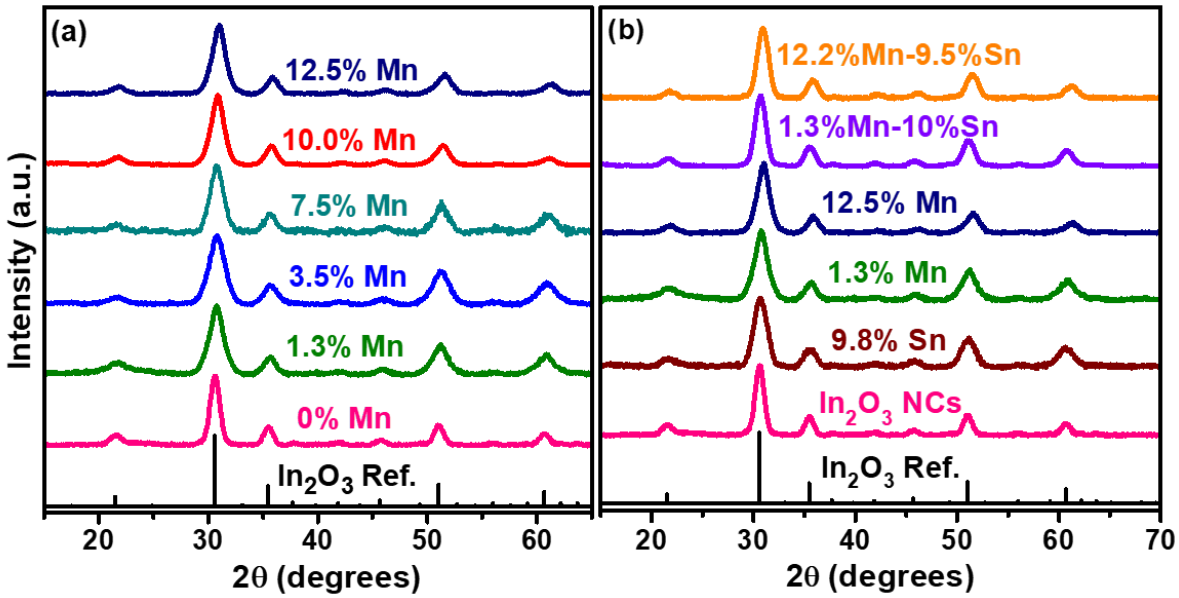

Figure 3.1: Powder XRD patterns of (a) only Mn-doped In_2O_3 NCs (b) Mn-Sn codoped In_2O_3 NCs signifying the retention of the bulk In_2O_3 cubic bixbyite phase in NCs despite a huge variation in the Mn and Sn doping percentage.

While 9.8% Sn-doped In_2O_3 NCs exhibit similar lattice constants as undoped In_2O_3 NCs, the lattice constants decrease systematically as the extent of Mn doping/codoping in In_2O_3 NCs is increased (shown in Figure 3.2). This can be interpreted as lattice doping of Mn^{2+} ions by substituting In^{3+} ions which is a direct consequence of Vegard's law,[18] and the observation is in accordance with the literature reports on bulk samples.[19-20] We note here that this observation is not due to different sizes of Mn^{2+} and In^{3+} as crystal radii of Mn^{2+} is greater than In^{3+} (r_{Mn2+} = 82 pm, r_{In3+} = 79 pm).[21] Therefore, Mn^{2+} doping in In_2O_3 is expected to yield larger interplanar distances than undoped In_2O_3. However, Mn^{2+} ion and In^{3+} are not isovalent and an oxygen vacancy is created to compensate for the charge imbalance when Mn^{2+} substitutes In^{3+} in the lattice.[22] This increase in oxygen vacancy concentration with Mn doping would affect the position of diffraction peaks as loss of atoms shrinks the lattice. Therefore, the XRD data suggest that Mn and Sn are incorporated in the In_2O_3 substitutionally, both in the doped and the codoped form.

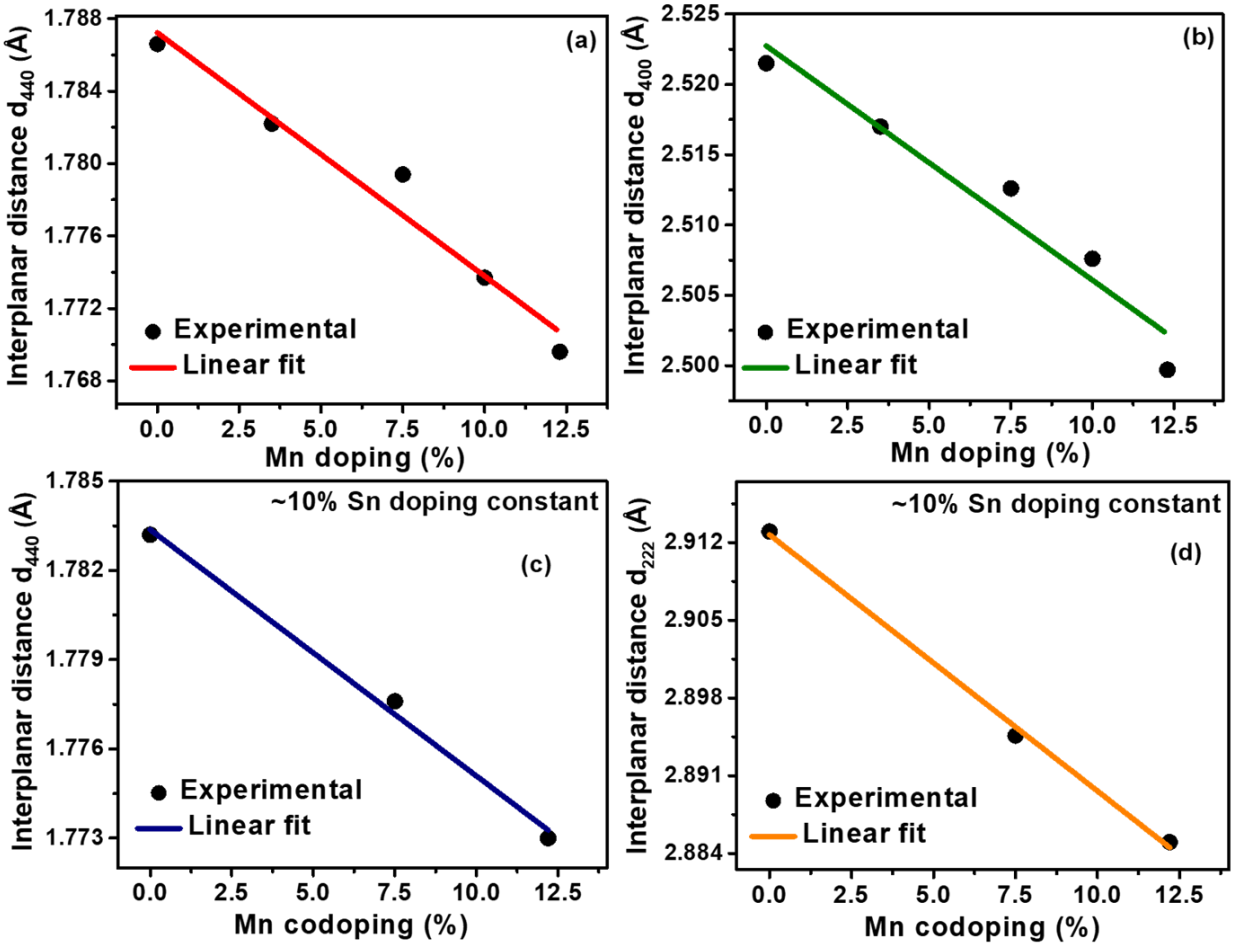

Figure 3.2: Evidence of lattice doping through variation in the interplanar distances of (a) {440} plane (b) {400} plane as Mn doping percentage is increased. (c) {400} plane (d) {222} plane as the Mn doping percentage is increased while keeping Sn codoping percentage constant.

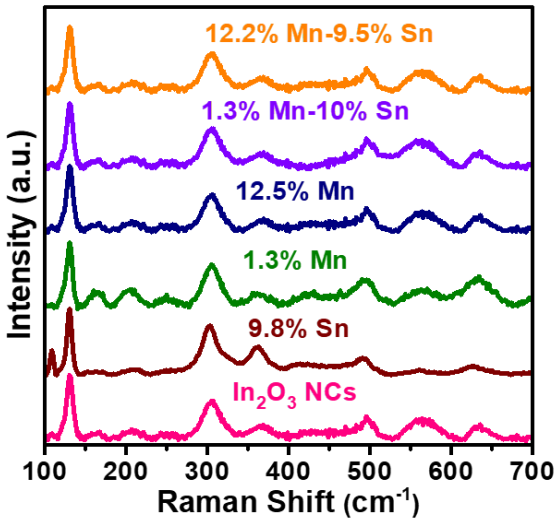

Figure 3.3: Comparison of Raman spectra of different Mn-Sn codoped In_2O_3 NCs with that of undoped In_2O_3 NCs to check the phase purity of NCs.

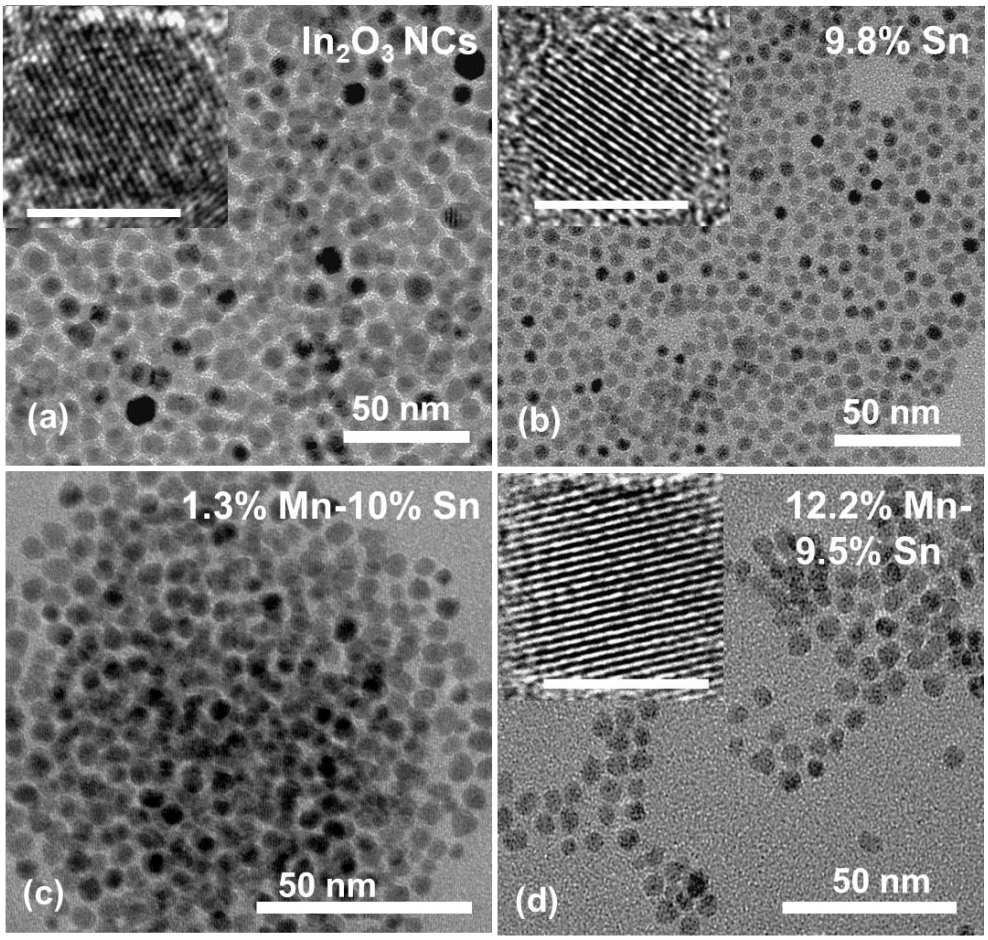

Figure 3.4: TEM micrographs of different Mn-Sn codoped In_2O_3 NCs with their high-resolution TEM (HRTEM) images in the inset showing highly crystalline nature of almost spherical NCs. Scale bars for insets in (a), (b) and (d) are 5 nm.

While XRD patterns can tell the absence of a crystalline impurity, it doesn't negate the presence of an amorphous impurity. We recorded Raman spectra of all Mn-Sn codoped In_2O_3 NCs to check for the presence of an amorphous impurity and plotted them in Figure 3.3. The Raman spectra of different Mn-Sn codoped In_2O_3 NCs exhibit the phonon modes identical to the undoped In_2O_3 NCs and reiterates the phase purity of our NCs. The observed Raman modes can be assigned to In-O vibrations of InO_6 structural units in the cubic bixbyite structure of In_2O_3.[23]

Figure 3.4 shows the TEM images of different Mn-Sn codoped In_2O_3 NCs with their respective HRTEM images in the inset. The morphology of all NCs is nearly spherical, however, the average diameter of undoped In_2O_3 NCs is markedly different from the Mn-Sn codoped In_2O_3 NCs. While the average diameter of undoped In_2O_3 NCs is ~9.1 nm, Mn-Sn codoped In_2O_3 NCs are sized between 6-7 nm across different doping percentages. This observation is supported by the narrower peaks for undoped In_2O_3 NCs as compared to the doped In_2O_3 NCs in their respective XRD patterns. Their respective HRTEM images (insets) show highly crystalline nature of all NCs and the lattice fringes observed correspond to the interplanar distance of the {222} plane of the cubic bixbyite structure. The interplanar distance of 2.94 Å calculated for undoped In_2O_3 NCs and 2.93 Å for 9.8% Sn-doped In_2O_3 NCs decreases to 2.86 Å for 12.2% Mn-10% Sn codoped In_2O_3 NCs which is in perfect correlation with the observed decrease in the interplanar distance in XRD patterns and reiterates our claim of lattice doping of Mn and Sn ions in In_2O_3 without segregation of an impurity phase.

3.3.2 Electrical conductivity of nanocrystal pellets

After characterization, now we probe the nature of electronic doping. Four-probe DC electrical measurement of a pellet of 9.8% Sn-doped In_2O_3 NCs exhibit a linear ohmic relationship in voltage vs current plot as shown in the inset of Figure 3.5a. Resistivity (ρ) of 9.8% Sn-doped In_2O_3 NCs decreases with increasing temperature (Figure 3.5b) exhibiting a non-metallic behavior in the temperature range of 298-373 K. Such non-metallic behavior can be attributed to extensive grain boundary effect of our NC samples (and other polycrystalline films), in spite of having metallic NC grain with sufficient density of delocalized CB electron.[24]

In order to separate the contribution from intra-grain (intra-NC) and grain boundary, we measured two-probe AC impedance of NC film (Figure 3.5c). The experimental data (wine red symbols) were fitted (black line) using a $R_gR_{gb}C_{gb}$ electrical circuit (shown in the inset of Figure 3.5c), where

C_{gb} is the capacitance across grain boundaries, R_g and R_{gb} stands for resistances within the grain and across grain boundaries, respectively. The obtained best fit parameters for 9.8% Sn-doped In_2O_3 NCs are R_g = 462 Ω, $R_{gb} = 1.1 \times 10^7$ Ω, and C_{gb} = 19 pF. A capacitance of 19 pF agrees with expected values across the grain boundary of a polycrystalline material.[25] This C_{gb} connected in parallel to R_{gb} results into the semicircular shape of the Nyquist plot, with minimal contribution of R_g. This observed dominance of grain boundary can shadow the property of delocalized CB electron within an individual grain.

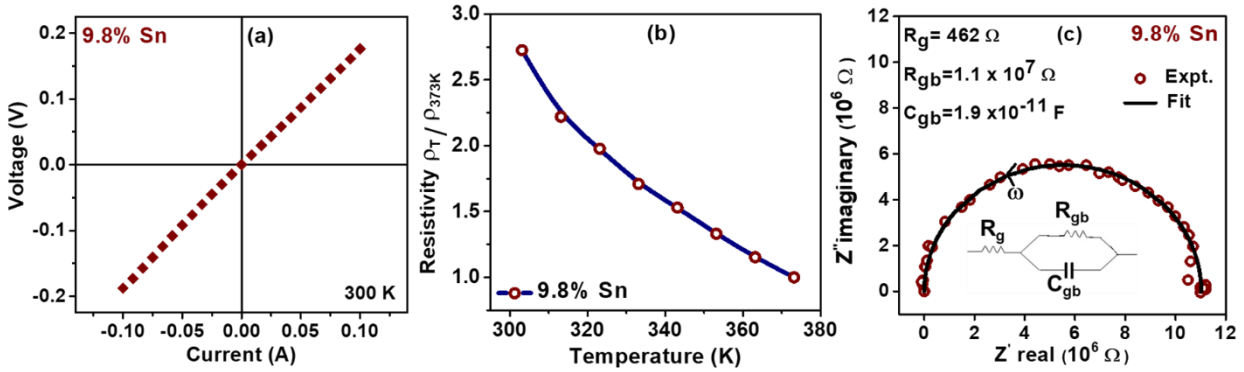

Figure 3.5: (a) Ohmic behavior through current vs voltage plot of 9.8% Sn-doped In_2O_3 NCs (b) Temperature dependent resistivity plots for 9.8% Sn-doped In_2O_3 NCs: ρ_T and ρ_{373K} are resistivity at temperature T, and at 373 K respectively. Open circles are data and solid line is a guide to the eye. (c) Nyqvist plot of AC impedance measurements in the frequency (ω) range of 100 mHz – 2 MHz for 9.8% Sn-doped In_2O_3 NCs.

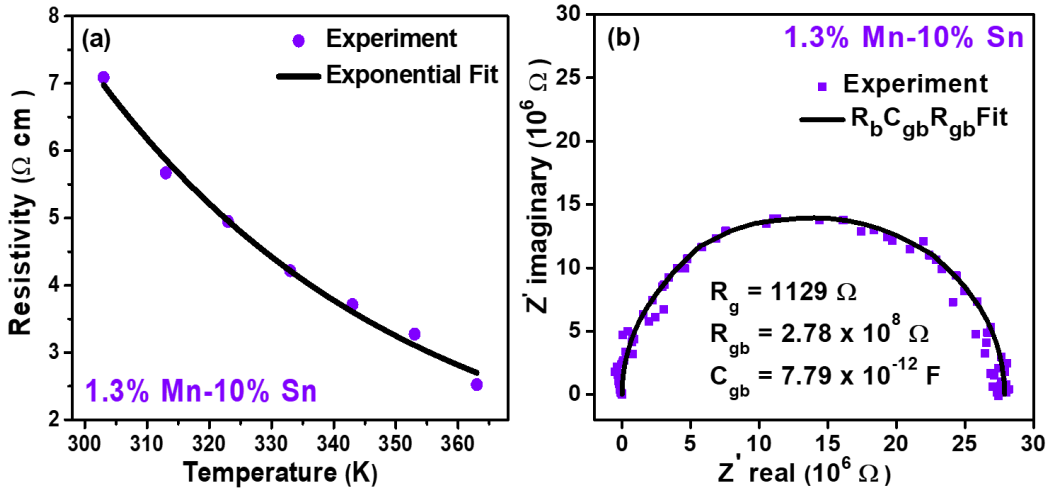

Figure 3.6: (a) Temperature-dependent resistivity data for 1.3% Mn-10% Sn codoped In_2O_3 NCs suggesting non-metallic behavior (or localized nature of charge carriers) (b) Nyqvist plot of AC impedance measurements in the frequency (ω) range of 100 mHz – 2 MHz for 1.3% Mn-10% Sn codoped In_2O_3 NCs.

A similar non-metallic behavior was observed in the DC electrical resistivity data of 1.3% Mn-10% Sn codoped In_2O_3 NCs (Figure 3.6a) and fitting the Nyqvist plot obtained AC impedance

measurements with $R_gR_{gb}C_{gb}$ (Figure 3.6b) yet again revealed that the localization of carriers at the grain boundaries is responsible for this non-metallic behavior even though carriers within the grain could be completely delocalized in nature.

On a different note, an increase in the Mn codoping percentage in ~10% Sn-doped In_2O_3 NCs leads to a progressive increase in the electrical resistivity (Figure 3.7) suggesting that the electron density is either being consumed or scattered by the addition of Mn^{2+} ions to the In_2O_3 lattice. This is fairly acceptable as Mn^{2+} substitution in In_2O_3 generates a hole which can re-combine with the electron released by the Sn^{4+} to decrease the total electron density. Moreover, Mn^{2+} doping leads to the generation of an additional charge on the In^{3+} lattice site along with introducing more oxygen vacancies both of which will lead to enhanced scattering of the existing electron density in the NC.

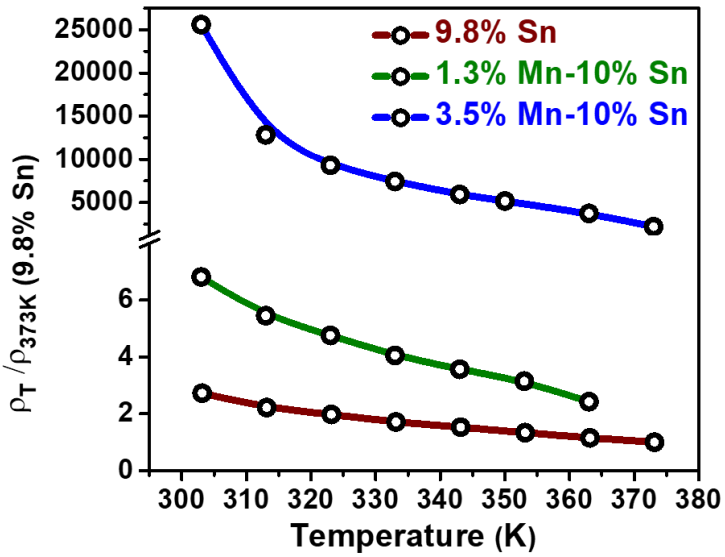

Figure 3.7: A systematic increase in the electrical resistivity of Mn-Sn codoped In_2O_3 NCs with increasing Mn codoping content. Here ρ_T is resistivity of a given sample at temperature T, and $\rho_{373K\ (9.8\%\ Sn)}$ is resistivity of 9.8% Sn-doped In_2O_3 NCs at 373 K. Open circles are experimental data and solid lines are a guide to the eye.

3.3.3 LSPR: Signature of delocalized electrons

For a better characterization of delocalized CB electrons, we employed an optical readout in the form of LSPR, instead of an electrical readout. 9.8% Sn-doped In_2O_3 NCs (Figure 3.8a), exhibit a strong LSPR band in the near-infrared region with a peak centered at 2160 nm (0.574 eV). In addition, an optical band gap is observed in the UV region, maintaining transparency in the visible region. This LSPR band arises due to the interaction of electromagnetic radiation with delocalized CB electrons generated through Sn^{4+} doping in the lattice of In_2O_3 NCs.[26-27] On codoping with

Mn^{2+}, a systematic decrease is observed in both absorbance and peak energy of LSPR (Figure 3.8b). Eventually, LSPR band disappears for a Mn codoping percentage greater than 3.5%.

Since the size and shape of NCs along with the refractive index of the medium remains unaltered, the observed decrease in both absorbance and the peak energy of LSPR is attributed to a decrease in delocalized CB electron density with increasing Mn content. Also, half width at half maximum (HWHM) of LSPR band increases with Mn codoping (Figure 3.8c), suggesting increased scattering of the electron by Mn^{2+} dopant ions. As described in the aforementioned section, Mn^{2+} doping in In_2O_3 leads to the generation of a hole which re-combines with the electron released by Sn^{4+} decreasing effective electron density and the increased concentration of charged point defects such as oxygen vacancies and Mn^{2+} lattice site with Mn codoping scatters the electron density. The decrease in electron density brings down both the peak LSPR absorbance and the LSPR energy whereas the scattering of electrons by point defects increases the HWHM of the LSPR band.

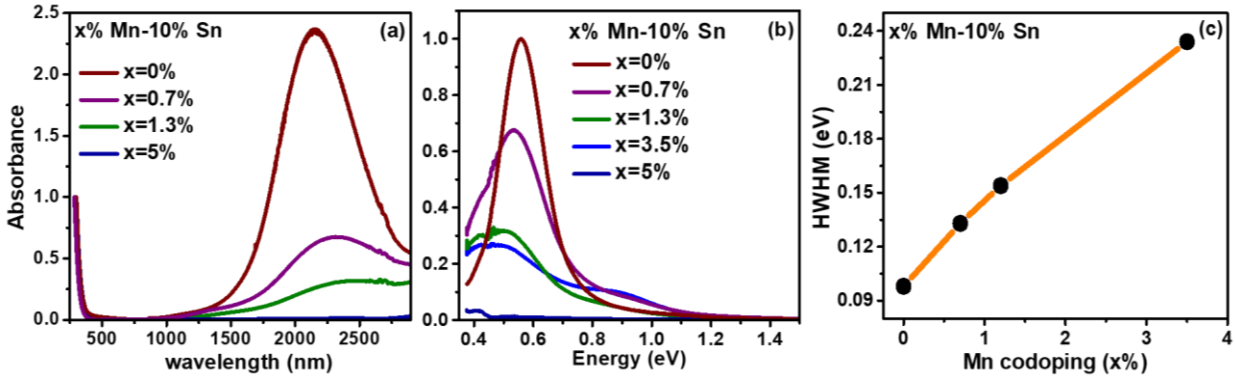

Figure 3.8: (a) UV-Vis-NIR absorption spectra of different Mn-Sn codoped In_2O_3 NCs showing the presence of LSPR band in the near-infrared region. (b) A systematic decrease in both the peak absorbance and the peak energy of the LSPR band with an increase in the Mn codoping percentage in Mn-Sn codoped In_2O_3 NCs. No LSPR can be observed for Mn codoping percentage greater than 3.5%. (c) An increase in the HWHM of the LSPR band with an increase in the Mn codoping percentage signifying increased scattering of electrons density.

The LSPR behavior discussed above is for colloidal Mn-Sn codoped In_2O_3 NCs dispersed in tetrachloroethylene. Spin-coated thin films of these NCs on a quartz substrate exhibit similar LSPR behavior (Figure 3.9) with a minor change in LSPR peak position because of the change in refractive index around NCs.[28]

More importantly, 1.3% Mn-10% Sn codoped In_2O_3 NCs exhibit LSPR band in both solution and solid state signifying the presence of delocalized CB electrons in both states, whereas, 1.3% Mn-doped In_2O_3 NCs do not exhibit LSPR because of the absence of sufficient CB electron density.

Therefore, a comparison of the magnetic behavior of these two samples will allow us to elucidate the presence of CB electron–Mn^{2+} ferromagnetic exchange interactions.

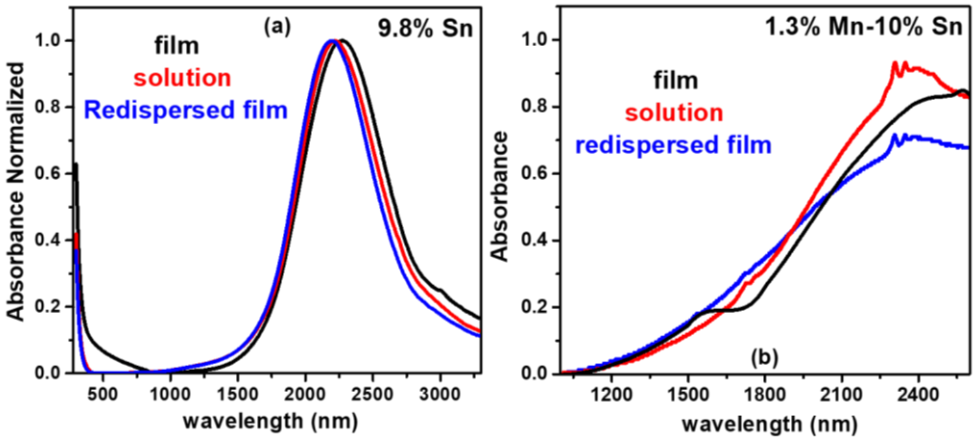

Figure 3.9: UV-Vis-NIR absorption spectra of solution and spin-coated films of (a) 9.8% Sn-doped In_2O_3 NCs (b) 1.3% Mn-10% Sn codoped In_2O_3 NCs signifying the presence of delocalized electrons in both liquid and solid state.

3.3.4 Electron-mediated magnetic coupling in Mn-Sn codoped In_2O_3 NCs

The interaction of delocalized CB electron with localized spins of Mn2+ ions will give rise to electron-mediated magnetic coupling. Now we will discuss about the experimental results probing such electron-mediated magnetic coupling. Q-band EPR spectra in Figure 3.10a showing sextet hyperfine splitting with g = 2.003, confirms that the Mn is in +2 oxidation state for both 1.3% Mn-doped and 1.3% Mn-10% Sn codoped In_2O_3 NCs. Hyperfine coupling constant has been found to be 7.1 mT for both samples and reported here for the first time for Mn^{2+} doped In_2O_3. This hyperfine splitting of 7.1 mT (66 x 10^{-4} cm^{-1}) is either smaller or similar to that in other Mn^{2+} doped in bulk oxides, suggesting significant covalent character of Mn-O bonds, and therefore, reiterating lattice doping of Mn^{2+} ion in our NCs.[29-30] Mn^{2+} on the surface of a NC is expected to have more ionic character and typically exhibits hyperfine splitting ~ 9 mT. Our results are in agreement with prior literatures on local structure of bulk Mn-doped In_2O_3, where X-ray absorption fine structure (EXAFS) has established that Mn remains in 2+ oxidation state, and, in order to maintain the charge neutrality after replacing In^{3+} with Mn^{2+} ion, oxygen vacancies are created in the vicinity of Mn^{2+} ions.[20] When Mn^{2+} and Sn^{4+} are codoped, the charge neutrality can be further maintained by this additional compensation Mn^{2+} + Sn^{4+} = $2In^{3+}$.[31] This equation suggests that an increase in Mn^{2+} doping will reduce effective CB electron density in Mn-Sn codoped In_2O_3 NCs, and our LSPR (Figure 3.8) and electrical resistivity (Figure 3.7) data indeed

agree with it. We note here that the absence of Mn^{3+} even at high-frequency Q-band EPR suggests insignificant amounts of Mn^{3+} ions in our NCs, similar to ref[20]. On the other hand, reference 13 and reference 31 suggested that in addition to Mn^{2+} ions, a reasonable amount of Mn^{3+} ion was also present in their Mn-doped In_2O_3 NCs. Overall, prior literature suggests Mn^{2+} as the major dopant in In_2O_3, however quantitative differences in the amount of Mn^{3+} ion in different reports might arise from the difference in sample preparation, yielding a difference in the local structure around a Mn ion, which in turn can influence the formation energies of different oxidation states.

To study the CB electron–Mn^{2+} exchange interaction, in other words, carrier-mediated magnetic coupling, we start by comparing the EPR spectra in Figure 3.10a. Broadening of the EPR signal of Mn^{2+} ion, after codoping with Sn^{4+} ion provides an indication of magnetic coupling among distant Mn^{2+} ions mediated by delocalized CB electrons. Influence of this electron-mediated magnetic coupling is more evident in the magnetic data. Figure 3.10b shows a clear increase in the magnetization value for Mn-Sn codoped In_2O_3 NCs compared to only Mn-doped In_2O_3 NCs. Near saturation (H = 70 kOe) magnetization M_s, of 1.3% Mn-10% Sn codoped NCs increases to 4.8 μ_B/Mn^{2+} ion (2.52 emu/g) compared to 3.5 μ_B/Mn^{2+} ion (1.86 emu/g) for 1.3% Mn-doped In_2O_3 NCs. This ~36% increase in M_s after Sn codoping is substantial and was found to be beyond any possible experimental uncertainty when multiple samples from different batches were measured. The difference in M_s values of two samples is 0.66 emu/g, which is more than one order of magnitude larger compared M_s value of 9.8% Sn-doped In_2O_3 NCs (0.045 emu/g, Figure 3.10b inset).

Therefore, the increase in magnetization for the codoped samples cannot be explained by additional magnetization arising from either Sn^{4+} or CB electrons. Furthermore, though no evidence of Mn^{3+} has been observed, still we consider an unlikely hypothesis of a significant Mn^{3+} concentration in Mn-doped In_2O_3 NCs, which converts to Mn^{2+} in the Mn-Sn codoped NCs. Even this unrealistic hypothesis cannot account for the observed increase in M_s by 1.3 μ_B/Mn^{2+} ion after codoping. Instead, M_s in both samples arises from Mn^{2+} ion and codoping with non-magnetic Sn^{4+} results into ferromagnetic exchange interaction among Mn^{2+} ions mediated by delocalized CB electron. TGA analysis (Figure 3.11) shows that 84 % of the total weight of our NCs is contributed by inorganic part, and the remaining 16 % is organic capping ligand. Our magnetic data has been normalized by the weight of 84 % inorganic part only excluding the weight of organic part.

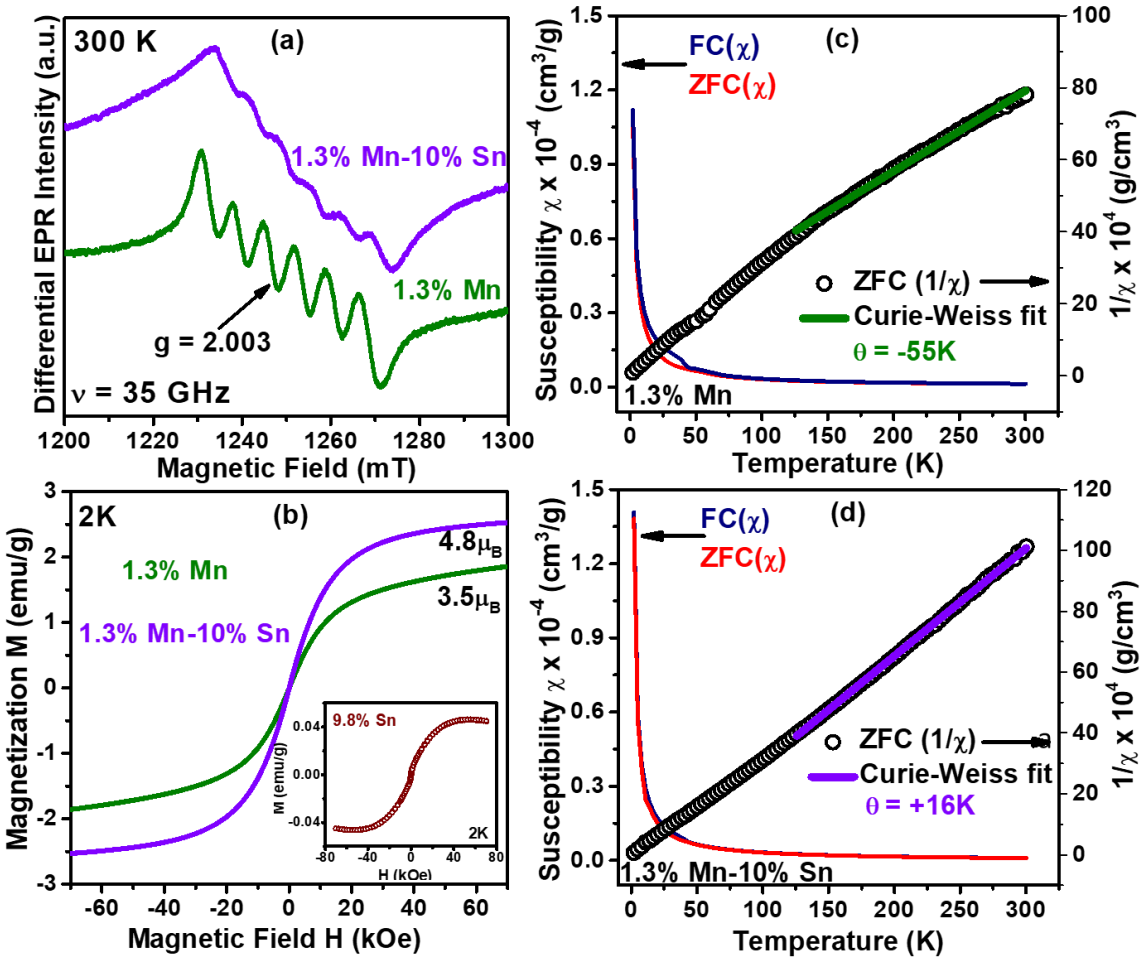

Figure 3.10: Comparison between 1.3% Mn-doped and 1.3% Mn-10% Sn codoped In_2O_3 NCs to establish electron-mediated magnetic coupling in the codoped sample (a) Q-band EPR spectra, the spectrum for the codoped sample was vertically shifted for better presentation. (b) Magnetization (M) vs magnetic field strength (H) curves; Inset shows M vs H curve for 9.8% Sn-doped In_2O_3 NCs at 2 K. (c,d) Magnetic susceptibility vs temperature, along with Curie-Weiss susceptibility plots.

Temperature-dependent magnetic susceptibility plots in Figure 3.10c-d, do not show significant divergence between field cooled (FC, 100 Oe) and zero field cooled (ZFC) data, apart from a small divergence in the range of 10-40 K. We fitted the temperature dependent magnetization data using Curie–Weiss law i.e. $1/\chi = (T - \theta)/C$, where χ is the magnetic susceptibility, T is the absolute temperature, θ stands for Curie-Weiss temperature and C is the Curie constant. Fitting linear part of the magnetization data at higher temperatures yielded $\theta = -54$ K for 1.3% Mn-doped In_2O_3 NCs. This negative value of θ signifies antiferromagnetic superexchange interactions between neighboring Mn^{2+} ions. Interestingly, $\theta = +16$ K for 1.3% Mn-10% Sn codoped In_2O_3 NCs, signifying a ferromagnetic interaction in this sample. Curie-Weiss analysis for samples with same

compositions, but prepared in different batches show that the signs of θ are reproducible, however, with variations in the magnitude of θ, probably because of larger experimental errors at higher temperatures. In any case, positive theta value in Curie-Weiss analysis, along with the broadening of EPR signal for Mn-Sn codoped In_2O_3 NCs suggest ferromagnetic interactions. This observed ferromagnetic interaction after Sn^{4+} codoping agrees with the proposed carrier-mediated ferromagnetic exchange interaction between Mn^{2+} ions, resulting in an increase in M_s for the codoped NCs. Similar enhancement in M_s (Figure 3.12) after Sn^{4+} codoping was also obtained for 1.8% Mn-doped and 1.8% Mn-10% Sn codoped In_2O_3 NCs (showing LSPR band)

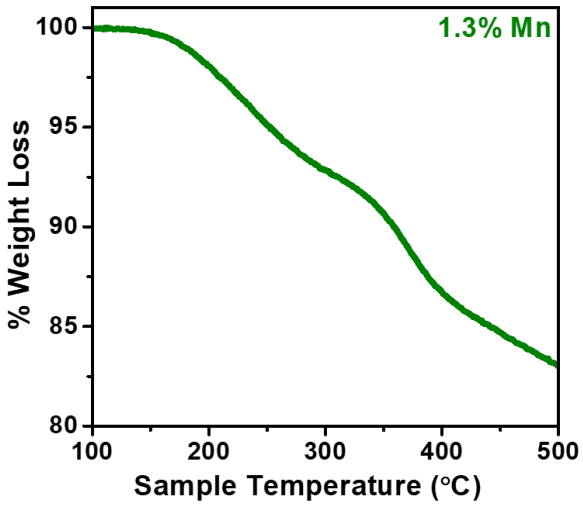

Figure 3.11: TGA of 1.3% Mn-doped In_2O_3 NCs showing NCs being composed of ~84% inorganic core and ~16% organic ligands. The hump around 350℃ corresponds to the decomposition of oleylamine ligand. A similar behavior was observed for other doped In_2O_3 NCs as well.

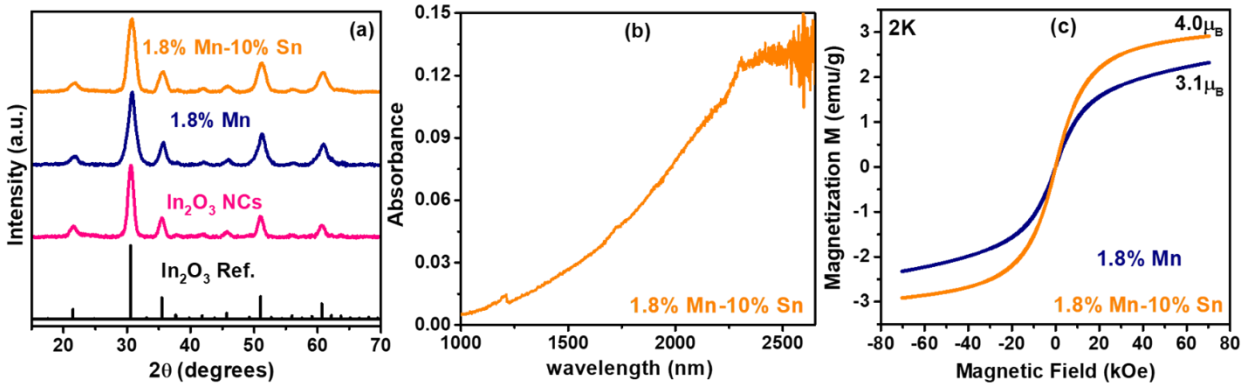

Figure 3.12: (a) XRD patterns for 1.8% Mn and 1.8% Mn-10% Sn codoped In_2O_3 NCs showing impurity free phase pure NCs. (b) UV-Vis-NIR absorption spectra of 1.8% Mn-10% Sn codoped In_2O_3 NCs showing existence of LSPR confirming presence of delocalized electrons. (c) Comparison of magnetization vs magnetic field strength curves for 1.8% Mn and 1.8% Mn-10% Sn codoped In_2O_3 NCs to establish electron-mediated magnetic ordering in another composition.

3.3.5 Proposed mechanism of electron-mediated magnetic coupling

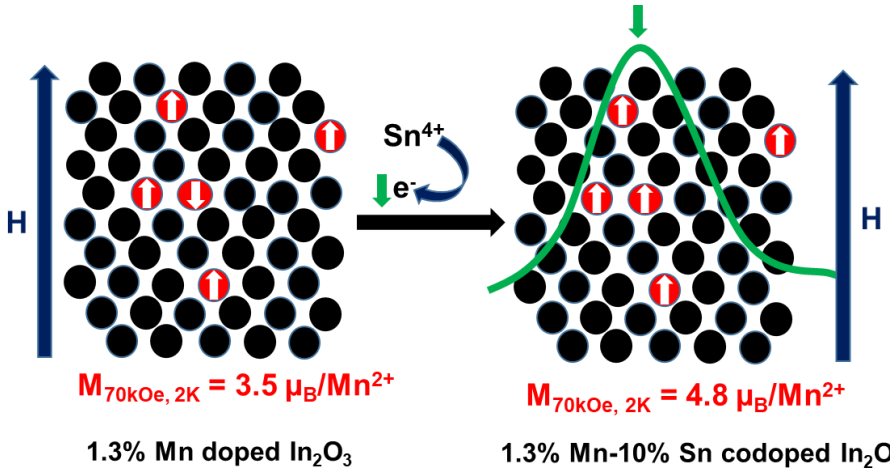

Figure 3.13: Schematic representing the mechanism of electron-mediated magnetic coupling in Mn-Sn codoped In_2O_3 NCs.

Ochsenbein et. al. provided an insight into the mechanism of this CB electron–Mn^{2+} ferromagnetic exchange interactions in photo-excited Mn-doped ZnO NCs as schematically shown in Figure 3.13.[3] Their theoretical calculations showed that the strength of Mn-O-Mn antiferromagnetic superexchange interaction is larger than that of a given ferromagnetic CB electron–Mn^{2+} s-d exchange interaction. However, the presence of multiple Mn^{2+} ions leads to multiple ferromagnetic interactions among distant Mn^{2+} ions via the CB electron, and the total strength of ferromagnetic interactions can become large enough to overcome the antiferromagnetic Mn-O-Mn superexchange interaction.[3] We propose a similar mechanism in our Mn-Sn codoped In_2O_3 NCs as well. Addition of CB electrons through Sn^{4+} codoping, 1.3% Mn-10% Sn codoped NCs exhibit strong enough total ferromagnetic exchange coupling through CB electrons–Mn^{2+} interactions, that overcomes the antiferromagnetic Mn-O-Mn superexchange interaction, finally yielding a near-ideal M_S = 4.8 μ_B/Mn^{2+} (ideal value 5.0 μ_B/Mn^{2+}) at 2 K. (showing LSPR band).

It has to be noted that the delocalization is within the dimension (~7 nm) of NCs. So CB electrons here are much more spread out compared to defect bound electrons which typically spread over ~ 1 nm diameter as discussed in the model of bound magnetic polarons (BMP),[1] however, compared to bulk systems, carriers are confined by the boundary of NCs. Therefore, BMP model can't explain the enhancement in the magnetization after addition of delocalized electrons. Furthermore, this delocalized electron-mediated ferromagnetic coupling is different than the charge transfer ferromagnetism[13] exhibited by annealed films of Mn-doped In_2O_3 NCs with mixed valent

Mn^{2+}/Mn^{3+} ions. This is because (i) our NCs do not show any evidence of the presence of mixed valence states for Mn, (ii) saturation magnetization values at 2 K are 3.5 and 4.8 μ_B/Mn for 1.3% Mn-doped and 1.3% Mn-10% Sn codoped samples respectively (Figure 3.10b), which are significantly larger than the theoretical upper limit 1 μ_B/Mn possible for charge-transfer ferromagnetism, (iii) magnetic moment of our samples increases drastically by decreasing the measurement temperature, which again is not the case in the reported charge transfer mechanism. Further theoretical studies are required to quantify the strength of different ferromagnetic and antiferromagnetic exchange interactions. We also note that the magnetization values of our Mn-Sn codoped In_2O_3 NCs are about two orders magnitude higher (Figure 3.10b) than defect-related magnetization reported for oxide NCs without magnetic doping,[32] but our NCs do not exhibit appreciable hysteresis in M vs H plot.

3.4 Conclusions

In conclusion, colloidal Mn-Sn codoped In_2O_3 NCs were synthesized. Traditional AC and DC electrical measurements get dominated by grain boundaries of NC films, and therefore unambiguous detection of metal-like delocalized electron within a NC grain becomes difficult. In order to overcome this problem, we used LSPR band of these NCs to distinguish between delocalized CB electrons from defect-bound localized electrons. This unambiguous detection of delocalized CB electrons allowed us to study CB electron–Mn^{2+} magnetic interactions. Curie–Weiss plot of 1.3% Mn-doped In_2O_3 NCs shows antiferromagnetic (θ = -54 K) superexchange interaction between neighboring Mn^{2+} ions (Mn-O-Mn) resulting into M_s = 3.5 μ_B/Mn^{2+} ion at 2K, which is significantly less compared to the ideal value of 5 μ_B/Mn^{2+}. Interestingly, after codoping with Sn^{4+} ions, 1.3% Mn–10% Sn codoped In_2O_3 NCs exhibit ferromagnetic interaction (θ = +16 K) with nearly ideal M_s of 4.8 μ_B/Mn^{2+} at 2 K. These results confirm CB electrons–Mn^{2+} ferromagnetic exchange interaction, which can lead to magneto-electric and magneto-plasmonic properties in the future.

3.5 References

1. Coey, J. M. D.; Venkatesan, M.; Fitzgerald, C. B. Donor Impurity Band Exchange in Dilute Ferromagnetic Oxides. *Nat. Mater.* **2005,** *4*, 173-179.
2. Dietl, T. A Ten-Year Perspective on Dilute Magnetic Semiconductors and Oxides. *Nat. Mater.* **2010,** *9*, 965-974.

3. Ochsenbein, S. T.; Feng, Y.; Whitaker, K. M.; Badaeva, E.; Liu, W. K.; Li, X. S.; Gamelin, D. R. Charge-Controlled Magnetism in Colloidal Doped Semiconductor Nanocrystals. *Nat. Nanotechnol.* **2009,** *4*, 681-687.
4. Bussian, D. A.; Crooker, S. A.; Yin, M.; Brynda, M.; Efros, A. L.; Klimov, V. I. Tunable Magnetic Exchange Interactions in Manganese-doped Inverted Core-Shell ZnSe-CdSe Nanocrystals. *Nat. Mater.* **2009,** *8*, 35-40.
5. Beaulac, R.; Schneider, L.; Archer, P. I.; Bacher, G.; Gamelin, D. R. Light-Induced Spontaneous Magnetization in Doped Colloidal Quantum Dots. *Science* **2009,** *325*, 973-976.
6. Singhal, A.; Achary, S. N.; Manjanna, J.; Jayakumar, O. D.; Kadam, R. M.; Tyagi, A. K. Colloidal Fe-Doped Indium Oxide Nanoparticles: Facile Synthesis, Structural, and Magnetic Properties. *J. Phys. Chem. C* **2009,** *113*, 3600-3606.
7. Zheng, W. W.; Strouse, G. F. Involvement of Carriers in the Size-Dependent Magnetic Exchange for Mn:CdSe Quantum Dots. *J. Am. Chem. Soc.* **2011,** *133*, 7482-7489.
8. Viswanatha, R.; Naveh, D.; Chelikowsky, J. R.; Kronik, L.; Sarma, D. D. Magnetic Properties of Fe/Cu Codoped ZnO Nanocrystals. *J. Phys. Chem. Lett.* **2012,** *3*, 2009-2014.
9. Farvid, S. S.; Sabergharesou, T.; Huffluss, L. N.; Hegde, M.; Prouzet, E.; Radovanovic, P. V. Evidence of Charge-Transfer Ferromagnetism in Transparent Diluted Magnetic Oxide Nanocrystals: Switching the Mechanism of Magnetic Interactions. *J. Am. Chem. Soc.* **2014,** *136*, 7669-7679.
10. Tandon, B.; Shanker, G. S.; Nag, A. Multifunctional Sn- and Fe-Codoped In_2O_3 Colloidal Nanocrystals: Plasmonics and Magnetism. *J. Phys. Chem. Lett.* **2014,** *5*, 2306-2311.
11. Shanker, G. S.; Tandon, B.; Shibata, T.; Chattopadhyay, S.; Nag, A. Doping Controls Plasmonics, Electrical Conductivity, and Carrier-Mediated Magnetic Coupling in Fe and Sn Codoped In_2O_3 Nanocrystals: Local Structure Is the Key. *Chem. Mater.* **2015,** *27*, 892-900.
12. Philip, J.; Punnoose, A.; Kim, B. I.; Reddy, K. M.; Layne, S.; Holmes, J. O.; Satpati, B.; Leclair, P. R.; Santos, T. S.; Moodera, J. S. Carrier-Controlled Ferromagnetism in Transparent Oxide Semiconductors. *Nat. Mater.* **2006,** *5*, 298-304.
13. Raebiger, H.; Lany, S.; Zunger, A. Electronic Structure, Donor and Acceptor Transitions, and Magnetism of 3d Impurities in In_2O_3 and ZnO. *Phys. Rev. B* **2009,** *79*, 165202.
14. Rao, C. N. R.; Deepak, F. L. Absence of Ferromagnetism in Mn- and Co-doped ZnO. *J. Mater. Chem.* **2005,** *15*, 573-578.
15. Hakimi, A.; Blamire, M. G.; Heald, S. M.; Alshammari, M. S.; Alqahtani, M. S.; Score, D. S.; Blythe, H. J.; Fox, A. M.; Gehring, G. A. Donor-band Ferromagnetism in Cobalt-doped Indium Oxide. *Phys. Rev. B* **2011,** *84*, 085202.
16. Wang, Y. S.; Thomas, P. J.; O'Brien, P. Optical Properties of ZnO Nanocrystals Doped with Cd, Mg, Mn, and Fe ions. *J. Phys. Chem. B* **2006,** *110*, 21412-21415.
17. Buonsanti, R.; Milliron, D. J. Chemistry of Doped Colloidal Nanocrystals. *Chem. Mater.* **2013,** *25*, 1305-1317.
18. Vegard, L. Die Konstitution der Mischkristalle und die Raumfüllung der Atome. *Z. Phys.* **1921,** *5*, 17-26.
19. Gilstrap, R. A.; Capozzi, C. J.; Carson, C. G.; Gerhardt, R. A.; Summers, C. J. Synthesis of a Nonagglomerated Indium Tin Oxide Nanoparticle Dispersion. *Adv. Mater.* **2008,** *20*, 4163-4166.
20. An, Y. K.; Wang, S. Q.; Duan, L. S.; Liu, J. W.; Wu, Z. H. Local Mn Structure and Room Temperature Ferromagnetism in Mn-doped In_2O_3 Films. *Appl. Phys. Lett.* **2013,** *102*, 212411.
21. Shannon, R. D.; Prewitt, C. T. Effective Ionic Radii in Oxides and Fluorides. *Acta Crystallogr. Sect. B* **1969,** *25*, 925-946.

22. An, Y.; Wang, S.; Duan, L.; Liu, J.; Wu, Z. Local Mn Structure and Room Temperature Ferromagnetism in Mn-doped In_2O_3 films. *Appl. Phys. Lett.* **2013,** *102*, 212411.
23. Jayakumar, O. D.; Gopalakrishnan, I. K.; Kulshreshtha, S. K.; Gupta, A.; Rao, K. V.; Louzguine-Luzgin, D. V.; Inoue, A.; Glans, P.-A.; Guo, J.-H.; Samanta, K.; Singh, M. K.; Katiyar, R. S. Structural and Magnetic Properties of $(In_{1-x}Fe_x)_2O_3(0.0\leqslant x\leqslant 0.25)$ System: Prepared by Gel Combustion Method. *Appl. Phys. Lett.* **2007,** *91*, 052504.
24. Sarma, D. D.; Jagadeeswararao, M.; Pal, S.; Nag, A. Electrical and Plasmonic Properties of Ligand-Free Sn^{4+}-Doped In_2O_3 (ITO) Nanocrystals. *ChemPhysChem* **2016,** *17*, 710-716.
25. Irvine, J. T. S.; Sinclair, D. C.; West, A. R. Electroceramics: Characterization by Impedance Spectroscopy. *Adv. Mater.* **1990,** *2*, 132-138.
26. Wang, T.; Radovanovic, P. V. Free Electron Concentration in Colloidal Indium Tin Oxide Nanocrystals Determined by Their Size and Structure. *J. Phys. Chem. C* **2011,** *115*, 406-413.
27. Schimpf, A. M.; Lounis, S. D.; Runnerstrom, E. L.; Milliron, D. J.; Gamelin, D. R. Redox Chemistries and Plasmon Energies of Photodoped In_2O_3 and Sn-Doped In_2O_3 (ITO) Nanocrystals. *J. Am. Chem. Soc.* **2015,** *137*, 518-524.
28. Garcia, G.; Buonsanti, R.; Runnerstrom, E. L.; Mendelsberg, R. J.; Llordes, A.; Anders, A.; Richardson, T. J.; Milliron, D. J. Dynamically Modulating the Surface Plasmon Resonance of Doped Semiconductor Nanocrystals. *Nano Letters* **2011,** *11*, 4415-4420.
29. Matumura, O. Electron Spin Resonance of Mn-activated Phosphors. *J. Phys. Soc. Jpn.* 1959, 14, 108-108
30. Norberg, N. S.; Kittilstved, K. R.; Amonette, J. E.; Kukkadapu, R. K.; Schwartz, D. A.; Gamelin, D. R. Synthesis of Colloidal Mn^{2+}: ZnO Quantum Dots and High-Tc Ferromagnetic Nanocrystalline Thin Films. *J. Am. Chem. Soc.* **2004,** *126*, 9387-9398.
31. Okazaki, T.; Yoshioka, T.; Kusakabe, Y.; Yamamoto, T.; Kitada, A. Valence State Analysis of Mn and Fe Ions in Room-temperature Ferromagnetic Mn- and Fe-codoped In_2O_3. *Solid State Commun.* **2011,** *151*, 1749-1752.
32. Sundaresan, A.; Bhargavi, R.; Rangarajan, N.; Siddesh, U.; Rao, C. N. R. Ferromagnetism as a Universal Feature of Nanoparticles of the Otherwise Nonmagnetic Oxides. *Phys. Rev. B* **2006,** *74*, 161306.

Chapter-4A

Size-Induced Enhancement of LSPR Quality Factor from Cr-Sn Codoped In_2O_3 Nanocrystals

---

Following article has been published from the work presented in this chapter.

1. Tandon, B.; Yadav, A.; Khurana, D.; Reddy, P.; Santra, P. K.; Nag, A.; "Size-Induced Enhancement of Carrier Density, LSPR Quality Factor and Carrier Mobility in Cr-Sn-doped In_2O_3 NCs" *Chem. Mater.* **2017**, *29*, 9360-9368.

Summary

Heterovalent dopant ions like Sn^{4+} in In_2O_3 nanocrystals (NCs) provide free electrons for localized surface plasmon resonance (LSPR). But the same heterovalent dopants act as electron scattering centers, both independently and by forming complexes with interstitial oxygen, thereby increasing LSPR linewidth. Also, such complexes decrease free electron density. These detrimental effects diminish the figure-of-merit of LSPR known as the quality factor (Q-factor). Herein, we designed colloidal Cr-Sn codoped In_2O_3 NCs, where both high carrier density and low carrier scattering can be achieved simultaneously, yielding a high LSPR Q-factor of 7.2, which is a record high number compared to prior reports of doped In_2O_3 NCs. Q-factors increase systematically from 3.2 for 6.6% Sn-doped In_2O_3 NCs to 7.2 for 23.8% Cr-6.6% Sn codoped In_2O_3 NCs by increasing the Cr codoping concentration, which is also accompanied by an increase in NC diameter from 6.7 to 22.1 nm. Detailed characterization and analysis of LSPR spectra using the Drude model suggest that the increase in NC diameter (induced by Cr codoping) is mainly responsible for the enhanced LSPR Q-factor. Sn^{4+} dopants on the surface of NCs are more vulnerable to form irreducible complexes with interstitial oxide ions, compared to Sn^{4+} ions in the core. Therefore, an increase in the concentration ratio of $[Sn_{core}]/[Sn_{surface}]$ (or [Sn]/[interstitial oxide]) by increasing the diameter of NCs, increases the electron density. With the increase in both NC diameter and Cr doping, multiple factors contribute towards reducing the scattering of charge carriers, thereby increasing the optical carrier mobility. This unique combination which increases both the density and mobility of charge carriers improves the LSPR Q-factor.

Graphical Abstract

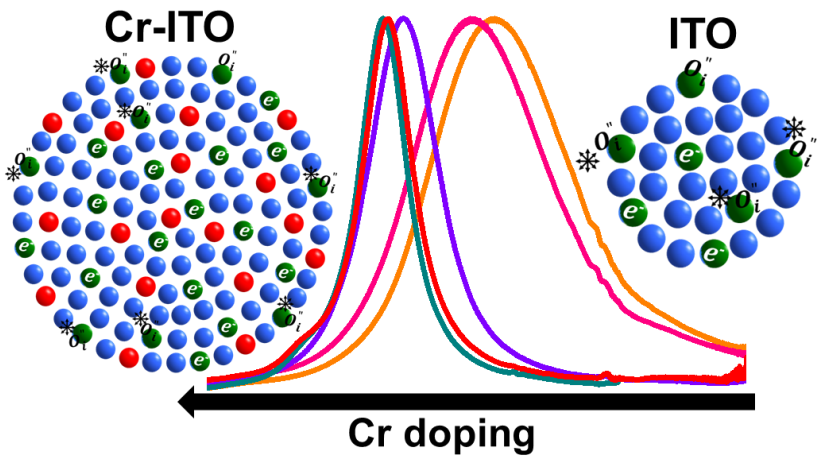

4A.1 Introduction

Nanocrystals (NCs) of degenerately doped semiconductors and metal oxides such as Sn-doped In_2O_3 (ITO)[1-3], Al-doped ZnO,[4] In-doped CdO,[5-6] self-doped $Cu_{2-x}S$, $Cu_{2-x}Se$,[7-8] WO_{3-x},[9] and other systems[10-13] display localized surface plasmon resonance (LSPR) in the near-infrared (NIR) to mid-infrared (MIR) range when their free charge carriers oscillate resonantly at frequencies of the impinged electromagnetic radiation.[14-16] Indifference with noble-metal nanostructures (for example Au and Ag)[17], free carriers in doped NCs are generated from impurity ions/vacancies, which unfortunately are also notorious for scattering charge carriers by different mechanisms (ionized impurity scattering and neutral donor scattering).[18-22] Such dopant-related scattering centers decrease the figure-of-merit of LSPR known as quality factor (Q-factor), along with decreasing carrier mobility. Q-factor is defined as the ratio of the peak energy to the full width at half maxima (FWHM) of the LSPR band. A high Q-factor implicates low level of electronic damping, extended plasmon lifetimes and intense near-field enhancements.[5, 22] It can, therefore, be a governing factor in determining the potential of an LSPR material to be utilized for applications such as photothermal therapy, photovoltaics, and sensing.[23-28] To achieve a high LSPR Q-factor, large free carrier density that increases the LSPR peak energy and less scattering of carriers that reduces the FWHM of the LSPR band, are necessary requirements. However, both these properties are generally mutually exclusive in nature resulting into lower LSPR Q-factors of doped semiconductor and metal oxide NCs.

Different strategies have been adopted in literature to optimize the trade-off between increasing the carrier density by heterovalent doping and at the same time preventing scattering of charge carriers by the same heterovalent dopant centers. For example, using Mo-doped In_2O_3 films, Bhachu et. al. suggested that scattering of charge carriers can be avoided if the dopant ions do not hybridize with the occupied energy levels near the conduction band minimum (CBM).[29] A similar claim was also substantiated by Runnerstrom et. al. where they found that Ce-doped In_2O_3 NCs exhibited high LSPR Q-factors of 4.0 in spite of having much smaller electron density than Sn-doped In_2O_3 NCs, because Ce^{4+} levels hybridize less with CBM of In_2O_3.[30] Through careful selection of dopants, Fang et. al. demonstrated that competition between electron trapping and activation can be controlled to achieve intense LSPR in the mid-IR region.[31] Another known fact is that high dielectric constant reduces Coulomb interactions between charge carriers and ionized dopants. Therefore, the high Q-factor in the LSPR from In-doped CdO[5] and F-In codoped CdO[6]

NCs was suggested as a consequence of large high-frequency dielectric constant of CdO host. A careful look at the literature Table 4A.1 shows that all the doped metal oxide NCs that show reasonably high Q-factor (> 4), are relatively large-sized NCs with a diameter larger than 10 nm. It appears that a smaller surface-to-volume ratio enhances Q-factor, but such an observation has neither been understood completely, nor been utilized as a strategy to improve Q-factor of metal oxide NCs.

Table 4A.1: A comparison table showing LSPR parameters of the best doped nanocrystal materials.

Host	**Dopant**	**Doping Level (%)**	**Diameter of NCs (nm)**	**λ_{max} (nm)**	**FWHM (meV)**	**Q-factor**	**Reference Number**
In_2O_3	Sn^{4+}	6.4	10.8	~1700	~150	4.85	2
In_2O_3	Ce^{4+}	5.2	~10	3965	77	4.08	30
CdO	In^{3+}	13.2	11.3	2265	67	8.15	5
CdO	F^- , In^{3+}	~10, 8.3	14	1726	59	12.23	6
ZnO	Al^{3+}	1.6	~30	~4000	~100	3.9	32
ZnO	Ga^{3+}	~2.5	26.2	~6000	-	<1.0	33
Zn-O	Sn^{4+}	1.37	9.4	790	1132	1.39	34
$Cu_{2-x}S$	Cu vacancy	~3	5.9	~1797	210	3.3	7
InN	N vacancy	5.5	30	~2900	89	4.83	35
WO_{3-x}	O vacancy	~5%	5.4 (b) 62 (l)	850-900	~900	1.6	9

Our previous work was largely focused on codoping magnetic ions (Fe^{3+} / Mn^{3+} / Mn^{2+}) in Sn-doped In_2O_3 NCs yielding Fe-Sn or Mn-Sn codoped In_2O_3 NCs.[36-39] Such codoping introduces magnetic response in the sample, however, decreases both electron density and LSPR Q-factors because the dopant magnetic ions introduce mid-gap trap states for charge carriers. According to the prior computational studies,[40-41] the unfilled level of Cr^{3+} lies well above the CBM of In_2O_3. Hence, codoping of Cr^{3+} ions in Cr-Sn codoped In_2O_3 NCs is not expected to give rise to any mid-

gap trap states. This was the primary motivation for us to prepare Cr-Sn codoped In_2O_3 NCs that were expected to exhibit LSPR with Q-factors close to Sn-doped In_2O_3 NCs. Interestingly, preliminary results of synthesis showed that Cr doping systematically increases the diameter of In_2O_3 NCs. This observation motivated us to examine the potential of Cr-Sn codoped In_2O_3 NCs as candidates to observe the effect of the surface-to-volume ratio of NCs on LSPR Q-factor, without changing other relevant reaction parameters. Indeed, we show here that the LSPR Q-factor of Cr-Sn codoped In_2O_3 NCs can be enhanced to a record high number of 7.2, by increasing the diameter of NCs and contribution from other factors induced by Cr codoping.

4A.2 Experimental Section

4A.2.1 Synthesis of Cr-Sn codoped In_2O_3 and 16.1 nm ITO NCs

To the best of our knowledge, this is the first report of colloidal synthesis of Cr-Sn codoped In_2O_3 NCs. Synthesis procedure is similar to our previous reports of Fe-Sn and Mn-Sn codoped In_2O_3 NCs,[36-39] involving standard Schlenk line techniques. Different amounts of In(III), Cr(III) and Sn(IV) precursors were taken to achieve desired compositions of product NCs. For example, to obtain 9.4% Cr - 6.6% Sn-doped In_2O_3 NCs, 1.2 mmol of indium(III) acetylacetonate, 0.15 mmol of tin(IV) bis(acetylacetonate)dichloride and 0.15 mmol of chromium(III) acetylacetonate were mixed with 10 mL of oleylamine solvent and degassed at 100℃ under vacuum conditions. Then the reaction temperature was increased to 250℃ with magnetic stirring under inert N_2 atmosphere. After 5 hours of reaction at 250℃, the reaction mixture was cooled to room temperature and precipitated using methanol as a non-solvent followed by centrifugation at 6000 rpm for 6 min. For characterization purposes, these NCs were re-dispersed in non-polar solvents like tetracholoroethylene, hexane and toluene.

The 16.1 nm 6.4% Sn-doped In_2O_3 NCs were prepared following a continuous NC growth model (slow injection synthesis).[42] Concisely, 0.5 M of total metal precursors i.e. indium(IV) acetate and tin(IV) acetate in stoichiometric ratio, were dissolved in 16 mL oleic acid and degassed at 100℃ under vacuum for 2 hours. The temperature was subsequently raised to 150℃ under N_2 environment where it was heated for 2 hours. In a separate 100 mL round bottom flask, 20 mL oleyl alcohol was first degassed and then heated to 290℃. Afterwards, 10 mL of the metal oleate solution was injected into the hot oleyl alcohol at the rate of 0.2 mL/min using an automated syringe pump. After injection, the solution was cooled down to room temperature and quenched

with ethanol to precipitate the NCs. The NCs were washed several times employing hexane/ethanol solvent/anti-solvent mixtures before they were finally dispersed in hexane for characterization purposes.

4A.2.2 Characterization of Cr-Sn codoped In_2O_3 NCs and 16.1 nm ITO NCs

Inductively coupled plasma atomic emission spectroscopy (ICP-AES): The elemental compositions were obtained through with ICP-AES technique performed on a Perkin−Elmer Optima 7000 DV machine. ~1-2 mg of NC powder was dissolved in 70% HNO_3 and the solution volume was diluted with milli-Q water to result in a 2% v/v HNO_3 acid solution. Standard solutions with variable concentrations of a particular element were prepared by diluting the commercial ICP standard with 2% v/v HNO_3 solution.

Energy dispersive X-ray analysis (EDX): The elemental compositions of all Cr-Sn codoped In_2O_3 NCs obtained from ICP-AES were complemented with those determined through EDX spectroscopy on a Zeiss Ultra Plus SEM instrument operating at an energy of 20 kV.

Powder x-ray diffraction (p-XRD): To determine the crystal structure and phase purity of different NCs, p-XRD patterns were recorded on a Bruker D8 Advance X-ray diffractometer employing monochromated Cu Kα (λ=1.5406 Å) as an X-ray source. Contribution from Cu Kα2 (λ=1.5444 Å) and the background was subtracted from the XRD pattern obtained from the instrument.

Transmission electron microscopy (TEM): Morphology of the Cr-Sn codoped In_2O_3 NCs was imaged through TEM. A dilute solution of NCs in hexane was drop-casted on a carbon coated TEM grid and analyzed in Tecnai G2 FEI F12 microscope being operated at 200 kV. The TEM micrographs obtained were processed in ImageJ software to calculate the average diameter and standard deviation of NCs.

X-ray photoelectron spectroscopy (XPS): To determine the oxidation state(s) of the host and the dopants, as well as their radial distribution within the NC, XPS spectra for different Cr-Sn codoped In2O3 NCs, were recorded on a VersaProbe II PHI 5000 x-ray photoelectron spectrophotometer equipped with a monochromatic Al Kα (1486.6 eV) X-ray source and, a hemispherical analyzer.

To determine the relative Sn and Cr content, we normalized the experimental XPS data by the respective photoionization cross-sections for different elements[43], after performing a background

correction using the XPSPeak41 software. We then took the ratio of the intensity of Sn 3d peaks (I_{Sn}) to the combined total intensity of In 3d (I_{In}), Sn 3d (I_{Sn}) and Cr 2p (I_{Cr}) peaks. So concentration of Sn dopant is I_{Sn} / (I_{In} + I_{Cr} + I_{Sn}). Likewise, concentration of Cr dopant is I_{Cr} / (I_{In} + I_{Cr} + I_{Sn}).

Escape depth of a photoelectron is the maximum depth within the sample, from where the photoelectron can escape to the vacuum (come out of the sample) without suffering any inelastic scattering, thereby, retaining its initial kinetic energy. So the escape depth depends upon the inelastic mean free path (λ) of photoelectrons. The empirical relation, $\lambda = \frac{\sqrt{K.E.}}{2}$, where K.E. is the kinetic energy of photoelectrons in eV and λ is in Å, has been found to be valid for a wide range of K. E. > 150 eV.[44] The calculated λ for photoelectrons coming from In 3d, Sn 3d, and Cr 2p core levels are 1.6, 1.6 and 1.5 nm, respectively. Therefore, the elemental compositions obtained from XPS for all these samples have very similar depth sensitivity.

UV-Vis-NIR spectroscopy: To avoid the vibrational peaks of different bonds in the infrared region which would interfere in the NIR LSPR spectra, dilute solution of NCs were prepared in tetrachloroethylene solvent and UV-Vis-NIR spectra were recorded on Perkin Elmer, Lambda-950 UV/Vis spectrometer and Shimadzu UV-3600 Plus UV-Vis-NIR spectrophotometer.

Frequency-dependent and frequency-independent Drude Modeling: The optical properties of a material are governed by its complex dielectric function which gives us an idea about the electrical polarization of conduction and valence band electrons as we apply an external electromagnetic field. The Drude contribution ε_D to this complex dielectric function takes the form[45]

$$\varepsilon_D = \varepsilon_\infty - \frac{\omega_P^2}{\omega^2 + i\omega\gamma} \quad (1)$$

Where ω is the frequency of incident radiation, ε_∞ is the high frequency dielectric constant bearing a value of 3.9 for Sn-doped In_2O_3 (ITO) nanocrystals (NCs)[46], ω_P is the bulk plasma frequency which is related to the free electron density (N) through the relation,

$$\omega_P^2 = \frac{Ne^2}{\varepsilon_O m^*} \quad (2)$$

where e is the elementary charge on an electron (a constant with a value equaling to 1.6 x 10^{-19} C), ε_O stands for the permittivity of free space with a value of 8.85 x 10^{-12} F/m in SI units and m^* is

the effective mass of the carrier. Since electrons are the majority carriers in our Cr-Sn codoped In_2O_3 NCs, the effective mass of our carriers can be approximated by those in ITO NCs (i.e. $0.39m_e$, where m_e is the rest mass of an electron in vacuum).

Here, the quantity γ represents the damping function of the charge carriers and could either be a constant or take the form of a frequency dependent function depending upon the mechanism of scattering of charge carriers.

If the scattering of charge carriers is majorly governed by mechanisms like electron-electron, electron-phonon, and phonon-phonon interactions, then γ is frequency independent and could be considered as a constant and equation (1) is followed whereas if the charge carriers get scattered majorly due to Coulomb interactions between the carriers and heterovalent dopants, then the damping is approximated by a frequency dependent empirical equation given by (3)

$$\Gamma(\omega) = \Gamma_L - \frac{\Gamma_L - \Gamma_H}{\pi}\left[tan^{-1}\left(\frac{\omega - \Gamma_X}{\Gamma_W}\right) + \frac{\pi}{2}\right] \quad (3)$$

Where Γ_L and Γ_H are damping constants corresponding to low and high frequencies respectively, Γ_x is the crossover frequency as scattering transits from a low frequency to a high-frequency regime and Γ_w represents the width over which region of this crossover frequency spans.

Based upon the mechanism of scattering, we have divided our modeling approach as:

(I) Frequency-independent Drude modeling where we observe almost the same damping at all frequencies and thus γ is a constant.

(II) Frequency-dependent Drude modeling where the damping is frequency dependent and takes the form of the empirical equation (3)

Furthermore, the electric field at the surface of a NC doesn't stay limited to itself and extends to the space around it. Therefore, it can have interactions with the solvent and other NCs in its vicinity which will modify its dielectric response to the incident radiation. For this purpose, we employed Maxwell-Garnett effective medium approximation (MG-EMA) which ignores interparticle coupling assuming that NCs are not linked electronically to each other but takes into account far-field interactions between the NCs and the dielectric interactions between the NCs and the solvent.

Thus, the dielectric function of the material is modified and takes shape of an effective dielectric function ε_{eff} which using EMA is given by[47],

$$\frac{\varepsilon_{eff} - \varepsilon_H}{\varepsilon_{eff} + 2\varepsilon_H} = f_v \frac{\varepsilon_D - \varepsilon_H}{\varepsilon_D + 2\varepsilon_H} \tag{4}$$

where ε_H is dielectric constant of the host solvent in which NCs are dispersed, f_v is the particle volume fraction of NCs in the solvent and other parameters have the same descriptions as mentioned already. From here, the absorbance of the solution can be determined by just calculating $\mathrm{Im}\{(\varepsilon_{eff})^{1/2}\}$ where $\mathrm{Im}(\varepsilon_{eff})$ stands for the imaginary part of the effective dielectric function.

By developing a MATLAB code, we have least-square fitted the absorbance spectra of our NCs using the frequency dependent and frequency independent Drude model.

(I) for frequency independent Drude model, we combined equations (1), and (4) and used them to extract the free parameters ω_P, γ and f_v.

(II) for frequency dependent Drude model, we combined equations (1), (3) and (4) and used them to extract the free parameters ω_P, Γ_L, Γ_H, Γ_x, Γ_w and f_v.

We note here that even though in the manuscript we acknowledge that high-frequency dielectric constant may change after high amounts of Cr codoping (alloying), modeling of LSPR spectra for all Cr-Sn codoped In_2O_3 NCs has been done assuming a constant value of 3.9.

Once these parameters were obtained, we

(1) input the value of ω_P in equation (2) to obtain the free electron density.

(2) Since the damping parameters give us an estimation of the scattering of charge carriers, they can be correlated with the optical D.C. mobility (μ_{opt}) of charge carriers using the equation

$$\sigma = Ne\mu_{opt} = \frac{Ne^2}{m^* \gamma} \tag{5}$$

Where σ is the DC electrical conductivity of the sample. Since carrier mobility is a D.C. quantity, the above formula is strictly valid for the frequency independent Drude model approach. However,

at low frequencies, $\Gamma_L \cong \gamma$ and therefore, for the frequency dependent approach, we can substitute Γ_L instead of γ to compute the optically derived carrier mobility i.e.

$$\sigma = Ne\mu_{opt} = \frac{Ne^2}{m^*\Gamma_L} \tag{6}$$

4A.3 Results and Discussion

4A.3.1 Structure and morphology

Elemental analysis of the product was carried out using both EDX and ICP-AES techniques. Elemental compositions obtained through both techniques match largely with each other and also with the precursor ratios (Table 4A.2), within the experimental uncertainties. Since ICP-AES is a more reliable technique to estimate small amount of dopant ions, all the dopant values reported hereafter in this manuscript are the estimated dopant concentrations from ICP-AES. While Cr doping percentage has been varied from 0 to 23.8 % of total cation concentration, a constant Sn doping level of 6.6% has been maintained for all the Cr-Sn codoped In_2O_3 NCs. We use the generic term doping throughout the chapter for all compositions, but we note here that when the dopant concentration is as high as ~20%, then it is essentially alloying.

Table 4A.2: Comparison of the nanocrystal compositions estimated by the ICP-AES technique with the EDX technique and the precursor molar ratios used in the synthesis.

In: Sn: Cr		
Precursor Ratio	**EDX Composition**	**ICP-AES Composition**
95 : 0 : 5	95.1 : 0 : 4.9	94.6 : 0 : 5.4
90 : 0 : 10	90.8 : 0 : 9.2	88.4 : 0 : 11.6
85 : 0 : 15	86.8 : 0 : 13.2	85.2 : 0 : 14.8
80 : 0 : 20	83.3 : 0 : 16.7	81.4 : 0 : 18.6
75 : 0 : 25	81.8 : 0 : 19.2	78.5 : 0 : 21.5
90 : 10 : 0	91.3 : 8.7 : 0	93.3 : 6.7 : 0
85 : 10 : 5	87.9 : 8.6 : 3.5	86.9 : 6.5 : 4.6
80 : 10 : 10	88.9 : 8.8 : 8.8	84.0 : 6.6 : 9.4
75 : 10 : 15	84.8 : 8.8 : 19.0	71.6 : 6.4 : 22.0
70 : 10 : 20	73.0 : 9.0 : 18.0	69.6 : 6.6 : 23.8

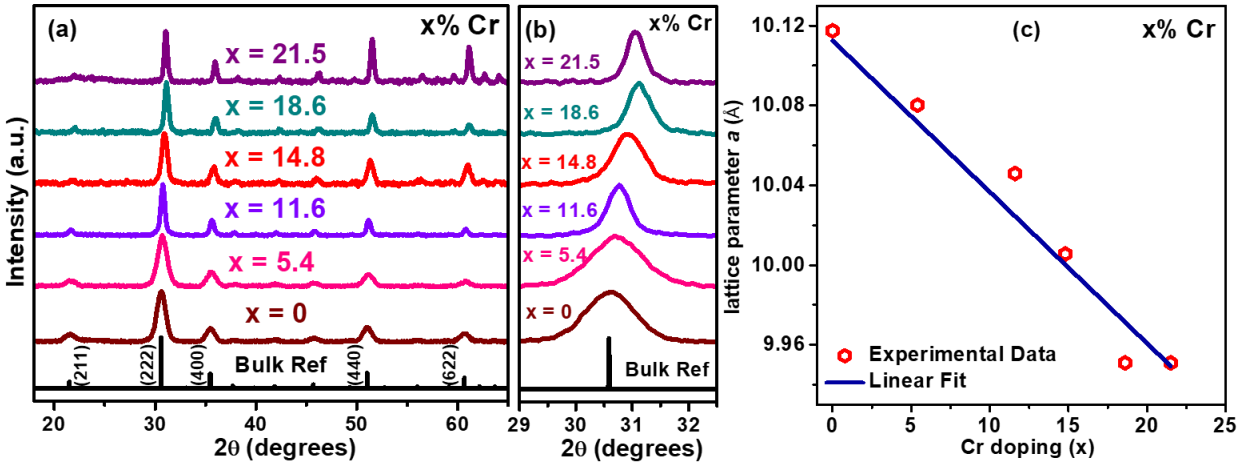

Figure 4A.1: (a) Powder XRD patterns of different Cr-doped In_2O_3 NCs signifying the retention of the bulk In_2O_3 cubic bixbyite phase in NCs across different doping percentages. Systematic shift of (b) diffraction peaks and, (c) lattice parameters with an increase in the Cr doping percentage signifying lattice doping of Cr^{3+} ions.

Figure 4A.1a compares the XRD patterns of Cr-doped In_2O_3 NCs with reference data (JCPDS 88-2160) of bulk In_2O_3. All samples exhibit the cubic bixbyite structure (space group 206, *Ia3*) with no signs of an impurity phase. Importantly, the diffraction peaks shift to higher 2θ values with increase in Cr doping (Figure 4A.1b), which indicates that the unit cell is contracting in size with the incorporation of Cr ions into the In_2O_3 lattice. This shift is an evidence of lattice doping where Cr^{3+} ions with smaller effective ionic radii (64 pm)[48] replace larger In^{3+} ions (80 pm).[48] Figure 4A.1c establishes that the lattice parameters decrease in a linear fashion with increase in Cr doping concentration following Vegard's law,[49] confirming the incorporation of Cr^{3+} ions into the In_2O_3 lattice.

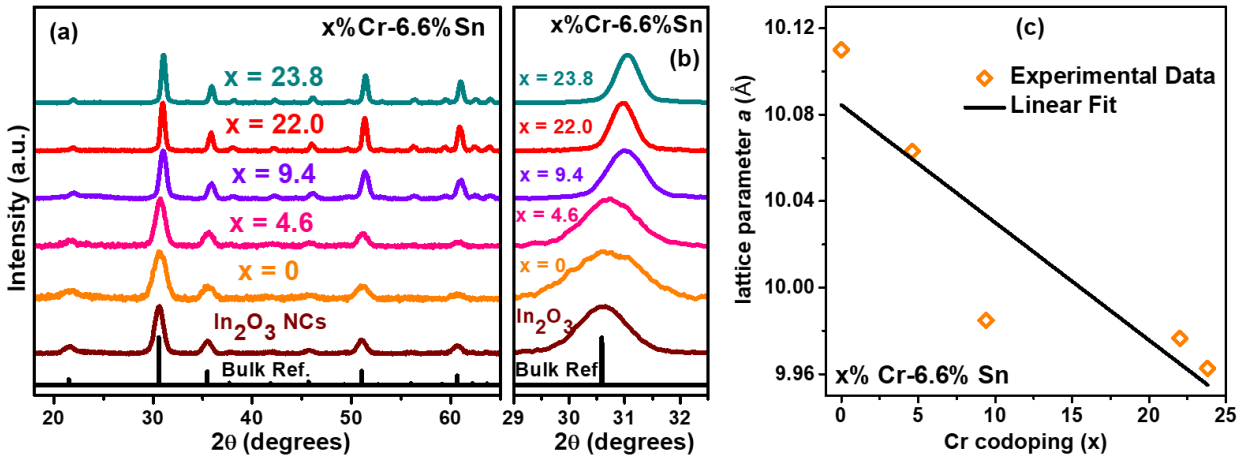

Figure 4A.2: (a) Powder XRD patterns of different Cr-Sn codoped In_2O_3 NCs exhibiting cubic bixbyite structure of bulk In_2O_3 despite a large amount of doping in the lattice. Shift of (b) diffraction peaks and, (c) lattice parameters with an increase in the Cr codoping percentage.

XRD patterns of Cr-Sn codoped In_2O_3 NCs (Figure 4A.2) also show a similar effect on lattice parameters with Cr codoping. However, unlike Cr-doped In_2O_3 NCs, the variation of lattice parameters with Cr codoping concentration for Cr-Sn codoped In_2O_3 NCs somewhat deviates from Vegard's law (Figure 4A.2c) probably because the decrease in lattice parameters due to Cr doping could be countered by a corresponding increase in lattice parameters due to the repulsions between Sn ions in the proximity of each other.[50-52] Thus, XRD data suggest that Cr is incorporated substitutionally into the In_2O_3 lattice, both in the Cr-doped and Cr-Sn codoped samples. Moreover, the linewidth of diffraction peaks for both Cr-doped and Cr-Sn codoped In_2O_3 NCs becomes narrower with an increase in Cr concentration, suggesting that the diameter of NCs increases with Cr doping.

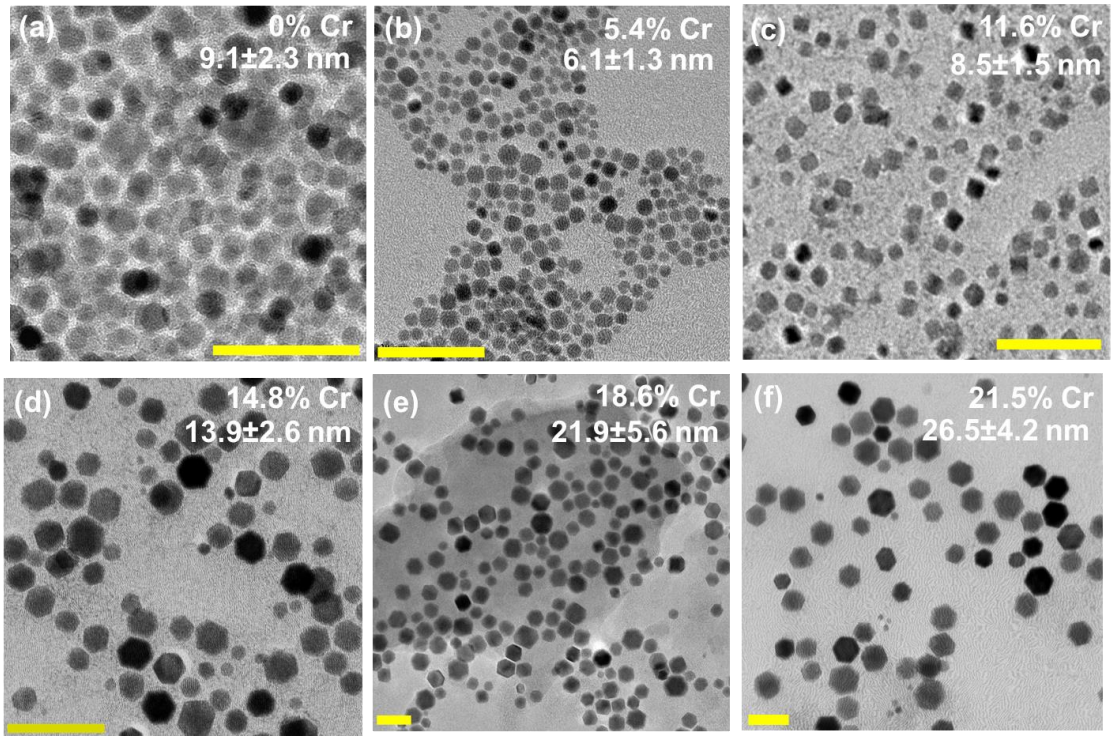

Figure 4A.3: TEM micrographs of different Cr-doped In_2O_3 NCs showing an increase in the diameter of the NCs with an increase in the Cr doping concentration.

Figure 4A.3 shows the TEM images of different Cr-doped In_2O_3 NCs. With an increase in the Cr doping percentage, the diameter of the NCs first decreases and then increases while the morphology transforms from a nearly spherical to hexagonal-shaped NCs. The overall trend observed from Figure 4A.4 signifies presence of an almost linear correlation between the NC diameter and Cr doping percentage which allows the NC diameter to vary from 6.1 nm to 26.5 nm.

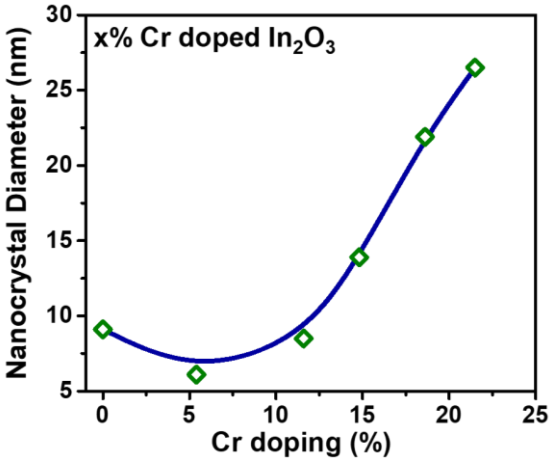

Figure 4A.4: Correlation between the NC diameter obtained from TEM and the Cr doping percentage displaying that the increase in the Cr doping percentage leads to an increase in the NC diameter.

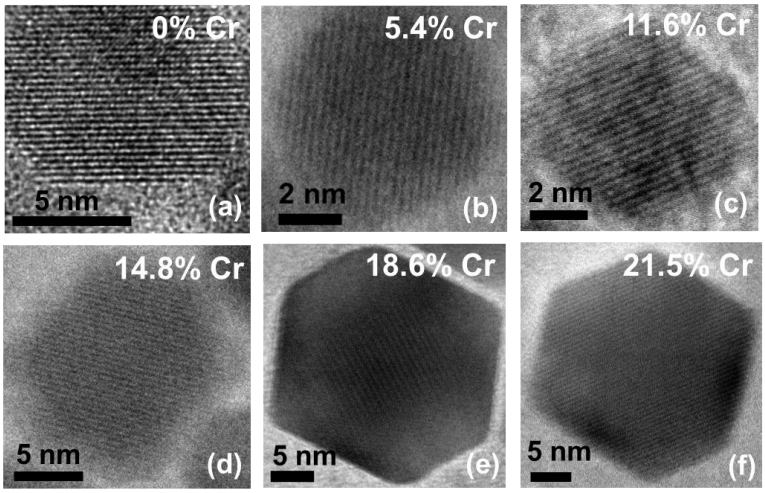

Figure 4A.5: High-resolution TEM (HRTEM) images of different Cr-doped In_2O_3 NCs.

The HRTEM images of different Cr-doped In_2O_3 NCs in Figure 4A.5 shows the highly crystalline nature of the NCs with lattice fringes corresponding the different planes of the In_2O_3 cubic bixbyite structure. Furthermore, it is again evident that other than increasing the diameter of the NCs, increase in the Cr doping percentage leads to more well-defined facets and translates the NC morphology from nearly-spherical to hexagonal shaped.

Figure 4A.6 shows the TEM images of Cr-Sn codoped In_2O_3 NCs with an almost constant Sn doping percentage of 6.6% while the Cr codoping percentage is varied from 0-23.6%. Similar to the results obtained for Cr-doped In_2O_3 NCs, an increase in the Cr codoping percentage indeed cause an increase in the NC diameter from 6.7 nm for 6.6% Sn-doped In_2O_3 to 22.1 nm for 23.8%

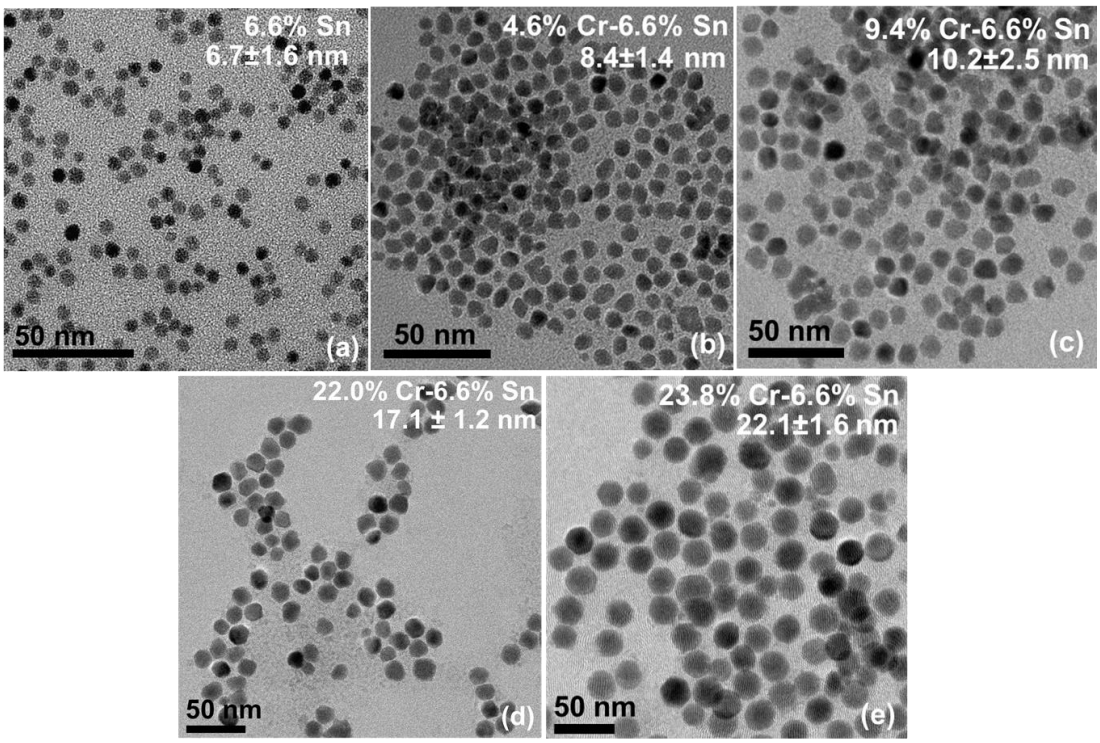

Figure 4A.6: TEM micrographs of different Cr-Sn codoped In_2O_3 NCs with a constant Sn doping percentage of 6.6% while Cr codoping percentage is varied from 0% to 23.6%.

Cr-6.6% Sn codoped In_2O_3 NCs. Also, a statistical increase in faceted (nearly hexagonal) NCs is observed with the increasing diameter of NCs. HRTEM images of Cr-Sn codoped In_2O_3 NCs in Figure 4A.7 show single crystalline NCs with lattice planes corresponding to In_2O_3 cubic bixbyite structure. So, the TEM results reconfirm that the diameter of NCs and their lattice parameters, both vary systematically with the concentration of Cr dopants.

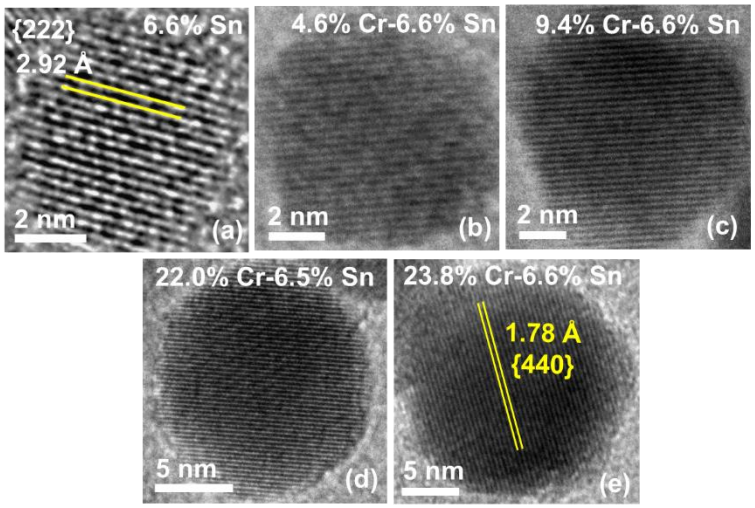

Figure 4A.7: HRTEM images of different Cr-Sn codoped In_2O_3 NCs exhibiting lattice fringes corresponding to different planes of the In_2O_3 cubic bixbyite structure.

Figure 4A.8 summarizes the effect of Cr doping concentration on crystallite size of Cr-Sn codoped In_2O_3 NCs, obtained from TEM and FWHM of XRD peaks (using Scherer equation[53]). This change in NC diameter with Cr doping is not surprising as the influence of doping on the nucleation and growth process of nanocrystals has been observed quite frequently in literature.[54-59] For example, Schwartz et al reported Co^{2+} doping in ZnO increases the critical nucleation radius and consequently smaller NCs are obtained.[54] In difference, Tuinenga et. al observed an increase in the size of CdSe NCs by doping In^{3+} ions, where it was suggested that the dopant ions accelerated the formation of monomers required for NC growth.[55] There are many other different reported mechanisms through which dopant ions can influence the diameter of NCs. However, the reasons provided behind how a particular dopant ion influences the nucleation and growth of NCs varies from system to system, without any generic understanding.[60] This difficulty in understanding is because of many overlapping parameters such as interaction of dopant ions with the host, rates of precursor dissociations, nucleation threshold, the interaction of capping ligands with dopants and host, and optimization of the surface energy of different facets during growth process which determine the final size and shape of NCs. Due to these complexities, elucidating of the microscopic mechanism behind the observed increase in diameter of NCs with Cr doping is beyond the scope of the present study.

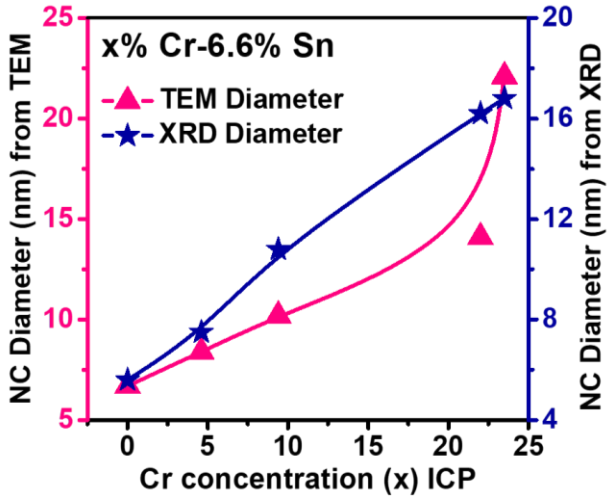

Figure 4A.8: Correlation between the diameters of Cr-Sn codoped In_2O_3 NCs obtained from TEM and XRD (using Scherer equation $D_{hkl} = \frac{K\lambda}{B_{hkl}cos\theta}$ where D_{hkl} is the crystallite size in a direction perpendicular to the lattice plane {hkl}, B_{hkl} is the full width at half maxima of the diffraction peak in radians, θ is the Bragg angle at which diffraction occurs and K is a numerical factor). {222} diffraction plane was used to estimate the crystallite size of all Cr-Sn codoped In_2O_3 NCs.

4A.3.2 Dopant oxidation state and radial distribution

After elucidating the size and crystal structure of Cr-Sn codoped In_2O_3 NCs, we begin to discuss the results of XPS to reveal both the oxidation state of metal ions and their relative distribution across the radius of NCs. Figure 4A.9 shows In *3d*, Sn *3d*, and Cr *2p* spectra respectively for a representative sample of 23.8% Cr-6.6% Sn codoped In_2O_3 NCs. All three core-level spectra show two peaks because of spin-orbital splitting. The binding energy of peak for In $3d_{5/2}$ and In $3d_{3/2}$ is located at 444.4 eV and 451.9 eV respectively which corresponds to an oxidation state of 3+ and corroborates well with Cr and Sn-doped In_2O_3 NCs literature.[61-62] The slight asymmetry in the In 3d peaks has been attributed to defects like oxygen vacancies in the immediate environment.[63-64] Likewise, Sn displaying $3d_{5/2}$ and $3d_{3/2}$ peaks at 486.3 eV and 494.6 eV and Cr exhibiting $2p_{3/2}$ and $2p_{1/2}$ peaks at 576.6 eV and 584.4 eV respectively, relate to incorporation of Sn^{4+} and Cr^{3+} ions in In_2O_3 lattice.[65-66] These observations verify that oxidation states of all metal ions in the product NCs are identical to those in their corresponding precursors used during the synthesis. More importantly, these XPS results confirm that in Cr-Sn codoped In_2O_3 NCs, the substitution of In^{3+} with Cr^{3+} is isovalent in nature and such a substitution does not alter the electron density. The fact that Cr^{3+} is a stable state in both precursors and products, and the observed complete conversion of Cr precursor into the product (Table 4A.2), suggest that there is no other oxidation state of Cr that might have left over as a side product after precipitating the product NC.

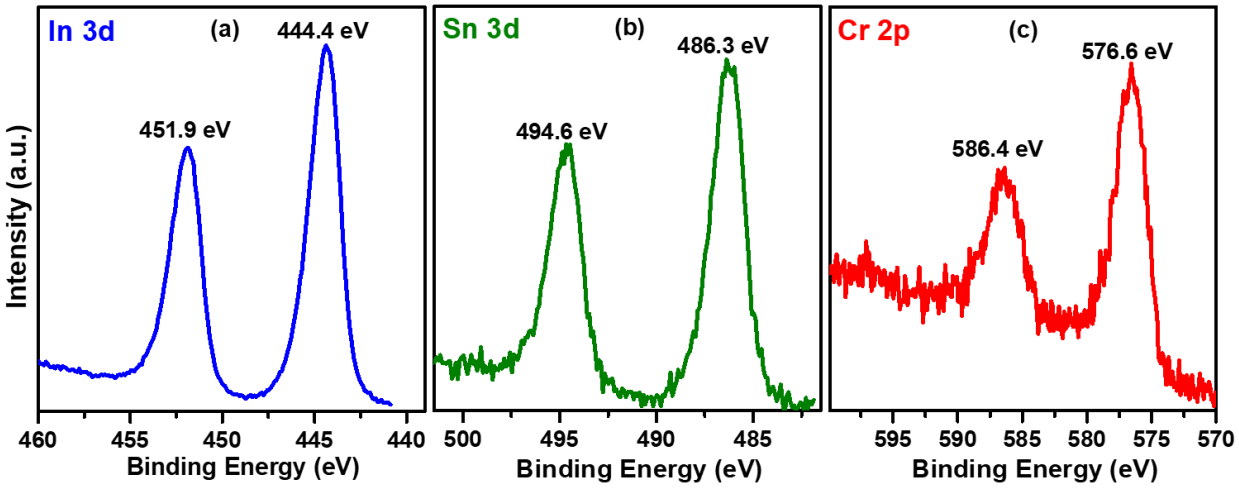

Figure 4A.9: XPS analysis of Cr-Sn codoped In_2O_3 NCs. (a), (b) and (c) show the XPS peaks for In 3d, Sn 3d and Cr 2p core levels respectively, for 23.8% Cr-6.6% Sn codoped In_2O_3 NCs. Binding energy values suggest the presence of In, Sn, and Cr in oxidation states +3, +4 and +3 respectively.

Additionally, being a surface sensitive probe, XPS can provide information regarding the heterogeneity in the radial distribution of elements within NC.[44-67] This is particularly important because radial distribution of Sn is known to have huge implications on the quality factor of LSPR.[2] The infinitesimal XPS intensity contribution dI, originating from a volume element dv, located at a depth x from the surface, is given by $dI = I_0 \exp(-x/\lambda)$, where I_0 is average photoionization signal per unit volume, and λ is mean free path of photoelectrons before suffering any inelastic collision.[57] We employed Al Kα radiation as a photon source for our XPS measurements, which provide photoelectrons from In *3d*, Sn *3d* and Cr *2p* core levels with similar λ of ~1.6 nm (calculation shown in experimental section). Therefore all three elements exhibit similar sampling depths, which are some atomic layers from the surface of NCs. Thus, determining the ratio of Sn and Cr concentration using XPS data will provide the elemental ratio present closer to the surface of NCs, excluding the core of NCs. On the other hand, similar elemental ratio obtained by ICP-AES will probe entire NCs including core and surface of NCs. If the dopant concentrations determined by both techniques match with each other, then the doping would be uniform throughout the NC, otherwise, surface or core of the NCs would be preferentially doped.

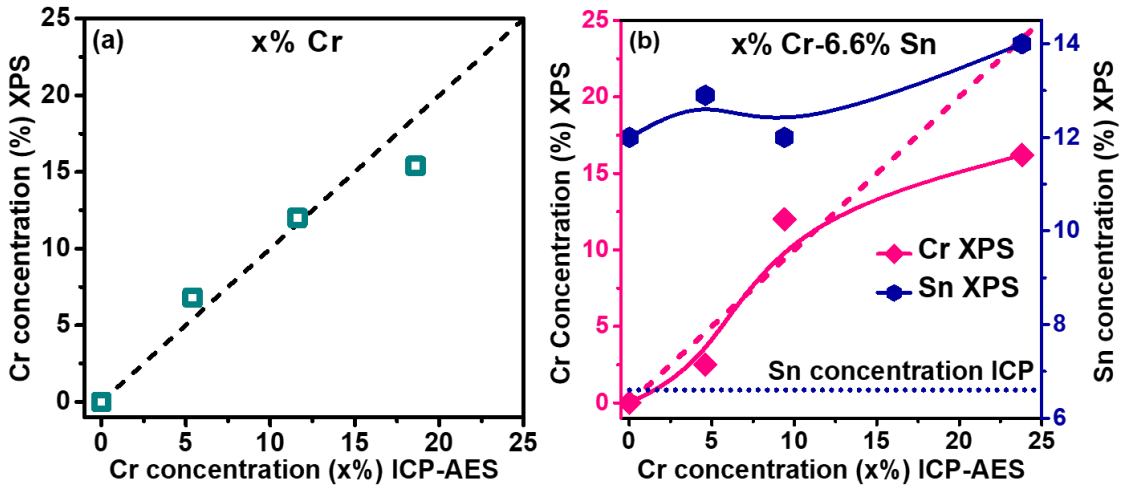

Figure 4A.10: Equating the doping concentrations of Cr and Sn obtained from XPS with those measured from ICP-AES in (a) Cr-doped In_2O_3 NCs (b) Cr-Sn codoped In_2O_3 NCs, to obtain their radial distribution within the NC. Symbols are experimental data, while solid lines are just guides to the eye. Blue dotted line shows the constant 6.6% Sn obtained from ICP-AES. Black and pink dashed-lines are an ideal case of homogenous Cr doping where concentrations of Cr obtained from ICP-AES and XPS are equal.

Figure 4A.10a and Figure 4A.10b show that the Cr doping levels measured by XPS and ICP-AES for Cr-doped and Cr-Sn codoped In_2O_3 NCs respectively, agree with each other over a wide range of Cr doping, suggesting largely homogeneous doping of Cr throughout the NCs. But at higher Cr

concentration, we note somewhat preferential Cr doping towards the core, which needs to be verified further. Nonetheless, these XPS data, in conjunction with XRD and TEM results, again confirm the doping of high concentrations of Cr into the In_2O_3 lattice. On the other hand, XPS shows (Figure 4A.10b) more Sn content (12-14%) compared to the 6.6% Sn obtained from ICP-AES, for all Cr-Sn codoped In_2O_3 NC samples. This 12-14% Sn corresponds to an averaging over higher Sn content at the (outer-most a few Å) NC surface along with the smaller Sn contributions coming from the parts of NCs reasonably below the surface. This finding suggests that Sn doping in our NCs is heterogeneous in nature, with higher Sn content near the surface of a NC, compared to its core. This observation of relatively higher concentration of Sn dopants on the surface compared to the core of NCs is consistent with prior literature of Sn-doped In_2O_3 NCs synthesized through a similar procedure.[2] Codoping with Cr does not influence the intrinsic heterogeneity of Sn doping, since for all the Cr-Sn codoped In_2O_3 NCs, a similar (12-14%) concentration of Sn was estimated using XPS. Importantly, since the Cr doping decreases the surface-to-volume-ratio (increases diameter), Figure 4A.10b suggests an increase in the ratio of $[Sn_{core}]/[Sn_{surface}]$ with increasing diameter (Cr content), where $[Sn_{core}]$ and $[Sn_{surface}]$ represent the concentration of Sn dopants in the core and at the surface of NCs respectively.

4A.3.3 LSPR from Cr-Sn codoped In_2O_3 NCs

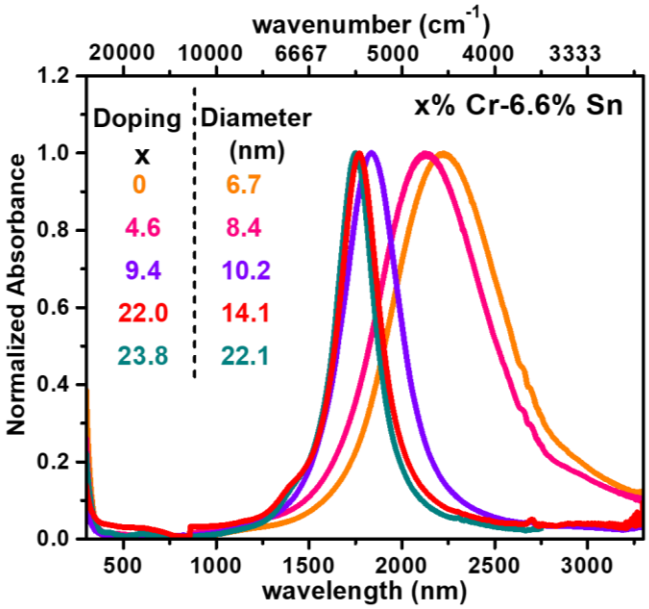

Figure 4A.11: LSPR spectra of Cr-Sn codoped In_2O_3 NCs depicting shift of LSPR bands to shorter wavelengths along with a decline in FWHM on increasing the magnitude of Cr codoping percentage.

We will now discuss the effect of dopants and NC diameter in governing the LSPR properties of Cr-Sn codoped In_2O_3 NCs. Figure 4A.11 shows that the LSPR peak position shifts to higher energies along with a decrease in FWHM, as the Cr codoping percentage is increased, which is also accompanied by an increase in NC diameter. Consequently, Q-factors also increase with Cr codoping or increasing diameter of Cr-Sn codoped In_2O_3 NCs. Table 4A.3 summarizes all these parameters. Our 23.8% Cr-6.6% Sn codoped In_2O_3 NCs exhibit a Q-factor of 7.2, which is more than twice the Q-factor of 3.2 exhibited by 6.6% Sn-doped In_2O_3 NCs. This is by far a record high number for any reported metal doped In_2O_3 NCs (see Table 4A.4). Till now, the best Q-factor for metal doped In_2O_3 NCs was reported as 4.85 for a random batch of ITO NCs[2] and 4.0 for Ce-doped In_2O_3 NCs.[30] Furthermore, 3 of the 5 Cr-Sn codoped In_2O_3 NC systems have LSPR Q-factors superior to all other systems, apart from CdO NCs doped with In,[5] or codoped with F-In.[6]

Table 4A.3: Tabulated experimental LSPR parameters and Q-factors of Cr-Sn codoped In_2O_3 NCs with constant 6.6% Sn doping and variable Cr codoping concentrations. This table was obtained from the data shown in Figure 4A.11.

Cr concentration %	**Diameter of NCs (nm)**	**λ_{max} (nm) at LSPR peak**	**LSPR energy (cm^{-1})**	**FWHM (eV)**	**Q-Factor**
0	6.7	2207	4531	0.174	3.2
4.6	8.4	2131	4692	0.187	3.1
9.4	10.2	1838	5441	0.135	5.0
22.0	14.1	1771	5646	0.106	6.6
23.8	22.1	1749	5718	0.099	7.2

It is thought-provoking to what could be the reason for this systematic increase in peak energy and a decrease in FWHM of LSPR resulting into the high Q-factors with an increase in Cr doping? Isovalent doping of Cr^{3+} does not introduce extra charge carriers, whereas, the concentration of heterovalent Sn^{4+} ions remained constant for all our Cr-Sn codoped In_2O_3 NCs. So, the factor (s) responsible for tuning of LSPR peak over a wide range of 2000 cm^{-1} is not intuitive. Other than depending upon the free electron density, LSPR is also dependent upon the size, solvent of dispersion and dielectric constant of the material. Since measurements for all Cr-Sn codoped In_2O_3 NCs were performed in tetrachloroethylene solvent, this shift can't be attributed to the difference in a solvent of dispersion. However, at high doping (or alloying) concentrations such as 23.8% of Cr doping, the dielectric constant of the material can change, but that alone does not explain the simultaneous decrease in both peak wavelength and FWHM of LSPR. Details regarding the effect

of dielectric constant have been discussed in section 4A.3.5. Then, the sizes of our NCs vary amid 6.7-22.1 nm, but still, all the diameters lie within the quasi-static perimeter. This means that the electric field experienced by the NC can be considered as identical over its entire volume, and hence LSPR could be considered independent of size in this regime. However, with a change in diameter, the surface to volume ratio of NC changes and it would be important to find out if this change in surface-to-volume ratio is influencing the LSPR properties of Cr-Sn codoped In_2O_3 NCs. For this purpose, it is imperative to find out the fundamental parameters that are changing when the diameter of the NCs is tuned through Cr codoping.

Table 4A.4: Comparison of the LSPR Q-factors of Cr-Sn codoped In_2O_3 NCs with the best doped nanocrystal LSPR materials in the NIR range, arranged in descending order of Q-factors.

Host	**Dopant**	**Doping Level (%)**	**Diameter of NCs (nm)**	**λ_{max} (nm)**	**FWHM (meV)**	**Q-factor**	**Reference Number**
CdO	F^- , In^{3+}	~10, 8.3	14	1726	59	12.23	6
CdO	In^{3+}	13.2	11.3	2265	67	8.15	5
In_2O_3	Sn^{4+}, Cr^{3+}	6.6, 23.8	22.1	1749	99	7.2	Present Case
In_2O_3	Sn^{4+}, Cr^{3+}	6.6, 22.0	14.1	1771	106	6.6	Present Case
In_2O_3	Sn^{4+}, Cr^{3+}	6.6, 9.4	10.2	1848	135	5.0	Present Case
In_2O_3	Sn^{4+}	6.4	10.8	~1700	~150	4.85	2
InN	N vacancy	5.5	30	~2900	89	4.83	35
In_2O_3	Ce^{4+}	5.2	~10	3965	77	4.08	30
ZnO	Al^{3+}	1.6	~30	~4000	~100	3.9	32
$Cu_{2-x}S$	Cu vacancy	~3	5.9	~1797	210	3.3	7
WO_{3-x}	O vacancy	~5%	5.4 (b) 62 (l)	850-900	~900	1.6	9
Zn-O	Sn^{4+}	1.37	9.4	790	1132	1.39	34
ZnO	Ga^{3+}	~2.5	26.2	~6000	-	<1.0	33

4A.3.4 Frequency-dependent and frequency-independent Drude modeling

To address the questions and concerns raised above, we fitted the LSPR data of all Cr-Sn codoped In_2O_3 NCs using frequency-dependent and frequency-independent Drude model (see section 4A.2.2 for details) by employing a MATLAB code. LSPR peaks for all the samples were fitted well using both frequency-independent and frequency-dependent models as shown in Figure 4A.12. Parameters obtained from both fittings are shown in Table 4A.5 and Table 4A.6. Lounis et al. showed that when the extent of free-electron scattering by ionized impurities is less significant, then both frequency-dependent and independent model can fit the experimental data.[2] Therefore, fitting of our experimental data using both the models suggests ionized impurities do not have much influence on the LSPR data.

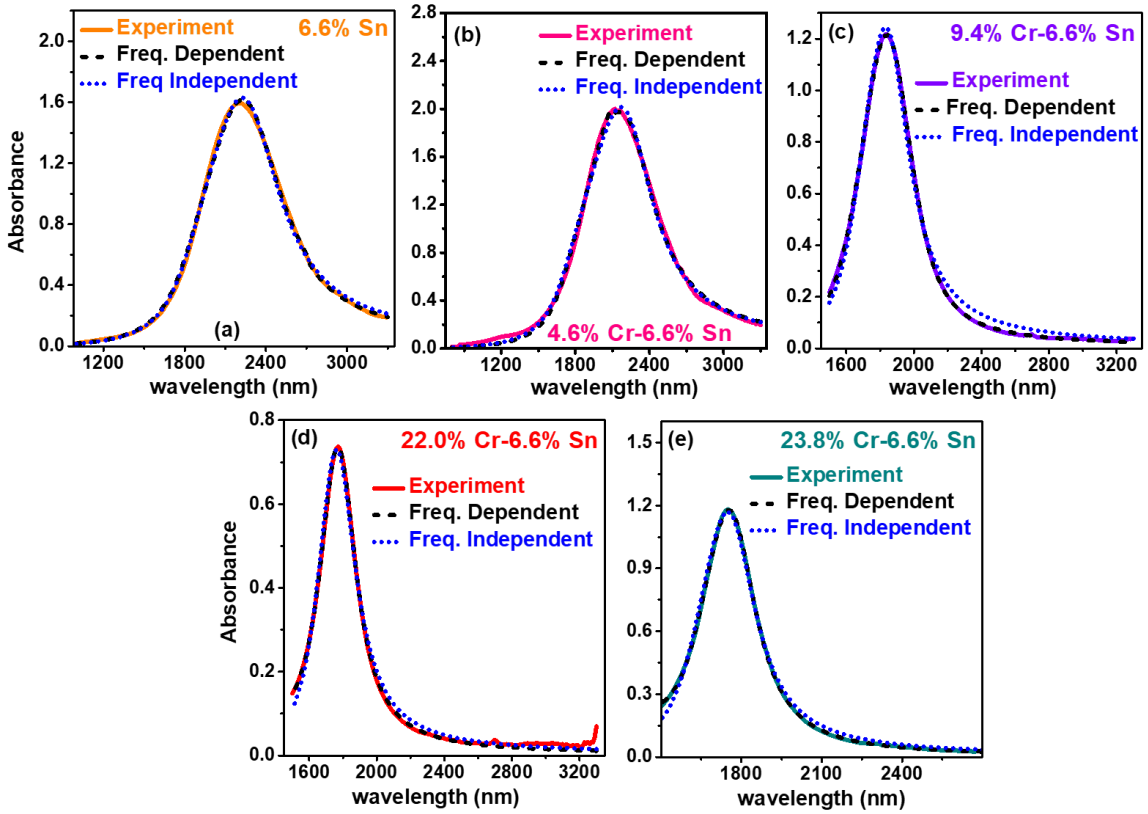

Figure 4A.12: Frequency-independent and frequency-dependent model fits to the experimental NIR absorption spectra of different Cr-Sn codoped In_2O_3 NCs.

This essence of ionized impurity scattering can be quantitatively estimated by parameters obtained from the frequency-dependent approach. Precisely, the magnitude of Γ_L measures the essence of ionized impurity scattering and therefore, if $\Gamma_L >> \Gamma_H$, then ionized impurity scattering contributes

maximum towards damping of electron density. Hence, to obtain a LSPR with high Q-factor, $\Gamma_L << \Gamma_H$ should be ensured to minimize the damping by ionized impurity scattering.[2, 30]

Analyzing the parameters obtained from frequency dependent scattering approach (Table 4A.5), we observe that at low codoping concentrations of Cr, the magnitude of Γ_L is comparable to Γ_H, but as the extent of Cr codoping is increased, $\Gamma_{L<<} \Gamma_H$ which suggests suppression of ionized impurity scattering in these NCs. In fact, the best Γ_L value (307 cm^{-1}) observed for Cr-Sn codoped In_2O_3 NCs are the lowest ever observed for any doped In_2O_3 system and beats Ce-doped In_2O_3 NCs (713 cm^{-1}),[30] and Sn-doped In_2O_3 NCs (913 cm^{-1}),[2] by a huge margin. Moreover, since a low Γ_L is expected to reflect as enhanced mobility of charge carriers, the optically derived mobility obtained for Cr-Sn codoped In_2O_3 NCs is much higher than that for ITO NCs.

Table 4A.5: Bulk plasma frequency (ω_P) and damping parameters obtained by extended Drude model fitting to the absorption spectra of Cr-Sn codoped In_2O_3 NCs. Here Γ_L and Γ_H represent damping constants corresponding to low and high frequencies respectively, Γ_x stands for the crossover frequency as scattering transits from a low frequency to a high-frequency regime and Γ_w represents the width over which region of this crossover frequency spans. Electron density (N) and optical carrier mobility (μ_{opt}) were calculated from the fitting parameters.

Cr Concent-ration	**ω_P (cm^{-1})**	**N (10^{21} cm^{-3})**	**Γ_L (cm^{-1})**	**Γ_H (cm^{-1})**	**Γ_X (cm^{-1})**	**Γ_W (cm^{-1})**	**μ_{opt} (cm^2/V.s)**
0%	14021±7	0.88	929±3	1091±3	3688±5	16±4	25.1
4.6%	14664±2	0.96	1046±1	903±2	4742±2	30±0	22.3
9.4%	16377±4	1.20	373±75	1123±98	4892±42	698±283	62.6
22.0%	16765±37	1.25	544±30	2675±439	6464±273	319±47	42.9
23.8%	17301±65	1.33	307±37	3989±323	6285±11	281±8	76.3

Since, it is pretty evident now that ionized impurity scattering is suppressed in our NCs, we will use the parameters obtained from the frequency-independent approach (Table 4A.6) of Drude model to unravel the quantities changing when the LSPR band is tuned by changing the diameter of NCs (induced by changing the Cr codoping concentration). As shown in Table 4A.6, Cr codoping increases the bulk plasma frequency or more specifically increases the electron density, while the concentration of Sn remained constant at 6.6%. This increase in electron density while keeping the Sn doping concentration constant signifies that the number of free electrons per Sn

dopant (N/ρ_{Sn}) increases with Cr doping where ρ_{Sn} represents the total dopant density of Sn ions. Since electron density directly controls the LSPR peak position through the bulk plasma frequency, an increase in the electron density driven by an increase in NC diameter increases the LSPR energy. On the other hand, the damping constant decreases progressively with an increase in the NC diameter which decreases the LSPR FWHM. The decrease in the scattering of electron density is also reflected in the enhanced electron mobility values for NCs with high Q-factors. Now that we know that the enhancement in LSPR energy is due to an increase in electron density and the decrease in LSPR FWHM is due to the suppression of the ionized impurity scattering (which decreases the damping constant), it is necessary to find out how a change in the NC diameter can drive this unexpected enhancement in the LSPR Q-factor and the parameters therein.

Table 4A.6: Bulk plasma frequency (ω_P) and damping parameter (γ) obtained by frequency independent Drude model fitting to the absorption spectra of Cr-Sn codoped In_2O_3 NCs. Electron density (N) and optical carrier mobility (μ_{opt}) were calculated from the fitting parameters.

Cr concentration	**ω_P (cm^{-1})**	**N (10^{21} cm^{-3})**	**γ (cm^{-1})**	**μ_{opt} ($cm^2/V.s$)**
0%	14016±2	0.876	1063±1	22.0
4.6%	14716±3	0.966	1022±1	22.9
9.4%	16350±2	1.19	844±2	27.7
22.0%	16727±3	1.25	795±5	29.4
23.8%	16984±5	1.29	692±6	33.7

4A.3.5 Explanation for the size-dependence of LSPR energy and LSPR FWHM

To investigate how a change in the NC diameter (or surface-to-volume ratio) can increase the electron density (increasing LSPR energy) and decrease the electronic damping (decreasing LSPR FWHM), we need to first understand the fundamental mechanisms of electron density generation and electronic damping in Sn-doped In_2O_3 NCs.

The increase in electron density while keeping the Sn doping percentage constant at 6.6% signifies that the number of free electrons per Sn dopant (N/ρ_{Sn}) increases with Cr codoping where ρ_{Sn} represents the total dopant density of Sn ions. Unlike noble-metals, where each atom contributes to a free electron, in Sn-doped In_2O_3, each Sn dopant ion does not contribute a free electron. When Sn gets incorporated into the lattice of In_2O_3, it forms $(O_i'' 2Sn_{\dot{In}})^x$ complex, where two Sn defects

combine with an oxygen interstitial to form a neutral (denoted by *x*) complex.[50] $Sn_{In}^{\bullet}$ represents Sn^{4+} substituting In^{3+} ions leaving a positive charge (notation $^{\bullet}$) at the lattice site, whereas O_i'' represents incorporation of interstitial O^{2-} ions (-2 charge is indicated by $''$) to neutralize the excess positive charge. Therefore, incorporation of Sn^{4+} into the lattice of In_2O_3 does not ensure generation of free the electrons. Only when the $(O_i''2Sn_{In}^{\bullet})^x$ complex gets reduced following the equation 7,

$$(O_i''2Sn_{In}^{\bullet})^x \leftrightarrow 2Sn_{In}^{\bullet} + 2e' + \frac{1}{2}O_2 \qquad (7)$$

then free electrons are generated.[50, 68-70] Equilibrium in equation 7 shifts under different reaction conditions, changing (N/ρ_{Sn}), which is also termed as dopant activation. Results in Figure 4A.13a indicate that (N/ρ_{Sn}) increases with Cr codoping, shifting the LSPR peak towards higher energies. This increase in (N/ρ_{Sn}) could not be directly correlated with Cr codoping, apart from the indirect relationship that diameter of NCs also increases with Cr codoping concentration.

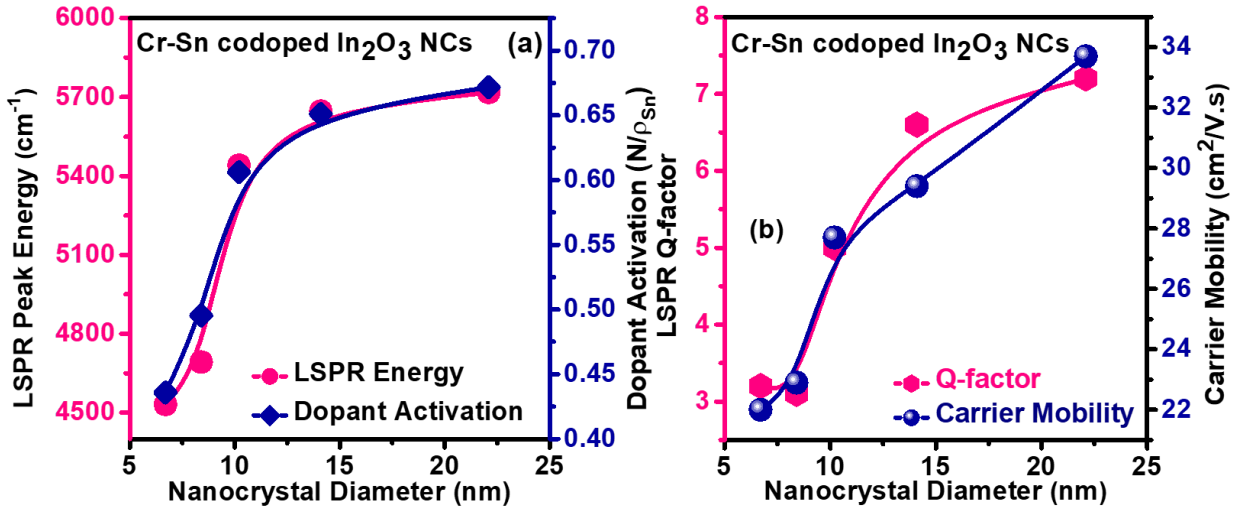

Figure 4A.13: (a) Graph representing an increase in the Sn dopant activation and LSPR energy with an increase of NC diameter. (b) Dependence of the carrier mobility and LSPR Q-factor on the diameter of Cr-Sn codoped In_2O_3 NCs.

It has been shown earlier that $(O_i''2Sn_{In}^{\bullet})^x$ complex on the surface is less likely to undergo reduction yielding free electrons, decreasing the overall (N/ρ_{Sn}).[42, 71-73] Furthermore, XPS data in Figure 4A.10b shows that the concentration of Sn dopant on the surface of NCs is >12%, though the overall concentration of Sn obtained from ICP-AES is only 6.6%. It has been also established in the literature that at higher Sn concentrations, the complex between Sn^{4+} and interstitial O^{2-} becomes irreducible, reducing the (N/ρ_{Sn}).[50, 70, 74] Therefore, reduction of the surface-to-volume

ratio by increasing the NC diameter is expected to facilitate the reduction of Sn^{4+} - interstitial O^{2-} complex, in our Cr-Sn codoped In_2O_3 NCs.

The majority electron scattering mechanism in doped oxide NCs is ionized impurity scattering with additional contributions from grain boundary scattering and neutral donor scattering. Lounis et al[2] and Crockett et al[75] have earlier shown that the ionized impurity scattering in ITO NCs can be decreased through segregation of Sn dopants towards the surface/sub-surface region, which allows electron density to move inside the undoped/low-doped core freely facing much lesser scattering by Sn dopants present on the surface. All our Cr-Sn codoped In_2O_3 NCs have surface segregated Sn doping, however, the extent of surface segregation doesn't change for different NC diameter. Therefore, surface segregation alone can't explain the decrease in ionized impurity scattering and low LSPR FWHM of Cr-Sn codoped In_2O_3 NCs. With an increase in the diameter of the NCs, the extent of ionized impurity scattering in our Cr-Sn codoped In_2O_3 NCs keeps on decreasing as suggested by the damping constants obtained from Drude modeling. We believe that decrease in ionized impurity scattering is due to a decrease in the $[O_i'']$ which are also the source of scattering centers and decrease as the NC diameter is increased (see equation 7). Additionally, with an increase in the NC diameter, there will also be a decrease in the concentration of neutral $(O_i''2Sn_{In})^x$ complexes,[76-77] contributing to neutral donor scattering and decrease in grain boundary scattering with increasing NC diameter which are likely to be responsible in further decreasing the observed damping constants in Table 4A.6 and consequently, the LSPR FWHM.

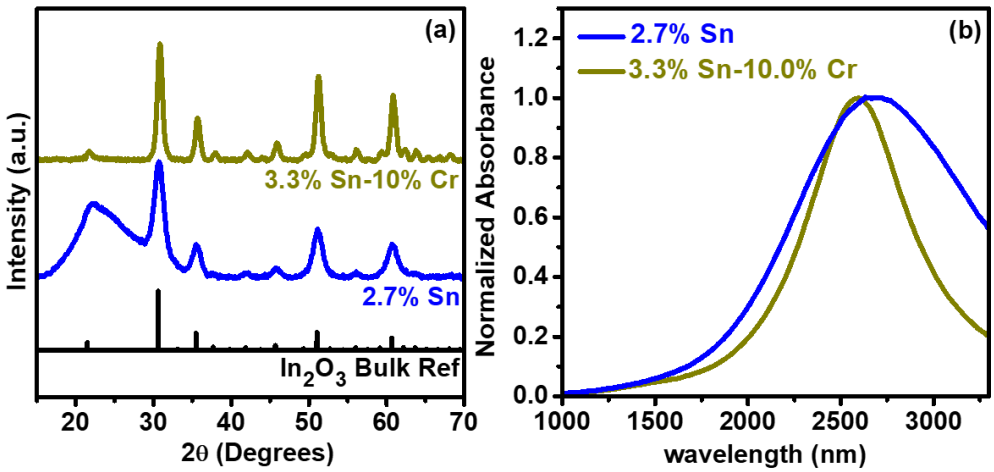

Figure 4A.14: (a) XRD pattern of 3% Sn and 3% Sn-9.6% Cr doped In_2O_3 NCs showing a decrease in the FHWM of diffraction peaks indicating an increase in diameter of NCs (b) 3% Sn-9.6% Cr codoped In_2O_3 NCs having a higher LSPR energy and decreased LSPR linewidth as compared to only 3% Sn-doped In_2O_3 NCs.

On a different note, an increase in Cr codoping concentration which increases the NC diameter, might also increase the dielectric constant of the lattice, since Cr_2O_3 has a static dielectric constant larger than that of Sn-doped In_2O_3.[46, 78-79] Therefore, at a high level of Cr codoping (or alloying), the dielectric constant of the material (overall medium) might increase, reducing electrostatic interactions between the electrons and doped impurities (decrease of ionized impurity scattering),[22] resulting into decrease in γ which is also reflected in record high mobility values observed from the Drude fitting of Cr-Sn codoped In_2O_3 NCs (Figure 4A.13b). All these observations suggest that in addition to the suppression of ionized impurities through dopant segregation and larger core size, increase in NC diameter also suppresses scattering related to neutral impurities and grain boundaries, which in turn helps to yield the low LSPR FWHM and ultimately record high Q-factor from Cr-Sn codoped In_2O_3 NCs. A similar enhancement in LSPR Q-factors was also observed for ~3% Sn-doped In_2O_3 NCs after they were codoped with ~10% Cr (Figure 4A.14).

If the above arguments for increase in LSPR energy and decrease in LSPR FWHM stand true, then it would suggest that the job of Cr codoping is mostly only to increase the diameter of NCs while preserving the surface segregation of Sn doping. Therefore, if one to synthesize large-size ITO NCs of similar doping percentage and Sn surface segregation, high LSPR Q-factors should be obtained. We synthesized 6.4% Sn-doped In_2O_3 NCs of 16.1 nm with a similar degree of Sn surface segregation (Figure 4A.15a). Analyzing the NIR absorption spectra of these NCs shown in Figure 4A.15b, the LSPR Q-factor was found to be 5.8 which is the highest reported from ITO NCs thereby confirming that a decrease in surface-to-volume ratio enhances the LSPR Q-factor.

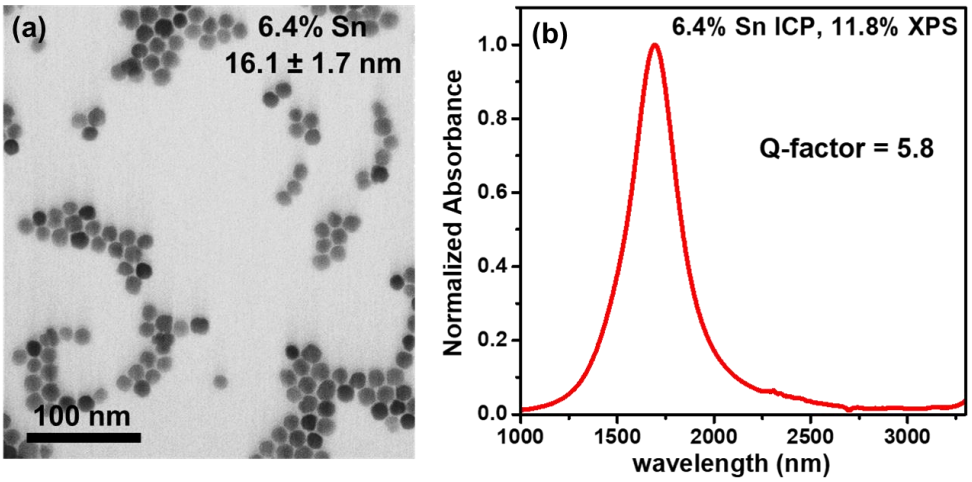

Figure 4A.15: (a) TEM image of 6.4% Sn-doped In_2O_3 NCs with an average diameter of 16.1 nm (b) NIR absorption spectra of NCs showing a narrow LSPR band with a high LSPR Q-factor of 5.8.

4A.4 Conclusions

We summarize our results here with a schematic diagram shown in Figure 4A.16. While keeping the Sn concentration constant at 6.6%, increase in Cr codoping from 0% to 23.8% in Cr-Sn codoped In_2O_3 NCs increases the diameter of NCs from 6.7 to 22.1 nm. In all these samples, Sn doping is preferred towards the surface of NCs. Also, prior literature suggests that Sn on the surface of the crystal is more prone to form irreducible complexes with interstitial oxides, compared to Sn in the core of NCs where $(O_i'' 2Sn_{In})^x$ complexes reduces easily providing free electron following equation 7.[71-72] Therefore, as the diameter of NC is increased, ratio of $[Sn_{core}]/[Sn_{surface}]$ or $[Sn]/[O_i'']$ or (N/ρ_{Sn}) increases. This increase in (N/ρ_{Sn}) increases electron density and subsequently, increases the energy of LSPR peak. On the other hand, in addition to suppression of ionized impurity scattering through surface segregation of Sn dopants, an increase in the NC diameter decreases $[O_i'']$ which further reduces ionized impurity scattering along with decrease in contributions from neutral donor and grain boundary related carrier scattering mechanisms and possible increase the in dielectric constant with increasing Cr codoping. Consequently, γ decreases or μ_{opt} increases with an increase in NC diameter. This exclusive combination of an increase in electron density and decrease in γ gives rise to exceptionally high LSPR Q-factor from Cr-Sn codoped In_2O_3 NCs. These results show a new strategy, where Q-factor can be improved by decreasing the surface-to-volume ratio of doped metal oxide and semiconductor NCs.

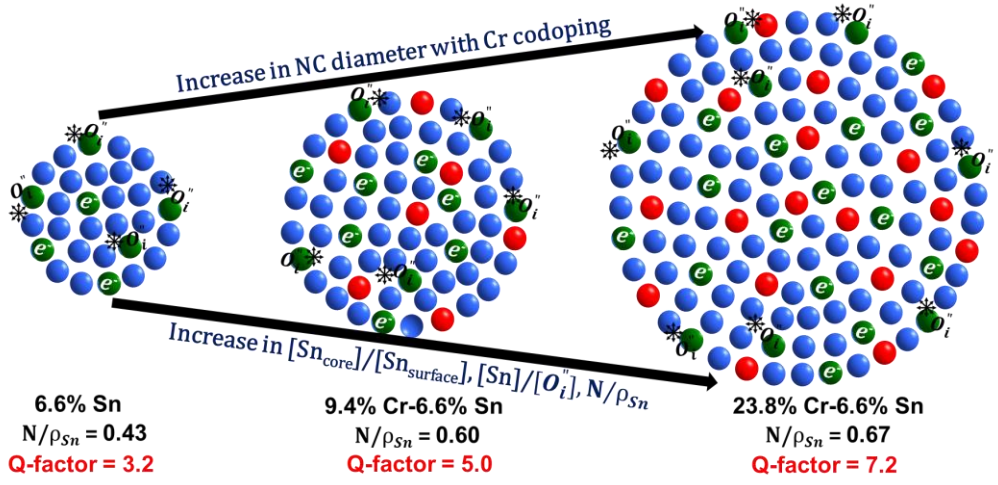

Figure 4A.16: Schematic model summarizing the reasons behind the increase in energy and decrease in FWHM of LSPR peak, responsible for record high Q-factors exhibited by Cr-Sn codoped In_2O_3 NCs.

4A.5 References

1. Kanehara, M.; Koike, H.; Yoshinaga, T.; Teranishi, T. Indium Tin Oxide Nanoparticles with Compositionally Tunable Surface Plasmon Resonance Frequencies in the Near-IR Region. *J. Am. Chem. Soc.* **2009,** *131*, 17736-17737.
2. Lounis, S. D.; Runnerstrom, E. L.; Bergerud, A.; Nordlund, D.; Milliron, D. J. Influence of Dopant Distribution on the Plasmonic Properties of Indium Tin Oxide Nanocrystals. *J. Am. Chem. Soc.* **2014,** *136*, 7110-7116.
3. Schimpf, A. M.; Lounis, S. D.; Runnerstrom, E. L.; Milliron, D. J.; Gamelin, D. R. Redox Chemistries and Plasmon Energies of Photodoped In_2O_3 and Sn-Doped In_2O_3 (ITO) Nanocrystals. *J. Am. Chem. Soc.* **2015,** *137*, 518-524.
4. Buonsanti, R.; Llordes, A.; Aloni, S.; Helms, B. A.; Milliron, D. J. Tunable Infrared Absorption and Visible Transparency of Colloidal Aluminum-Doped Zinc Oxide Nanocrystals. *Nano Lett.* **2011,** *11*, 4706-4710.
5. Gordon, T. R.; Paik, T.; Klein, D. R.; Naik, G. V.; Caglayan, H.; Boltasseva, A.; Murray, C. B. Shape-Dependent Plasmonic Response and Directed Self-Assembly in a New Semiconductor Building Block, Indium-Doped Cadmium Oxide (ICO). *Nano Lett.* **2013,** *13*, 2857-2863.
6. Ye, X.; Fei, J.; Diroll, B. T.; Paik, T.; Murray, C. B. Expanding the Spectral Tunability of Plasmonic Resonances in Doped Metal-Oxide Nanocrystals through Cooperative Cation–Anion Codoping. *J. Am. Chem. Soc.* **2014,** *136*, 11680-11686.
7. Luther, J. M.; Jain, P. K.; Ewers, T.; Alivisatos, A. P. Localized Surface Plasmon Resonances arising from Free Carriers in Doped Quantum Dots. *Nat. Mater.* **2011,** *10*, 361-366.
8. Dorfs, D.; Härtling, T.; Miszta, K.; Bigall, N. C.; Kim, M. R.; Genovese, A.; Falqui, A.; Povia, M.; Manna, L. Reversible Tunability of the Near-Infrared Valence Band Plasmon Resonance in $Cu_{2-x}Se$ Nanocrystals. *J. Am. Chem. Soc.***2011,** *133*, 11175-11180.
9. Manthiram, K.; Alivisatos, A. P. Tunable Localized Surface Plasmon Resonances in Tungsten Oxide Nanocrystals. *J. Am. Chem. Soc.* **2012,** *134*, 3995-3998.
10. Kriegel, I.; Jiang, C.; Rodríguez-Fernández, J.; Schaller, R. D.; Talapin, D. V.; da Como, E.; Feldmann, J. Tuning the Excitonic and Plasmonic Properties of Copper Chalcogenide Nanocrystals. *J. Am. Chem. Soc.* **2012,** *134*, 1583-1590.
11. Rowe, D. J.; Jeong, J. S.; Mkhoyan, K. A.; Kortshagen, U. R. Phosphorus-Doped Silicon Nanocrystals Exhibiting Mid-Infrared Localized Surface Plasmon Resonance. *Nano Lett.* **2013,** *13*, 1317-1322.
12. Polking, M. J.; Jain, P. K.; Bekenstein, Y.; Banin, U.; Millo, O.; Ramesh, R.; Alivisatos, A. P. Controlling Localized Surface Plasmon Resonances in GeTe Nanoparticles Using an Amorphous-to-Crystalline Phase Transition. *Phys. Rev. Lett.* **2013,** *111* (3), 037401.
13. Schimpf, A. M.; Thakkar, N.; Gunthardt, C. E.; Masiello, D. J.; Gamelin, D. R. Charge-Tunable Quantum Plasmons in Colloidal Semiconductor Nanocrystals. *ACS Nano* **2014,** *8*, 1065-1072.
14. Faucheaux, J. A.; Stanton, A. L. D.; Jain, P. K. Plasmon Resonances of Semiconductor Nanocrystals: Physical Principles and New Opportunities. *J. Phys. Chem. Lett.* **2014,** *5*, 976-985.
15. Kovalenko, M. V.; Manna, L.; Cabot, A.; Hens, Z.; Talapin, D. V.; Kagan, C. R.; Klimov, V. I.; Rogach, A. L.; Reiss, P.; Milliron, D. J.; Guyot-Sionnnest, P.; Konstantatos, G.; Parak, W. J.; Hyeon, T.; Korgel, B. A.; Murray, C. B.; Heiss, W. Prospects of Nanoscience with Nanocrystals. *ACS Nano* **2015,** *9*, 1012-1057.
16. Pradhan, N.; Das Adhikari, S.; Nag, A.; Sarma, D. D. Luminescence, Plasmonic, and Magnetic Properties of Doped Semiconductor Nanocrystals. *Angew. Chem. Int. Ed.* **2017,** *56*, 7038-7054.

17. Wang, H.; Brandl, D. W.; Nordlander, P.; Halas, N. J. Plasmonic Nanostructures: Artificial Molecules. *Acc. Chem. Res.* **2007,** *40*, 53-62.
18. Hamberg, I.; Granqvist, C. G. Optical Properties of Transparent and Heat-reflecting Indium Tin Oxide Films: The Role of Ionized Impurity Scattering. *Appl. Phys. Lett.* **1984,** *44*, 721-723.
19. Hamberg, I.; Granqvist, C. G. Evaporated Sn-doped In_2O_3 films: Basic Optical Properties and Applications to Energy-Efficient Windows. *J. Appl. Phys.* **1986,** *60*, R123-R160.
20. Zhang, D. H.; Ma, H. L. Scattering Mechanisms of Charge Carriers in Transparent Conducting Oxide Films. *Appl. Phys. A* **1996,** *62*, 487-492.
21. Buonsanti, R.; Milliron, D. J. Chemistry of Doped Colloidal Nanocrystals. *Chem. Mater.* **2013,** *25*, 1305-1317.
22. Lounis, S. D.; Runnerstrom, E. L.; Llordés, A.; Milliron, D. J. Defect Chemistry and Plasmon Physics of Colloidal Metal Oxide Nanocrystals. *J. Phys. Chem. Lett.* **2014,** *5*, 1564-1574.
23. Haes, A. J.; Hall, W. P.; Chang, L.; Klein, W. L.; Van Duyne, R. P. A Localized Surface Plasmon Resonance Biosensor: First Steps toward an Assay for Alzheimer's Disease. *Nano Lett.* **2004,** *4*, 1029-1034.
24. Jain, P. K.; Huang, X.; El-Sayed, I. H.; El-Sayed, M. A. Noble Metals on the Nanoscale: Optical and Photothermal Properties and Some Applications in Imaging, Sensing, Biology, and Medicine. *Acc. Chem. Res.* **2008,** *41*, 1578-1586.
25. Sannomiya, T.; Hafner, C.; Voros, J. In situ Sensing of Single Binding Events by Localized Surface Plasmon Resonance. *Nano Lett.* **2008,** *8*, 3450-3455.
26. Verellen, N.; Van Dorpe, P.; Huang, C.; Lodewijks, K.; Vandenbosch, G. A. E.; Lagae, L.; Moshchalkov, V. V. Plasmon Line Shaping Using Nanocrosses for High Sensitivity Localized Surface Plasmon Resonance Sensing. *Nano Lett.* **2011,** *11*, 391-397.
27. Ding, I. K.; Zhu, J.; Cai, W.; Moon, S.-J.; Cai, N.; Wang, P.; Zakeeruddin, S. M.; Grätzel, M.; Brongersma, M. L.; Cui, Y.; McGehee, M. D. Plasmonic Dye-Sensitized Solar Cells. *Adv. Energy Mater.* **2011,** *1*, 52-57.
28. Liu, X.; Lee, C.; Law, W.-C.; Zhu, D.; Liu, M.; Jeon, M.; Kim, J.; Prasad, P. N.; Kim, C.; Swihart, M. T. Au–Cu_{2-x}Se Heterodimer Nanoparticles with Broad Localized Surface Plasmon Resonance as Contrast Agents for Deep Tissue Imaging. *Nano Lett.* **2013,** *13*, 4333-4339.
29. Bhachu, D. S.; Scanlon, D. O.; Sankar, G.; Veal, T. D.; Egdell, R. G.; Cibin, G.; Dent, A. J.; Knapp, C. E.; Carmalt, C. J.; Parkin, I. P. Origin of High Mobility in Molybdenum-Doped Indium Oxide. *Chem. Mater.* **2015,** *27*, 2788-2796.
30. Runnerstrom, E. L.; Bergerud, A.; Agrawal, A.; Johns, R. W.; Dahlman, C. J.; Singh, A.; Selbach, S. M.; Milliron, D. J. Defect Engineering in Plasmonic Metal Oxide Nanocrystals. *Nano Lett.* **2016,** *16*, 3390-3398.
31. Hanbing Fang, Manu Hegde, Penghui Yin, and Pavle V. Radovanovic Tuning Plasmon Resonance of In_2O_3 Nanocrystals throughout the Mid-Infrared Region by Competition between Electron Activation and Trapping *Chem. Mater.*, **2017**, *29*, 4970–4979.
32. Johns, R. W.; Bechtel, H. A.; Runnerstrom, E. L.; Agrawal, A.; Lounis, S. D.; Milliron, D. J. Direct Observation of Narrow Mid-Infrared Plasmon Linewidths of Single Metal Oxide Nanocrystals *Nat. Commun.* **2016,** *7*, 11583.
33. Della Gaspera, E.; Bersani, M.; Cittadini, M.; Guglielmi, M.; Pagani, D.; Noriega, R.; Mehra, S.; Salleo, A.; Martucci, A. Low-Temperature Processed Ga-Doped ZnO Coatings from Colloidal Inks. *J. Am. Chem. Soc.* **2013,** *135*, 3439-3448.
34. Ghosh, S.; Saha, M.; Dev Ashok, V.; Dalal, B.; De, S. K. Tunable Surface Plasmon Resonance in Sn-Doped Zn–Cd–O Alloyed Nanocrystals. *J. Phys. Chem. C* **2015,** *119*, 1180-1187.

35. Askari, S.; Mariotti, D.; Stehr, J. E.; Benedikt, J.; Keraudy, J.; Helmersson, U. Low-Loss and Tunable Localized Mid-Infrared Plasmons in Nanocrystals of Highly Degenerate InN. *Nano Lett.* **2018,** *18*, 5681-5687.
36. Tandon, B.; Shanker, G. S.; Nag, A. Multifunctional Sn- and Fe-Codoped In_2O_3 Colloidal Nanocrystals: Plasmonics and Magnetism. *J. Phys. Chem. Lett.* **2014,** *5*, 2306-2311.
37. Shanker, G. S.; Tandon, B.; Shibata, T.; Chattopadhyay, S.; Nag, A. Doping Controls Plasmonics, Electrical Conductivity, and Carrier-Mediated Magnetic Coupling in Fe and Sn Codoped In_2O_3 Nanocrystals: Local Structure Is the Key. *Chem. Mater.* **2015,** *27*, 892-900.
38. Tandon, B.; Yadav, A.; Nag, A. Delocalized Electrons Mediated Magnetic Coupling in Mn–Sn Codoped In_2O_3 Nanocrystals: Plasmonics Shows the Way. *Chem. Mater.* **2016,** 28, 3620-3624.
39. Yadav, A.; Tandon, B.; Nag, A. Reduction of Mn^{3+} to Mn^{2+} and Near Infrared Plasmonics from Mn-Sn Codoped In_2O_3 Nanocrystals. *RSC Adv.* **2016,** *6*, 79153-79159.
40. Raebiger, H.; Lany, S.; Zunger, A. Electronic Structure, Donor and Acceptor Transitions, and Magnetism of 3d Impurities in In_2O_3 and ZnO. *Phys. Rev. B* **2009,** *79*, 165202.
41. Alippi, P.; Cesaria, M.; Fiorentini, V. Impurity-Vacancy Complexes and Ferromagnetism in Doped Sesquioxides. *Phys. Rev. B* **2014,** *89* (13), 134423.
42. Jansons, A. W.; Hutchison, J. E. Continuous Growth of Metal Oxide Nanocrystals: Enhanced Control of Nanocrystal Size and Radial Dopant Distribution. *ACS Nano* **2016,** *10*, 6942-6951.
43. Yeh, J. J.; Lindau, I. Atomic Subshell Photoionization Cross Sections and Asymmetry Parameters: $1 \leqslant Z \leqslant 103$. *At. Data Nucl. Data Tables* **1985,** *32*, 1-155.
44. Sarma, D. D.; Santra, P. K.; Mukherjee, S.; Nag, A. X-ray Photoelectron Spectroscopy: A Unique Tool To Determine the Internal Heterostructure of Nanoparticles. *Chem. Mater.* **2013,** *25*, 1222-1232.
45. Mendelsberg, R. J.; Garcia, G.; Li, H.; Manna, L.; Milliron, D. J. Understanding the Plasmon Resonance in Ensembles of Degenerately Doped Semiconductor Nanocrystals. *J. Phys. Chem. C* **2012,** *116*, 12226-12231.
46. Gerfin, T.; Grätzel, M. Optical Properties of Tin-doped Indium Oxide determined by Spectroscopic Ellipsometry. *J. Appl. Phys.* **1996,** *79*, 1722-1729.
47. Ghosh, S. K.; Pal, T. Interparticle Coupling Effect on the Surface Plasmon Resonance of Gold Nanoparticles: From Theory to Applications. *Chem. Rev.* **2007,** *107*, 4797-4862.
48. Shannon, R. D.; Prewitt, C. T. Effective Ionic Radii in Oxides and Fluorides. *Acta Crystallogr. Sect. B* **1969,** *25*, 925-946.
49. Vegard, L. Die Konstitution der Mischkristalle und die Raumfüllung der Atome. *Z. Phys.* **1921,** *5*, 17-26.
50. Frank, G.; Köstlin, H. Electrical Properties and Defect Model of Tin-doped Indium Oxide Layers. *Appl. Phys. A* **1982,** *27*, 197-206.
51. Nadaud, N.; Lequeux, N.; Nanot, M.; Jové, J.; Roisnel, T. Structural Studies of Tin-Doped Indium Oxide (ITO) and $In_4Sn_3O_{12}$. *J. Solid State Chem.* **1998,** *135*, 140-148.
52. Brewer, S. H.; Franzen, S. Calculation of the Electronic and Optical Properties of Indium Tin Oxide by Density Functional Theory. *Chem. Phys.* **2004,** *300*, 285-293.
53. Patterson, A. L. The Scherrer Formula for X-Ray Particle Size Determination. *Phys. Rev.* **1939,** *56*, 978-982.
54. Schwartz, D. A.; Norberg, N. S.; Nguyen, Q. P.; Parker, J. M.; Gamelin, D. R. Magnetic Quantum Dots: Synthesis, Spectroscopy, and Magnetism of Co^{2+}- and Ni^{2+}-Doped ZnO Nanocrystals. *J. Am. Chem. Soc.* **2003,** *125*, 13205-13218.

55. Tuinenga, C.; Jasinski, J.; Iwamoto, T.; Chikan, V. In Situ Observation of Heterogeneous Growth of CdSe Quantum Dots: Effect of Indium Doping on the Growth Kinetics. *ACS Nano* **2008,** *2*, 1411-1421.
56. Yang, Y.; Jin, Y.; He, H.; Wang, Q.; Tu, Y.; Lu, H.; Ye, Z. Dopant-Induced Shape Evolution of Colloidal Nanocrystals: The Case of Zinc Oxide. *J. Am. Chem. Soc.* **2010,** *132*, 13381-13394.
57. Wang, T.; Radovanovic, P. V. Free Electron Concentration in Colloidal Indium Tin Oxide Nanocrystals Determined by Their Size and Structure. *J. Phys. Chem. C* **2011,** *115*, 406-413.
58. De Trizio, L.; Buonsanti, R.; Schimpf, A. M.; Llordes, A.; Gamelin, D. R.; Simonutti, R.; Milliron, D. J. Nb-Doped Colloidal TiO_2 Nanocrystals with Tunable Infrared Absorption. *Chem. Mater.* **2013,** *25*, 3383-3390.
59. Guria, A. K.; Pradhan, N. Doped or Not Doped: Ionic Impurities for Influencing the Phase and Growth of Semiconductor Nanocrystals. *Chem. Mater.* **2016,** *28*, 5224-5237.
60. Bryan, J. D.; Gamelin, D. R. Doped Semiconductor Nanocrystals: Synthesis, Characterization, Physical Properties, and Applications. In *Progress in Inorganic Chemistry*, John Wiley & Sons, Inc.: **2005**, 47-126.
61. Ba, J.; Fattakhova Rohlfing, D.; Feldhoff, A.; Brezesinski, T.; Djerdj, I.; Wark, M.; Niederberger, M. Nonaqueous Synthesis of Uniform Indium Tin Oxide Nanocrystals and Their Electrical Conductivity in Dependence of the Tin Oxide Concentration. *Chem. Mater.* **2006,** *18*, 2848-2854.
62. Wang, S.; An, Y.; Feng, D.; Wu, Z.; Liu, J. The Local Structure, Magnetic, and Transport Properties of Cr-doped In_2O_3 Films. *J. Appl. Phys.* **2013,** *113*, 153901.
63. Thermo Fischer Scientific XPS Tutorial www.xpssimplified.com
64. Pujilaksono, B.; Klement, U.; Nyborg, L.; Jelvestam, U.; Hill, S.; Burgard, D. X-ray Photoelectron Spectroscopy Studies of Indium Tin Oxide Nanocrystalline Powder. *Mater. Charact.* **2005,** *54*, 1-7.
65. Xing, G. Z.; Yi, J. B.; Wang, D. D.; Liao, L.; Yu, T.; Shen, Z. X.; Huan, C. H. A.; Sum, T. C.; Ding, J.; Wu, T. Strong Correlation between Ferromagnetism and Oxygen Deficiency in Cr-doped In_2O_3 Nanostructures. *Phys. Rev. B* **2009,** *79*, 174406.
66. Mirzaee, M.; Dolati, A. Effect of Cr Doping on the Structural, Morphological, Optical and Electrical Properties of Indium Tin Oxide Films. *Appl. Phys. A* **2015,** *118*, 953-960.
67. Ravi, V. K.; Santra, P. K.; Joshi, N.; Chugh, J.; Singh, S. K.; Rensmo, H.; Ghosh, P.; Nag, A. Origin of the Substitution Mechanism for the Binding of Organic Ligands on the Surface of $CsPbBr_3$ Perovskite Nanocubes. *J. Phys. Chem. Lett.* **2017**, *8*, 4988-4994.
68. Warschkow, O.; Ellis, D. E.; González, G. B.; Mason, T. O. Defect Cluster Aggregation and Nonreducibility in Tin-Doped Indium Oxide. *J. Am. Ceram. Soc.* **2003,** *86*, 1707-1711.
69. Mason, T. O.; Gonzalez, G. B.; Hwang, J. H.; Kammler, D. R. Point Defects and related Properties of Highly Co-doped Bixbyite In_2O_3. *Phys. Chem. Chem. Phys.* **2003,** *5*, 2183-2189.
70. González, G. B.; Mason, T. O.; Okasinski, J. S.; Buslaps, T.; Honkimäki, V. Determination of the Solubility of Tin in Indium Oxide Using In Situ and Ex Situ X-Ray Diffraction. *J. Am. Ceram. Soc.* **2012,** *95*, 809-815.
71. Cox, P. A.; Flavell, W. R.; Egdell, R. G. Solid-state and Surface Chemistry of Sn-doped In_2O_3 Ceramics. *J. Solid State Chem.* **1987,** *68*, 340-350.
72. Gassenbauer, Y.; Klein, A. Electronic Surface Properties of RF-magnetron Sputtered In_2O_3:Sn. *Solid State Ion.* **2004,** *173*, 141-145.

73. Gassenbauer, Y.; Schafranek, R.; Klein, A.; Zafeiratos, S.; Hävecker, M.; Knop-Gericke, A.; Schlögl, R. Surface States, Surface Potentials, and Segregation at Surfaces of Tin-doped In_2O_3 *Phys. Rev. B* **2006,** *73*, 245312.
74. González, G. B.; Mason, T. O.; Quintana, J. P.; Warschkow, O.; Ellis, D. E.; Hwang, J.-H.; Hodges, J. P.; Jorgensen, J. D. Defect Structure Studies of Bulk and Nano Indium Tin Oxide. *J. Appl. Phys.* **2004,** *96*, 3912-3920.
75. Crockett, B. M.; Jansons, A. W.; Koskela, K. M.; Johnson, D. W.; Hutchison, J. E. Radial Dopant Placement for Tuning Plasmonic Properties in Metal Oxide Nanocrystals. *ACS Nano* **2017,** *11*, 7719-7728.
76. Mergel, D.; Qiao, Z. Correlation of Lattice Distortion with Optical and Electrical Properties of In_2O_3:Sn Films. *J. Appl. Phys.* **2004,** *95*, 5608-5615.
77. Valla, A.; Carroy, P.; Ozanne, F.; Muñoz, D. Understanding the Role of Mobility of ITO Films for Silicon Heterojunction Solar Cell Applications. *Sol. Energy Mater. Sol. Cells* **2016,** *157*, 874-880.
78. Fang, P. H.; Brower, W. S. Dielectric Constant of Cr_2O_3 Crystals. *Phys. Rev.* **1963,** *129*, 1561-1561.
79. Abdullah, M. M.; Rajab, F. M.; Al-Abbas, S. M. Structural and Optical Characterization of Cr_2O_3 Nanostructures: Evaluation of its Dielectric Properties. *AIP Adv.* **2014,** *4*, 027121.

Chapter-4B

Dopant Selection Strategy for High LSPR Quality Factor from Doped In_2O_3 Nanocrystals

---

The work presented in this chapter was carried out under the supervision of Prof. Delia J. Milliron at the University of Texas at Austin, USA.

Summary

The performance of degenerately doped metal oxide nanocrystals (NCs) exhibiting localized surface plasmon resonance (LSPR) is frequently judged by its figure of merit known as the quality factor (Q-factor), defined as the ratio of the LSPR peak energy to its full width at half maximum (FWHM). However, the aliovalent dopants generating the free charge carriers (increasing LSPR energy), and responsible for the LSPR response in the first place, also serve as centers of ionized impurity scattering (decreasing FWHM). Thus, low Q-factors associated with lossy, broadband LSPR response are obtained which limits their application requiring concentration of light in small regions of space (hot spots). Appropriate dopant selection becomes of paramount importance in such scenarios. Here, we describe the properties of an aliovalent cationic dopant that would facilitate its selection for both high dopant activation and low LSPR FWHM and subsequently, high LSPR Q-factor. We then utilize the same properties to identify Zr^{4+} as a model aliovalent dopant for high LSPR Q-factor in In_2O_3 lattice. The resulting Zr-doped In_2O_3 NCs show one of the best LSPR Q-factors reported in the literature while also performing equivalently to the recognized materials for high dopant activation (Sn-doped In_2O_3 NCs) and low LSPR FWHM (Ce-doped In_2O_3 NCs), simultaneously. Drude model fits to the LSPR spectra reveals that the carrier mobility of 57 $cm^2V^{-1}s^{-1}$ in Zr-doped In_2O_3 NCs is almost 3 times that of Sn-doped In_2O_3 NCs and similar to the undoped In_2O_3 NCs which advocates a drastic reduction in the scattering of charge carriers. We found that the optimized position of Zr donor level in the conduction band of In_2O_3 coupled with the surface segregated Zr doping allows us to achieve of low levels of carrier scattering, leading to high carrier mobilities and, the combination of low carrier scattering with high dopant activation of Zr^{4+} ions is responsible for the high LSPR Q-factors. The understanding provided in the manuscript can be used to design a variety of doped metal oxide systems for high Q-factor LSPR.

Graphical Abstract

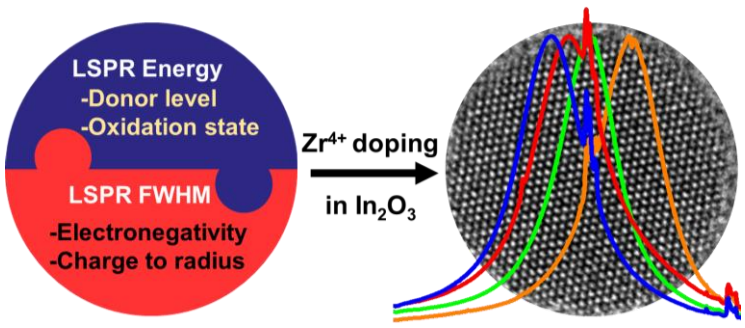

4B.1 Introduction

Degenerately doped metal oxide nanocrystals (NCs) exhibit mid- to near-infrared (MIR/NIR) localized surface plasmon resonance (LSPR) among many composition-dependent intriguing phenomena.[1-6] The LSPR response is induced by the generation of free charge carriers (electrons in case of n-doped metal oxides) which collectively oscillate at resonant frequencies. These LSPR active NCs find applications in sensing,[7-9] photothermal therapy,[10] photovoltaics,[11] electrochromic coatings,[12-14] and advanced spectroscopies.[1] Furthermore, these NCs are especially well-suited for applications requiring the formation of intense localized electric fields (hot spots) around them. The efficiency of this hot spot generation can be assessed by the figure of merit of LSPR, known as the Quality factor (or Q-factor) and is defined as the ratio of the LSPR peak energy and its full width at half maximum (FWHM). Here, the LSPR peak energy is a measure of the carrier density accumulation in the NCs, while the FWHM reflects the extent of carrier scattering mainly by the charged point defects in the NC lattice.[15] Consequently, a high Q-factor signifies stronger near-field enhancements, longer plasmon lifetimes and weaker electronic damping.

In some cases, the relatively high value of the high-frequency dielectric constant of the host material enables unusually high LSPR Q-factors, through shielding the electrostatic interactions between the dopants and the electrons. This is generally the case for doped CdO,[16] such as NCs of In-doped CdO,[17] and F-In codoped CdO.[18] However, disregarding the dielectric characteristics of the host material, the onus to generate a high LSPR Q-factor customarily falls on the selection of the aliovalent dopant.[15] This requires identification of the fundamental properties of a dopant that affect both the LSPR energy and the FWHM, which should facilitate high LSPR Q-factors in a NC host lattice of choice.

LSPR energy ω_{LSPR} can be estimated from equation (1)

$$\omega_{LSPR} = \sqrt{\frac{\omega_P^2}{(\varepsilon_\infty + 2\varepsilon_m)} - \gamma^2} \quad (1)$$

where ε_∞ is the high-frequency dielectric constant of the material, ε_m is the dielectric constant of the medium surrounding the NCs and γ is the damping constant. Since, ε_∞ is a characteristic property of the material that isn't expected to change with small amount of doping and ε_m is fixed by the solvent of dispersion, LSPR energy is largely determined by the damping constant (that determines LSPR FWHM) and the bulk plasma frequency ω_P which is given by,

$$\omega_p^2 = \frac{ne^2}{\varepsilon_0 m^*} \qquad (2)$$

where n is the carrier density, e is the electronic charge, ε_o is the permittivity of air/vacuum and m^* is the effective mass of the free charge carriers (electrons/holes).[19] Since e and ε_o are constants, the LSPR energy is directly dependent on the carrier density and the effective carrier mass. This electron density can be generated by two types of dopants (a) when the dopant state exists close to the conduction band minimum (CBM), a shallow donor, and (b) when the dopant states reside inside the conduction band of the host. However, a shallow donor (such as Sn in In_2O_3) hybridizes with the CBM triggering renormalization of band curvature and therefore a flatter band with higher effective carrier mass is obtained.[20] This ultimately leads to a lower ω_P and hence, a donor level inside the conduction is preferred over a shallow donor for generation of carrier density.[20-22] Nevertheless, this generation of carrier density by a donor gets hindered if the dopant exhibits multiple oxidation states or electron acceptor species are present in the vicinity.[22-26] This is highly undesirable as it decreases the dopant activation (number of electrons generated per dopant). The requirement of single oxidation state is thus an essential one, considering that a dopant does not always contribute to the generation of free charge carrier density in the host lattice due to detrimental factors like formation of irreducible clusters.[27-30] One can estimate the feasibility of change in oxidation state through the standard reduction potentials. Metal ions exhibiting multiple oxidation states with large positive values of standard reduction potentials are not likely to perform as ideal dopants for generation of electron density. For example, the standard reduction potential for reduction of Ce^{4+} to Ce^{3+} is +1.44 V[31] as a result of which Ce^{4+} doping in In_2O_3 suffers with the problem of low dopant activation.[22]

On a different note, electron scattering mechanisms such as electron-electron, electron-phonon and phonon-phonon scattering prominent in noble metal NCs are not dominant in doped metal oxide NCs. The major electron scattering mechanism in doped metal oxide NCs is attributed to electrostatic interactions between the dopant ions and the electrons. This phenomenon is known as ionized impurity scattering,[15] and the LSPR FWHM is determined by the strength of this electrostatic interaction. Therefore, to decrease the LSPR FWHM, the strength of these electrostatic interaction can be decreased. This can be done by (a) employing a dopant with a high charge to radius ratio which increases covalency in the interaction (b) employing a dopant with low electronegativity value than the host cation. A smaller electronegativity value than the host

cation ensures that the interactions between the free electrons and dopant cations are minimized. In terms of electronic band structure, this means that the dopant levels assume a higher energy position with respect to the CBM of the host lattice. It is due to this reason, Ce with a low χ value leads to much smaller LSPR FWHM than Sn, [22, 32] despite Sn exhibiting a higher charge to radius ratio.[33] Hence, to obtain a low LSPR FWHM in the lattice of In_2O_3, a dopant with a charge-to-radius ratio greater than In and an electronegativity value smaller than In is desired. However, a large change in charge to radius ratio with respect to the host cation can also bring significant lattice strain in the host lattice and may lead to the formation of a secondary phase.

Adapting the aforementioned understanding to the In_2O_3 lattice identifies Zr^{4+} as a dopant capable of exhibiting all the desirable characteristics discussed above. Zr is almost always found in the +4 oxidation state (standard reduction potential Zr^{4+}/Zr = -1.45 V)[31] which makes it an aliovalent dopant in the In_2O_3 lattice. Recent calculations by Xu et al. have shown that donor levels for Zr lie deep inside the conduction band (mostly due to its lower electronegativity relative to In) and proposed it to be a prospective dopant of choice for high mobility transparent conducting oxides.[20] The occurrence of Zr donor levels deep inside the conduction band means that the curvature of CBM is not affected and electrons generated will have a low carrier effective mass of $0.22m_e$ as that of the parent In_2O_3 lattice. Moreover, the ionic radius of Zr^{4+} (74 pm) matches with that of In^{3+} (79 pm) signifying that no substantial lattice strain is anticipated from the substitution of In with Zr.[34] We, therefore, hypothesized that Zr doping in In_2O_3 NCs can lead to a high Q-factor LSPR with high dopant activation and low FWHM, which will also be reflected as increased mobility of electrons inside the lattice. Prior experimental reports showing high electron mobilities in Zr-doped In_2O_3 thin films,[35-37] encouraged us further to synthesize Zr-doped In_2O_3 NCs and examine their mettle as an LSPR active material.

4B.2 Experimental Section

4B.2.1 Synthesis of Zr-doped and Zr-Sn codoped In_2O_3 NCs

Different Zr-doped In_2O_3, Sn-doped In_2O_3, and Sn-Zr codoped In_2O_3 NCs were synthesized by minor modifications of the slow-injection synthetic procedure developed by the Hutchison group.[38] Using standard Schlenk line techniques, a 0.5M mixture of In and Zr precursors in 10 mL oleic acid was degassed at 100˚C under vacuum conditions which was followed by an undisturbed heating and vigorous stirring at 150˚C under N_2 atmosphere for 2 hours. 8 mL of this mixture was

subsequently injected into an already degassed 13mL solution of oleyl alcohol kept at 290℃ (under N_2 conditions) at the rate of 0.2 mL/min using a syringe pump. NCs were separated from the reaction mixture impurities by repeatedly precipitating with ethanol, centrifugation at 9000 rpm for 5 min and re-dispersing in hexane before finally being prepared as a colloidal solution of NCs in hexane. Same synthesis protocol was followed for Sn-doped In_2O_3 NCs and Sn-Zr codoped In_2O_3 NCs.

For different Zr doping percentages, the amount of Zr and In precursor was varied accordingly. It is customary to note here that the incorporation of Zr in In_2O_3 has been found to be difficult under the aforementioned experimental conditions. With the slow-injection synthesis strategy adopted here, Zr doping efficiency was limited at approximately 25%. Therefore, to synthesize 1.3% Zr-doped In_2O_3 NCs, 0.25 mmol of zirconium(IV) acetylacetonate was mixed with 4.75 mmol of indium(III) acetate in 10 mL oleic acid. Similar calculations can be performed for other Zr doping percentages in both Zr-doped In_2O_3 NCs and Sn-Zr codoped In_2O_3 NCs with tin(IV) acetate as Sn precursor while keeping in consideration that irrespective of the target composition, the total metal concentration in the solution should be 0.5 M.

4B.2.2 Nanocrystal characterization

X-ray diffraction (XRD): For determining the crystal structure and phase purity using XRD, as-synthesized NCs were drop-casted on a small piece of Si wafer. Powder XRD patterns were then obtained through a Rigaku Miniflex 600 instrument operating in a Bragg-Brentano geometry with Cu Kα (λ = 1.5406 Å) as the x-ray source. The same samples were also used in the x-ray photoelectron spectroscopy (XPS).

Raman Spectroscopy: Presence of an amorphous ZrO_2/In_2O_3 phase and other impurities undetected in powder- XRD was checked via a Horiba LabRAM Aramis instrument equipped with a confocal aperture. Samples were prepared by drop-casting a solution of Zr-doped In_2O_3 NCs on 2x2 glass slide followed by air-drying. All Raman spectra were obtained with a ×50 microscope objective at an excitation wavelength of 532 nm and an acquisition time of 180 s.

Transmission electron microscopy (TEM): Size and morphology of the NCs were examined using a low-resolution scanning TEM (STEM). Sample preparation for STEM involved drop-casting and subsequently air-drying 20 μL dilute solution of NCs in hexane (~15 mg/mL of NCs

in 1mL hexane) on the copper TEM grid. STEM micrographs were obtained on a Hitachi S5500 operating at an accelerating voltage of 30 mV in the STEM mode. The average diameter and standard deviation in sizes of different NCs were obtained by analyzing 100 particles from their respective STEM image using ImageJ software and fitting the statistics to a Gaussian size distribution. High-resolution TEM (HRTEM) images of the same NCs were obtained on a JEOL 2010F TEM operating at 200 kV accelerating voltage.

Inductively coupled plasma-atomic emission spectroscopy (ICP-AES): Doping percentages of Zr and/or Sn in In_2O_3 were experimentally attained by employing ICP-AES technique on a Varian 720-ES ICP Optical Emission Spectrometer. Samples for the ICP-AES were prepared by digesting 1-2mg of the powder NCs in aqua-regia solution (a mixture of 35% concentrated HCl and 70% HNO_3 in 3:1 ratio respectively) for 24 hours. This was followed by diluting the acid solution with milli-Q water such that the total acid concentration becomes approximately 2% v/v. Standard solutions of variable concentration for different elements were prepared by diluting the commercial ICP-AES standard with 2% HNO_3 solution in milli-Q water.

X-ray photoelectron spectroscopy (XPS): To develop an understanding about the oxidation state of different elements and their doping percentages within the NCs, XPS spectra of different NCs was recorded on a Kratos X-ray Photoelectron Spectrometer – Axis Ultra DLD using a monochromatic Al Kα radiation (λ = 1486.6 eV) and a charge neutralizer. The XPS spectra obtained for different elements were carbon corrected by fixing the adventitious C1s peak to 284.8 eV and analyzed through CasaXPS software. Doping percentages for Zr and/or Sn were calculated by taking a ratio of the integrated area under the Zr 3d peak and/or Sn 3d peak with that under the In 3d, Zr 3d and Sn 3d XPS peaks while taking into consideration the sensitivity factors of the different elements involved.

Optical Absorption Spectroscopy: The optical extinction spectra of different NCs which helped us to visualize the LSPR bands of different Zr-doped In_2O_3 NCs were collected through FTIR liquid cell in a Bruker Vertex 70 FTIR. The dispersion of NCs in tetrachloroethylene was injected through a syringe in the liquid cell between two IR transparent KBr windows separated by a path length of 0.5 mm. For highly doped Sn-doped In_2O_3 NCs and Sn-Zr codoped In_2O_3 NCs, NIR absorption spectra was recorded in Agilent Cary 5000 spectrophotometer using quartz cuvette with a path length of 10 mm.

Frequency-dependent and frequency-independent Drude Modeling: The electric field of the incoming electromagnetic radiation interacts with the total electron density present in the material, in a form of light-matter interaction. The essence of polarization of conduction and valence band electrons by the external electric field is recorded by the complex dielectric function which ultimately governs the optical properties of the material. Since LSPR has contribution only from conduction band electrons (free electrons), the frequency-dependent complex dielectric function ε_D can be defined just by the contribution of free electrons, given by the simple Drude model

$$\varepsilon_D(\omega) = \varepsilon_\infty - \frac{\omega_p^2}{\omega^2 - i\omega\Gamma} \qquad (3)$$

Where ε_∞ is the high-frequency dielectric constant for the material (taken as 3.9 for all NCs), ω_P is the bulk plasma frequency given by equation (2) and Γ is the frequency-independent damping constant.

$$\omega_p^2 = \frac{ne^2}{\varepsilon_0 m^*} \qquad (2)$$

here, *n* is the free carrier density in the material (per cm^3), *e* is the electronic charge, ε_0 is the dielectric permittivity of vacuum and *m** is the effective mass of the carrier.

However, the simple Drude model is valid only when the damping of charge carriers occurs by a frequency-independent mechanism such as electron-electron scattering, electron-photon scattering or phonon-phonon scattering. This is not the case with doped semiconductors as the scattering of charge carriers takes place majorly through the ionized impurity scattering where the electric field experienced by the charge carrier is different above and below the bulk plasma frequency.[15, 19]

To take into account the frequency-dependent scattering of charge carriers, an extended Drude model is proposed where the essence of frequency-dependent carrier scattering is considered through an empirical equation

$$\Gamma(\omega) = \Gamma_L - \frac{\Gamma_L - \Gamma_H}{\pi}\left[tan^{-1}\left(\frac{\omega - \Gamma_X}{\Gamma_W}\right) + \frac{\pi}{2}\right] \qquad (4)$$

here $\Gamma(\omega)$ in the extended Drude model is the frequency-dependent analogue of the Γ (frequency-independent) in the simple Drude model. Γ_L and Γ_H are the low-frequency and high-frequency

damping constants respectively, Γ_X is the crossover-frequency from the low to high frequency region and Γ_W is the width of the crossover region.[32]

On a different note, the electric field at the surface of a NC extends to the space around it. Since NCs are well-separated from each other in a dilute solution, any near-field interaction between them can be negated, however, one can't completely rule far-field interactions between NCs and, interactions between the NCs and the solvent molecules. This could result in a change in the overall dielectric environment around the NCs thereby modifying its optical response to the incident electromagnetic radiation. We employed Maxwell-Garnett effective medium approximation (MG-EMA) which neglects near-field interactions between adjacent NCs (electronically linked to each other) but takes into account the far-field interactions between NCs and interaction between the NCs and the solvent molecules. Using MG-EMA, the effective dielectric function ε_{eff} is given by[39],

$$\frac{\varepsilon_{eff} - \varepsilon_H}{\varepsilon_{eff} + 2\varepsilon_H} = f_v \frac{\varepsilon_D - \varepsilon_H}{\varepsilon_D + 2\varepsilon_H} \qquad (5)$$

where ε_H is the dielectric medium of the solvent (2.26 for tetrachloroethylene), f_v is the volume fraction of NCs in the solution and ε_D is the complex dielectric function of the material as described before in equation (4). From equation (6), the absorbance of the solution can be approximated as $4\pi L\ \mathrm{Im}(\{\varepsilon_{eff}\}^{1/2})$ where Im (ε_{eff}) is the imaginary quotient of the effective dielectric function and L is the path length of the solution.

The MATLAB code developed by us combines

a) Equations (2), (3) and (5) for simple Drude model considering ω_P, Γ and f_v as floating parameters.

b) Equations (2)-(5) for extended Drude model considering ω_P, Γ_L, Γ_H, Γ_X, Γ_w and f_v as floating parameters, to model the absorbance of our NC solution. Multiple fits were performed for each sample to ensure that the parameter value obtained after fitting do not deviate drastically between different fits.

ω_P can then be used to calculate the free electron density in the NCs. We note here that for calculating the electron density, we used effective carrier mass of $0.22m_e$ for Zr-doped In_2O_3 NCs

as suggested by Xu et. al. and $0.39m_e$ for Sn-doped In_2O_3 and Sn-Zr codoped In_2O_3 NCs. Moreover, using the respective effective masses, one can optically derive DC mobility (μ_{opt}) of charge carriers in the material using equation 6.

$$\mu_{opt} = \frac{e}{m^*\Gamma} \qquad (6)$$

Even though the above equation is valid only for the simple Drude model (DC mobility has zero frequency and hence no frequency dependence), one can also employ it for the extended Drude model by using $\Gamma(0)$ in equation (4), i.e. damping constant at zero frequency. Average values of different parameters along with their standard deviation obtained from the extended Drude and simple Drude model have been tabulated in Table 4B.3 and Table 4B.4 respectively.

4B.3 Results and Discussion

4B.3.1 Structure and morphology

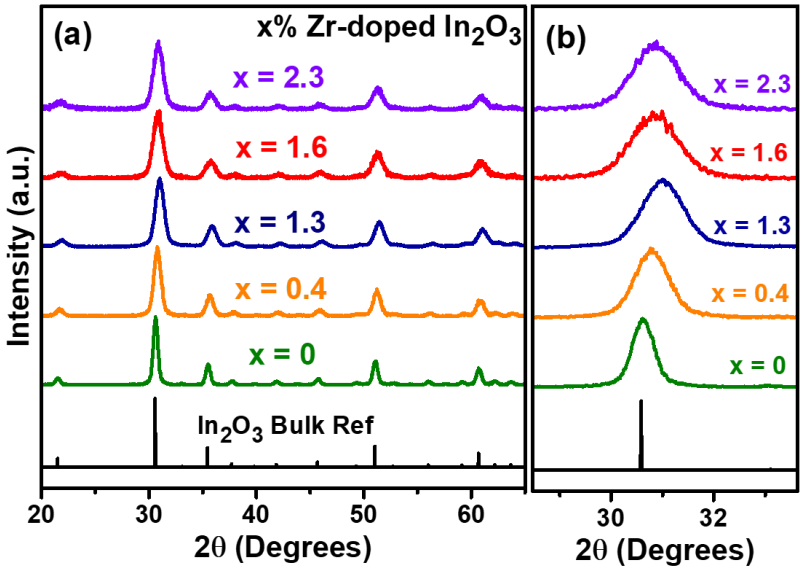

Figure 4B.1: (a) Comparison of powder XRD patterns of Zr-doped In_2O_3 NCs with bulk In_2O_3 reference suggesting retention of the cubic bixbyite structure for all NCs. (b) shift in the XRD peaks signifying lattice doping of Zr^{4+} ions.

The doping percentages reported herein have been obtained ICP-AES. Figure 4B.1a shows the XRD patterns of different Zr-doped In_2O_3 NCs with respect to the bulk reference of In_2O_3 (JCPDS 88-2160). It can be easily observed that all NCs (across different doping percentages) show the same cubic bixbyite structure as that of the parent In_2O_3 and no impurity peaks are present. Moreover, As the Zr doping percentage is increased, the diffraction peaks first shift to higher 2θ

values (signifying a decrease in the interplanar distances) and then shift back to smaller 2θ values resembling the interplanar distance of undoped In_2O_3 NCs (Figure 4B.1b). The ionic radius of Zr^{4+} is smaller than that of In^{3+} ion,[34] which should lead to a gradual decrease in the interplanar distances with an increase in the Zr doping percentage, in accordance with the Vegard's law.[40] Therefore, this trend might be interpreted as unsuccessful incorporation of Zr ions at higher doping percentages. However, such phenomena are of regular occurrence in the Sn-doped In_2O_3 literature and are attributed to the repulsion between the Sn^{4+} ions which cannot be compensated entirely by the electron density in the lattice.[41-43] We believe that a similar scenario is prevailing in the present case and despite the trend suggesting otherwise, Zr^{4+} ions are actually incorporated in the In_2O_3 lattice. This is further substantiated by the systematic increase in the FWHM of the XRD peaks with an increase in the Zr doping. This signifies a systematic decrease in the crystallite size with Zr doping, which would be difficult to materialize if Zr was a surface doped species.[44] We used Raman spectroscopy on the respective Zr-doped In_2O_3 NCs to check for the formation of any amorphous or impurity phases, shown in Figure 4B.2. All the Zr-doped In_2O_3 NCs exhibit the same phonon modes as that of undoped In_2O_3 NCs, signifying that no amorphous or crystalline impurity phases are present. [25, 45-46] Figure 4B.3a-e shows STEM images of different Zr-doped In_2O_3 NCs. As indicated by the XRD, the average diameter of NCs, in general, indeed decreases with an increase in the Zr doping percentage. The HRTEM image in Figure 4B.3f show the highly crystalline nature of Zr-doped In_2O_3 NCs and the interplanar distances corresponding to different lattice planes of In_2O_3.

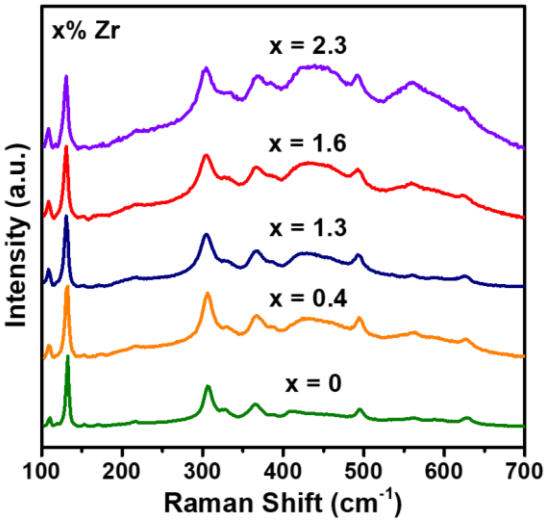

Figure 4B.2: Raman spectroscopy on Zr-doped In_2O_3 NCs shows same phonon modes as that of parent In_2O_3 signifying the absence of any impurity phase, amorphous or crystalline.

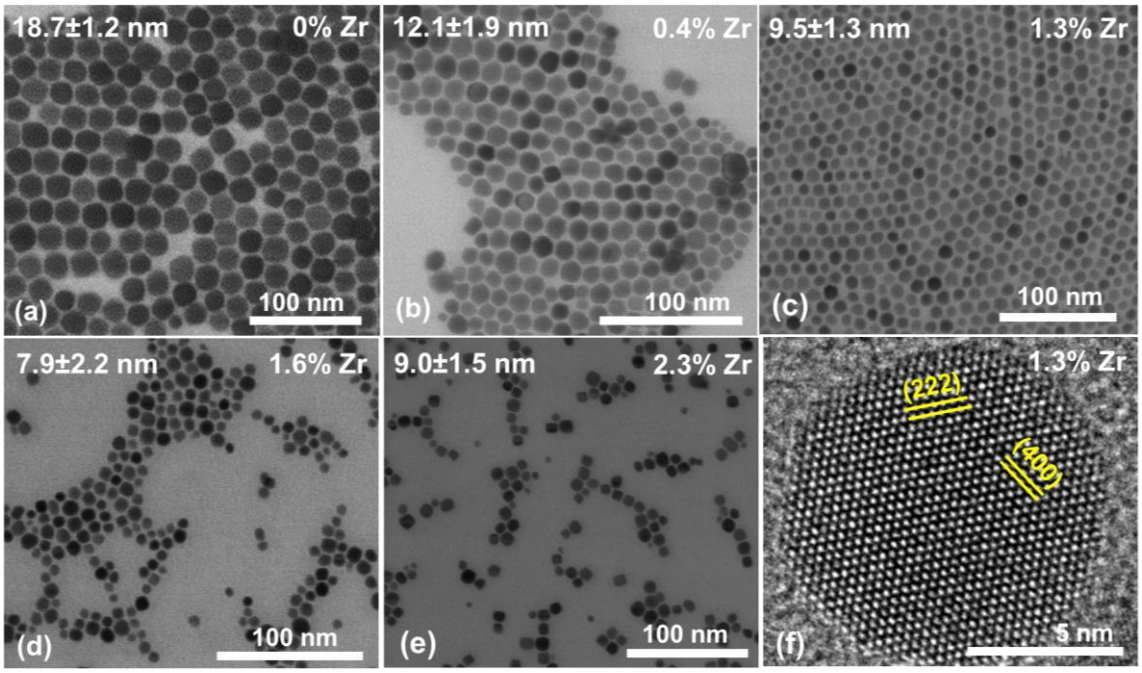

Figure 4B.3: (a-e) STEM images of Zr-doped In_2O_3 NCs with different doping percentages showing nearly spherical NCs with narrow size distribution. (f) HRTEM image of 1.3% Zr-doped In_2O_3 NCs showing the highly crystalline nature of NCs with interplanar distances corresponding to different planes in the In_2O_3 structure.

4B.3.2 Oxidation state and radial distribution of dopant

In order to ascertain the oxidation state of the Zr ions in the Zr-doped In_2O_3 NCs, we employed XPS on all the Zr-doped In_2O_3 NCs and plotted the obtained spectra for In 3d and Zr 3d core levels in Figure 4B.4. The binding energy (BE) values of 444.4 eV and 452.0 eV for In $3d_{5/2}$ and In $3d_{3/2}$ peaks respectively are separated by a spin-orbital splitting energy of 7.6 eV correspond to an oxidation state of +3 for all In ions (Figure 4B.4a). Additionally, the XPS spectra of In 3d peaks can be de-convoluted into 2 components which corresponds to two different type of In^{3+} species which can be rationalized by considering two different type of In lattice positions in the cubic bixbyite structure of In_2O_3. Zr $3d_{5/2}$ and Zr $3d_{3/2}$ BE peaks located at 182.3 eV and 184.7 eV, correspond to Zr in the +4 oxidation state,[47-48] progressively increasing in intensity with an increase in the Zr doping (Figure 4B.4b). The spectra could be fitted using only one component, which further indicates the presence of Zr in a single oxidation state.

To determine the radial distribution of Zr in the NC, we compared the doping percentages obtained from XPS and ICP-AES. XPS gives an estimation of the surface doping percentage whereas ICP-AES is a measure of overall NC composition (surface and core). This comparison shows that percentages obtained from XPS are significantly greater those from ICP-AES (Figure 4B.5) and

suggests that Zr doping is slightly surface segregated or in other words, Zr^{4+} ions preferentially substitutes In positions that are present near the surface than those in the core of NC. This finding can prove beneficial as previous work has shown that surface segregated doping is associated with low LSPR FWHM and high LSPR Q-factors.[32, 43, 49] This is because dopants segregated on the surface allows charge carriers to move inside the lightly doped/undoped NC core without getting scattered. This decreases damping of charge carriers, thereby decreasing the LSPR FWHM and enhancing carrier mobilities.

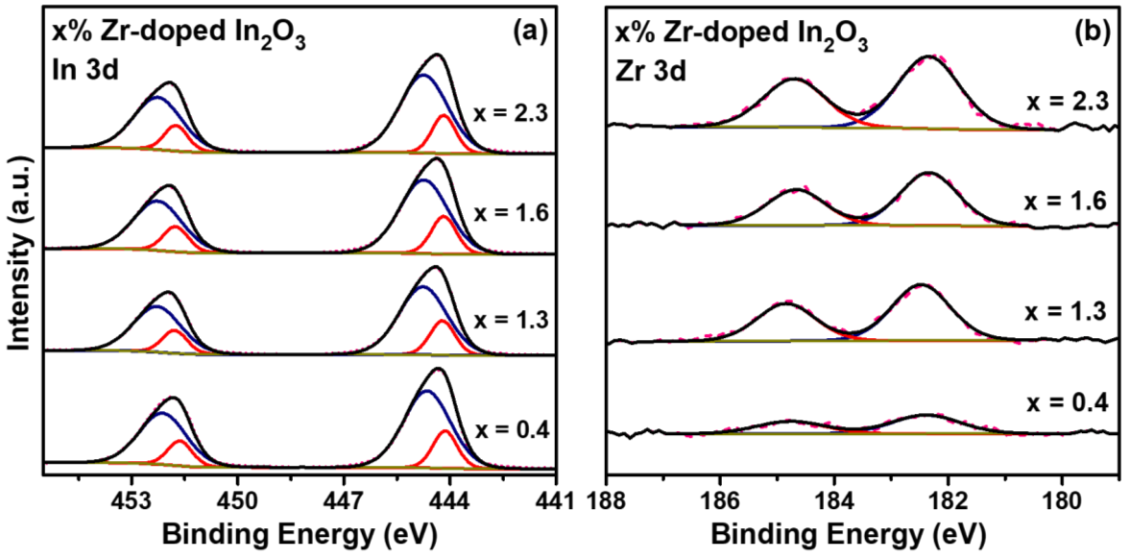

Figure 4B.4: XPS spectra of (a) In 3d and (b) Zr 3d levels of the different Zr-doped In_2O_3 NCs. The spectra have been shifted vertically for better representation.

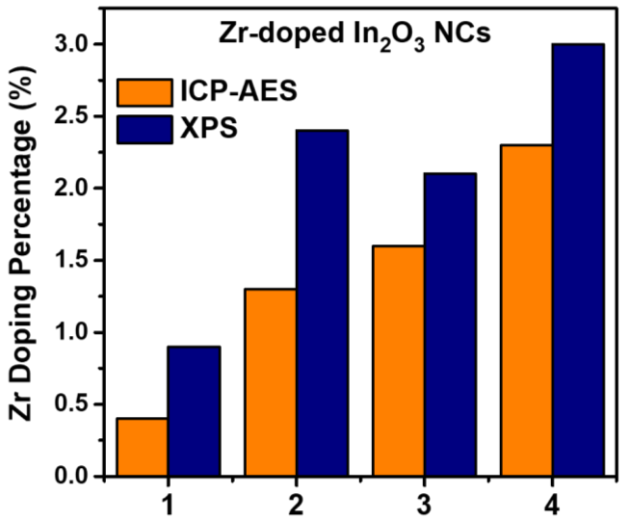

Figure 4B.5: Comparison of ICP-AES and XPS doping percentages revealing that Zr doping is surface segregated. The notations 1 to 4 on the x-axis just represents NCs with 4 different Zr doping percentages.

4B.3.3 LSPR from Zr-doped In_2O_3 NCs

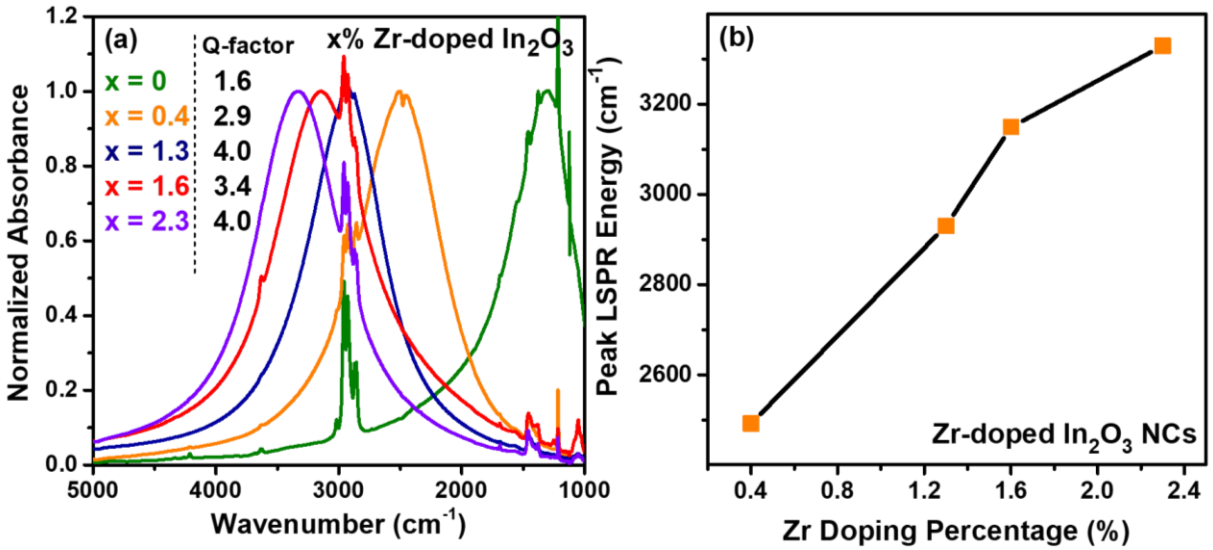

Figure 4B.6: (a) Optical extinction spectra of different Zr-doped In_2O_3 NCs displaying narrow and symmetric LSPR bands. (b) Increase in the LSPR energy with an increase in Zr doping.

Table 4B.1: Tabulated experimental LSPR parameters of different NCs obtained from their optical extinction spectra.

ICP-AES Composition	LSPR Peak Energy (cm^{-1})	LSPR FWHM (cm^{-1})	LSPR Q-Factor
0% Doping	1296	648	2.0
0.4% Zr	2492	870	2.9
1.3% Zr	2930	735	4.0
1.6% Zr	3149	936	3.4
2.3% Zr	3329	840	4.0
0.6% Sn	2001	1038	1.9
2.8% Sn	4058	1188	3.4
4.1% Sn	4732	1274	3.7
7.5% Sn	5695	1204	4.7
1.9% Sn-0.9% Zr	3652	696	5.3
0.9% Sn-0.4% Zr	3026	860	3.5
4.5% Sn-0.8% Zr	4838	1071	4.6
7.5% Sn-1.0% Zr	5531	1066	5.3

The optical extinction spectra of the different Zr-doped In_2O_3 NCs in tetrachloroethylene solvent are shown in Figure 4B.6a. All the Zr-doped In_2O_3 NCs show remarkably narrow LSPR bands with their LSPR energies consistently increasing with an increase in the Zr doping, signifying the generation of electron density with Zr^{4+} doping (Figure 4B.6b). We note here that the LSPR of undoped In_2O_3 NCs is attributed to the accumulation of electron density by oxygen vacancies whereas in Zr-doped In_2O_3 NCs, Zr doping is largely responsible for the electron density. The highly symmetric shapes of the LSPR bands in Figure 4B.6a further indicates decrease in the ionized impurity scattering,[15, 19, 32, 43] and is consistent with our initial hypothesis. The LSPR parameters of different Zr-doped In_2O_3 NCs are listed in Table 4B.1. Quantitatively, the LSPR FWHM of 735 cm^{-1} (91 meV) for 1.3% Zr-doped In_2O_3 NCs is very close to that reported for Ce-doped In_2O_3 NCs (77 meV),[22] and smaller than the best reported LSPR FWHM for Sn-doped In_2O_3,[43] and other doped metal oxide NCs (Table 4B.2) and one of the lowest in the literature.

Table 4B.2: Comparison of the LSPR parameters and Q-factors of Zr-doped In_2O_3 and Sn-Zr codoped In_2O_3 NCs with the benchmark doped semiconductor NCs for near- to mid-IR LSPR.

Host	**Dopant**	**Doping Level (%)**	**LSPR Peak (cm^{-1})**	**FWHM (meV)**	**Q-factor**	**Reference Number**
CdO	F^- , In^{3+}	~10, 8.3	5793	59	12.23	18
CdO	In^{3+}	13.2	4415	67	8.15	17
In_2O_3	Sn^{4+}, Cr^{3+}	6.6, 23.8	5717	99	7.2	50
In_2O_3	Zr^{4+}, Sn^{4+}	0.9, 1.9	3652	86	5.3	Present case
In_2O_3	Zr^{4+}, Sn^{4+}	1.0, 7.5	5531	132	5.3	Present case
In_2O_3	Sn^{4+}	6.4	5882	~150	4.85	32
In_2O_3	Zr^{4+}	1.3	2930	91	4.0	Present case
In_2O_3	Zr^{4+}	2.3	3329	104	4.0	Present case
In_2O_3	Ce^{4+}	5.2	2522	77	4.08	22
ZnO	Al^{3+}	1.6	~2500	~100	3.9	51
$Cu_{2-x}S$	Cu vacancy	~3	5564	210	3.3	52
WO_{3-x}	O vacancy	~5%	~11700	~900	1.6	53

In terms of LSPR Q-factor, Zr-doped In_2O_3 NCs display rather high values over a range of LSPR energies which are almost identical to that of Ce-doped In_2O_3 NCs and subsequently, one of the highest in the literature. We note here that, Ce^{4+} ions convert to Ce^{3+} at high doping percentages, thereby reducing the dopant activation. Consequently, the high Q-factors in Ce-doped In_2O_3 NCs were achieved in the same wavelength range.[22] Therefore, Zr-doped In_2O_3 NCs will serve as a better system than NCs of Ce-doped In_2O_3 and most doped metal oxides in applications where high LSPR Q-factors over a wide range of wavelengths are desirable.

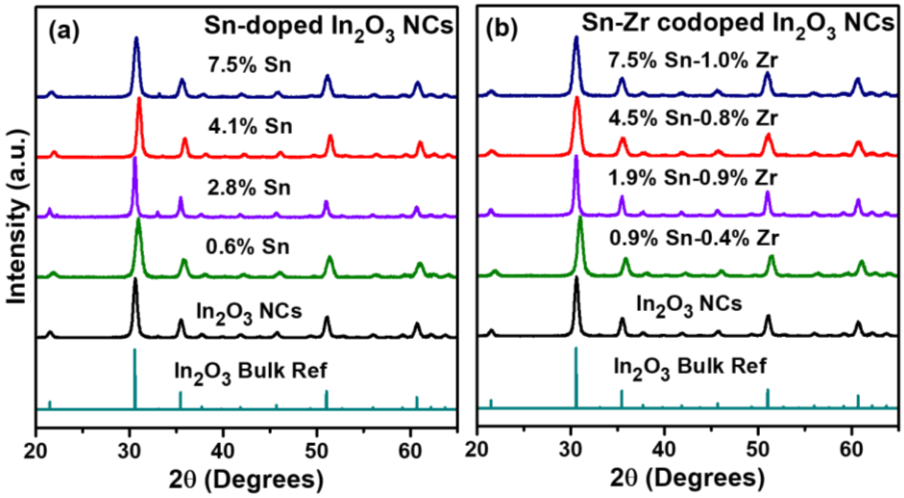

Figure 4B.7: XRD patterns of (a) Sn-doped In_2O_3 NCs and, (b) Sn-Zr codoped In_2O_3 NCs with reference to that of bulk In_2O_3 reference showing the absence of any impurity phase and retention of the cubic bixbyite structure.

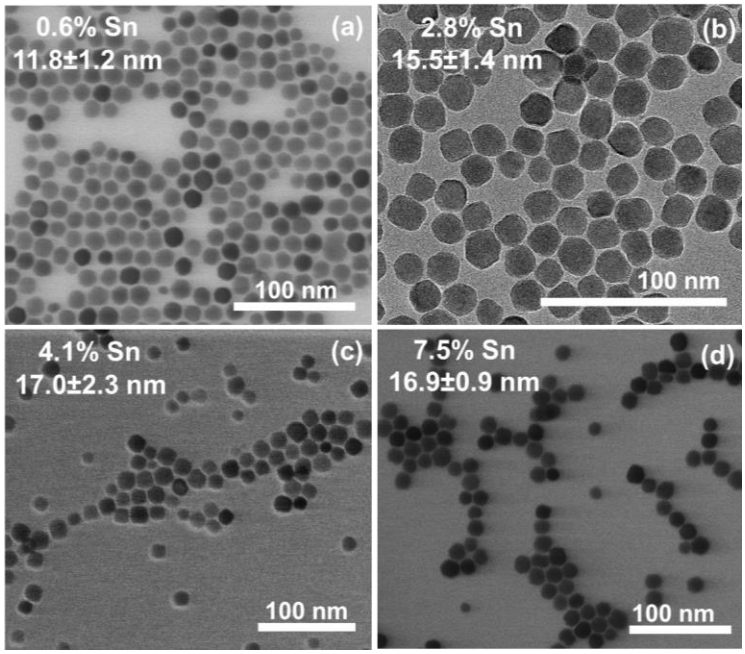

Figure 4B.8: STEM images for Sn-doped In_2O_3 NCs with different Sn doping percentages.

In addition to low LSPR FWHM and high Q-factors, we investigated dopant activation in Zr-doped In_2O_3 NCs, which is a measure of the extent of electron density accumulation with a particular doping percentage. One of the best dopant activation in doped metal oxide NCs can be attained in Sn-doped In_2O_3 NCs,[32, 43, 49] courtesy of the shallow Sn donor levels in proximity to the CBM of In_2O_3.

To demonstrate that Zr^{4+} is as effective an electron donor as Sn^{4+}, but a better aliovalent dopant (due to minimized electron scattering), we compare LSPR spectra of Zr-doped In_2O_3 NCs with Sn-doped In_2O_3 NCs and Sn-Zr codoped In_2O_3 NCs. The characterization data for Sn-doped In_2O_3 NCs and Sn-Zr codoped In_2O_3 NCs (XRD and STEM images) is given in Figure 4B.7-4B.9. The optical extinction spectra are plotted in Figure 4B.10 and their respective LSPR parameters are tabulated in Table 4B.1.

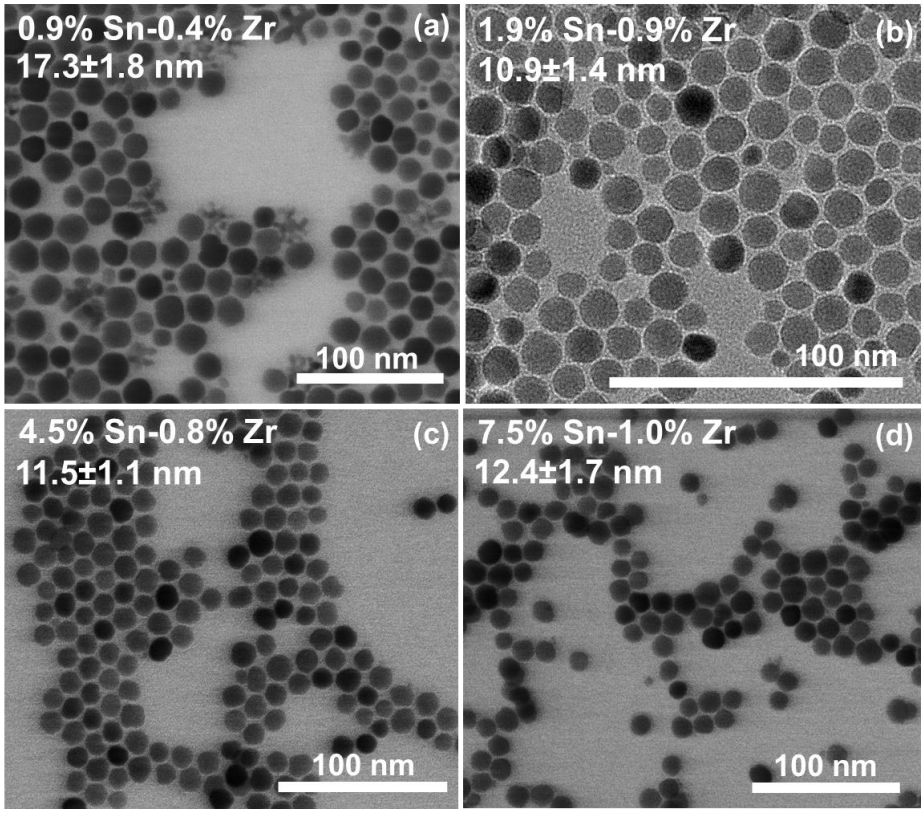

Figure 4B.9: STEM images for Sn-Zr codoped In_2O_3 NCs with different Sn doping percentages but small Zr doping percentage (~0.5-1.0%).

Figure 4B.10a shows Zr-doped In_2O_3 NCs and Sn-doped In_2O_3 NCs at two different doping percentages, small (~0.5%) and intermediate (~2.5%). It can be easily perceived that for both doping levels, the LSPR energy for Zr and Sn doping in In_2O_3 are in the same range, indicating

that both of them have similar donor efficiency. The difference, however, lies in the shape and FWHM of LSPR. For similar doping percentages, the LSPR bands of Zr-doped In_2O_3 NCs are highly symmetric against the asymmetric bands of Sn-doped In_2O_3 NCs. The LSPR FWHM of the Zr-doped In_2O_3 NCs is at least 20% smaller than that of Sn-doped In_2O_3 NCs (Table 4B.1), which is eventually reflected in the significantly higher LSPR Q-factors of Zr-doped In_2O_3 NCs. Even when the same doping percentage was obtained through Zr-doped In_2O_3, Sn-doped In_2O_3 and Sn-Zr codoped In_2O_3 NCs, it was found that the LSPR energy in each case is similar, however, the LSPR FWHM of Zr-doped In_2O_3 and Sn-Zr codoped In_2O_3 NCs is much smaller than Sn-doped In_2O_3 NCs (Figure 4B.10b). In fact, as listed in Table 4B.1, the LSPR FWHM of 1.9% Sn-0.9% Zr codoped In_2O_3 NCs is almost half of that of 2.8% Sn-doped In_2O_3 NCs. Consequently, there is a 50% enhancement in the LSPR Q-factor for the former compared to the latter. The Q-factor of 5.3 for 1.9% Sn-0.9% Zr codoped In_2O_3 NCs is the highest LSPR Q-factor reported in the MIR region (Table 4B.2).

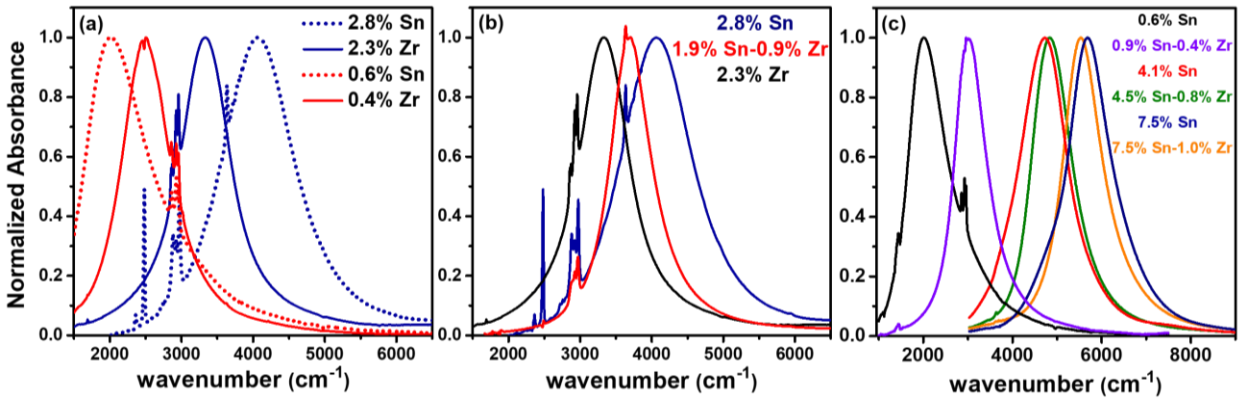

Figure 4B.10: Establishing the high dopant activation behavior but better aliovalent nature of Zr^{4+} ions over Sn^{4+} ions by comparing optical extinction spectra in (i) Zr-doped In_2O_3 and Sn-doped In_2O_3 NCs with similar doping percentage, (ii) Zr-doped In_2O_3, Sn-Zr codoped In_2O_3 and Sn-doped In_2O_3 NCs with similar total cation doping percentage, (iii) Sn-Zr codoped In_2O_3 and Sn-doped In_2O_3 NCs with similar Sn doping percentage.

To check the efficiency of Zr^{4+} in reducing electron scattering, we prepared Sn-Zr codoped In_2O_3 NCs with small Zr doping percentages and compared it with Sn-doped In_2O_3 NCs having roughly the same Sn doping percentage. In Figure 4B.10c, one can easily observe that Zr codoping in Sn-doped In_2O_3 NCs leads to an increase in the LSPR energy (as compared to Sn-doped In_2O_3 NCs with the same Sn doping percentage) except for large Sn doping concentration where irreducible clusters that do not contribute to the total electron density can form.[27, 29] Additionally, Zr codoping

in Sn-doped In_2O_3 NCs decreases the LSPR FWHM and gives a highly symmetric line shape to the LSPR band which enhances the LSPR Q-factors (Table 4B.1). We note here that this observation cannot be attributed to a change in the radial distribution of Sn with Zr codoping as radially, both Sn and Zr are surface segregated and found to be independent of each other, whether in a doped or codoped manner (Figure 4B.11 and 4B.12). Therefore, Zr doping in In_2O_3 can be associated with high Q-factors. 7.5% Sn-1.0% Zr codoped In_2O_3 NCs exhibit an LSPR Q-factor of 5.3 which is one of the highest in the literature (Table 4B.2). Hence, Zr doping in In_2O_3 NCs leads to a combination of high dopant activation, small LSPR linewidth and record high Q-factors.

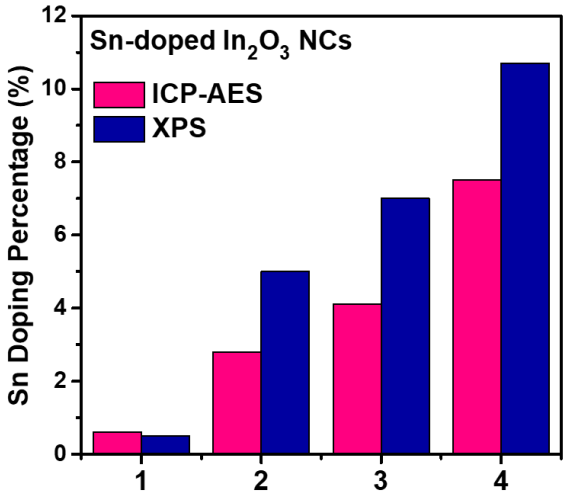

Figure 4B.11: Correlation between the XPS and ICP-AES doping percentages of different Sn-doped In_2O_3 NCs establishing that the radial distribution of Sn is slightly surface segregated. The notations 1 to 4 on the x-axis represents 4 different samples with different Sn doping percentages.

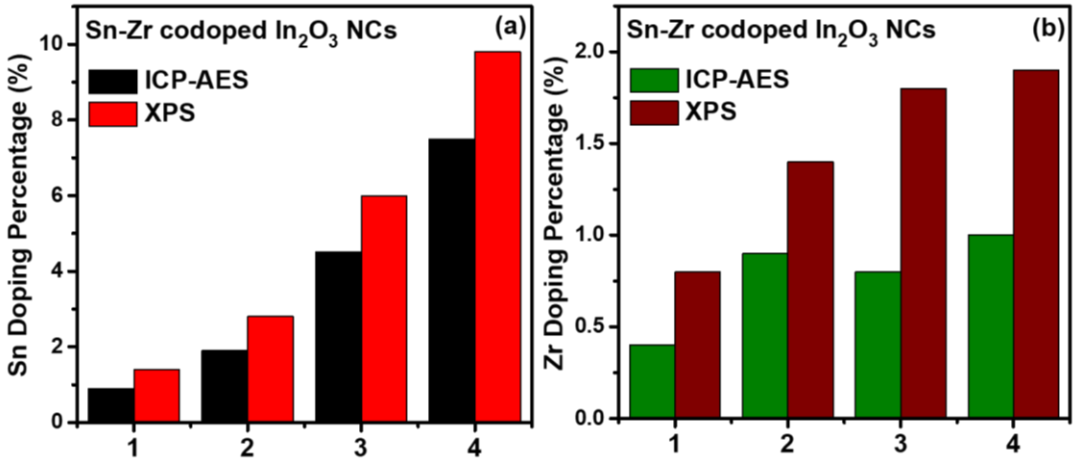

Figure 4B.12: Correlation between the XPS and ICP-AES doping percentages of different Sn-Zr codoped In_2O_3 NCs establishing that the radial distribution of (a) Sn and (b) Zr is surface segregated. The notations 1 to 4 on the x-axis represents 4 different samples with different compositions.

4B.3.4 Drude modeling and significance of the parameters obtained

For a further quantitative interpretation, we modeled the LSPR response of all our NCs with the simple Drude and the extended Drude models by employing a MATLAB code. Since the optical properties of a material are ruled by its complex dielectric function, both the carrier density and damping of charge carriers can be accounted for by considering the free carrier contribution to the complex dielectric function.[15, 19] For noble metals, this is given by the simple Drude model which can be represented as

$$\varepsilon_D = \varepsilon_\infty - \frac{\omega_p^2}{\omega^2 - i\omega\Gamma} \qquad (3)$$

where ω_P is the bulk plasma frequency defined in equation (2), ε_∞ is the high-frequency dielectric constant, Γ is the damping constant and ω is the angular frequency of the incoming electromagnetic radiation. However, this simple Drude model does not take into account the contribution of ionized impurity scattering, which is the major scattering mechanism in doped semiconductors. For this purpose, in doped semiconductor systems, one uses the extended Drude model where the frequency-independent damping constant Γ in simple Drude is replaced by a frequency-dependent analogue Γ(ω) symbolized through the empirical equation[15],

$$\Gamma(\omega) = \Gamma_L - \frac{\Gamma_L - \Gamma_H}{\pi}\left[tan^{-1}\left(\frac{\omega - \Gamma_X}{\Gamma_W}\right) + \frac{\pi}{2}\right] \qquad (4)$$

where Γ_L and Γ_H are the low-frequency and high-frequency damping constants respectively, Γ_X is the crossover-frequency from the low to high frequency region and Γ_W is the width of the crossover region. The value of Γ_L signifies the extent of scattering by ionized dopants and therefore, to achieve a low LSPR FWHM and symmetric LSPR band, Γ_L should be minimized. Since the extent of carrier scattering is determined by the damping constants, carrier mobilities can also be derived optically from the damping constants using

$$\mu_{opt} = \frac{e}{m^*\Gamma(0)} \qquad (6)$$

where we assume that the electrostatic potentials at low frequencies would be equivalent to the carriers moving under the influence of a DC electric field and therefore, we employ $\Gamma(0)$, which is the value of the damping function at zero frequency.[32]

Using the methodology given in Section 4B.2.2, we fitted the optical absorption spectra of all NCs with both the simple and the extended Drude models and extracted the values of bulk plasma

frequency, electron density, damping constants, and the optical electron mobilities. Drude fittings for all NCs is shown in Figure 4B.13 respectively and fitting parameters tabulated for simple Drude and extended Drude model in Table 4B.3 and 4B.4 respectively. Excellent fits could be achieved for all the NCs, for both simple Drude and extended Drude model indicating that only the free electron density is responsible for the optical absorption.

Discussing the parameters of the extended Drude model first, almost all Zr-doped In_2O_3 and Sn-Zr codoped In_2O_3 NCs have a small Γ_L (and $\Gamma_L \ll \Gamma_H$), crossover frequency Γ_x at energies much higher than the LSPR peak position and narrow crossover width (Γ_w) regions. These observations are strong indications that there is minimized impurity scattering in both Zr-doped In_2O_3 and Sn-Zr codoped In_2O_3 NCs and electron scattering in these NCs is governed through a frequency-independent regime. Correspondingly, both Zr-doped In_2O_3 and Sn-Zr codoped In_2O_3 NCs are found to exhibit record high LSPR Q-factors. In comparison, Sn-doped In_2O_3 NCs with the similar doping concentration are found to have a$\Gamma_L \gg \Gamma_H$, small crossover frequencies and large crossover widths. This designates that the ionized impurity scattering is still prominent in these NCs which contributes to enhanced LSPR linewidths.

Regardless of this, both 4.1% and 7.5% Sn-doped In_2O_3 NCs display appreciably high LSPR Q-factors which can be attributed to the observed surface segregation of Sn at high doping percentages that has been found to decrease the electrostatic interactions between the electrons and the ionized dopants. However, the overall trend that Zr-doped In_2O_3 NCs and Sn-Zr codoped In_2O_3 NCs exhibit much smaller Γ_L than Sn-doped In_2O_3 NCs (which leads to high LSPR Q-factors) with the same doping percentage, is still followed, as evident by Figure 4B.14.

We note here that the smallest Γ_L is exhibited by undoped In_2O_3 NCs, which is understandable because electrons therein are only scattered by the oxygen vacancies unlike doped In_2O_3 NCs where both oxygen vacancies and aliovalent dopants act as scattering centers. Furthermore, comparing the electron density obtained from the extended Drude (Table 4B.3) fittings reveals that both Sn and Zr have similar electron density for the same doping percentage which is in agreement with our initial hypothesis and the results obtained in Figure 4B.10.

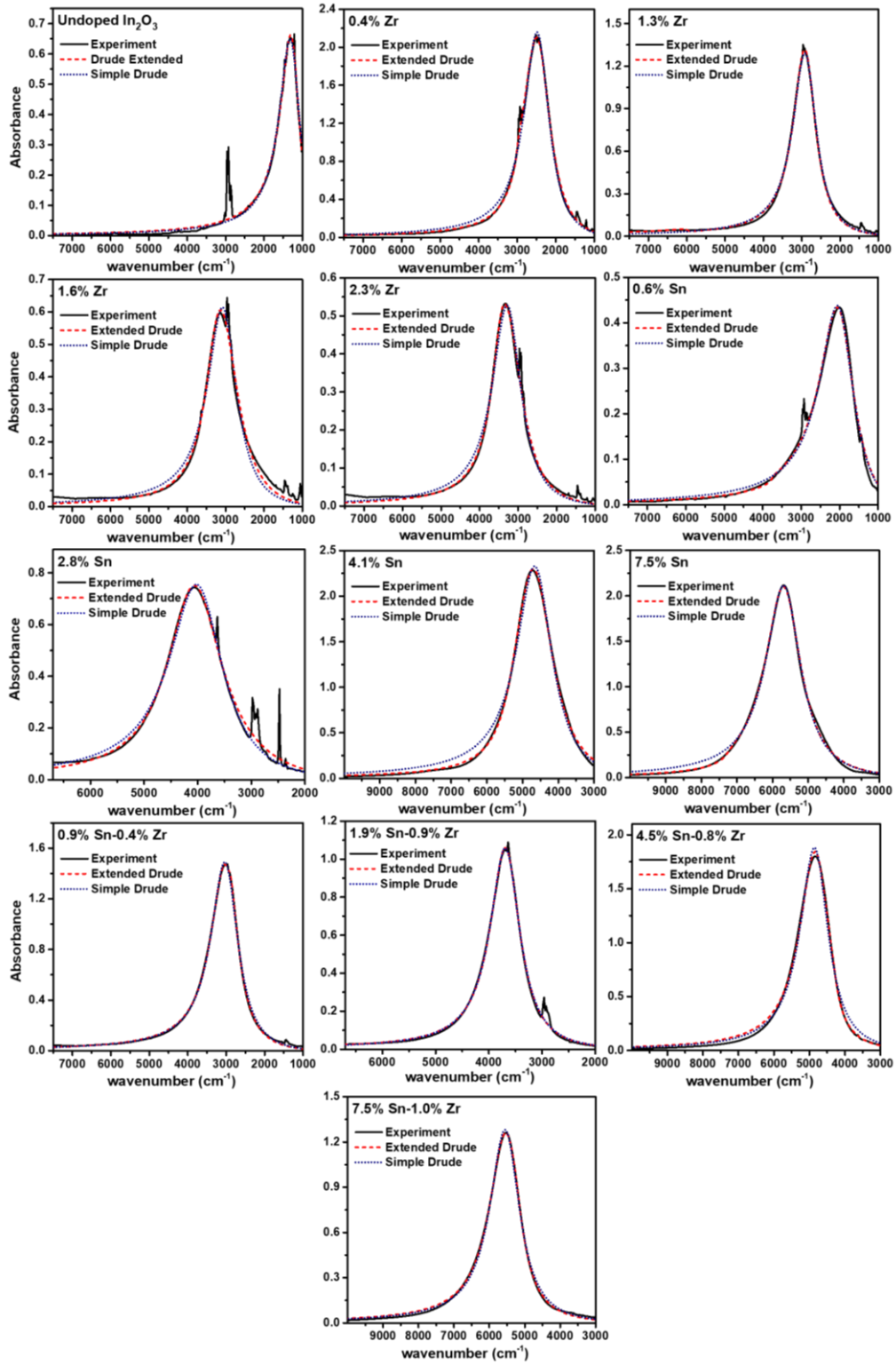

Figure 4B.13: Simple Drude and extended Drude model fits to the optical absorption spectra of different Zr-doped In_2O_3, Sn-doped In_2O_3 and Sn-Zr codoped In_2O_3 NCs.

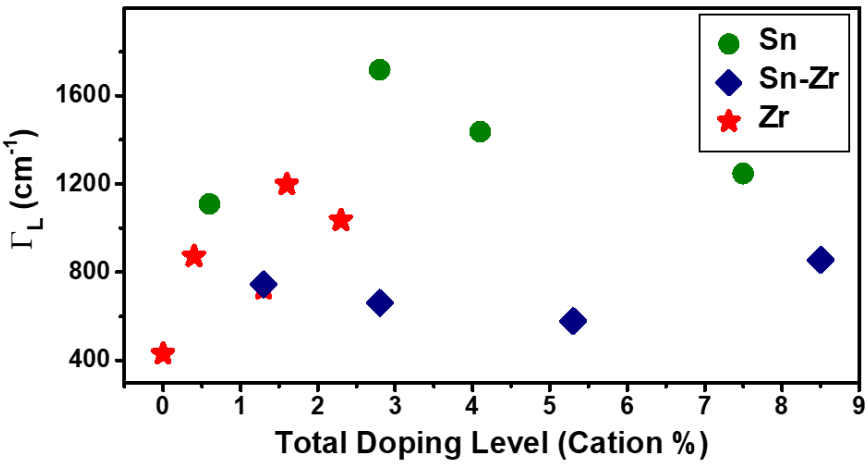

Figure 4B.14: Comparison of the low-frequency damping constants obtained from extended Drude model fits for different NCs indicating much smaller values of Γ_L and hence low carrier scattering for Zr-doped In_2O_3 and Sn-Zr codoped In_2O_3 NCs than Sn-doped In_2O_3 NCs.

A direct consequence of the low Γ_L is reflected in the high mobility values obtained for Zr-doped In_2O_3 and Sn-Zr codoped In_2O_3 NCs (Table 4B.3). However, since electron scattering in our NCs seems to be operating through a frequency-independent mechanism, we will use parameters of the simple Drude model to draw final conclusions on the electron mobilities in different NCs. Moreover, the optical spectra of some NCs have a contribution from the ligand absorption at 3000 cm^{-1}, other than the LSPR band, which may lead to unreasonably large variations in the value of the parameters in some cases, due to more number of parameters employed for fitting.

Nonetheless, as described before, excellent fits could be achieved by modeling the absorption spectra through the simple Drude model signifying that electron scattering mechanism in Zr-doped In_2O_3 and Sn-Zr codoped In_2O_3 NCs, is similar to that of the noble metal NCs. The estimated values of bulk plasma frequency and electron density (Table 4B.4) are roughly equivalent to those determined from the extended Drude model. From Table 4B.4, one can observe that the damping constants for both Zr-doped In_2O_3 and Sn-Zr codoped In_2O_3 NCs are very close to that of the undoped In_2O_3 NCs and significantly smaller than those of the Sn-doped In_2O_3 NCs, which reiterates our claims of minimized ionized impurity scattering in Zr-doped In_2O_3 and Sn-Zr codoped In_2O_3 NCs from the experimental findings and the parameter values of the extended Drude model.

A good correlation was observed between the damping constants and the experimental LSPR FWHM for almost all the NCs, as shown in Figure 4B.15a. This signifies that the simple Drude model is probably a better representation of the electron scattering mechanisms in our NCs,

Table 4B.3: Parameters obtained through fits of optical extinction spectra by the extended Drude model. Carrier density and optical carrier mobility have been calculated from the fitting parameters using equation (2) and (6) respectively.

Composition	**ω_P (cm^{-1})**	**n (10^{20} cm^{-3})**	**Γ_L (cm^{-1})**	**Γ_H (cm^{-1})**	**Γ_X (cm^{-1})**	**Γ_W (cm^{-1})**	**μ_{opt} (cm^2/V.s)**
0% Doping	3880±2	0.37	389±59	841±23	1269±85	441±63	97.7±9.4
0.4% Zr	7290±1	1.31	872±3	536±3	2996±4	22.0±5	48.7±0.2
1.3% Zr	8535±1	1.79	725±4	1324±2	6021±33	48±24	58.4±0.3
1.6% Zr	8970±4	1.98	1196±5	617±6	3274±14	326±11	35.9±0.1
2.3% Zr	9572±2	2.25	1035±23	682±22	3393±20	162±29	41.2±0.9
0.6% Sn	6027±4	1.58	1109±1	767±7	3780±20	62±10	21.6±0.1
2.8% Sn	11719±5	5.98	1718±200	853±85	3926±231	808±336	14.5±1.4
4.1% Sn	13626±3	8.08	1437±34	611±83	5318±117	448±129	16.9±0.1
7.5% Sn	16624±1	12.0	1247±9	611±29	7261±27	202±46	19.3±0.1
1.9% Sn-0.9% Zr	10778±1	5.06	661±9	2319±164	7436±49	135±55	35.6±0.3
0.9% Sn-0.4% Zr	8876±2	3.43	745±7	886±3	2892±9	55±8	32.1±0.3
4.5% Sn-0.8% Zr	14156±2	8.72	579±14	1060±8	4306±4	98±19	41.1±0.8
7.5% Sn-1.0% Zr	16240±3	11.5	856±14	1103±11	5329±18	136±12	27.9±0.4

especially Zr-doped In_2O_3 and Sn-Zr codoped In_2O_3 NCs. Substituting the value of damping constant in equation (6), we determined the electron mobilities of different NCs and plotted them in Figure 4B.15b. It is unambiguously clear that the electron mobilities of Zr-doped In_2O_3 NCs is almost 3 times as that of Sn-doped In_2O_3 NCs and lie very close to that of the undoped In_2O_3 NCs. Even the Sn-Zr codoped In_2O_3 NCs exhibit electron mobilities 30-80% greater than Sn-doped In_2O_3 NCs and close to those reported for Ce-doped In_2O_3 NCs. For the electron mobility calculations, the effective carrier mass for Sn-doped In_2O_3 and Sn-Zr codoped In_2O_3 NCs was approximated as $0.39m_e$ whereas that for Zr-doped In_2O_3 NCs was $0.22m_e$ as suggested by Xu et

al.[20] Even if the same effective carrier mass is assumed, the electron mobilities in Zr-doped In_2O_3 NCs would be equivalent if not greater to that of Ce-doped In_2O_3 NCs.[22]

We attribute this extraordinary performance of Zr-doped In_2O_3 NCs to the optimized position of the Zr defect levels in the electronic band structure of In_2O_3 coupled with surface segregated Zr doping which ensures that the electrostatic potentials experienced by the electrons do not change significantly through the lattice of In_2O_3 and allows us to achieve a rare combination of high LSPR Q-factor, high dopant activation and low levels of electron scattering reflecting as high electron mobilities, all from the same system.

Table 4B.4: Parameters obtained through the fitting of the optical extinction spectra using the simple Drude model. Carrier density and optical carrier mobilities were obtained by substituting the fitting parameters in equation (2) and equation (6) respectively.

Composition	**ω_P (cm^{-1})**	**n (10^{20} cm^{-3})**	**Γ (cm^{-1})**	**μ_{opt} ($cm^2/V.s$)**
0% Doping	3879	0.37	680	62.4
0.4% Zr	7260	1.29	790	53.7
1.3% Zr	8516	1.78	752	56.4
1.6% Zr	8998	1.99	932	45.5
2.3% Zr	9597	2.26	905	46.9
0.6% Sn	6020	1.58	1074	22.3
2.8% Sn	11745	6.0	1219	19.6
4.1% Sn	13613	8.06	1221	19.6
7.5% Sn	16613	12.0	1198	19.9
1.9% Sn-0.9% Zr	10780	5.06	686	34.9
0.9% Sn-0.4% Zr	8865	3.42	860	27.8
4.5% Sn-0.8% Zr	14185	8.76	960	24.8
7.5% Sn-1.0% Zr	16228	11.5	1022	23.4

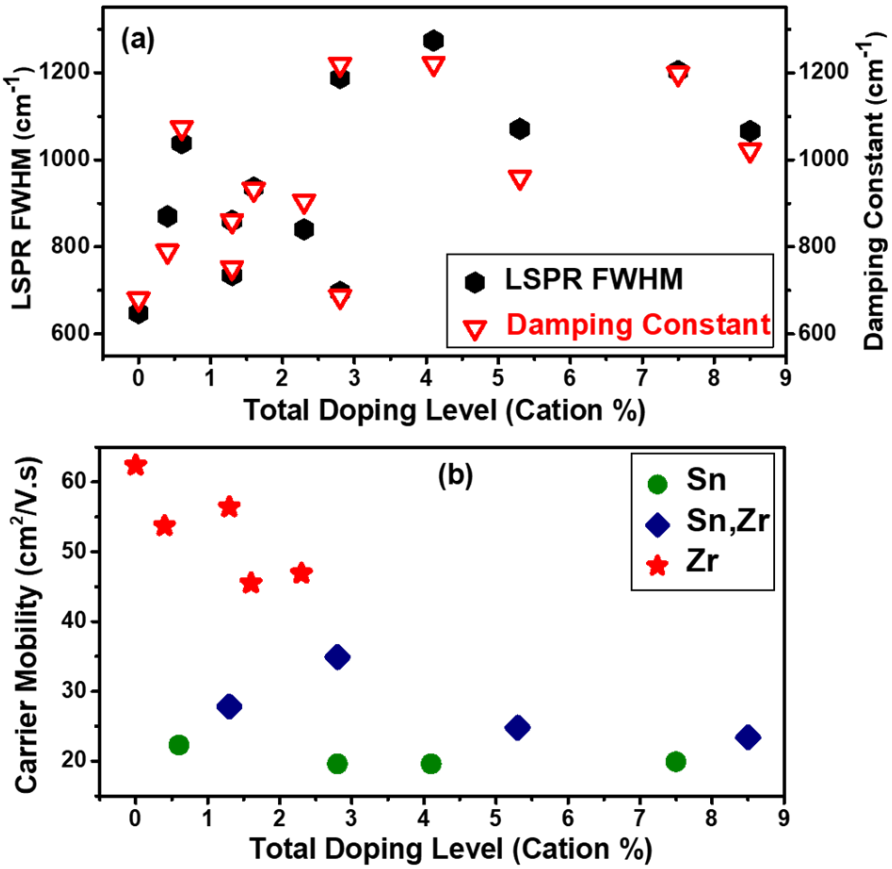

Figure 4B.15: (a) Correlation between damping constant obtained from simple Drude model and experimental LSPR FWHM signifying frequency independence of carrier scattering in almost all our NCs. (b) Comparison of optical carrier mobilities obtained from the simple Drude model shows 3 times enhancement by changing the dopant from Sn^{4+} to Zr^{4+} in In_2O_3 due to less scattering of charge carriers.

4B.4 Conclusions

In conclusion, we describe the salient properties of an aliovalent dopant that determines its merit in generating high LSPR Q-factor in doped metal oxide NCs. For high LSPR energy, a donor state deep in the conduction band of the host and a stable oxidation state is required. While an oxidation state deep in the conduction band can be predicted from the electronegativity difference between the host and the dopant, the stability of the oxidation state can be predicted from the standard reduction potential values. On the other hand, a small LSPR FWHM demands a higher charge to radius ratio and lower electronegativity of the dopant cation with respect to the host cation to minimize the electrostatic interactions between the charge carriers and the ionized dopants. Using these selection criteria, we propose Zr^{4+} as an ideal aliovalent dopant in the In_2O_3 lattice and report the synthesis of Zr-doped In_2O_3 NCs for the first time. The resulting Zr-doped In_2O_3 NCs exhibit

a rare combination of high dopant activation and low LSPR FWHM which eventually lead to one of the highest Q-factors in the sizeable literature of plasmonic nanomaterials. We further prove that our Zr-doped In_2O_3 NCs are comparable to the best materials for dopant activation (Sn-doped In_2O_3 NCs) and LSPR FWHM (Ce-doped In_2O_3 NCs), simultaneously. Drude fittings of the optical spectra reveal that the electron mobilities in our Zr-doped In_2O_3 NCs are 3 times as that of Sn-doped In_2O_3 NCs and equivalent to the undoped In_2O_3 NCs reiterating that the essence of ionized impurity scattering is not present in our Zr-doped In_2O_3 NCs. We believe that the optimized placement of Zr donor levels in the conduction band of In_2O_3 and surface segregated doping of Zr is responsible for the enhanced electron mobilities and could very much enable Zr-doped In_2O_3 NCs to emerge as a benchmark material for transparent conducting electrodes to be used in flat panel displays and thin-film photovoltaics. Since a high Q-factor also facilitates enhanced hot spot generation and near-field enhancement, we believe that Zr-doped In_2O_3 NCs would be a good system for applications like plasmonic sensing and infrared spectroscopy. The approach for this rational dopant selection can ideally be applied to some other metal oxide systems like TiO_2, ZnO, SnO_2 and additional research in this direction could allow acquiring these properties from a much more commercially viable material. This strategy would benefit and encourage researchers in the community to discover and design LSPR materials in a more logical manner.

4B.5 References

1. Willets, K. A.; Duyne, R. P. V. Localized Surface Plasmon Resonance Spectroscopy and Sensing. *Annu. Rev. Phys. Chem.* **2007,** *58*, 267-297.
2. Liu, X.; Swihart, M. T. Heavily-Doped Colloidal Semiconductor and Metal Oxide Nanocrystals: An Emerging New Class of Plasmonic Nanomaterials. *Chem. Soc. Rev.* **2014,** *43*, 3908-3920.
3. Faucheaux, J. A.; Stanton, A. L. D.; Jain, P. K. Plasmon Resonances of Semiconductor Nanocrystals: Physical Principles and New Opportunities. *J. Phys. Chem. Lett.* **2014,** *5*, 976-985.
4. Tandon, B.; Ashok, A.; Nag, A. Colloidal Transparent Conducting Oxide Nanocrystals: A New Infrared Plasmonic Material. *Pramana: J. Phys.* **2015,** *84*, 1087-1098.
5. Agrawal, A.; Johns, R. W.; Milliron, D. J. Control of Localized Surface Plasmon Resonances in Metal Oxide Nanocrystals. *Annu. Rev. Mater. Res.* **2017,** *47*, 1-31.
6. Agrawal, A.; Cho, S. H.; Zandi, O.; Ghosh, S.; Johns, R. W.; Milliron, D. J. Localized Surface Plasmon Resonance in Semiconductor Nanocrystals. *Chem. Rev.* **2018,** *118*, 3121-3207.
7. Haes, A. J.; Hall, W. P.; Chang, L.; Klein, W. L.; Van Duyne, R. P. A Localized Surface Plasmon Resonance Biosensor: First Steps toward an Assay for Alzheimer's Disease. *Nano Lett.* **2004,** *4*, 1029-1034.
8. Sannomiya, T.; Hafner, C.; Voros, J. In situ Sensing of Single Binding Events by Localized Surface Plasmon Resonance. *Nano Lett.* **2008,** *8*, 3450-3455.

9. Verellen, N.; Van Dorpe, P.; Huang, C.; Lodewijks, K.; Vandenbosch, G. A. E.; Lagae, L.; Moshchalkov, V. V. Plasmon Line Shaping Using Nanocrosses for High Sensitivity Localized Surface Plasmon Resonance Sensing. *Nano Lett.* **2011,** *11*, 391-397.
10. Jain, P. K.; Huang, X.; El-Sayed, I. H.; El-Sayed, M. A. Noble Metals on the Nanoscale: Optical and Photothermal Properties and Some Applications in Imaging, Sensing, Biology, and Medicine. *Acc. Chem. Res.* **2008,** *41*, 1578-1586.
11. Atwater, H. A.; Polman, A. Plasmonics for Improved Photovoltaic Devices. *Nat. Mater.* **2010,** *9*, 205-213.
12. Garcia, G.; Buonsanti, R.; Runnerstrom, E. L.; Mendelsberg, R. J.; Llordes, A.; Anders, A.; Richardson, T. J.; Milliron, D. J. Dynamically Modulating the Surface Plasmon Resonance of Doped Semiconductor Nanocrystals. *Nano Lett.* **2011,** *11*, 4415-4420.
13. Garcia, G.; Buonsanti, R.; Llordes, A.; Runnerstrom, E. L.; Bergerud, A.; Milliron, D. J. Near-Infrared Spectrally Selective Plasmonic Electrochromic Thin Films. *Adv. Opt. Mater.* **2013,** *1*, 215-220.
14. Wang, Y.; Runnerstrom, E. L.; Milliron, D. J. Switchable Materials for Smart Windows. *Annu. Rev. Chem. Biomol. Eng.* **2016,** *7*, 283-304.
15. Lounis, S. D.; Runnerstrom, E. L.; Llordés, A.; Milliron, D. J. Defect Chemistry and Plasmon Physics of Colloidal Metal Oxide Nanocrystals. *J. Phys. Chem. Lett.* **2014,** *5*, 1564-1574.
16. Rueben, J. M.; Yuankun, Z.; André, A. Determining the Nonparabolicity Factor of the CdO Conduction Band using Indium Doping and the Drude theory. *J. Phys. D: Appl. Phys.* **2012,** *45*, 425302.
17. Gordon, T. R.; Paik, T.; Klein, D. R.; Naik, G. V.; Caglayan, H.; Boltasseva, A.; Murray, C. B. Shape-Dependent Plasmonic Response and Directed Self-Assembly in a New Semiconductor Building Block, Indium-Doped Cadmium Oxide (ICO). *Nano Lett.* **2013,** *13*, 2857-2863.
18. Ye, X.; Fei, J.; Diroll, B. T.; Paik, T.; Murray, C. B. Expanding the Spectral Tunability of Plasmonic Resonances in Doped Metal-Oxide Nanocrystals through Cooperative Cation–Anion Codoping. *J. Am. Chem. Soc.* **2014,** *136*, 11680-11686.
19. Mendelsberg, R. J.; Garcia, G.; Li, H.; Manna, L.; Milliron, D. J. Understanding the Plasmon Resonance in Ensembles of Degenerately Doped Semiconductor Nanocrystals. *J. Phys. Chem. C* **2012,** *116*, 12226-12231.
20. Xu, J.; Liu, J. B.; Liu, B. X.; Li, S. N.; Wei, S. H.; Huang, B. Design of n-Type Transparent Conducting Oxides: The Case of Transition Metal Doping in In_2O_3. *Adv. Electron. Mater.* **2018,** *4*, 1700553.
21. Bhachu, D. S.; Scanlon, D. O.; Sankar, G.; Veal, T. D.; Egdell, R. G.; Cibin, G.; Dent, A. J.; Knapp, C. E.; Carmalt, C. J.; Parkin, I. P. Origin of High Mobility in Molybdenum-Doped Indium Oxide. *Chem. Mater.* **2015,** *27*, 2788-2796.
22. Runnerstrom, E. L.; Bergerud, A.; Agrawal, A.; Johns, R. W.; Dahlman, C. J.; Singh, A.; Selbach, S. M.; Milliron, D. J. Defect Engineering in Plasmonic Metal Oxide Nanocrystals. *Nano Lett.* **2016,** *16*, 3390-3398.
23. Tandon, B.; Shanker, G. S.; Nag, A. Multifunctional Sn- and Fe-Codoped In_2O_3 Colloidal Nanocrystals: Plasmonics and Magnetism. *J. Phys. Chem. Lett.* **2014,** *5*, 2306-2311.
24. Shanker, G. S.; Tandon, B.; Shibata, T.; Chattopadhyay, S.; Nag, A. Doping Controls Plasmonics, Electrical Conductivity, and Carrier-Mediated Magnetic Coupling in Fe and Sn Codoped In_2O_3 Nanocrystals: Local Structure Is the Key. *Chem. Mater.* **2015,** *27*, 892-900.
25. Tandon, B.; Yadav, A.; Nag, A. Delocalized Electrons Mediated Magnetic Coupling in Mn–Sn Codoped In_2O_3 Nanocrystals: Plasmonics Shows the Way. *Chem. Mater.* **2016**, *28*, 3620-3624.

26. Yadav, A.; Tandon, B.; Nag, A. Reduction of Mn^{3+} to Mn^{2+} and Near Infrared Plasmonics from Mn-Sn Codoped In_2O_3 nanocrystals. *RSC Adv.* **2016,** *6*, 79153-79159.
27. Frank, G.; Köstlin, H. Electrical Properties and Defect Model of Tin-Doped Indium Oxide Layers. *Appl. Phys. A* **1982,** *27*, 197-206.
28. Hamberg, I.; Granqvist, C. G. Optical Properties of Transparent and Heat-Reflecting Indium Tin Oxide Films: The Role of Ionized Impurity Scattering. *Appl. Phys. Lett.* **1984,** *44*, 721-723.
29. Warschkow, O.; Ellis, D. E.; González, G. B.; Mason, T. O. Defect Cluster Aggregation and Nonreducibility in Tin-Doped Indium Oxide. *J. Am. Ceram. Soc.* **2003,** *86*, 1707-1711.
30. González, G. B.; Mason, T. O.; Quintana, J. P.; Warschkow, O.; Ellis, D. E.; Hwang, J.-H.; Hodges, J. P.; Jorgensen, J. D. Defect Structure Studies of Bulk and Nano-Indium-Tin Oxide. *J. Appl. Phys.* **2004,** *96*, 3912-3920.
31. Bard, A. J.; Parsons, R.; Jordan, J.; International Union of, P.; Applied, C. *Standard Potentials in Aqueous Solution*. M. Dekker: New York, 1985.
32. Lounis, S. D.; Runnerstrom, E. L.; Bergerud, A.; Nordlund, D.; Milliron, D. J. Influence of Dopant Distribution on the Plasmonic Properties of Indium Tin Oxide Nanocrystals. *J. Am. Chem. Soc.* **2014,** *136* , 7110-7116.
33. Zhang, Y. Electronegativities of Elements in Valence States and Their Applications. *Inorg. Chem.* **1982,** *21*, 3886-3889.
34. Shannon, R. D.; Prewitt, C. T. Effective Ionic Radii in Oxides and Fluorides. *Acta Crystallogr. Sect. B* **1969,** *25*, 925-946.
35. Koida, T.; Kondo, M. High-Mobility Transparent Conductive Zr-doped In_2O_3. *Appl. Phys. Lett.* **2006,** *89*, 082104.
36. Koida, T.; Kondo, M. Improved Near-Infrared Transparency in Sputtered In_2O_3-based Transparent Conductive Oxide Thin Films by Zr-doping. *J. Appl. Phys.* **2007,** *101*, 063705.
37. Guilmeau, E.; Bérardan, D.; Simon, C.; Maignan, A.; Raveau, B.; Ovono, D. O.; Delorme, F. Tuning the Transport and Thermoelectric Properties of In_2O_3 Bulk Ceramics through Doping at In-site. *J. Appl. Phys.* **2009,** *106*, 053715.
38. Jansons, A. W.; Hutchison, J. E. Continuous Growth of Metal Oxide Nanocrystals: Enhanced Control of Nanocrystal Size and Radial Dopant Distribution. *ACS Nano* **2016,** *10*, 6942-6951.
39. Ghosh, S. K.; Pal, T. Interparticle Coupling Effect on the Surface Plasmon Resonance of Gold Nanoparticles: From Theory to Applications. *Chem. Rev.* **2007,** *107*, 4797-4862.
40. Vegard, L. Die Konstitution der Mischkristalle und die Raumfüllung der Atome. *Z. Phys.* **1921,** *5*, 17-26.
41. Nadaud, N.; Lequeux, N.; Nanot, M.; Jové, J.; Roisnel, T. Structural Studies of Tin-Doped Indium Oxide (ITO) and $In_4Sn_3O_{12}$. *J. Solid State Chem.* **1998,** *135*, 140-148.
42. Brewer, S. H.; Franzen, S. Calculation of the Electronic and Optical Properties of Indium Tin Oxide by Density Functional Theory. *Chem. Phys.* **2004,** *300*, 285-293.
43. Tandon, B.; Yadav, A.; Khurana, D.; Reddy, P.; Santra, P. K.; Nag, A. Size-Induced Enhancement of Carrier Density, LSPR Quality Factor, and Carrier Mobility in Cr–Sn Doped In_2O_3 Nanocrystals. *Chem. Mater.* **2017,** *29*, 9360-9368.
44. Guria, A. K.; Pradhan, N. Doped or Not Doped: Ionic Impurities for Influencing the Phase and Growth of Semiconductor Nanocrystals. *Chem. Mater.* **2016,** *28*, 5224-5237.
45. Jayakumar, O. D.; Gopalakrishnan, I. K.; Kulshreshtha, S. K.; Gupta, A.; Rao, K. V.; Louzguine-Luzgin, D. V.; Inoue, A.; Glans, P. A.; Guo, J. H.; Samanta, K.; Singh, M. K.; Katiyar, R. S. Structural and Magnetic Properties of $(In_{1-x}Fe_x)_2O_3$ ($0.0 \leqslant x \leqslant 0.25$) System: Prepared by Gel Combustion Method. *Appl. Phys. Lett.* **2007,** *91*, 052504.

46. Farvid, S. S.; Hegde, M.; Radovanovic, P. V. Influence of the Host Lattice Electronic Structure on Dilute Magnetic Interactions in Polymorphic Cr(III)-Doped In_2O_3 Nanocrystals. *Chem. Mater.* **2013,** *25*, 233-244.
47. Wagner, C. D.; Muilenberg, G. E. Handbook of X-ray Photoelectron Spectroscopy : A Reference Book of Standard Data for use in X-ray Photoelectron Spectroscopy. Physical Electronics Division, Perkin-Elmer Corp.: Eden Prairie, Minn., **1979**.
48. Dementjev, A. P.; Ivanova, O. P.; Vasilyev, L. A.; Naumkin, A. V.; Nemirovsky, D. M.; Shalaev, D. Y. Altered Layer as Sensitive Initial Chemical State Indicator. *J. Vac. Sci. Technol., A* **1994,** *12*, 423-427.
49. Crockett, B. M.; Jansons, A. W.; Koskela, K. M.; Johnson, D. W.; Hutchison, J. E. Radial Dopant Placement for Tuning Plasmonic Properties in Metal Oxide Nanocrystals. *ACS Nano* **2017,** *11*, 7719-7728.
50. Tandon, B.; Yadav, A.; Khurana, D.; Reddy, P.; Santra, P. K.; Nag, A. Size-Induced Enhancement of Carrier Density, LSPR Quality Factor, and Carrier Mobility in Cr–Sn Doped In_2O_3 Nanocrystals. *Chem. Mater.* **2017,** *29*, 9360-9368.
51. Johns, R. W.; Bechtel, H. A.; Runnerstrom, E. L.; Agrawal, A.; Lounis, S. D.; Milliron, D. J. Direct Observation of Narrow Mid-Infrared Plasmon Linewidths of Single Metal Oxide Nanocrystals *Nat. Commun.* **2016,** *7*, 11583.
52. Luther, J. M.; Jain, P. K.; Ewers, T.; Alivisatos, A. P. Localized Surface Plasmon Resonances Arising from Free Carriers in Doped Quantum Dots. *Nat. Mater.* **2011,** *10*, 361-366.
53. Manthiram, K.; Alivisatos, A. P. Tunable Localized Surface Plasmon Resonances in Tungsten Oxide Nanocrystals. *J. Am. Chem. Soc.* **2012,** *134*, 3995-3998.

Chapter-5

Understanding Electrochemical Modulation of LSPR from Cr-Sn Codoped In_2O_3 Nanocrystals

---

The work presented in this chapter was carried out under the supervision of Prof. Delia J. Milliron at the University of Texas at Austin, USA.

Simulations presented in section 5.3.4c were performed by Dr. Ankit Agarwal at the University of Texas at Austin, USA.

Following article has been published from the work presented in this chapter.

1. Tandon, B.; Agrawal, A.; Heo, S.; Milliron, D.J.; "Competition between Depletion Effects ahd Coupling in Plasmon Modulation of Metal Oxide Nanocrystals" *Nano. Lett.*. **2019**, *19*, 2012-2019.

Summary

Degenerately doped metal oxide nanocrystals (NCs) exhibit strong light-matter interaction due to localized surface plasmon resonance (LSPR) in the near to mid-infrared region. Besides being readily tuned through dopant concentration introduced during synthesis, this LSPR can also be dynamically modulated by applying an external electrochemical potential. This characteristic makes these materials candidates for electrochromic window applications. Here, using prototypical doped indium oxide NCs as a model system, we find that the extent of electrochemical modulation achieved of LSPR frequency is governed by the depletion width and the extent of inter-NC LSPR coupling, which are indirectly controlled by the dopant density, size, and packing density of the NCs. The depletion layer is a near-surface region with a sharply reduced free carrier population that occurs whenever the surface potential lies below the Fermi level. Changes in the depletion width under applied bias substantially control the spectral modulation of the LSPR of individual NCs, but also modify the inter-NC LSPR coupling, which additionally modulates the LSPR absorption on the NC film scale. Here, we show that both of these effects must be considered as primary factors determining the extent of LSPR frequency modulation and that the dominant factor depends on NC size. For a constant doping concentration, depletion effects govern LSPR modulation for smaller NCs while LSPR coupling is prevalent in larger NCs. Consequently, as the size of the NCs is increased while keeping the doping concentration constant, we observe a reversal in the sign of the LSPR frequency modulation from positive to negative.

Graphical Abstract

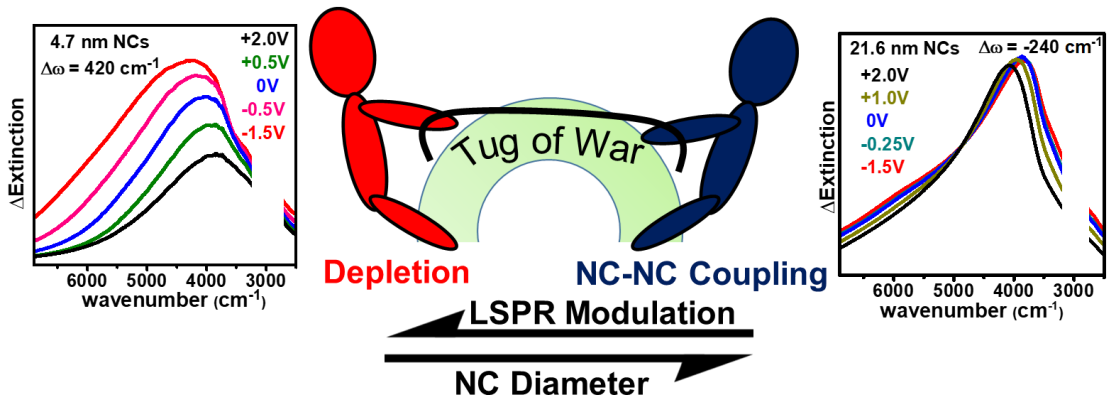

5.1 Introduction

Degenerately doped semiconductor and metal oxide nanocrystals (NCs) such as Sn-doped In_2O_3[1-3], Al-doped ZnO[4], In-doped CdO[5-6], Cu_xS/Se[7-8], and WO_{3-x}[9] can sustain localized surface plasmon resonance (LSPR) on interaction with electromagnetic radiation due to the presence of large free carrier concentrations (10^{19}-10^{21} cm^{-3}). Because the free carrier concentration in these NCs is an order of magnitude or more lower than in noble metals such as gold or silver, the LSPR lies in the near-infrared (NIR) to mid-infrared region instead of the visible region. Moreover, the LSPR in semiconductor NCs is readily tunable by changing the concentration of dopants introduced during NC synthesis, which contrasts with conventional metal nanoparticles where free carrier concentration is fixed and tuning LSPR relies on changing size and morphology.[10-13]

The LSPR in semiconductor NCs can also be tuned dynamically by chemical, photochemical, or electrochemical external stimuli.[3, 14-18] Electrochemical modulation of LSPR in particular has opened new possibilities for application of metal oxide NCs as active materials in electrochromic window applications.[17] NCs and composites of benchmark materials such as Sn-doped In_2O_3 and WO_{3-x} have already been shown to independently modulate transmittance in the visible and infrared regions with high dynamic range and fast switching kinetics.[17, 19-26] Applying an external applied potential results in capacitive charging of NCs modifying the number of free electrons and their spatial distribution inside the NCs which induces a change in the LSPR peak energy and LSPR peak intensity. Depending on the synthetically introduced dopant concentration and on the applied external potential, dynamic LSPR modulation allows semiconductor NCs to absorb over a wide infrared spectral window.

It was recently shown that the application of electrochemical potential to Sn-doped In_2O_3 NCs changes the depletion width and thereby modulates the volume fraction of a non-depleted, LSPR-active NC core.[27-28] For films of highly doped NCs, a decrease in depletion width manifests a change in LSPR based on two competing factors (i) decrease in effective surrounding refractive index leading to a blue shift of the plasmon band, and (ii) decrease in the distance between adjacent LSPR-active NC cores[29] resulting in increased inter-NC LSPR coupling, which causes a red shift of the LSPR. Zandi et al. showed that for a constant size of NCs, the extent of LSPR frequency modulation decreases at higher Sn dopant density due to a decrease in the thickness of the depletion layer, extra carriers are added to the thin depletion layer leaving a nearly constant carrier

concentration in the plasmonic core.[27] For a constant Sn doping concentration, with an increase in the NC size, LSPR frequency modulation is also suppressed as a larger fraction of the NC volume is effectively screened from the applied potential and experiences negligible change in carrier concentration. Schematic in Figure 5.1 summarizes the effect of depletion in governing the LSPR modulation of Sn-doped In_2O_3 NCs. Electrochemical studies of LSPR modulation in a Sn-doped In_2O_3 NC dispersion showed that for a similar doping percentage and size, LSPR frequency modulation is much greater than in NC films.[28] This difference can be rationalized by recognizing that LSPR coupling impacts dynamic optical properties of NC films, while in dispersions NCs are well isolated from each other.

Nonetheless, depletion effects were found to dominate the LSPR modulation of Sn-doped In_2O_3 NCs with coupling playing a secondary role in governing the specifics of electrochemical LSPR modulation in films. The conditions under which inter-NC LSPR coupling could dominate the LSPR modulation remains an open question. According to the plasmon hybridization model,[30] the LSPR modes of two NCs can couple if the distance of closest approach *d* between them is less than or equal to 2.5 times the diameter of the particle and the strength of this coupling decays as $1/d^3$.[31-32] This model suggests that larger NCs will couple more strongly and that coupling will persist at larger distances compared to smaller NCs. A systematic study of LSPR modulation using NCs of different sizes was therefore conceived to ascertain if the strength of LSPR coupling between NCs can dominate over depletion effects at any size.

To maximize the LSPR coupling, synthesized NCs should have small depletion width. For a constant size, depletion width is influenced by at least two major factors (i) doping concentration, where a higher concentration reduces depletion width and (ii) dopant distribution, as surface segregation of dopants decreases the depletion width.[29] To satisfy the first condition, we choose NC with high nominal overall doping concentration of around 10%. As a simple approach to tune dopant distribution in larger NCs, we adopted the synthesis reported in Chapter-4A, where we displayed that through Cr codoping in Sn-doped In_2O_3 NCs, the diameter of the NCs can be increased while yielding NCs with highly surface segregated Sn dopants.[33] Additionally, fitting the LSPR of Cr-Sn codoped In_2O_3 NCs with the Drude model suggested that very high carrier mobilities could be expected from these materials, which is also favorable for strong LSPR

coupling between adjacent NCs. Consequently, in this study, we study the LSPR modulation behavior in films of highly doped Cr-Sn codoped In_2O_3 NCs of varied sizes (4.7-21.6 nm).

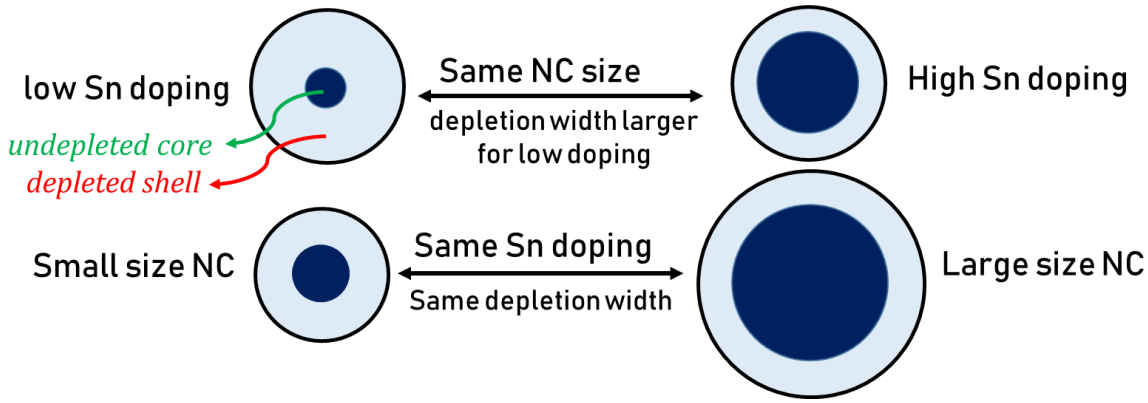

Figure 5.1: Schematic representing the effect of a change in the doping percentage and size, independently on the thickness of the depletion layer at the surface of a doped NC.

5.2 Experimental Section

5.2.1 Synthesis of Cr-Sn codoped In_2O_3 NCs

Different Cr-Sn codoped In_2O_3 NCs were synthesized using standard schlenk line techniques following an strategy reported in Chapter-4A. To summarize, for a target composition, appropriate amounts of Cr, In and Sn precursor was taken in a 50 mL round bottom flask and 10.0 mL of oleylamine was added to it. This mixture was subjected to alternating N_2 and vacuum atmosphere for 30 min at room temperature to get rid of the dissolved gases followed by degassing at 100℃ for 30 min under vacuum conditions. The temperature was then increased to 250℃ at a heating rate of approximately 10℃/min with vigorous stirring under N_2 conditions and kept undisturbed for 4 hours. The solution was then cooled to room temperature and precipitated using ~30mL methanol solution followed by centrifugation at 6000 rpm for 6 min. The washing procedure was repeated twice to get rid of excess solvents and the oleylamine capped NCs were then dispersed in different non-polar solvents such as hexane and tetrachloroethylene for characterization purposes.

5.2.2 Synthesis of 16.1 nm 10% Sn-doped In_2O_3 NCs

These NCs were prepared following a continuous NC growth model (slow injection synthesis) developed by the Hutchison group.[34] Concisely, 0.5 M of total metal precursors i.e. indium(IV) acetate and tin(IV) acetate in stoichiometric ratio, were dissolved in 16 mL oleic acid and degassed at 100℃ under vacuum for 2 hours. The temperature was subsequently raised to 150℃ under N_2 environment where it was heated uninterruptedly for 2 hours. In a separate 100 mL round bottom

flask, 20 mL oleyl alcohol was first degassed and then heated to 290℃. Afterwards, 10 mL of the metal oleate solution was injected into the hot oleyl alcohol at the rate of 0.2 mL/min using an automated syringe pump. After injection, the solution was cooled down to room temperature and quenched with ethanol to precipitate the NCs. The NCs were washed several times employing hexane/ethanol solvent/anti-solvent mixtures before they were finally dispersed in hexane for characterization purposes.

5.2.3 Nanocrystal film preparation

NCs dispersed in hexane were first stripped of organic ligands and exchanged with inorganic ligands by consuming $NOBF_4$ in a N,N-dimethylformamide (DMF) : Hexane bilayer.[35] The ligand exchanged NCs were washed several times with toluene as an antisolvent and then dispersed in a 2:3 mixture of DMF:acetonitrile. The solution was then spin coated at 1500 rpm on commercial Sn-doped In_2O_3 glass (~50 nm Sn-doped In_2O_3 layer) and undoped Si wafers for 2 min followed by 4000 rpm for 10 s yielding uniform films of thickness between 100-200 nm. Additionally, the solvent was evaporated from the films by annealing in a tube furnace at 190℃ for 30 min in 50 sscm flow of N_2 gas.

5.2.4 Fabrication of the sandwich electrochemical cell

The NCs films were assembled into a sandwich electrochemical device for *in-situ* FTIR spectroelectrochemistry (SEC) experiments. The annealed NC films functioned as working electrodes whereas a Pt film on Sn-doped In_2O_3 glass (prepared by drop casting a solution of Pt nanoparticles in ethanol or Platisol onto Sn-doped In_2O_3 glass followed by annealing at 350℃ in air) served as both counter and ra eference electrode. The counter and working electrode were merged by melting a piece of 25 μm thick thermoplastic polymer Surlyn between them. A 1.0 cm^2 hole was punched in the Surlyn film prior to fusing the two electrodes which was later filled with a non-intercalating electrolyte solution (0.1 M tetramethylammonium bis(trifluoromethanesulfonyl)imide (TBATFSI) in tetraglyme).

5.2.5 Modeling details for mimicking the electrochemical cells

To solve for the carrier concentration profile, we adapted the dimensionless form of Poisson's equation derived by Seiwatz and Green[36] to solve numerically for a spherical nanoparticle in Cartesian coordinates as,

$$\nabla^2 u = -\frac{e^2 \rho}{\varepsilon \varepsilon_0 k_B T} \qquad \text{S1}$$

The non-dimensional potential is defined as, $u = \frac{E_F - E_I}{k_B T}$, and k_B is the Boltzmann constant and T is temperature. ε_0 is the vacuum permittivity, ε is the static dielectric constant, and ρ is the charge density.

$$\rho = \{\rho_D(r) - n(r)\} \qquad \text{S2}$$

where, $\rho_D(r)$ is the radially changing donor dopant density, and $n(r)$ is electron density. Detailed mathematical derivation of the non-dimensional equation can be found elsewhere[27-29].

iven the carrier concentration distribution profile inside the nanocrystal, the optical property of the periodic film of NC was obtained by solving the Maxwell equation using finite element methodology in COMSOL. The detailed mathematical derivation and discussion on the simulation methodology can be found elsewhere[27-28].

5.2.6 Characterization

Inductively coupled plasma atomic emission spectroscopy (ICP-AES): The elemental composition of NCs was determined through ICP-AES on a Varian 720-ES ICP Optical Emission Spectrometer. Samples were digested in aqua-regia (made by adding 70% HNO_3 dropwise to 35% HCl acid solution in a 1:3 ratio) solution after drying in air for 24 hours. All standards and samples had 2% (v/v) acid concentration.

X-ray diffraction (XRD): The crystal structure and phase of different Cr-Sn codoped In_2O_3 NCs was determined through powder XRD recorded on a Rigaku Miniflex 600 fitted with a monochromated Cu Kα source (λ =1.5406 Å).

Scanning transmission electron microscopy (STEM): The size determination and distribution of different NCs was obtained by employing STEM on a Hitachi S5500 with an electron gun voltage of 30 kV. Samples were drop-casted on Carbon coated 400 mesh TEM grids and dried under vacuum overnight prior to measurement.

X-ray photoelectron spectroscopy (XPS): A Kratos X-ray Photoelectron Spectrometer – Axis Ultra DLD using a monochromatic Al Kα radiation (λ = 1486.6 eV) was used to probe the 20% Cr-10% Sn codoped In_2O_3 NC films for change in oxidation states as they were charged and

discharged. For sample preparation, an electrochemical cell inside the glove box with 0.1 M TBA-TFSI as electrolyte, Pt wire as both reference and counter electrode and the NC film on Sn-doped In_2O_3 coated glass as the working electrode was prepared. The film was then charged at -1.5 V (or discharged at +2.0 V or no charging) and mounted inside an air-free XPS sample holder for transfer to the XPS chamber without air exposure. The XPS spectra obtained were calibrated based on the C1s peak, fixed at 284.8 eV, and analyzed using CasaXPS software.

Electrochemistry: A S200 Biologic potentiostat was employed to carry out electrochemical experiments. For carrying our electrochemical experiments, the sandwich electrochemical devices was joined with adhesive copper tapes and connected with terminals of the potentiometer. Before running the *in-situ* FTIR SEC experiment, all devices were subjected to 3 cycles of charging and discharging between the potentials -1.5 V and +2.0 V.

Fourier transform infrared (FTIR) spectroscopy: The optical absorption spectra of different NCs and *in situ* FTIR spectra of devices were recorded on Bruker Vertex 70 FTIR. All devices were tilted at an angle of 20˚ to avoid contributions of internal reflections from the device in the absorption spectrum. The optical spectra of all devices was referenced with respect to the ambient atmosphere.

Ellipsometric porosimetry: A J.A. Woollam M-2000 spectroscopic ellipsometer with wavelength range from 193 to 1690 nm was used to acquire spectroscopic ellipsometry data. Each sample was positioned in the J.A. Woollam '*Environmental Cell*' chamber in which toluene partial pressure was controlled using the CompleteEASE program. Film optical constants at different partial pressure were obtained over the spectral range from 300 to 850 nm using two Gaussian and one Lorentz oscillator with a Gen-Osc function. The Lorentz-Lorentz equation was used to calculate the volume of condensed toluene in the pores, corresponding to the film porosity.

5.3 Results and Discussion

5.3.1 Structure and morphology

Cr-Sn codoped In_2O_3 NCs of different sizes were prepared by varying the Cr codoping concentration following protocol reported in Chapter-4A. Details of synthesis are mentioned in the experimental section. The elemental composition of the NCs was determined by the ICP-AES

(Table 5.1). The doping percentages obtained from the ICP-AES technique lie close to those in the precursor concentration or nominal doping percentages within the limits of the experimental error.

Table 5.1: Comparison of elemental compositions of Cr-Sn codoped In_2O_3 NCs obtained by the ICP-AES with those in the precursor ratios.

In : Sn : Cr	
Precursor Ratio	ICP-AES Composition
90 : 10 : 0	93.4 : 6.6
85 : 10 : 5	88.2 : 8.3 : 3.5
80 : 10 : 10	85.1 : 7.8 : 7.1
75 : 10 : 15	81.9 : 7.1 : 11.0
70 : 10 : 20	77.5 : 6.2 : 16.3
16.1 nm 90 : 10 : 0	93.6 : 6.4 : 0

The powder XRD patterns (Figure 5.2) show phase pure Cr-Sn codoped In_2O_3 NCs without any impurity. The STEM images (Figure 5.3) show an increase in the NC size from 4.7 nm to 21.6 nm as the Cr codoping percentage is increased from 0% to 20% respectively, consistent with the reported observations in Chapter-4A.[33]

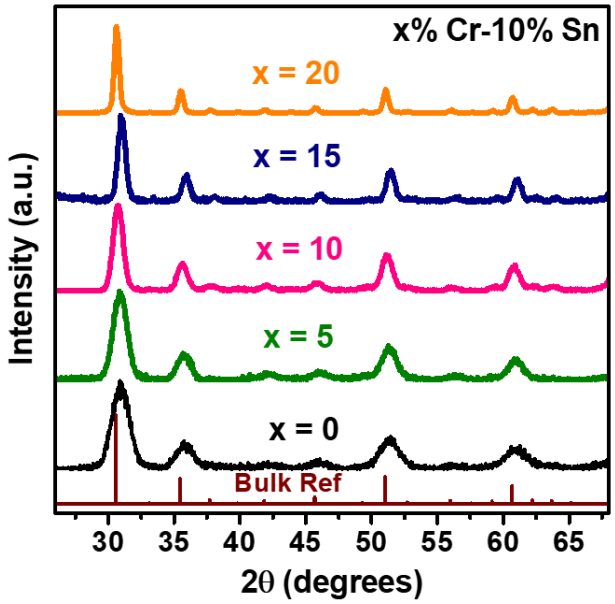

Figure 5.2: Comparison of XRD patterns of different Cr-Sn codoped In_2O_3 NCs with the bulk In_2O_3 reference (JCPDS 88-2160) signifying phase purity and retention of the cubic bixbyite phase of In_2O_3.

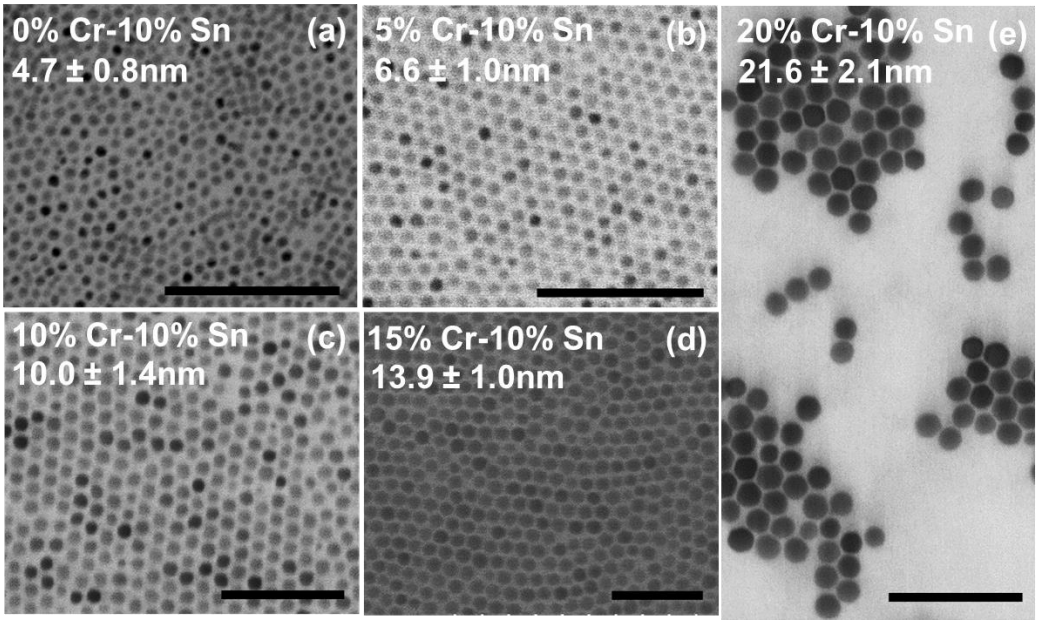

Figure 5.3: STEM images of different Cr-Sn codoped In_2O_3 NCs depicting an increase in the NC size as a function of the Cr codoping percentage. All scale bars are 100 nm.

5.3.2 LSPR coupling in nanocrystal films

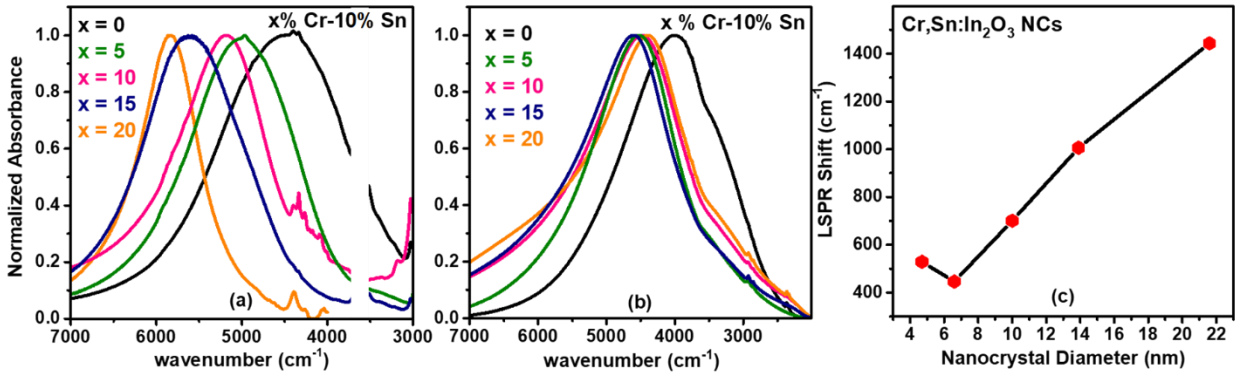

Figure 5.4: (a) Solution FTIR spectra of different Cr-Sn codoped In_2O_3 NCs showing a shift of LSPR to higher wavenumbers with an increase in Cr codoping. (b) FTIR spectra of annealed NC films showing red shifted LSPR peak positions as compared to the solution spectra. (c) Difference in the LSPR peak position between the solution and annealed films as a function of NC diameter.

As observed in Chapter-4A, solution phase NIR spectra of different Cr-Sn codoped In_2O_3 NCs (Figure 5.4a) show that increasing NC diameter via an increase in the Cr codoping percentage leads to blue-shifting of the LSPR while the LSPR peak narrows. The peak masked at 3600 cm^{-1} corresponds to the free hydroxyl group of residual ethanol that was used as an antisolvent for washing the NCs. Using the $NOBF_4$ ligand exchange method developed by Dong et al.,[35] we stripped the oleylamine from the surface of the NCs (Figure 5.5a) to reduce barriers to electron transport in the NC films. Based on the binding energy seen in the F 1s XPS, most of the F exists

as F^- ions (Figure 5.5b), rather than BF_4^-.[37] It is possible that BF_4^- decomposes into stable BF_3 leaving F^- ions at the NC surface. This ligand exchange strategy is different from the previously adopted formic acid ligand exchange used by Zandi et al.[27] and was deliberately adopted to decrease the porosity of the films and increase the NC volume fraction to maximize the potential for LSPR coupling between adjacent NCs. The ligand exchanged NCs were dispersed in a DMF: ACN mixture and spin coated to make uniform thin films on commercial Sn-doped In_2O_3 coated glass. Residual solvent was removed by annealing at 190 ℃ in N_2 atmosphere. The thickness of all films was within the 100-200 nm range as probed by profilometry. Normalized FTIR spectra (Figure 5.4b) of the annealed films of different Cr-Sn codoped In_2O_3 NCs show prominent LSPR peaks and minimal peaks in the 3000 cm^{-1} range where C-H stretching vibrations occur that could originate from residual solvent or organic ligands. The LSPR peaks of the films, however, are shifted to much lower wavenumbers compared to the corresponding spectra of NC dispersions due to the increased dielectric constant of the surroundings and LSPR coupling between NCs.[14] We observe that with an increase in the size of NCs, there is an almost linear increase in the extent of shift between the dispersion and annealed film spectra (Figure 5.4c) thereby establishing that larger NCs couple much more strongly than smaller ones, which is in accordance with the plasmon hybridization model,[30] and consistent with spectra of variably sized Sn-doped In_2O_3 cubes previously reported.[38] Later in the text we will discuss how the increase in the strength of LSPR coupling between NCs as a function of NC diameter affects the plasmonic modulation of Cr-Sn codoped In_2O_3 NCs under an applied external potential.

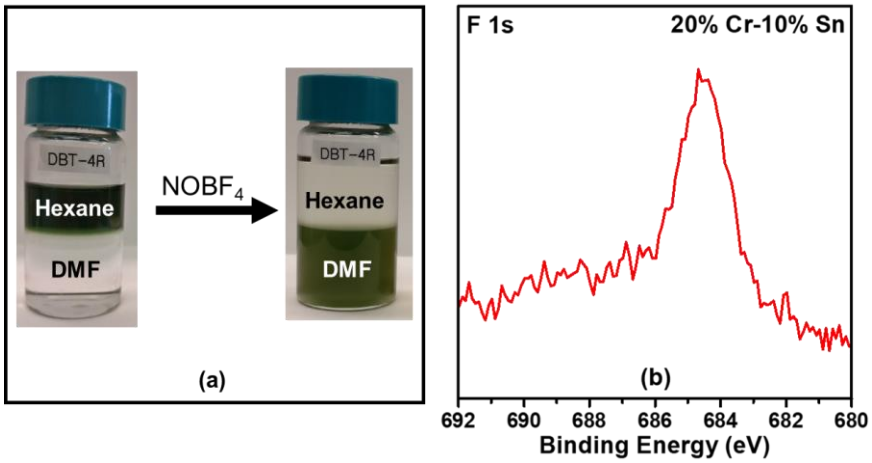

Figure 5.5: (a) Ligand exchange process showing the transfer of organic capped NCs to the DMF layer after addition of $NOBF_4$. (b) Binding energy position of the F 1s XPS spectra of 20% Cr-10% Sn codoped In_2O_3 NCs showing that majority of the F species exist in the form of F^- ions and not BF_4^-.

5.3.3 *in situ* FTIR spectroelectrochemistry of the electrochemical devices

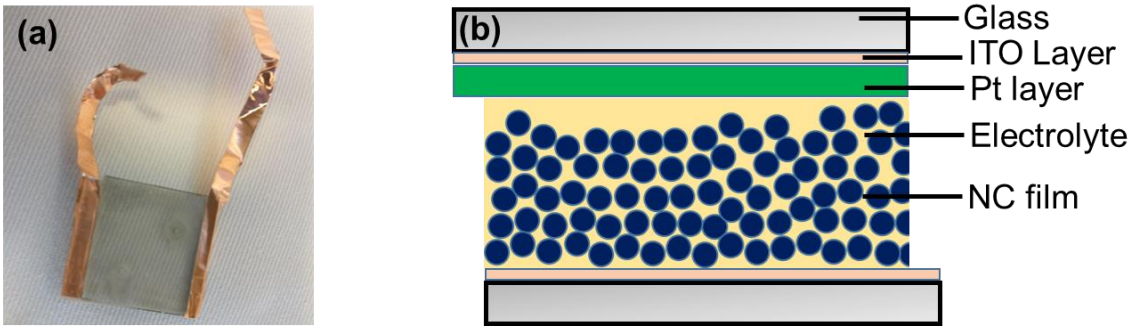

Figure 5.6: (a) A picture of the electrochemical cell (b) Schematic representation of the layers involved in the fabrication of the electrochemical cell.

In this work, we investigate LSPR modulation by assembling NC thin films of different Cr-Sn codoped In_2O_3 NCs into tailor-made sandwich electrochemical devices (see Section 5.2.4 for experimental details and Figure 5.6 for device schematic) and studied their spectroelectrochemical (SEC) response using *in situ* FTIR spectroscopy while a potential is being applied. The potential applied was first increased from -1.5 V to +2.0 V with a step size of 250 mV followed by a reverse cycle from +2.0 V to -1.5 V with a step size of -250 mV (Figure 5.7). The optical response of the electrochemical cell was measured after the current equilibrated to the leakage current at a particular potential.

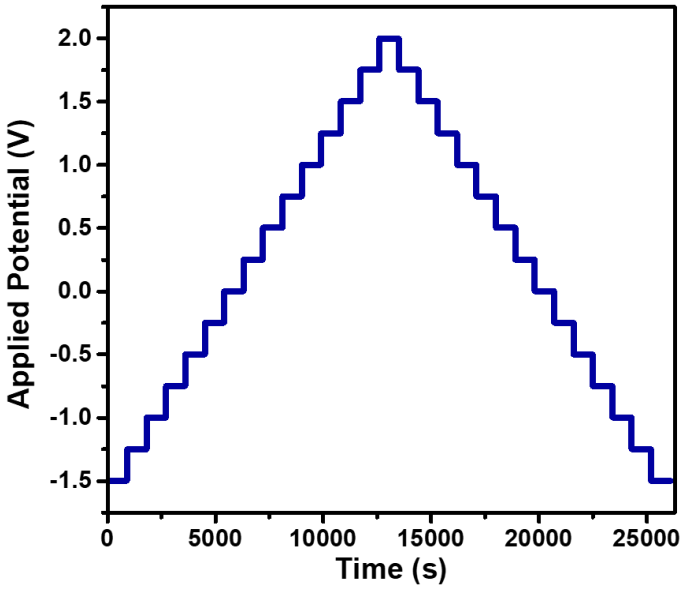

Figure 5.7: Potentiodynamic cycling with galvanostatic acceleration (PCGA) curve depicting the cycling of the electrochemical cell at the fixed potential for 15 min and then increasing with a step size of 250 mV within the potential range -1.5 V to +2.0 V.

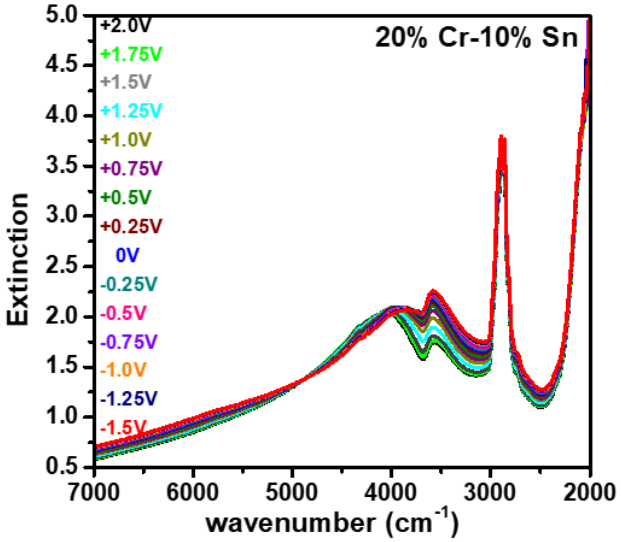

Figure 5.8: The SEC response of 20% Cr-10% Sn codoped In_2O_3 NCs in the potential range -1.5 V to +2.0 V as probed by *in situ* FTIR spectroscopy.

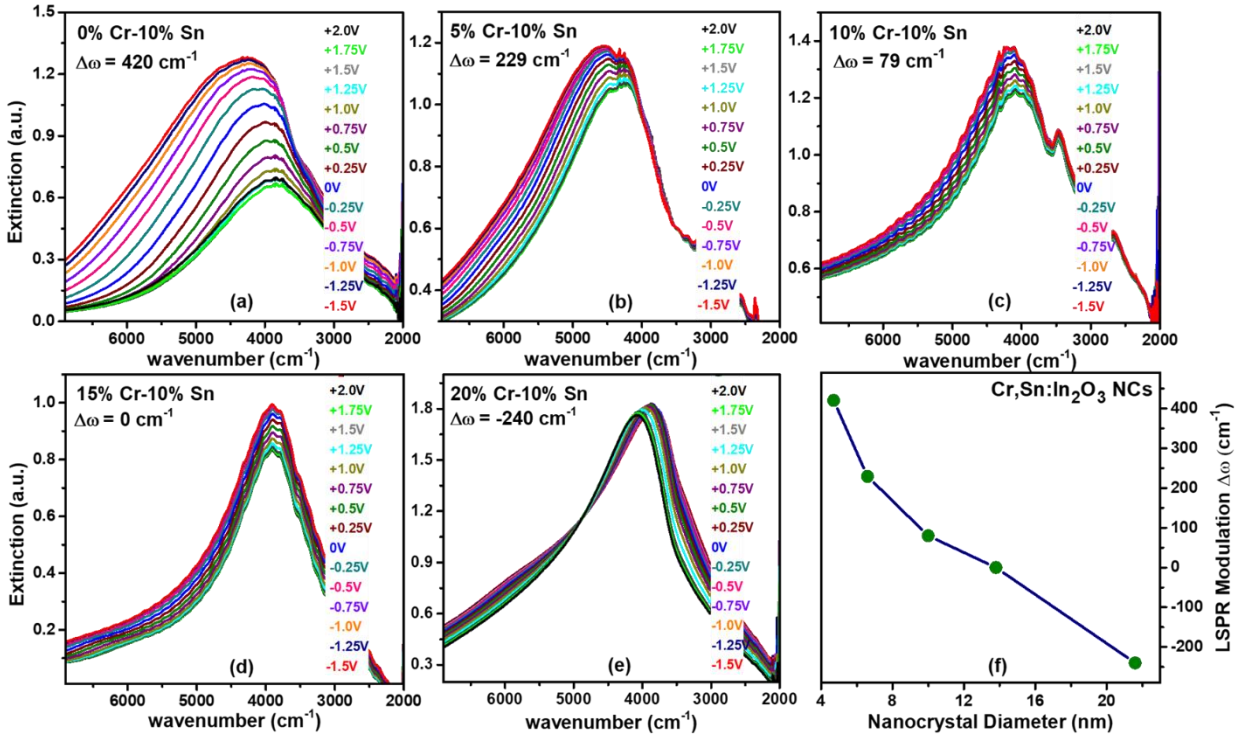

Figure 5.9: (a-e) Results of *in situ* FTIR SEC on different Cr-Sn codoped In_2O_3 NCs recorded during the reverse cycle from +2.0 V to -1.5 V at a step size of 250 mV. The spectra shown were obtained by backgrounding the FTIR signal of the NC electrochemical device with a blank device (no NCs). Δω represents the maximal LSPR frequency modulation and is obtained by subtracting the LSPR peak position at +2.0 V from the one at -1.5 V. The spectral bands observed due to absorbance by the electrolyte have been masked. (f) Summary of the LSPR modulation achieved as a function of NC size shows that the sign of modulation changes from positive to negative as the NC size is increased. Green circles are data points and the blue solid line is a guide to the eye.

A typical FTIR spectrum while potential is increased from -1.5 V to +2.0 V has contributions from LSPR of NCs, 0.1 M TBA-TFSI electrolyte in tetraglyme and Sn-doped In_2O_3 coated glass (Figure 5.8). To obtain the optical signature of LSPR active NC film, the FTIR signal of a blank device (without NCs) was subtracted from that of a NC device. The optical signature of the electrolyte and the Sn-doped In_2O_3 coated glass isn't expected to change with the change in applied potential.

For 0% Cr-10% Sn codoped In_2O_3 NCs (Figure 5.9a), there is a shift of LSPR peak to higher energy accompanied by an increase in the LSPR intensity as the applied potential becomes more reducing. These NCs are 4.7 nm in average diameter and therefore, even at the relatively high 10% Sn doping concentration the depletion region is expected to include a significant fraction of the total NC volume and, consequently, a large LSPR modulation of 420 cm^{-1} towards higher energy is observed. However, for larger NCs (10.0 nm) prepared by Cr codoping, we observe that the extent of frequency change decreases. We understand this, based on the related previous analysis as due to the diminished fraction of the NC volume represented by the depleted region.[27]

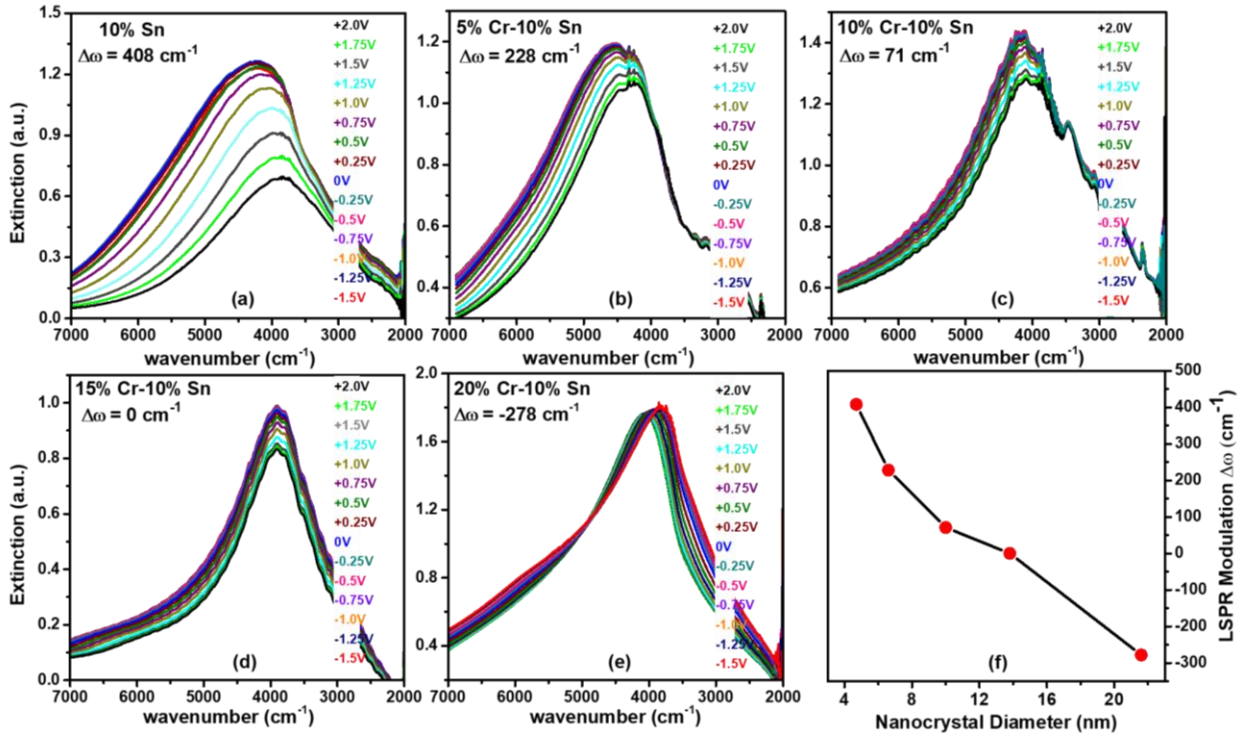

Figure 5.10: (a-e) Results of the *in situ* FTIR SEC on different Cr-Sn codoped In_2O_3 NCs recorded during the forward cycle from -1.5 V to +2.0 V at a step size of 250 mV. The spectra have been processed in the same manner as described in Figure 5.9 (f) LSPR modulation achieved as a function of NC size during the forward cycle shows the same trend as that obtained during the reverse cycle i.e. the sign of LSPR modulation changes from positive to negative as the NC size is increased. Red diamonds are data points and the black solid line is just a guide to the eye.

Surprisingly, as the size of NCs is further increased, the LSPR modulation passes beyond 0 cm^{-1} becomes negative, reaching -240 cm^{-1} for 21.6 nm sized 20% Cr-10% Sn codoped In_2O_3 NCs, with 13.9 nm 15% Cr-10% Sn codoped In_2O_3 NCs showing near-zero modulation (Figure 5.9). In other words, for these larger codoped NCs, the direction of the LSPR frequency shift reverses from that reported in all previous reports, shifting to lower energy on application of reducing potential. Similar values of LSPR modulation are observed for different NCs during the forward cycle from -1.5 to +2.0 V (Figure 5.10) and hence the trend of the LSPR shift is preserved during both the reverse (+2.0 V to -1.5V) and the forward cycle (-1.5 V to +2.0 V) (Figure 5.11).

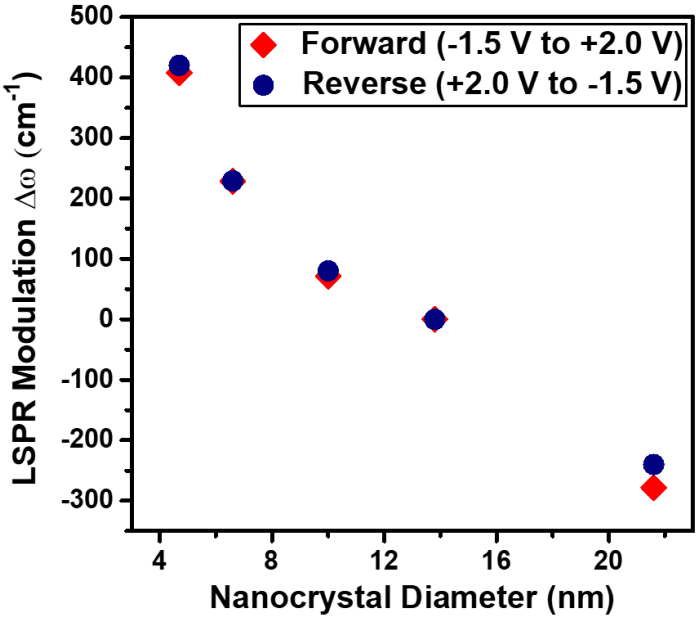

Figure 5.11: Summary of LSPR frequency modulation achieved as a function of NC size during the forward cycle (-1.5 V to +2.0 V) and reverse cycle (+2.0 V to -1.5 V) showing the same trend, *i.e.* the sign of net LSPR modulation changes from positive to negative as the NC size is increased.

5.3.4 Decoding the trend of LSPR modulation

In Cr-Sn codoped In_2O_3 NCs, we identify at least three factors that could potentially contribute to the differences in LSPR modulation as a function of NC size, namely (i) differences in LSPR coupling between NCs due to different NC volume fractions in their respective films (ii) contribution of the localized states of Cr dopants (iii) differences in LSPR coupling between NCs due to the different size of the NCs.

5.3.4A The role of NC volume fractions on the film

To assess the potential for different NC volume fraction, porosity was measured as a function of Cr doping concentration using EP (see Section 5.2.6 for measurement and analysis procedure, Figures 5.12 and 5.13a-e). EP measurements reveal minimal variation in porosity for different Cr-Sn codoped In_2O_3 NCs (Figure 5.13f). This result removed the first potential factor influencing LSPR modulation from consideration and suggests that the difference in LSPR coupling between NCs due to a diverse range of volume fraction in different NCs films isn't the principal factor leading to negative shifts in the LSPR modulation.

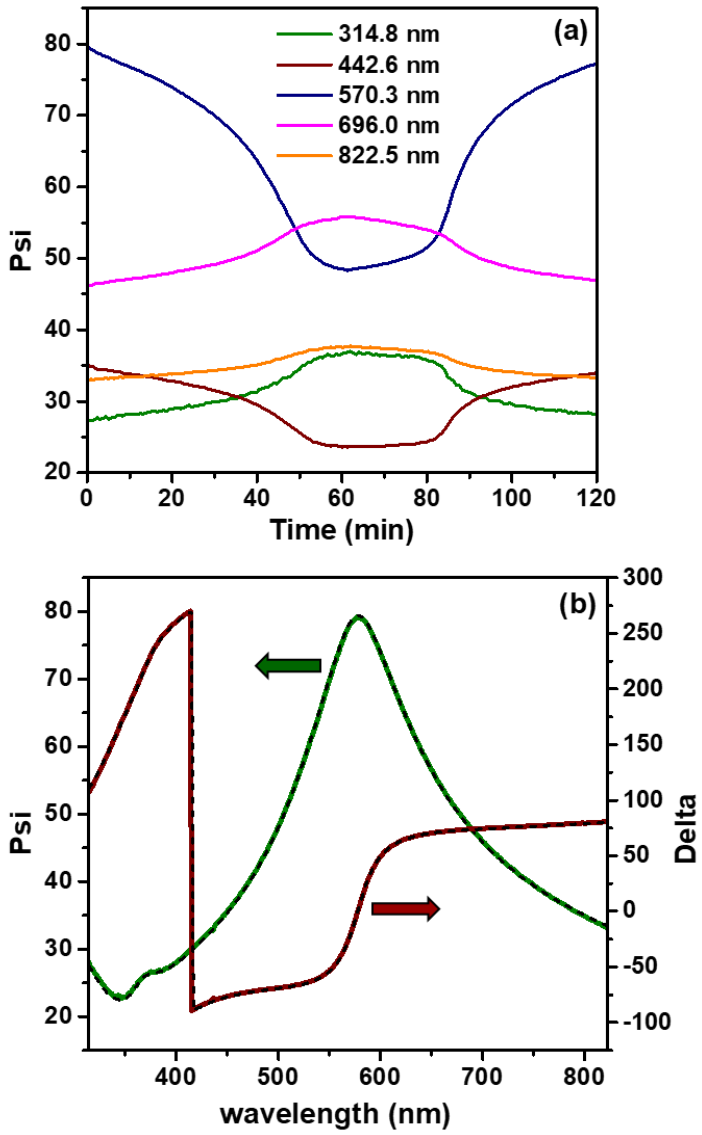

Figure 5.12: (a) Evolution of Psi with time as solvent toluene is incorporated into the NC film on a Si wafer under reduced pressure conditions (b) Fitting of Psi and Delta with optical models (dashed black line).

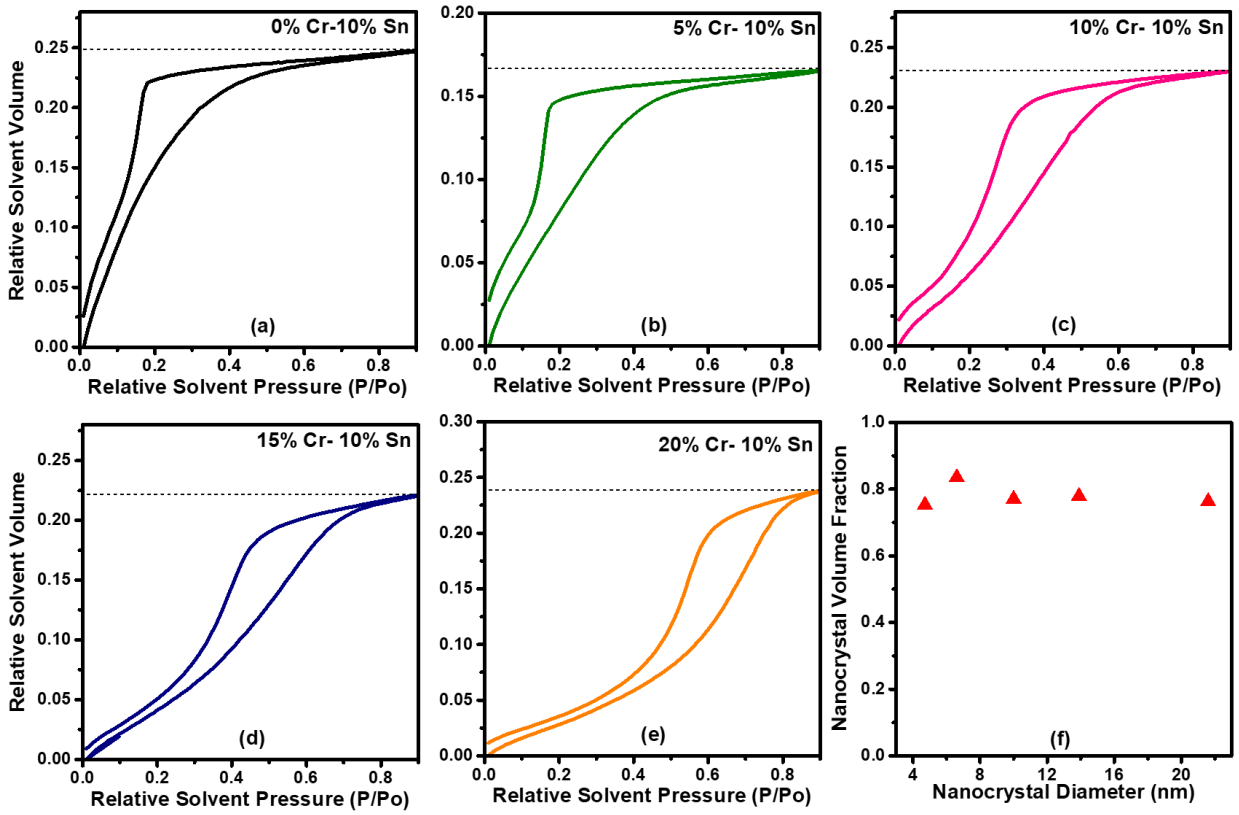

Figure 5.13: (a-e) Variation of relative solvent volume with relative solvent pressure for different Cr-Sn codoped In_2O_3 NCs in EP. The dashed black line at the maximum solvent volume represents the porosity of the film. (f) Volume fraction of NCs (derived from the porosity values obtained from EP) as a function of NC diameter showing no drastic change in the volume fraction of NCs in their corresponding films.

5.3.4B Contribution of the Cr localized states

Computational studies suggest that Cr doping in In_2O_3 introduces localized bands in the proximity of the In_2O_3 conduction band and these localized bands may either be situated deep inside the conduction band (CB),[39-40] or lie just below the conduction band minimum (CBM).[41] It is possible that while we tune the applied potential (changing the Fermi level at the surface), we may access redox processes involving the localized levels of Cr which would then contribute to either donating extra charge carriers to the CB or depleting the CB of electron density. To probe the above possibility, using an air-free sample holder, XPS measurements were performed on NC films charged at different potentials (see Section 5.2.6 for experimental details). XPS will detect any change in the oxidation state of Cr ions that would arise due the change in the binding energy of the Cr core levels resulting from charging or discharging of Cr localized state. XPS (Figure 5.14) shows that the peak positions of Cr 2p XPS peaks are nearly unaffected for different charging

potentials and correspond in all cases to an oxidation state of +3 with a binding energy of ~577.1 eV for $2p_{3/2}$ and a spin orbital splitting energy of 9.8 eV.[42] The binding energy corresponding to Cr^{3+} ions strongly suggests that the localized levels of Cr are not accessible within the electrochemical window utilized for the SEC measurements. This observation is consistent with calculations by Allipi et al. who found that Cr levels are expected to be at least 2 eV higher than the CBM of In_2O_3,[3] and hence not accessible with a -1.5 V reducing potential, which is even more likely to be the case when considering the CBM in our codoped NCs should be lowered substantially by the presence of Sn dopants.[43]

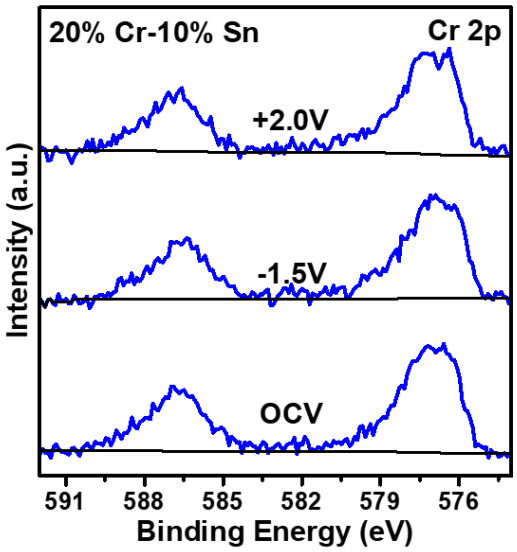

Figure 5.14: A comparison of Cr 2p XPS spectra at different charging potentials showing no change in the peak position indicating no role of Cr in modulating the LSPR spectra of NCs. The spectra have been shifted vertically for better representation.

5.3.4C Dominance of the LSPR coupling due to different NC diameters

To study the third factor, *i.e.*, differences in LSPR coupling between NCs due to their different diameters, a theoretical model was developed that takes into account the influence of depletion both on the optical properties of individual NCs and on the coupling between NCs, which together impact the LSPR modulation of NC films under applied potential (see Section 5.2.5 for simulation methods). The simulated band profiles (Figure 5.15a,b) and carrier concentration profiles (Figure 5.15c,d) show that for both sizes (4 nm and 22 nm) and reducing potentials, the depletion width is around 0.5 nm. However, this depletion width translates to 57% of the NC volume being depleted for 4 nm NCs while constituting only 13% of the volume lying in the depleted region for 22 nm NCs. This difference implies that the blue shift in LSPR due to changes in number of free carrier

and its spatial distribution as well as the surrounding dielectric environment will be much greater for 4 nm NCs compared to 22 nm NCs. Moreover, the ratio between the depletion width and radius of the particle (d/a), which determines the coupling strength between adjacent NCs in physical contact, is 0.25 for 4 nm NCs and 0.045 for 22 nm NCs. The low d/a for 22 nm NCs suggests that NC-NC optical coupling that leads to LSPR red shift[31-32] is much stronger for 22 nm NC compared to 4 nm NC, in agreement with the larger red shifts between dispersions and films that we observed at higher Cr concentration (Figure 5.4).

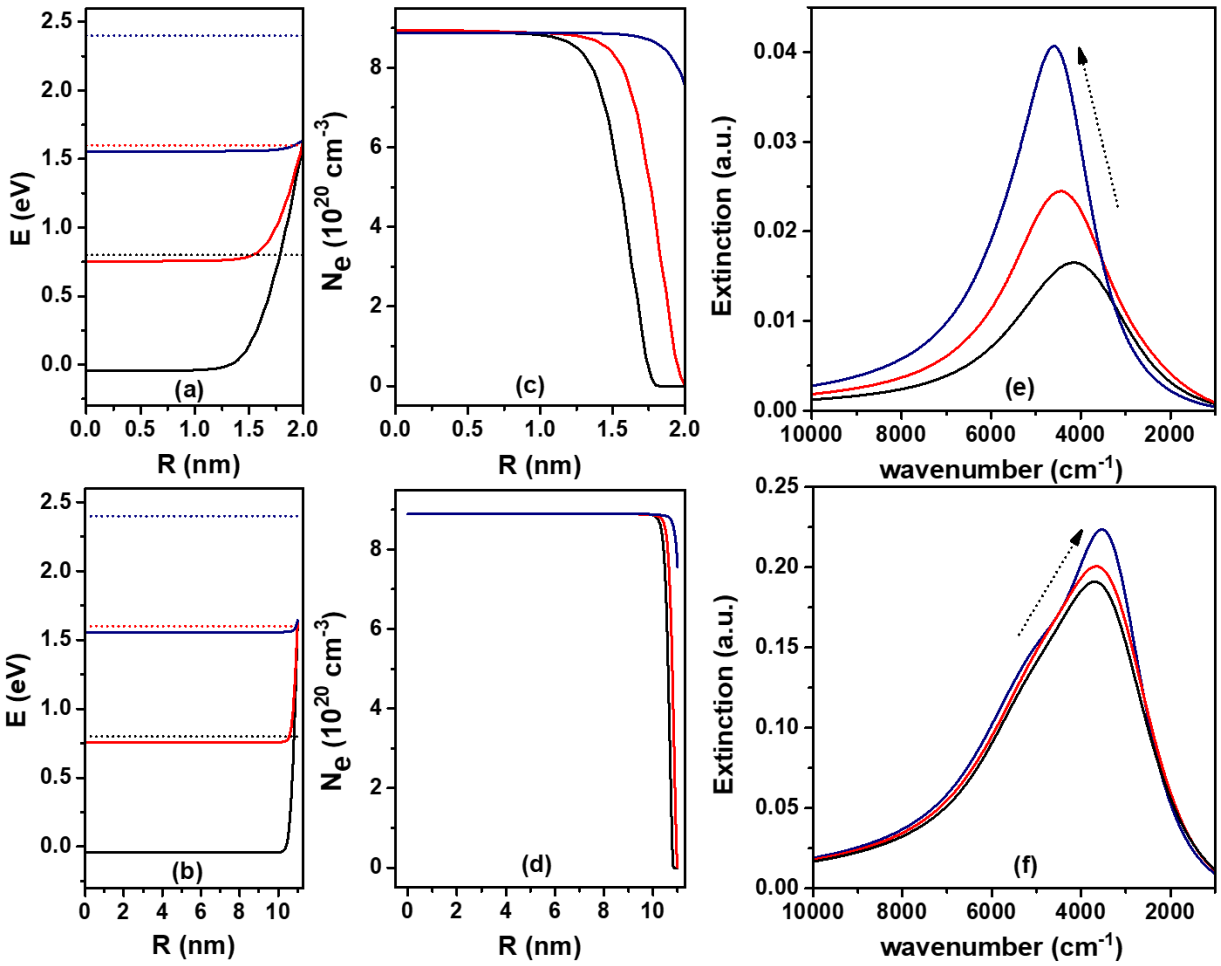

Figure 5.15: Simulated (a,b) band profiles (c,d) carrier concentration profile (e,f) optical extinction profiles for 10% Sn-doped In_2O_3 NCs with diameter 4 nm (top part) and 22 nm (bottom part) using a theoretical model that accounts for both depletion and LSPR coupling between NCs. Here R represents the nanocrystal diameter and E is the applied external potential. Black, red and blue curves in all panels correspond to surface potential equals 0.8, 1.6 and 2.4 eV, respectively. Flat band fermi level for 10% Sn-doped In_2O_3 NCs corresponds to 2.45 eV.

The simulated extinction spectra at variable applied potential shows that these differences in coupling strength change the balance between modulation due to NC coupling and isolated NC

effects in determining the net modulation of LSPR spectra. Specifically, at reducing potentials there a large LSPR blue shift toward higher energy for 4 nm NCs and a slight red shift for 22 nm NC (Figure 5.15e,f). The simulated trends are consistent with the experimental observations made by SEC. In the simulation, the predicted extent of red shift for 22 nm NCs was smaller than the observed experimental shift. This difference may arise from the assumption of uniform dopant distribution used to simplify the system for simulations, while Cr-Sn codoped In_2O_3 NCs have surface-rich Sn concentration, as mentioned above. Earlier, Staller et al. showed that the depletion width of Sn-doped In_2O_3 NCs with surface-rich Sn concentration is compressed compared to uniformly doped NCs.[29] The smaller depletion width will further increase NC-NC coupling leading to amplified red shifts of LSPR spectra, as observed in our experimental data.

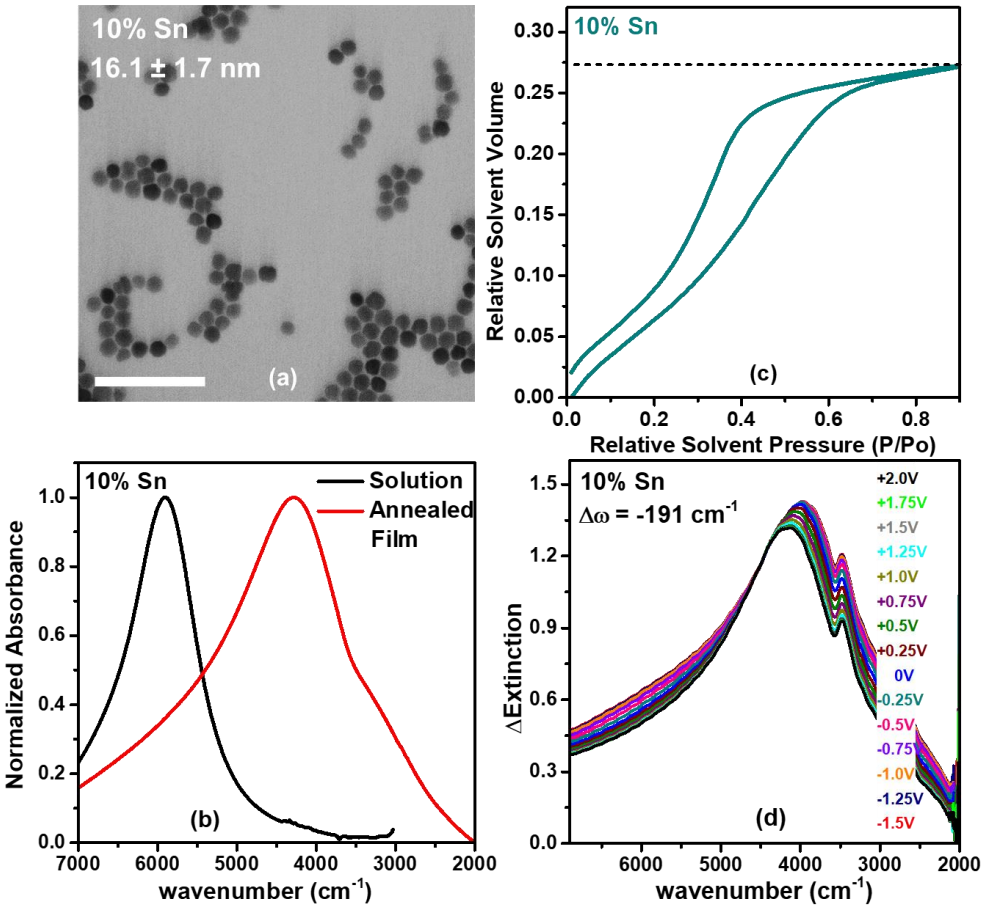

Figure 5.16: (a) STEM image of 10% Sn-doped In_2O_3 NCs synthesized by the slow-growth method. Scale bar is 100 nm. Image reproduced from Chapter-4A. (b) FTIR spectra of NCs in the solution phase and annealed film on Sn-doped In_2O_3 substrate. (c) Relative solvent volume vs relative solvent pressure curve obtained from EP indicating volume fraction of these NCs is similar to the Cr-Sn codoped In_2O_3 NCs in their corresponding films (d) *in situ* FTIR SEC of the Sn-doped In_2O_3 NCs showing a negative LSPR modulation on application of a reducing potential similar to Cr-Sn codoped In_2O_3 NCs with large diameters.

The influence of surface segregation on LSPR modulation should not be unique to Cr-Sn codoped In_2O_3 NCs, but universal to any In_2O_3 NCs with surface-rich doping. Accordingly, we synthesized 16.1 nm surface segregated Sn-doped In_2O_3 NCs (overall 6.4% Sn doping by ICP-AES, 11.6% near-surface Sn doping by XPS) (see Section 5.12 for synthesis details and Figure 5.16a for characterization). Similar to what was observed for Cr-Sn codoped In_2O_3 NCs, the spectrum of an annealed Sn-doped In_2O_3 NC film is significantly red shifted and broadened as compared to the spectrum of dispersed NCs (Figure 5.16b). The volume fraction (0.73) of the Sn-doped In_2O_3 NC film as obtained by EP is very similar to that obtained for Cr-Sn codoped In_2O_3 NCs (Figure 5.16c). Similar to our larger Cr-Sn codoped In_2O_3 NCs, the LSPR modulation of films of surface segregated Sn-doped In_2O_3 NCs displays negative LSPR modulation (-191 cm^{-1}) (Figure 5.16d). In contrast, for similar sized uniformly doped NCs, Zandi et al. previously reported a blue shift of LSPR spectra on application of reducing potentials.[27] These observations reinforce our earlier assertion that surface segregation of Sn dopants reduces the depletion width and results in stronger NC-NC coupling. Stronger coupling thus leads to the red shift of LSPR spectra for films of large and surface segregated NCs on application of reducing potentials.

5.4 Conclusions

In conclusion, using Cr-Sn codoped In_2O_3 NCs as a model system, we demonstrated that in addition to change in surrounding refractive index and carrier concentration, LSPR coupling between NCs plays a major role in determining the extent and nature of modulation of LSPR on application of external potential to NC films. When a reducing potential is applied, the plasmonically active NC volume expands, resulting in an increase in LSPR intensity and a shift of the LSPR peak to higher energy. On the other hand, these changes also increase LSPR coupling between NCs, which tends to decrease the intensity and broaden the LSPR while shifting it to lower energy. These effects trade off against one another and their relative importance is determined by the diameter of the NCs and the radial distribution of dopants within the NCs. For small NCs, the former factors dominate while for larger NCs, the depletion layer represents a small volume fraction and even a slight change in depletion width increases NC-NC optical coupling substantially, resulting in red shifting of LSPR spectra. These differences are amplified for large NCs with surface segregated Sn dopants wherein the depletion width is additionally compressed. Therefore, when progressing from small to large NCs with surface segregated dopants, we observed a transition of LSPR modulation from positive to negative values. These results

qualitatively change the NC design strategies for tuning LSPR modulation and even open the new opportunity to control the direction of LSPR shift (to lower or higher energy) upon electrochemical charging.

5.5 References

1. Kanehara, M.; Koike, H.; Yoshinaga, T.; Teranishi, T. Indium Tin Oxide Nanoparticles with Compositionally Tunable Surface Plasmon Resonance Frequencies in the Near-IR Region. *J. Am. Chem. Soc.* **2009,** *131*, 17736-17737.
2. Lounis, S. D.; Runnerstrom, E. L.; Bergerud, A.; Nordlund, D.; Milliron, D. J. Influence of Dopant Distribution on the Plasmonic Properties of Indium Tin Oxide Nanocrystals. *J. Am. Chem. Soc.* **2014,** *136*, 7110-7116.
3. Schimpf, A. M.; Lounis, S. D.; Runnerstrom, E. L.; Milliron, D. J.; Gamelin, D. R. Redox Chemistries and Plasmon Energies of Photodoped In_2O_3 and Sn-Doped In_2O_3 (ITO) Nanocrystals. *J. Am. Chem. Soc.* **2015,** *137*, 518-524.
4. Buonsanti, R.; Llordes, A.; Aloni, S.; Helms, B. A.; Milliron, D. J. Tunable Infrared Absorption and Visible Transparency of Colloidal Aluminum-Doped Zinc Oxide Nanocrystals. *Nano Lett.* **2011,** *11*, 4706-4710.
5. Gordon, T. R.; Paik, T.; Klein, D. R.; Naik, G. V.; Caglayan, H.; Boltasseva, A.; Murray, C. B. Shape-Dependent Plasmonic Response and Directed Self-Assembly in a New Semiconductor Building Block, Indium-Doped Cadmium Oxide (ICO). *Nano Lett.* **2013,** *13*, 2857-2863.
6. Ye, X.; Fei, J.; Diroll, B. T.; Paik, T.; Murray, C. B. Expanding the Spectral Tunability of Plasmonic Resonances in Doped Metal-Oxide Nanocrystals through Cooperative Cation–Anion Codoping. *J. Am. Chem. Soc.* **2014,** *136*, 11680-11686.
7. Luther, J. M.; Jain, P. K.; Ewers, T.; Alivisatos, A. P. Localized Surface Plasmon Resonances arising from Free Carriers in Doped Quantum Dots. *Nat. Mater.* **2011,** *10*, 361-366.
8. Dorfs, D.; Härtling, T.; Miszta, K.; Bigall, N. C.; Kim, M. R.; Genovese, A.; Falqui, A.; Povia, M.; Manna, L. Reversible Tunability of the Near-Infrared Valence Band Plasmon Resonance in $Cu_{2-x}Se$ Nanocrystals. *J. Am. Chem. Soc.* **2011,** *133*, 11175-11180.
9. Manthiram, K.; Alivisatos, A. P. Tunable Localized Surface Plasmon Resonances in Tungsten Oxide Nanocrystals. *J. Am. Chem. Soc.* **2012,** *134*, 3995-3998.
10. Faucheaux, J. A.; Stanton, A. L. D.; Jain, P. K. Plasmon Resonances of Semiconductor Nanocrystals: Physical Principles and New Opportunities. *J. Phys. Chem. Lett.* **2014,** *5*, 976-985.
11. Kovalenko, M. V.; Manna, L.; Cabot, A.; Hens, Z.; Talapin, D. V.; Kagan, C. R.; Klimov, V. I.; Rogach, A. L.; Reiss, P.; Milliron, D. J.; Guyot-Sionnnest, P.; Konstantatos, G.; Parak, W. J.; Hyeon, T.; Korgel, B. A.; Murray, C. B.; Heiss, W. Prospects of Nanoscience with Nanocrystals. *ACS Nano* **2015,** *9*, 1012-1057.
12. Agrawal, A.; Johns, R. W.; Milliron, D. J. Control of Localized Surface Plasmon Resonances in Metal Oxide Nanocrystals. *Ann. Rev. Mater. Res.* **2017,** *47*, 1-31.
13. Agrawal, A.; Cho, S. H.; Zandi, O.; Ghosh, S.; Johns, R. W.; Milliron, D. J. Localized Surface Plasmon Resonance in Semiconductor Nanocrystals. *Chem. Rev.* **2018,** *118*, 3121-3207.
14. Garcia, G.; Buonsanti, R.; Runnerstrom, E. L.; Mendelsberg, R. J.; Llordes, A.; Anders, A.; Richardson, T. J.; Milliron, D. J. Dynamically Modulating the Surface Plasmon Resonance of Doped Semiconductor Nanocrystals. *Nano Lett.* **2011,** *11*, 4415-4420.

15. Garcia, G.; Buonsanti, R.; Llordes, A.; Runnerstrom, E. L.; Bergerud, A.; Milliron, D. J. Near-Infrared Spectrally Selective Plasmonic Electrochromic Thin Films. *Adv. Opt. Mater.* **2013,** *1*, 215-220.
16. Mendelsberg, R. J.; McBride, P. M.; Duong, J. T.; Bailey, M. J.; Llordes, A.; Milliron, D. J.; Helms, B. A. Dispersible Plasmonic Doped Metal Oxide Nanocrystal Sensors that Optically Track Redox Reactions in Aqueous Media with Single-Electron Sensitivity. *Adv. Opt. Mater.* **2015,** *3*, 1293-1300.
17. Wang, Y.; Runnerstrom, E. L.; Milliron, D. J. Switchable Materials for Smart Windows. *Ann. Rev. Chem. Biomol. Eng.* **2016,** *7*, 283-304.
18. Ou, W.; Zou, Y.; Wang, K.; Gong, W.; Pei, R.; Chen, L.; Pan, Z.; Fu, D.; Huang, X.; Zhao, Y.; Lu, W.; Jiang, J. Active Manipulation of NIR Plasmonics: the Case of $Cu_{2-x}Se$ through Electrochemistry. *J. Phys. Chem. Lett.* **2018,** *9*, 274-280.
19. Llordés, A.; Garcia, G.; Gazquez, J.; Milliron, D. J. Tunable Near-Infrared and Visible-Light Transmittance in Nanocrystal-in-Glass Composites. *Nature* **2013,** *500*, 323-326.
20. Korgel, B. A. Composite for Smarter Windows. *Nature* **2013,** *500*, 278-279.
21. Runnerstrom, E. L.; Llordes, A.; Lounis, S. D.; Milliron, D. J. Nanostructured Electrochromic Smart Windows: Traditional Materials and NIR-Selective Plasmonic Nanocrystals. *Chem. Commun.* **2014,** *50*, 10555-10572.
22. Granqvist, C. G. Electrochromics for Smart Windows: Oxide-Based Thin Films and Devices. *Thin Solid Films* **2014,** *564*, 1-38.
23. Guo, P.; Schaller, R. D.; Ketterson, J. B.; Chang, R. P. H. Ultrafast Switching of Tunable Infrared Plasmons in Indium Tin Oxide Nanorod Arrays with Large Absolute Amplitude. *Nat. Photonics* **2016,** *10*, 267.
24. Heo, S.; Kim, J.; Ong, G. K.; Milliron, D. J. Template-Free Mesoporous Electrochromic Films on Flexible Substrates from Tungsten Oxide Nanorods. *Nano Lett.* **2017,** *17*, 5756-5761.
25. Jiang, N.; Zhuo, X.; Wang, J. Active Plasmonics: Principles, Structures, and Applications. *Chem. Rev.* **2017,** *118*, 3054-3099.
26. Granqvist, C. G.; Arvizu, M. A.; Bayrak Pehlivan, İ.; Qu, H. Y.; Wen, R. T.; Niklasson, G. A. Electrochromic Materials and Devices for Energy Efficiency and Human Comfort in Buildings: A Critical Review. *Electrochim. Acta* **2018,** *259*, 1170-1182.
27. Zandi, O.; Agrawal, A.; Shearer, A. B.; Reimnitz, L. C.; Dahlman, C. J.; Staller, C. M.; Milliron, D. J. Impacts of Surface Depletion on the Plasmonic Properties of Doped Semiconductor Nanocrystals. *Nat. Mater.* **2018,** *17*, 710-717.
28. Agrawal, A.; Kriegel, I.; Runnerstrom, E. L.; Scotognella, F.; Llordes, A.; Milliron, D. J. Rationalizing the Impact of Surface Depletion on Electrochemical Modulation of Plasmon Resonance Absorption in Metal Oxide Nanocrystals. *ACS Photonics* **2018,** *5*, 2044-2050.
29. Staller, C. M.; Robinson, Z. L.; Agrawal, A.; Gibbs, S. L.; Greenberg, B. L.; Lounis, S. D.; Kortshagen, U. R.; Milliron, D. J. Tuning Nanocrystal Surface Depletion by Controlling Dopant Distribution as a Route Toward Enhanced Film Conductivity. *Nano Lett.* **2018,** *18*, 2870-2878.
30. Nordlander, P.; Oubre, C.; Prodan, E.; Li, K.; Stockman, M. I. Plasmon Hybridization in Nanoparticle Dimers. *Nano Lett.* **2004,** *4*, 899-903.
31. Rechberger, W.; Hohenau, A.; Leitner, A.; Krenn, J. R.; Lamprecht, B.; Aussenegg, F. R. Optical Properties of Two Interacting Gold Nanoparticles. *Opt. Commun.* **2003,** *220*, 137-141.
32. Funston, A. M.; Novo, C.; Davis, T. J.; Mulvaney, P. Plasmon Coupling of Gold Nanorods at Short Distances and in Different Geometries. *Nano Lett.* **2009,** *9*, 1651-1658.

33. Tandon, B.; Yadav, A.; Khurana, D.; Reddy, P.; Santra, P. K.; Nag, A. Size-Induced Enhancement of Carrier Density, LSPR Quality Factor, and Carrier Mobility in Cr–Sn Doped In_2O_3 Nanocrystals. *Chem. Mater.* **2017,** *29*, 9360-9368.
34. Jansons, A. W.; Hutchison, J. E. Continuous Growth of Metal Oxide Nanocrystals: Enhanced Control of Nanocrystal Size and Radial Dopant Distribution. *ACS Nano* **2016,** *10*, 6942-6951.
35. Dong, A.; Ye, X.; Chen, J.; Kang, Y.; Gordon, T.; Kikkawa, J. M.; Murray, C. B. A Generalized Ligand-Exchange Strategy Enabling Sequential Surface Functionalization of Colloidal Nanocrystals. *J. Am. Chem. Soc.* **2011,** *133*, 998-1006.
36. Seiwatz, R.; Green, M. Space Charge Calculations for Semiconductors. *J. Appl. Phys.* **1958,** *29*, 1034-1040.
37. Handbook of X-ray Photoelectron Spectroscopy C. D. Wanger, W. M. Riggs, L. E. Davis, J. F. Moulder and G. E.Muilenberg Perkin-Elmer Corp., Physical Electronics Division, Eden Prairie, Minnesota, USA, 1979. 190.
38. Agrawal, A.; Singh, A.; Yazdi, S.; Singh, A.; Ong, G. K.; Bustillo, K.; Johns, R. W.; Ringe, E.; Milliron, D. J. Resonant Coupling between Molecular Vibrations and Localized Surface Plasmon Resonance of Faceted Metal Oxide Nanocrystals. *Nano Lett.* **2017,** *17*, 2611-2620.
39. Raebiger, H.; Lany, S.; Zunger, A. Electronic Structure, Donor and Acceptor Transitions, and Magnetism of 3d Impurities in In_2O_3 and ZnO. *Phys. Rev. B* **2009,** *79*, 165202.
40. Alippi, P.; Cesaria, M.; Fiorentini, V. Impurity-Vacancy Complexes and Ferromagnetism in Doped Sesquioxides. *Phys. Rev. B* **2014,** *89*, 134423.
41. Xu, J.; Liu, J. B.; Liu, B. X.; Li, S. N.; Wei, S. H.; Huang, B. Design of n-Type Transparent Conducting Oxides: The Case of Transition Metal Doping in In_2O_3. *Adv. Electron. Mater.* **2018,** *4*, 1700553.
42. Xing, G. Z.; Yi, J. B.; Wang, D. D.; Liao, L.; Yu, T.; Shen, Z. X.; Huan, C. H. A.; Sum, T. C.; Ding, J.; Wu, T. Strong Correlation between Ferromagnetism and Oxygen Deficiency in Cr-doped In_2O_3 Nanostructures. *Phys. Rev. B* **2009,** *79*, 174406.
43. Walsh, A.; Da Silva, J. L. F.; Wei, S.-H. Origins of Band-Gap Renormalization in Degenerately Doped Semiconductors. *Phys. Rev. B* **2008,** *78*, 075211.

Thesis Outlook and Future Directions

Thesis Outlook

From the data presented in this thesis and the conclusions drawn therein, a new understanding of defect chemistry of metal oxides, codoping in nanocrystals (NCs) and localized surface plasmon resonance (LSPR) modulation from metal oxide NCs can be drawn. While referring to the different objective of the thesis discussed in Chapter-1, this new understanding is summarized in different sections mentioned below.

A. The viability of codoping in NCs: By synthesizing codoped In_2O_3 NCs using different dopants through Chapter 2-4, we have provided enough experimental proof that codoping in these NCs is possible with a high doping efficiency. Recently synthesized F-In codoped CdO NCs[1] and F-Sn codoped In_2O_3 NCs[2] substantiate our claim of incorporating two different dopants in the host lattice. The lattice strain and charge imbalance introduced from the incorporation of dopants is partially balanced by a modification in the concentration of dopants and other point defects in the host. While we chose to incorporate dopants that enable the system to exhibit LSPR, high electrical conductivity, and magnetism, in principle, as long as the defect chemistry allows it, any combination of properties can be introduced in similar codoped NCs. We expect that in the years to come, the technique of codoping would allow synthesis of many new codoped systems with wide variety and combinations of properties.

B. Interactions in the codoped system: In Chapter-1 section 1.9, we described the different types of interactions that could result from codoping in NCs. We hypothesized that interactions could be observed between the two dopants Sn^{4+} and the transition metal ion, between the delocalized electron generated by Sn^{4+} codoping and the localized spins of the transition metal ion and, between the different properties introduced by the dopants.

In Chapter 2, we see an example of interactions between the two dopants where a small fraction of Fe^{3+} consumes some of the electrons released by Sn^{4+} and converts to Fe^{2+} which leads to tunability in LSPR and electrical conductivity. In Chapter 3 (and Chapter 2), we see an interaction between the functionalities introduced by the two dopants. The free electrons generated by Sn^{4+} mediated magnetic coupling between the localized spins of the transition metal dopant. In Chapter 5, we see an interaction between the two properties where the LSPR (an optical property) could be controlled by applying an electric potential (an electrical property). Even though the optoelectronic behavior of Sn-doped In_2O_3 NCs was already known in the literature, the primary factors

responsible for the LSPR modulation on applying an electric potential could only be revealed after this study. However, we have not explored the magneto-optics and magneto-electric properties from the codoped system till now and remain topics for future studies.

C. High Q-factor LSPR in metal oxide NCs: Through codoping Cr in Sn-doped In_2O_3 NCs, in Chapter-4A, we revealed that even within the quasi-static limit, LSPR is not independent of the size of the NCs. This anomaly doesn't come as a violation of the quasi-static approximation, rather due to the change in defect chemistry of Sn-doped In_2O_3 NCs as the size of the NCs is modified (while keeping the radial distribution almost constant). We achieved the highest Q-factor obtained from doped In_2O_3 NCs and one of the highest among doped semiconductor LSPR materials.

In Chapter-4B, we developed a selection strategy that would help to predict whether a dopant could give high Q-factor LSPR or not, even before the system is synthesized. This prediction strategy lead to a new LSPR system namely Zr-doped In_2O_3 NCs. The high Q-factor systems synthesized by us (Cr-Sn codoped In_2O_3 NCs, Zr-doped In_2O_3 NCs, Zr-Sn codoped In_2O_3 NCs) carry great potential for use in sensing, surface enhanced infrared absorption spectroscopy and near-field enhancement studies.

Future Direction:

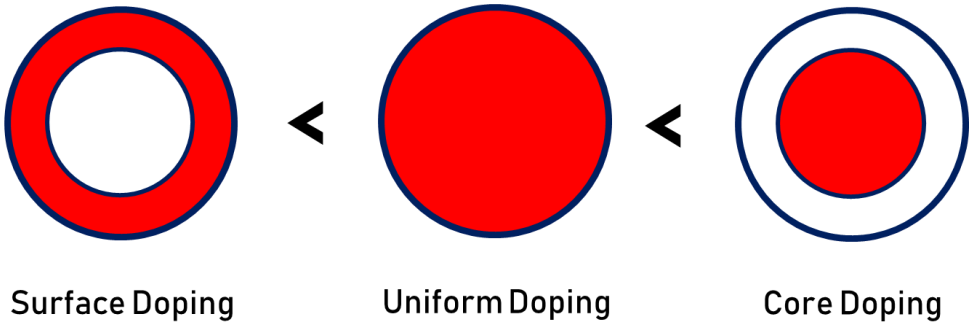

Figure 6.1: Since the width of the depletion layer at the surface would be dependent upon the number of ionized dopants near the surface, for the same doping percentage and size of the NCs, the depletion width or the volume fraction of the depletion layer would be least for surface segregated doping and highest for core segregated doping. These NCs have been arranged in order of increasing depletion width from left to right. Here the red shade represents presence of a dopant whereas white represents no doping.

Electrochemical modulation of LSPR is being perceived as a major application in future smart window materials. But the mechanistic insights of such LSPR modulation is not completely understood yet. As explained in Chapter-5, the surface of a doped semiconductor can contain a

depletion layer if the surface potential lies below the Fermi level. Just like in a p-n junction, this depletion layer is characterized with sharply reduced electron density at the surface and has been found to dictate the LSPR modulation under an applied potential.[3] Since, the width of the depletion layer is dependent upon the density of ionized dopants in the proximity of the space-charge region, we believe that other than through size and doping, the LSPR modulation would also be dependent upon the radial distribution of the dopant. As shown in the schematic in Figure 6.1, for the same doping percentage and size, the depletion width for uniformly doped NCs would be markedly different from core doped NCs and surface doped NCs.[4]

Therefore, to check the dependence of LSPR modulation on radial distribution of dopants, using already established synthesis protocol for control over size and radial distribution,[4-5] one can synthesize NCs such as those listed below.

(a) Different radial distribution such as in Figure 6.1 while keeping the same overall doping percentage and size.

(b) Different radial distribution for a low-doped NCs and highly-doped NCs.

(c) Different radial distribution for small-sized and large-sized NCs.

As proved in Chapter-5 that other than depletion effects, inter-NC LSPR coupling can also affect LSPR modulation. This proposed study would define limits of dominance for depletion effects and inter-NC LSPR coupling for NCs having different radial distribution.

References:

1. Ye, X.; Fei, J.; Diroll, B. T.; Paik, T.; Murray, C. B. Expanding the Spectral Tunability of Plasmonic Resonances in Doped Metal-Oxide Nanocrystals through Cooperative Cation–Anion Codoping. *J. Am. Chem. Soc.* **2014,** *136*, 11680-11686.
2. Agrawal, A.; Singh, A.; Yazdi, S.; Singh, A.; Ong, G. K.; Bustillo, K.; Johns, R. W.; Ringe, E.; Milliron, D. J. Resonant Coupling between Molecular Vibrations and Localized Surface Plasmon Resonance of Faceted Metal Oxide Nanocrystals. *Nano Lett.* **2017,** *17*, 2611-2620.
3. Zandi, O.; Agrawal, A.; Shearer, A. B.; Reimnitz, L. C.; Dahlman, C. J.; Staller, C. M.; Milliron, D. J. Impacts of Surface Depletion on the Plasmonic Properties of Doped Semiconductor Nanocrystals. *Nat. Mater.* **2018,** *17*, 710-717.
4. Staller, C. M.; Robinson, Z. L.; Agrawal, A.; Gibbs, S. L.; Greenberg, B. L.; Lounis, S. D.; Kortshagen, U. R.; Milliron, D. J. Tuning Nanocrystal Surface Depletion by Controlling Dopant Distribution as a Route Toward Enhanced Film Conductivity. *Nano Lett.* **2018,** *18*, 2870-2878.
5. Jansons, A. W.; Hutchison, J. E. Continuous Growth of Metal Oxide Nanocrystals: Enhanced Control of Nanocrystal Size and Radial Dopant Distribution. *ACS Nano* **2016,** *10*, 6942-6951.

List of Publications

Included in Thesis:

1. **Tandon, B**.; Shanker, G. S.; Nag, A.; "Multifunctional Sn- and Fe-Codoped In_2O_3 Colloidal Nanocrystals: Plasmonics and Magnetism" *J. Phys. Chem. Lett.* **2014,** *5*, 2306-2311.

2. Shanker, G. S.†; **Tandon, B**†.; Shibata, T†.; Chattopadhyay, S.; Nag, A.; "Doping Controls Plasmonics, Electrical Conductivity, and Carrier-Mediated Magnetic Coupling in Fe and Sn Codoped In_2O_3 Nanocrystals: Local Structure Is the Key" *Chem. Mater.* **2015**, *27*, 892-900. († = equal contribution)

3. **Tandon, B.**; Yadav, A.; Nag, A.; "Delocalized Electrons Mediated Magnetic Coupling in Mn-Sn codoped In_2O_3 NCs" *Chem. Mater.* **2016**, *28*, 3620-3624.

4. **Tandon, B.**; Yadav, A.; Khurana, D.; Reddy, P.; Santra, P. K.; Nag, A.; "Size-Induced Enhancement of Carrier Density, LSPR Quality Factor and, Carrier Mobility in Cr-Sn codoped In_2O_3 NCs, *Chem. Mater.* **2017**, *29*, 9360-9368.

5. **Tandon, B**.; Agrawal, A.; Heo, S.; Milliron D. J.; "Competition Between Depletion Effects and Coupling in Plasmon Modulation of Metal Oxide Nanocrystals" *Nano Lett.* **2019**, *19*, 2012-2019.

6. **Tandon, B.**; Ghosh, S.; Milliron, D. J.; "Dopant Selection Strategy for High Dopant Activation, LSPR Quality Factor and Carrier Mobility in Metal Oxide Nanocrystals" *Manuscript under preparation*

Not Included in Thesis:

7. **Tandon, B.**; Ashok, A.; Nag, A.; "Colloidal Transparent Conducting Oxide Nanocrystals: A New Infrared Plasmonic Material" *Pramana-J. Phys.* **2015**, *84*, 1087-1098.

8. Yadav, A.; **Tandon, B**; Nag, A; "Reduction of Mn^{3+} to Mn^{2+} and Near Infrared Plasmonics from Mn–Sn Codoped In_2O_3 Nanocrystals" *RSC Adv.* **2016**, *6*, 79153-79159.

Title: Tunable Infrared Absorption and Visible Transparency of Colloidal Aluminum-Doped Zinc Oxide Nanocrystals

Author: Raffaella Buonsanti, Anna Llordes, Shaul Aloni, et al

Publication: Nano Letters

Publisher: American Chemical Society

Date: Nov 1, 2011

PERMISSION/LICENSE IS GRANTED FOR YOUR ORDER AT NO CHARGE

This type of permission/license, instead of the standard Terms & Conditions, is sent to you because no fee is being charged for your order. Please note the following:

- Permission is granted for your request in both print and electronic formats, and translations.
- If figures and/or tables were requested, they may be adapted or used in part.
- Please print this page for your records and send a copy of it to your publisher/graduate school.
- Appropriate credit for the requested material should be given as follows: "Reprinted (adapted) with permission from (COMPLETE REFERENCE CITATION). Copyright (YEAR) American Chemical Society." Insert appropriate information in place of the capitalized words.
- One-time permission is granted only for the use specified in your request. No additional uses are granted (such as derivative works or other editions). For any other uses, please submit a new request.

If credit is given to another source for the material you requested, permission must be obtained from that source.

Title: Synthesis of Colloidal Mn2 :ZnO Quantum Dots and High-TC Ferromagnetic Nanocrystalline Thin Films

Author: Nick S. Norberg, Kevin R. Kittilstved, James E. Amonette, et al

Publication: Journal of the American Chemical Society

Publisher: American Chemical Society

Date: Aug 1, 2004

PERMISSION/LICENSE IS GRANTED FOR YOUR ORDER AT NO CHARGE

This type of permission/license, instead of the standard Terms & Conditions, is sent to you because no fee is being charged for your order. Please note the following:

- Permission is granted for your request in both print and electronic formats, and translations.
- If figures and/or tables were requested, they may be adapted or used in part.
- Please print this page for your records and send a copy of it to your publisher/graduate school.
- Appropriate credit for the requested material should be given as follows: "Reprinted (adapted) with permission from (COMPLETE REFERENCE CITATION). Copyright (YEAR) American Chemical Society." Insert appropriate information in place of the capitalized words.
- One-time permission is granted only for the use specified in your request. No additional uses are granted (such as derivative works or other editions). For any other uses, please submit a new request.

If credit is given to another source for the material you requested, permission must be obtained from that source.

Copyright Clearance Center

Note: Copyright.com supplies permissions but not the copyrighted content itself.

1 PAYMENT 2 REVIEW 3 CONFIRMATION

Step 3: Order Confirmation

Thank you for your order! A confirmation for your order will be sent to your account email address. If you have questions about your order, you can call us 24 hrs/day, M-F at +1.855.239.3415 Toll Free, or write to us at info@copyright.com. This is not an invoice.

Confirmation Number: 11782075
Order Date: 01/14/2019

If you paid by credit card, your order will be finalized and your card will be charged within 24 hours. If you choose to be invoiced, you can change or cancel your order until the invoice is generated.

Payment Information

Bharat Tandon
bharat.tandon@students.iiserpune.ac.in
+91 7028014655
Payment Method: n/a

Order Details

Chemical communications

Order detail ID:	71765019
Order License Id:	4507520706118
ISSN:	1364-548X
Publication Type:	e-Journal
Volume:	
Issue:	
Start page:	
Publisher:	ROYAL SOCIETY OF CHEMISTRY
Author/Editor:	Royal Society of Chemistry (Great Britain)

Permission Status: Granted

Permission type: Republish or display content
Type of use: Thesis/Dissertation

Requestor type	Academic institution
Format	Print, Electronic
Portion	image/photo
Number of images/photos requested	1
The requesting person/organization	Bharat Tandon
Title or numeric reference of the portion(s)	Chapter-1 Figure 1.3b
Title of the article or chapter the portion is from	Introduction
Editor of portion(s)	N/A

Author of portion(s)	Bharat Tandon
Volume of serial or monograph	N/A
Page range of portion	6
Publication date of portion	April 2019
Rights for	Main product
Duration of use	Life of current edition
Creation of copies for the disabled	no
With minor editing privileges	no
For distribution to	Worldwide
In the following language(s)	Original language of publication
With incidental promotional use	no
Lifetime unit quantity of new product	Up to 499
Title	Plasmonics and Magnetism from Doped Colloidal Indium Oxide Nanocrystals
Institution name	Indian Institute of Science Education and Research
Expected presentation date	Jan 2019

Note: This item will be invoiced or charged separately through CCC's **RightsLink** service. More info **$ 0.00**

Total order items: 1

This is not an invoice.

Order Total: 0.00 USD

Title: Free Electron Concentration in Colloidal Indium Tin Oxide Nanocrystals Determined by Their Size and Structure

Author: Ting Wang, Pavle V. Radovanovic

Publication: The Journal of Physical Chemistry C

Publisher: American Chemical Society

Date: Jan 1, 2011

PERMISSION/LICENSE IS GRANTED FOR YOUR ORDER AT NO CHARGE

This type of permission/license, instead of the standard Terms & Conditions, is sent to you because no fee is being charged for your order. Please note the following:

- Permission is granted for your request in both print and electronic formats, and translations.
- If figures and/or tables were requested, they may be adapted or used in part.
- Please print this page for your records and send a copy of it to your publisher/graduate school.
- Appropriate credit for the requested material should be given as follows: "Reprinted (adapted) with permission from (COMPLETE REFERENCE CITATION). Copyright (YEAR) American Chemical Society." Insert appropriate information in place of the capitalized words.
- One-time permission is granted only for the use specified in your request. No additional uses are granted (such as derivative works or other editions). For any other uses, please submit a new request.

If credit is given to another source for the material you requested, permission must be obtained from that source.

Title: Magnetic Quantum Dots: Synthesis, Spectroscopy, and Magnetism of Co2 - and Ni2 - Doped ZnO Nanocrystals

Author: Dana A. Schwartz, Nick S. Norberg, Quyen P. Nguyen, et al

Publication: Journal of the American Chemical Society

Publisher: American Chemical Society

Date: Oct 1, 2003

PERMISSION/LICENSE IS GRANTED FOR YOUR ORDER AT NO CHARGE

This type of permission/license, instead of the standard Terms & Conditions, is sent to you because no fee is being charged for your order. Please note the following:

- Permission is granted for your request in both print and electronic formats, and translations.
- If figures and/or tables were requested, they may be adapted or used in part.
- Please print this page for your records and send a copy of it to your publisher/graduate school.
- Appropriate credit for the requested material should be given as follows: "Reprinted (adapted) with permission from (COMPLETE REFERENCE CITATION). Copyright (YEAR) American Chemical Society." Insert appropriate information in place of the capitalized words.
- One-time permission is granted only for the use specified in your request. No additional uses are granted (such as derivative works or other editions). For any other uses, please submit a new request.

If credit is given to another source for the material you requested, permission must be obtained from that source.

Title: Localized Surface Plasmon Resonance in Semiconductor Nanocrystals

Author: Ankit Agrawal, Shin Hum Cho, Omid Zandi, et al

Publication: Chemical Reviews

Publisher: American Chemical Society

Date: Mar 1, 2018

PERMISSION/LICENSE IS GRANTED FOR YOUR ORDER AT NO CHARGE

This type of permission/license, instead of the standard Terms & Conditions, is sent to you because no fee is being charged for your order. Please note the following:

- Permission is granted for your request in both print and electronic formats, and translations.
- If figures and/or tables were requested, they may be adapted or used in part.
- Please print this page for your records and send a copy of it to your publisher/graduate school.
- Appropriate credit for the requested material should be given as follows: "Reprinted (adapted) with permission from (COMPLETE REFERENCE CITATION). Copyright (YEAR) American Chemical Society." Insert appropriate information in place of the capitalized words.
- One-time permission is granted only for the use specified in your request. No additional uses are granted (such as derivative works or other editions). For any other uses, please submit a new request.

If credit is given to another source for the material you requested, permission must be obtained from that source.

Copyright Clearance Center

Note: Copyright.com supplies permissions but not the copyrighted content itself.

1 PAYMENT 2 REVIEW 3 CONFIRMATION

Step 3: Order Confirmation

Thank you for your order! A confirmation for your order will be sent to your account email address. If you have questions about your order, you can call us 24 hrs/day, M-F at +1.855.239.3415 Toll Free, or write to us at info@copyright.com. This is not an invoice.

Confirmation Number: 11782078
Order Date: 01/14/2019

If you paid by credit card, your order will be finalized and your card will be charged within 24 hours. If you choose to be invoiced, you can change or cancel your order until the invoice is generated.

Payment Information

Bharat Tandon
bharat.tandon@students.iiserpune.ac.in
+91 7028014655
Payment Method: n/a

Order Details

Annual review of physical chemistry

Order detail ID:	71765023
Order License Id:	4507520940106
ISSN:	1545-1593
Publication Type:	e-Journal
Volume:	
Issue:	
Start page:	
Publisher:	ANNUAL REVIEWS

Permission Status: Granted

Permission type: Republish or display content
Type of use: Thesis/Dissertation

Requestor type	Academic institution
Format	Print, Electronic
Portion	image/photo
Number of images/photos requested	1
The requesting person/organization	Bharat Tandon
Title or numeric reference of the portion(s)	Chapter-1 Figure 1.6
Title of the article or chapter the portion is from	Introduction
Editor of portion(s)	N/A

Author of portion(s)	Bharat Tandon
Volume of serial or monograph	N/A
Page range of portion	9
Publication date of portion	April 2019
Rights for	Main product
Duration of use	Life of current edition
Creation of copies for the disabled	no
With minor editing privileges	no
For distribution to	Worldwide
In the following language(s)	Original language of publication
With incidental promotional use	no
Lifetime unit quantity of new product	Up to 499
Title	Plasmonics and Magnetism from Doped Colloidal Indium Oxide Nanocrystals
Institution name	Indian Institute of Science Education and Research
Expected presentation date	Jan 2019

Note: This item will be invoiced or charged separately through CCC's **RightsLink** service. More info **$ 0.00**

Total order items: 1

This is not an invoice.

Order Total: 0.00 USD

Title: Indium Tin Oxide Nanoparticles with Compositionally Tunable Surface Plasmon Resonance Frequencies in the Near-IR Region

Author: Masayuki Kanehara, Hayato Koike, Taizo Yoshinaga, et al

Publication: Journal of the American Chemical Society

Publisher: American Chemical Society

Date: Dec 1, 2009

PERMISSION/LICENSE IS GRANTED FOR YOUR ORDER AT NO CHARGE

This type of permission/license, instead of the standard Terms & Conditions, is sent to you because no fee is being charged for your order. Please note the following:

- Permission is granted for your request in both print and electronic formats, and translations.
- If figures and/or tables were requested, they may be adapted or used in part.
- Please print this page for your records and send a copy of it to your publisher/graduate school.
- Appropriate credit for the requested material should be given as follows: "Reprinted (adapted) with permission from (COMPLETE REFERENCE CITATION). Copyright (YEAR) American Chemical Society." Insert appropriate information in place of the capitalized words.
- One-time permission is granted only for the use specified in your request. No additional uses are granted (such as derivative works or other editions). For any other uses, please submit a new request.

If credit is given to another source for the material you requested, permission must be obtained from that source.

Title: Reversible Tunability of the Near-Infrared Valence Band Plasmon Resonance in Cu2−xSe Nanocrystals

Author: Dirk Dorfs, Thomas Härtling, Karol Miszta, et al

Publication: Journal of the American Chemical Society

Publisher: American Chemical Society

Date: Jul 1, 2011

PERMISSION/LICENSE IS GRANTED FOR YOUR ORDER AT NO CHARGE

This type of permission/license, instead of the standard Terms & Conditions, is sent to you because no fee is being charged for your order. Please note the following:

- Permission is granted for your request in both print and electronic formats, and translations.
- If figures and/or tables were requested, they may be adapted or used in part.
- Please print this page for your records and send a copy of it to your publisher/graduate school.
- Appropriate credit for the requested material should be given as follows: "Reprinted (adapted) with permission from (COMPLETE REFERENCE CITATION). Copyright (YEAR) American Chemical Society." Insert appropriate information in place of the capitalized words.
- One-time permission is granted only for the use specified in your request. No additional uses are granted (such as derivative works or other editions). For any other uses, please submit a new request.

If credit is given to another source for the material you requested, permission must be obtained from that source.

Title: Dynamically Modulating the Surface Plasmon Resonance of Doped Semiconductor Nanocrystals

Author: Guillermo Garcia, Raffaella Buonsanti, Evan L. Runnerstrom, et al

Publication: Nano Letters

Publisher: American Chemical Society

Date: Oct 1, 2011

PERMISSION/LICENSE IS GRANTED FOR YOUR ORDER AT NO CHARGE

This type of permission/license, instead of the standard Terms & Conditions, is sent to you because no fee is being charged for your order. Please note the following:

- Permission is granted for your request in both print and electronic formats, and translations.
- If figures and/or tables were requested, they may be adapted or used in part.
- Please print this page for your records and send a copy of it to your publisher/graduate school.
- Appropriate credit for the requested material should be given as follows: "Reprinted (adapted) with permission from (COMPLETE REFERENCE CITATION). Copyright (YEAR) American Chemical Society." Insert appropriate information in place of the capitalized words.
- One-time permission is granted only for the use specified in your request. No additional uses are granted (such as derivative works or other editions). For any other uses, please submit a new request.

If credit is given to another source for the material you requested, permission must be obtained from that source.

SPRINGER NATURE

Title: Tunable near-infrared and visible-light transmittance in nanocrystal-in-glass composites

Author: Anna Llordés, Guillermo Garcia, Jaume Gazquez, Delia J. Milliron

Publication: Nature

Publisher: Springer Nature

Date: Aug 14, 2013

Order Completed

Thank you for your order.

This Agreement between Bharat Tandon ("You") and Springer Nature ("Springer Nature") consists of your license details and the terms and conditions provided by Springer Nature and Copyright Clearance Center.

Your confirmation email will contain your order number for future reference.

printable details

License Number	4482390467756
License date	Dec 05, 2018
Licensed Content Publisher	Springer Nature
Licensed Content Publication	Nature
Licensed Content Title	Tunable near-infrared and visible-light transmittance in nanocrystal-in-glass composites
Licensed Content Author	Anna Llordés, Guillermo Garcia, Jaume Gazquez, Delia J. Milliron
Licensed Content Date	Aug 14, 2013
Licensed Content Volume	500
Licensed Content Issue	7462
Type of Use	Thesis/Dissertation
Requestor type	academic/university or research institute
Format	print and electronic
Portion	figures/tables/illustrations
Number of figures/tables/illustrations	1

High-res required	no
Will you be translating?	no
Circulation/distribution	<501
Author of this Springer Nature content	no
Title	Bharat Tandon
Institution name	Indian Institute of Science Education and Research
Expected presentation date	Apr 2019
Portions	Figure S1
Requestor Location	Bharat Tandon Department of Chemistry IISER-Pune Dr. Homi Bhabha Road Pune, Maharashtra 411008 India Attn: Bharat Tandon
Billing Type	Invoice
Billing address	Bharat Tandon Department of Chemistry IISER-Pune Dr. Homi Bhabha Road Pune, India 411008 Attn: Bharat Tandon
Total	0.00 USD

ORDER MORE CLOSE WINDOW

Title: Multifunctional Sn- and Fe-Codoped In2O3 Colloidal Nanocrystals: Plasmonics and Magnetism

Author: Bharat Tandon, G. Shiva Shanker, Angshuman Nag

Publication: Journal of Physical Chemistry Letters

Publisher: American Chemical Society

Date: Jul 1, 2014

PERMISSION/LICENSE IS GRANTED FOR YOUR ORDER AT NO CHARGE

This type of permission/license, instead of the standard Terms & Conditions, is sent to you because no fee is being charged for your order. Please note the following:

- Permission is granted for your request in both print and electronic formats, and translations.
- If figures and/or tables were requested, they may be adapted or used in part.
- Please print this page for your records and send a copy of it to your publisher/graduate school.
- Appropriate credit for the requested material should be given as follows: "Reprinted (adapted) with permission from (COMPLETE REFERENCE CITATION). Copyright (YEAR) American Chemical Society." Insert appropriate information in place of the capitalized words.
- One-time permission is granted only for the use specified in your request. No additional uses are granted (such as derivative works or other editions). For any other uses, please submit a new request.

Title: Doping Controls Plasmonics, Electrical Conductivity, and Carrier-Mediated Magnetic Coupling in Fe and Sn Codoped In2O3 Nanocrystals: Local Structure Is the Key

Author: G. Shiva Shanker, Bharat Tandon, Tomohiro Shibata, et al

Publication: Chemistry of Materials

Publisher: American Chemical Society

Date: Feb 1, 2015

PERMISSION/LICENSE IS GRANTED FOR YOUR ORDER AT NO CHARGE

This type of permission/license, instead of the standard Terms & Conditions, is sent to you because no fee is being charged for your order. Please note the following:

- Permission is granted for your request in both print and electronic formats, and translations.
- If figures and/or tables were requested, they may be adapted or used in part.
- Please print this page for your records and send a copy of it to your publisher/graduate school.
- Appropriate credit for the requested material should be given as follows: "Reprinted (adapted) with permission from (COMPLETE REFERENCE CITATION). Copyright (YEAR) American Chemical Society." Insert appropriate information in place of the capitalized words.
- One-time permission is granted only for the use specified in your request. No additional uses are granted (such as derivative works or other editions). For any other uses, please submit a new request.

Title: Delocalized Electrons Mediated Magnetic Coupling in Mn–Sn Codoped In2O3 Nanocrystals: Plasmonics Shows the Way

Author: Bharat Tandon, Anur Yadav, Angshuman Nag

Publication: Chemistry of Materials

Publisher: American Chemical Society

Date: Jun 1, 2016

PERMISSION/LICENSE IS GRANTED FOR YOUR ORDER AT NO CHARGE

This type of permission/license, instead of the standard Terms & Conditions, is sent to you because no fee is being charged for your order. Please note the following:

- Permission is granted for your request in both print and electronic formats, and translations.
- If figures and/or tables were requested, they may be adapted or used in part.
- Please print this page for your records and send a copy of it to your publisher/graduate school.
- Appropriate credit for the requested material should be given as follows: "Reprinted (adapted) with permission from (COMPLETE REFERENCE CITATION). Copyright (YEAR) American Chemical Society." Insert appropriate information in place of the capitalized words.
- One-time permission is granted only for the use specified in your request. No additional uses are granted (such as derivative works or other editions). For any other uses, please submit a new request.

Title: Size-Induced Enhancement of Carrier Density, LSPR Quality Factor, and Carrier Mobility in Cr–Sn Doped In2O3 Nanocrystals

Author: Bharat Tandon, Anur Yadav, Deepak Khurana, et al

Publication: Chemistry of Materials

Publisher: American Chemical Society

Date: Nov 1, 2017

PERMISSION/LICENSE IS GRANTED FOR YOUR ORDER AT NO CHARGE

This type of permission/license, instead of the standard Terms & Conditions, is sent to you because no fee is being charged for your order. Please note the following:

- Permission is granted for your request in both print and electronic formats, and translations.
- If figures and/or tables were requested, they may be adapted or used in part.
- Please print this page for your records and send a copy of it to your publisher/graduate school.
- Appropriate credit for the requested material should be given as follows: "Reprinted (adapted) with permission from (COMPLETE REFERENCE CITATION). Copyright (YEAR) American Chemical Society." Insert appropriate information in place of the capitalized words.
- One-time permission is granted only for the use specified in your request. No additional uses are granted (such as derivative works or other editions). For any other uses, please submit a new request.

Title: Competition between Depletion Effects and Coupling in the Plasmon Modulation of Doped Metal Oxide Nanocrystals

Author: Bharat Tandon, Ankit Agrawal, Sungyeon Heo, et al

Publication: Nano Letters

Publisher: American Chemical Society

Date: Mar 1, 2019

PERMISSION/LICENSE IS GRANTED FOR YOUR ORDER AT NO CHARGE

This type of permission/license, instead of the standard Terms & Conditions, is sent to you because no fee is being charged for your order. Please note the following:

- Permission is granted for your request in both print and electronic formats, and translations.
- If figures and/or tables were requested, they may be adapted or used in part.
- Please print this page for your records and send a copy of it to your publisher/graduate school.
- Appropriate credit for the requested material should be given as follows: "Reprinted (adapted) with permission from (COMPLETE REFERENCE CITATION). Copyright (YEAR) American Chemical Society." Insert appropriate information in place of the capitalized words.
- One-time permission is granted only for the use specified in your request. No additional uses are granted (such as derivative works or other editions). For any other uses, please submit a new request.